

Integrated multimodality imaging for tissue diagnostics

Joseph, James

2013

Joseph, J. (2013). Integrated multimodality imaging for tissue diagnostics. Doctoral thesis, Nanyang Technological University, Singapore.

<https://hdl.handle.net/10356/54859>

<https://doi.org/10.32657/10356/54859>

INTEGRATED MULTIMODALITY IMAGING FOR TISSUE DIAGNOSTICS



James Joseph

A thesis submitted to the Nanyang Technological University in partial
fulfilment of the requirement for the degree of Doctor of Philosophy

School of Mechanical and Aerospace Engineering

Nanyang Technological University, Singapore

2013

INTEGRATED MULTIMODALITY IMAGING FOR TISSUE DIAGNOSTICS

James Joseph

A thesis submitted to the Nanyang Technological University in partial
fulfilment of the requirement for the degree of Doctor of Philosophy

School of Mechanical and Aerospace Engineering

Nanyang Technological University, Singapore

2013

“GOD IS LIGHT”†

“IT IS THE GLORY OF GOD TO CONCEAL A THING”†;

*“BUT A PRIVILEGE AND RESPONSIBILITY OF A SCIENTIFIC
RESEARCHER TO SEARCH FOR IT”*

† *Genesis 1:28*

† *Proverbs 25: 2*

ACKNOWLEDGEMENTS

My personal experiences show that when god showers gifts to his children, they nearly always come in the form of great fellow humans. Apparently, this has been again proven right to me during my research studies at Nanyang Technological University (NTU), Singapore. My profuse thanks are due to god almighty and all the wonderful people who made these last six years a truly rewarding and enjoyable time period.

This research thesis would never have gone by without the consistent support, guidance, encouragement and patience of my beloved and much respected thesis advisors, Prof. Lye Sun Woh and Prof. Murukeshan Vadakke Matham. They were always considerate and tolerant during the tough stages of my research. It really has been a truly delightful and enjoyable experience to work under their guidance. I really appreciate and earnestly thank them for their genuine efforts offered and their confidence in me throughout my research career at NTU. My heartfelt thanks to Prof. Muru for supporting me with a research job from the expiry of my stipend.

Dr. Krishnan Sathiyamoorthy had been a great mentor and truly an elder brother to me throughout my research. His great attitude towards educating and inspiring students with his cool head and experienced hands really inspired me to learn and apply several optical instrumentation skills. I greatly acknowledge and thank him for his sincere support and guidance along my journey through the world of optics. Dr. Sreejith Sivaramapanicker was always an encouragement for me to dwell into the world of chemicals where his patient guidance and support helped me to foresee the tremendous capabilities of nanoparticles in biology.

I am proud and delighted to count many of the lab mates, friends and my housemates who were always there to support and encourage me. I really wouldn't have enjoyed my life at NTU without their presence. I am also much thankful Mr. Antony and his family for their love and compassion during my stay in Singapore. I really felt home at your place.

Dr. Wei Jun and Dr. Ying Ming from Singapore Institute of Manufacturing Technology (SIMTech) supported me with their experimental equipment. Many thanks for their generous support. The technical staffs at NTU were truly great and consistently helpful; sincere thanks to Mr. Chia, Mr. Eng Cheng, Ms. Agnes, Mr. Yu, Mr. Teck Meng, Ms. Jace, Ms. Esther and Mr. Soh.

I also acknowledge Nanyang Technological University, Singapore for the financial support.

Finally and firstly, this research thesis is dedicated to my parents and siblings who were always there for me with their unflinching love, support and prayers. My heartfelt thanks to my dearest parents, Joseph Antony and Jolly Joseph and my siblings, Negel and Merin.

ABSTRACT

Imaging technologies based on distinct energy sources are capable of probing complex and dynamic biological processes. Multiple imaging modalities are widely used to interrogate the subject to derive information about the complex structural and bio-molecular heterogeneities of its tissues. Although the various multi-modal imaging approaches satisfy certain clinical requirements, the level of information that can be obtained in terms of accurate registration and localisation of imaging features is constrained requiring quite long interrogation times possibly exposing to harmful ionising radiations. Further, there are no imaging schemes or very little reported works which can employ only non-ionizing radiations for multi-scale and multi-level information from the diagnosed sample. A novel multimodality system has been successfully developed that combines and integrates selected individual modalities of non-ionizing radiations such as ultrasound and optical energies together to map multi-level and multi-scale complementary information from phantom tissues. This necessitated the establishment of configuration schemes, methodologies and algorithms.

Two variants of fluorescent microscopy systems were configured, investigated and compared, namely; inverted fluorescence microscope and flexible fluorescent microscope based on image fiber bundle (fluorescent microendoscope). The inverted fluorescence microscopy system was able to image at different focal planes of the sample and the lateral resolution measurements of sub-micron resolution while working with a 0.8 NA or higher NA objective lenses. The microendoscopy system configured with a gradient refractive index (GRIN) lens assembly at its distal end exhibited lateral and axial resolutions of $3.47\text{ }\mu\text{m}$ and $16\pm$

0.65 μm respectively. Imaging studies performed using carboxylate-modified polystyrene microspheres coated with Nile red showed that both systems can image fluorescent features from tissue surface achieving micron or sub-micron resolutions.

A proposed ultrasound imaging system having a 128 element linear array transducer supported with high end firmware and advanced post processing concepts was also developed. The system can achieve signal-to-noise ratio of 68 dB and 110 dB for single channel and whole system respectively. The in-plane and axial resolution of the system readings were $345 \pm 2.53 \mu\text{m}$ and $151 \pm 2.24 \mu\text{m}$ respectively. Imaging studies performed on a silicone based phantom showed that the ultrasound modality system was imaging at frame rate of 68 fps from depths greater than 2.5 cm.

Theoretical formulations and numerical studies to investigate the photoacoustic signal profile generated from spherical and planar geometries upon delta pulse excitation were conducted. Further, finite difference time domain (FDTD) based simulation models and related protocols for the determination of the optical properties of gold nanoparticles were formulated, modelled and verified. Selective multiple molecular targeting photoacoustic studies were demonstrated using gold nanorods with distinct aspect ratios. Further, multi-element transducer based on the photoacoustic imaging (PAI) system was established. The dual wavelength excitation of the phantom sample showed that the photoacoustic based mapping of optical absorption variations along the depth of the tissue could be performed. The imaging capabilities of the PAI system were also significantly enhanced by using spatial compounding and persistence techniques.

Two novel contrast enhancement mechanisms with fluorophore–metal nanoparticle systems and a novel hybrid nanoparticle were also formulated and examined using dual- optical mode detection and imaging scheme. Correlation of the emission intensities with the photoacoustic signal amplitudes showed that the enhancements in photoacoustic signals in the fluorophore–metal nanoparticle systems were owing to the increased heat generation from fluorescence quenching. Experimental studies on the nanohybrid showed that the permanent electrostatic wrapping of two dimensional GO on Au (22 nm)-SiO₂ (44nm) core-shell nanostructure enhanced the collective residual absorption of the final hybrid (GO-SiO₂@AuNP) at 527 nm excitation.

A novel integrated multi-modality integrated model implemented on two types of multi-modal imaging system (PAUSFI) (desktop version and flexible version) has been established. Both developed systems are able to perform and characterise near-simultaneous photoacoustic (PA), ultrasound (US) and fluorescence (FI) imaging. All the three forms of imaging modalities could map their targeted imaging features respectively. Thus, Multi-level optical and acoustic heterogeneities (complementary information) along the depth of the tissue at multi-scale resolution (<1 μ m to <0.5 mm) were obtained.

Table of Contents

Acknowledgements.....	III
Abstract.....	V
Table of Contents.....	VIII
List of Figures.....	XIV
List of Tables.....	XX
List of Symbols.....	XXII
List of Acronyms.....	XXV
Chapter 1: INTRODUCTION	1
1.1 Background Information and Motivation	1
1.2 Objective.	5
1.3 Scope.....	6
1.4 Organization of the Thesis	8
Chapter 2: LITERATURE REVIEW	11
2.1 Tissue Anatomy and Morphology	11
2.2 Medical Imaging Modalities.....	13
2.2.1 Brief Overview of Ionizing Medical Imaging Modalities.....	13
2.2.2 Brief Overview of Non-Ionizing Medical Imaging Modalities	14
2.3 Sequential Multi-Modal Imaging	19

2.4 Synchronous Multi-Modal Imaging Systems	20
2.4.1 Ionising Multimodality Imaging Systems	20
2.4.2 Non-ionising Multimodality Imaging Systems	23
2.5 Fluorescence Imaging	25
2.5.1 Reporter Strategies	26
2.5.2 Fluorescence Imaging Modalities.....	27
2.5.3 Mesoscopic Fluorescence Imaging.....	28
2.5.4 Microscopic Fluorescence Imaging.....	28
2.6 Photoacoustic Effect (PA).....	31
2.6.1 Low Frequency Photoacoustics	33
2.6.2 High Frequency Photoacoustics	34
2.7 Nanoparticle Assisted Optical Imaging	39
2.8 Ultrasound imaging	43
2.9 Summary of Literature Review Findings	45
 Chapter 3: PROPOSED INSTRUMENTATION SCHEMES FOR	
FLUORESCENCE MICROSCOPY SYSTEMS.....	49
 3.1 Introduction.....	49
3.2 Fluorescence Microscopy Instrumentation Schemes for	
Multimodality Imaging.....	50
3.2.1 Inverted Fluorescent Microscope	50
3.2.2 Fiber-Optic Fluorescence Microendoscope.....	59

3.3	Summary of Findings	65
 Chapter 4: ULTRASOUND IMAGING USING MULTI-ELEMENT TRANSDUCER.....68		
4.1	Fundamental Theoretical Concepts of Ultrasound Imaging	68
4.1.1	Ultrasound Reflection.....	69
4.1.2	Ultrasound Attenuation	69
4.1.3	Ultrasound Transducer	70
4.1.4	Linear Arrays.....	71
4.1.5	Focusing	71
4.1.6	Beamforming.....	74
4.2	Instrumentation and Configuration Schemes of the Proposed Ultrasound Imaging System.....	78
4.2.1	Signal Processing.....	81
4.2.2	Implementation of Advanced Signal Processing Routines	83
4.3	Characterization of the Proposed Ultrasound Imaging System	84
4.3.1	Signal-to-Noise Ratio (SNR) Measurement.....	85
4.3.2	Characterisation of the System Resolution.....	87
4.4	Investigations into the Effect of Scan Lines per Aperture	91
4.5	Implementation of Multi-Transmit Focal Zones and its Effect on Frame Rate	93
4.6	B – Mode Imaging of Silicone Phantom.....	96

4.7	Summary of Findings	98
 Chapter 5: DUAL-MODALITY PHOTOACOUSTIC IMAGING		
	WITH ENHANCED CONTRAST.....	100
5.1	Introduction.....	100
5.1.1	Theoretical Formulations and Concepts of Photoacoustic Imaging	101
5.2	Investigations into High Frequency Photoacoustic Signal Enhancement Using Plasmonic Nanoparticles	121
5.2.1	Nanoparticles as Contrast agents for Photoacoustic Imaging	121
5.2.2	Results and Discussion	129
5.3	Investigations into Selective Photoacoustic Signal Generation for Multiple Targeting Using Plasmonic Nanoparticles.....	139
5.3.1	FDTD Simulations for Selective Photoacoustic Signal Generation and Multiple Targeting	140
5.3.2	Experimental Investigations into Selective Photoacoustic Signal Generation and Multiple Targeting	142
5.4	Investigations into Photoacoustic Imaging using Multi-element Transducers	148
5.5	Photoacoustic Imaging of Optical Absorbers.....	148
5.5.1	Configuration of the Photoacoustic Imaging System.....	149
5.5.2	Experimental Methodology	152
5.5.3	Results and Discussion	154

5.5.4	Novel Approaches to Enhance Photoacoustic Imaging with Spatial (Angle) Compounding and Persistence	157
5.6	Investigations into Photoacoustic Contrast Enhancement Mechanisms Using Novel Dual – Optical Mode Detection and Imaging Scheme	161
5.6.1	Photoacoustic Signal Enhancement Using Fluorophore - Metal Nanoparticle System.....	162
5.6.2	Synergetic photoacoustic contrast-enhancement via graphene oxide wrapping on plasmonic core shell nanohybrids.	177
5.7	Summary of Findings	186
Chapter 6:	AN INTEGRATED MULTI-MODALITY IMAGING SCHEME FOR MULTI-LEVEL AND MULTI-SCALE INFORMATION MAPPING	188
6.1	Proposed Integrated Multi-Modality Imaging System.....	188
6.2	Inverted Optical Microscope Based Approach	192
6.2.1	Experimental Methodology	192
6.2.2	Results and Discussion	193
6.3	Fiber-Optic Based Approach	195
6.3.1	Results and Discussion	197
6.4	Summary of Findings	198
Chapter 7:	CONCLUSIONS AND FUTURE WORKS	202
7.1	Conclusion	202

7.2 Major Contributions.....	207
7.3 Suggestions for Future Work.....	208
APPENDICES.....	210
APPENDIX A - Configuration of The Inverted Fluorescent Microscope.....	211
APPENDIX B - Programming Interface for the Integrated Linear Array Ultrasound and Photacoustic Imaging System.....	214
APPENDIX C - Phantom Preparation	215
APPENDIX D- Design of The Transmission and Reflection Mode High Frequency Photoacoustic Setup.....	221
APPENDIX E – Preparation of the Novel Nanohybrid.....	234
APPENDIX F – Low Frequency Photoacoustic Studies.....	239
APPENDIX G – Methodology For Cancer Diagnostics Using The Proposed Multimodality Imaging System	255
PUBLICATIONS.....	259
REFERENCES.....	261

List of Figures

Figure 1.1 Research road map	7
Figure 3.1 Schematic of the proposed experimental set-up for fluorescence microscopy.....	54
Figure 3.2 USAF test target imaged with 0.3 NA microscope objective lens. The region inside the dotted lines shows the sixth element of the seventh group.....	56
Figure 3.3 a) Absorption and b) Emission spectra of the fluorescent microsphere, the red arrow indicates the zoomed in view of the encircled region in the fluorescence emission spectrum.....	56
Figure 3.4 Fluorescence images obtained using different microscope objective lens: a) 0.15 NA, b) 0.3 NA, c) 0.46 NA, d) 0.80 NA.....	57
Figure 3.5 Fluorescence images obtained with 0.8 NA objective lens at varying focal planes with a step resolution of $2 \pm 0.4 \mu\text{m}$ across each focal planes.....	58
Figure 3.6 Schematic of the fiber-optic fluorescence microendoscope	60
Figure 3.7 USAF test target imaged with GRIN lensed image fiber a) Raw image, b) Post processed image – The region inside the dotted lines shows the third element of the seventh group in USAF chart.....	61
Figure 3.8 Profile of the axial response of the fiber-optic microendoscope	63
Figure 3.9 Fluorescence image of the polystyrene microsphere imaged using fiber-optic microendoscope	64
Figure 3.10 Post processed fluorescence image of the polystyrene microsphere	64
Figure 4.1 Representation of the ultrasound focal point.....	75
Figure 4.2 Block diagram of the ultrasound imaging system	78
Figure 4.3 Schematic of the signal-to-noise ratio (SNR) measurement set-up.....	86
Figure 4.4 Schematic of the resolution measurement set-up	88

Figure 4.5 Profile of the axial response of the ultrasound imaging system	89
Figure 4.6 Profile of the in-plane response of the ultrasound imaging system.....	90
Figure 4.7 Effect of acoustic lines per aperture on the image quality and frame rate; The white pointers denote the regions of interest where a reduction in speckles and reflections were observed with an increase in number of scan lines; (a) 1 line, (b) 2 lines, (c) 3 lines, (d) 4 lines.....	92
Figure 4.8 Images with multi-transmit focal zones, The white pointers denote the position of different focal zones; (a) 1 focal zone, (b) 2 focal zones, (c) 3 focal zones, (d) 4 focal zones	94
Figure 4.9 Schematic of the silicone phantom.....	96
Figure 4.10 Schematic of the experimental set-up for B - mode imaging	97
Figure 4.11 B- mode image of the silicone phantom.....	97
Figure 5.1 Slab Object	105
Figure 5.2 Pressure propagation in mucosal layer for slab	111
Figure 5.3 Pressure propagation in submucosal layer for slab	111
Figure 5.4 Pressure propagation in muscle layer for slab	112
Figure 5.5 Pressure propagation from irradiated slab	113
Figure 5.6 Sphere Object	114
Figure 5.7 Pressure propagation in mucosal layer for sphere	119
Figure 5.8 Pressure propagation in submucosal layer for sphere	119
Figure 5.9 Pressure propagation in muscle layer for sphere	120
Figure 5.10 Geometry of simulated nanoparticles a) Nanosphere, b) core-shell nanoparticle, c) nanorod	124

Figure 5.11 Comparison of FDTD result with analytic solution, a) Absorption cross-section	
b) Scattering cross-section	127
Figure 5.12 Calculated spectra of the optical efficiencies from the FDTD model; R1=40nm	
and R2=70nm.....	128
Figure 5.13 Calculated spectra of the optical cross-sections of gold nanorod from the FDTD	
model; L=44.8 nm and W=19.8 nm, AR=2.26.	129
Figure 5.14 Optical efficiencies of gold nanospheres; a) Extinction, b) Absorption, c)	
Scattering	130
Figure 5.15 Optical efficiencies of core-shell (Silica core- Gold Shell) nanoparticles radius;	
a) R1=20 and R2=50, b) R1=30 and R2=50	132
Figure 5.16 Optical efficiencies of core-shell (Gold core- Silica Shell) nanoparticles: a)	
R1=20 and R2=50, b) R1=30 and R2=50	134
Figure 5.17 Extinction efficiencies of gold nanorods with varying aspect ratios.....	137
Figure 5.18 Optical efficiencies of gold nanorod with varying aspect ratios:	138
Figure 5.19 Optical efficiencies of gold nanorod with aspect ratio R =2.26 and varying	
Effective Radius: (a) Absorption, (b) Scattering	139
Figure 5.20 Optical cross-sections of gold nanorods determined from FDTD simulations; a)	
Type 1, b) Type 2, c) Type 3, d) Type 4.....	141
Figure 5.21 TEM images of gold nanorods; a) Type 1, b) Type 2, c) Type3, d) Type 4.....	143
Figure 5.22 UV-VIS absorption spectrum of gold nanorod solution; a) Type 1, b) Type 2, c)	
Type3, d) Type 4.....	144
Figure 5.23 Experimental set-up of the proposed single element high frequency	
photoacoustic system	146
Figure 5.24 Photoacoustic signal amplitude of gold nanorod solution.....	147

Figure 5.25 Block diagram of the proposed photoacoustic imaging system	149
Figure 5.26 Schematic of the experimental set-up for photoacoustic imaging.....	151
Figure 5.27 Schematic of the experimental set-up to measure timing jitter	152
Figure 5.28 Schematic of the silicone phantom with absorbing centers.....	153
Figure 5.29 Absorption spectra of the absorbing dyes: a) Direct Red 81, b) Methylene Blue	153
Figure 5.30 Photoacoustic image of the phantom at varying fluence: a) 3 mJ/cm ² , b) 6 mJ/cm ²	155
Figure 5.31 Photoacoustic imaging of the phantom tissue	156
Figure 5.32 Schematic of the experimental set-up for photoacoustic imaging with spatial compounding and persistence	159
Figure 5.33 Photoacoustic Images of the Phantom at Varying Angles: a) Angle 1, b) Angle 2, c) Angle 3, d) Angle 4, e) Angle 5, f) Angle 6, g) Angle 7, g) Angle 8, i) Angle 9.....	160
Figure 5.34 Photoacoustic images: a) Without spatial compounding, b) With spatial compounding	161
Figure 5.35 (a) Transmission electron microscopy images (TEM) of gold nanorod (AuNP), (b) UV/Vis absorption of AuNP, (c) Peak fluorescence emission intensities measured from the experimental sets, d) Relative AuNP concentrations in the experimental sets.....	164
Figure 5.36 Proposed experimental set-up for simultaneous photoacoustic and fluorescence studies	166
Figure 5.37 Experimental results from simultaneous photoacoustic and fluorescence studies at 526 nm excitation. a) Photoacoustic signal amplitude, b) Fluorescence emission intensity	167

Figure 5.38 Absorption measurements of the experimental sets. a) Absorption spectrum, b) Absorption at 526 nm excitation.....	169
Figure 5.39 Schematic of the fluorophore – gold nanoparticle based phantom tissue	173
Figure 5.40 Proposed experimental set-up for combined fluorescence and photoacoustic imaging	174
Figure 5.41 Images obtained from the proposed combined fluorescence and photoacoustic imaging system; a) Fluorescence image, b) Photoacoustic image. (Scale bar - 5 μm).....	175
Figure 5.42 Photoacoustic imaging at two distinct excitation wavelengths; a) 526 nm, b) 555 nm	176
Figure 5.43 Schematic diagram showing synthesis of graphene oxide (GO) enwrapped gold-silica core shell nanoparticles (GO-SiO ₂ @AuNP). <i>Step 1</i> : APTES modified silica coating on AuNP. <i>Step 2</i> : wrapping of graphene oxide on the surface of SiO ₂ @AuNP.	179
Figure 5.44 (a) UV/Vis absorption changes of AuNP (black curve), SiO ₂ @AuNP (red curve) and GO-SiO ₂ @AuNP (blue curve), (b) Digital image of aqueous solutions of ~0.5mg/mL corresponding nanoparticles in aqueous solution at pH 7.2.	180
Figure 5.45 a) Absorption cross-section of an isolated AuNP (black curve), SiO ₂ @AuNP (red curve) and GO-SiO ₂ @AuNP (blue curve) for the longitudinal polarization of the incident light calculated using FDTD. Contours of the electromagnetic near field enhancement at the excitation laser wavelength 527 nm for b) isolated AuNP, c) SiO ₂ @AuNP and d) GO-SiO ₂ @AuNP as a function of X, calculated using FDTD. The colour scale represents the electromagnetic field enhancement ($ E ^2$).	182

Figure 5.46 a) High resolution scan of photoacoustic signals from AuNP, SiO ₂ @AuNP and GO-SiO ₂ AuNP. b) Average peak-to-peak signal intensities of AuNP, SiO ₂ @AuNP and GO-SiO ₂ @AuNP nanoparticles	183
Figure 5.47 Photoacoustic image of a) AuNP, b) SiO ₂ @AuNP and c) GO-SiO ₂ @AuNP embedded in gelatin separate wells in agar phantom. Fluorescent micoroscopy images of microbeads (d-f) loaded randomly in the agar phantom (Loaded dye: Nile red) excited with the same laser pulses at 527 nm. (Scale bar 5 μm)	185
Figure 6.1 Configuration of the proposed multi-modality imaging system.....	189
Figure 6.2 Block diagram of the integrated ultrasound and photoacoustic imaging system	190
Figure 6.3 Schematic of the multi-modal imaging system based on inverted microscope.....	192
Figure 6.4 Images obtained from the inverted microscope based multi-modal system: a) Fluorescence image, b) Photoacoustic image, c) Ultrasound image.....	194
Figure 6.5 Schematic of the multi-modal imaging system based on fiber-optic microendoscope	196
Figure 6.6 Images obtained from the fiber-optic microendoscope based multi-modal system: a) Fluorescence image, b) Photoacoustic image, c) Ultrasound image.....	197
Figure 6.7 Imaging process flow of the proposed multi-modality imaging system.....	201

List of Tables

Table 1 Review of Imaging Modalities	18
Table 2 Nanoparticles in imaging applications.....	40
Table 3 Specifications of the microscope objective lens	55
Table 4 Number of scan lines versus frame rate.....	92
Table 5. Number of focal zones versus frame rate.	95
Table 6 Calculated peak optical efficiencies Q_{abs} , Q_{scat} and corresponding wavelengths λ_{ext} , λ_{abs} , λ_{scat} , absorption to scattering ratio at λ_{abs} and scattering to absorption ratio at λ_{scat} for nanospheres.....	131
Table 7 Calculated peak optical efficiencies Q_{abs} , Q_{scat} and corresponding wavelengths λ_{ext} , λ_{abs} , λ_{scat} , absorption to scattering ratio at λ_{abs} and scattering to absorption ratio at λ_{scat} for Silica core – Gold shell nanoparticles.....	134
Table 8 Calculated peak optical efficiencies Q_{abs} , Q_{scat} and corresponding wavelengths λ_{ext} , λ_{abs} , λ_{scat} , absorption to scattering ratio at λ_{abs} and scattering to absorption ratio at λ_{scat} for Gold core – Silica shell nanoparticles.....	135
Table 9 Calculated peak optical efficiencies Q_{abs} , Q_{scat} and corresponding wavelengths λ_{ext} , λ_{abs} , λ_{scat} , absorption to scattering ratio at λ_{abs} and scattering to absorption ratio at λ_{scat} for nanorods.....	136
Table 10 Dimensions and aspect ratios of gold nanorods.....	141
Table 11 SPR peaks wavelength of gold nanorods determined from FDTD simulations	142
Table 12 Absorption peaks of gold nanorods from FDTD simulation and UV-VIS absorption measurements.....	145
Table 13 Particle concentrations in the experimental fluorophore – nanoparticle solution.....	165

Table 14 Comparison of imaging parameters of the imaging systems during independent operation and multi-modal operation.....	199
---	-----

List of Symbols

<u>Symbol</u>	<u>Definition</u>
V_B	Average luminance for black areas
V_W	Average luminance for white areas
V_{min}	Minimum luminescence
V_{max}	Maximum luminescence
$P(0)$	Initial acoustic pressure
α	Acoustic attenuation
Z	Depth of interest
N_Z	Number of focal zones
C	Velocity of ultrasound
N	Number of line of sights per focal zone
F	Focal length
W_a	Aperture size
T	Propagation time
D	Acoustic line
R	Radial distance from the origin

A	Apodization
τ	Time-delay
i	Transducer element number.
i'_k, i_k	Persisted and unprocessed pixel
$p(\vec{r}, t)$	Acoustic pressure at location \vec{r} and time t
$T(\vec{r}, t)$	Local temperature
V_s	Speed of sound
ρ_m	Mass density
β	Isobaric thermal expansion coefficient
C_v	Specific heat capacity at constant volume
Γ	Grueneisen coefficient
H	Laser fluence
μ_a	Optical absorption co-efficient
E_{abs}	Absorbed energy density
(R_{eff})	Effective radii
p_0	Local pressure rise

k	Thermal conductivity
ρ	Density
C_p	Specific heat capacity
α	Thermal diffusivity
ω	Modulation frequency
γ	Ratio of specific heat capacity of air
P_0	Ambient pressure
T_0	Ambient temperature
I_0	Radiation intensity
f	Modulation frequency
α_a	Thermal diffusivity
k_i	Thermal conductivity
l	Length of the medium
g	Gas
s	Solid sample

LIST OF ACRONYMS

2D	Two Dimensional
3D	Three Dimensional
ADC	Analog to Digital Converter
AIUM	American Institute of Ultrasound in Medicine
A-mode	Amplitude Mode
APTES	Aminopropyl Triethyl Silane
BLI	Bioluminescence Imaging
B-Mode	Brightness Mode
BNC	Bayonet Neill–Concelman
CCD	Charge Coupled Device
CMOS	Complementary Metal–Oxide–Semiconductor
CMUT	Capacitive Micromachined Ultrasonic Transducer
CTAB	Cetyl Trimethyl Ammonium Bromide
DOT	Diffuse Optical Tomography
EPI	Echo Planar Imaging
FD-PAT	Frequency Domain Photoacoustic Tomography
FDTD	Finite Difference Time Domain
FIR	Finite Impulse Response
FL	Fluorescence
fMRI	Functional Magnetic Resonance Imaging
FMT	Fluorescence Molecular Tomography
FOT	Fluorescence Optical Tomography
FPGA	Field Programmable Gate Arrays
FRI	Fluorescence Reflectance Imaging
FWHM	Full Width at Half Maximum
GRIN	Gradient-Index

HV	High Voltage
LNA	Low Noise Amplifier
LoHR	Lines of Horizontal Resolution
LPF	Low Pass Filter
LP/mm	Line Pairs per Millimeter
MRI	Magnetic Resonance Imaging
MTF	Modulation Transfer Function
NIR	Near Infra-Red
OD	Optical Density
OPC	Open Photoacoustic Cell
PA	Photoacoustic
PAI	Photoacoustic Imaging
PAM	Photoacoustic Microscopy
PAT	Photoacoustic Tomography
PCB	Printed Circuit Board
PET	Positron Emission Tomography
PGA	Programmable Gain Amplifier
PSF	Point Spread Function
PVDF	PolyVinylidene DiFluoride
PZT	Lead Zirconate Titanate
RET	Resonance Energy Transfer
RF	Radio Frequency
ROI	Region of Interest
SNR	Signal-to-Noise Ratio
SPECT	Single Photon Emission Computed Tomography
TAI	Thermoacoustic Imaging
TD-PAT	Time Domain Photoacoustic Tomography
TEM	Transmission Electron Microscopy

TFSF	Total Field Scattered Field
TGC	Time Gain Control
Tx/Rx	Transmit/Receive
UI	Ultrasound Imaging
UM	Ultrasound Microscopy
US	Ultrasound
USAF	Unites States Air Force
UV	Ultra-Violet
VCA	Voltage Controlled Amplifier
VCAT	Voltage Controlled Attenuator
VGA	Variable Gain Amplifier
XCT	X-ray Computed Tomography

CHAPTER 1: INTRODUCTION

1.1 Background Information and Motivation

Tissue diagnostics benefits the process of health and disease management which include early detection of diseases, disease prevention, injury assessment, guided surgery and interventions and non-invasive monitoring of treatment effects. Several tissue diagnostic procedures have been evolved over the years and are extensively used for performing a variety of clinical investigations. Many of these procedures have also offered significant contributions towards the advancements in biomedical research community. Various diagnostic procedures performed ex-vivo, in-vitro and in-vivo that often aim to investigate the physical, mechanical, thermal, optical and various other tissue properties. Although much of the tissue diagnostic procedures can reveal the various tissue properties, they often fail to provide an accurate localization of the targeted traits. This led to a methodological shift from conventional assay based approach to imaging based approach as reported by Ntziachristos in Nature Biotechnology (Ntziachristos, Ripoll et al. 2005). Advanced imaging based technologies are capable of probing complex and dynamic biological processes thereby offering tremendous capabilities to accelerate basic research and clinical diagnosis.

The visualisation of the structural and molecular behaviour of the tissue constituents reveals the specific states of the tissue and often aids in early disease diagnosis. A variety of imaging modalities have been evolved to aid disease diagnostics where each of the imaging modalities operates with a specific type of energy input into the tissue. Though, an extensive armamentarium of medical

imaging modalities are being introduced into the field of biomedicine, they often fail to produce satisfactory results for early disease diagnostics. This is owing to the structural and molecular complexity of the tissue itself. Tissues are composed of complex and diverse structures and molecules with varying dimensions located along the depth of the tissue. Due to these structural and molecular heterogeneities, the energy-tissue interaction results in a variety of biophysical and biochemical reactions where each of the individual tissue constituents responds differently to the specific forms of energy input. Further, the type of energy input also determines the resolution and penetration depth obtained from a specific form of imaging modality because the wavelength of the source energy primarily determines the spatial resolution scales and the energy of the radiation determines the penetration depth. Hence, it is evident that the visualization capabilities of each of the specific imaging modalities are directly linked to the type of input energy. For example, X-ray based diagnostic modalities rely on tissue density variations and are excellent choice for hard tissue imaging across the entire volume of the subject. However, magnetic resonance imaging (MRI) is primarily based on nuclear spins in water molecules and is best suited for whole body soft tissue imaging. On the other hand, ultrasound imaging maps out the acoustic heterogeneities in tissue with higher resolution and comparable depths, whereas optical imaging maps out optical heterogeneities in tissue with the highest resolution but suffers from very poor penetration depth.

Each of the imaging modalities is therefore restricted to operate within certain defined parametric dimensions which make them suitable for certain applications while not making them adequate for other applications. These

parametric dimensions can be characterised in terms of spatial resolution (μm to mm), penetration depth (mm to cm) and the level of information (structural, functional or molecular) obtained. In addition to these basic parametric dimensions, each of the imaging modalities provides fundamentally different information from the diagnosed site.

Another important consideration for tissue diagnostics concerns the volume of tissue interrogation. Imaging modalities that involve the use of radio frequency waves and X-rays are capable of performing whole body imaging whereas high resolution imaging modalities such as optical and high frequency ultrasound can be used for interrogating small and accessible areas of the body (thickness $< 1\text{ cm}$). Therefore, it is evident that, it is not possible to extract all aspects of structural and molecular states of the tissue from a single imaging modality with varying interrogation area, spatial resolution and penetration depth. Hence, the most widely used approach is to sequentially interrogate the subject with multiple imaging modalities by moving the sample across the specific lines of imaging machines. Such an imaging approach should typically provide multi-level and multi-scale information along the depth of the diagnosed tissue. Multi-level in this context refers to structural, functional and molecular level information whereas multi-scale refers to the spatial resolution scales, i.e.; microscopic ($< 10\text{ }\mu\text{m}$) to mesoscopic ($10\text{ }\mu\text{m} - 1\text{ mm}$). To enhance the potential capabilities of this approach, powerful image registration techniques are also developed to map or co-register the images together from different imaging modalities (Hill, Batchelor et al. 2001). Further, much interests have been also drawn towards the development of multi-modal imaging systems which houses and operates more than two imaging modalities

near-simultaneously within a single instrumentation set-up. Significant efforts have also been made to develop imaging systems that can provide multi-modal images using a single instrument or detector.

In this regard, several multimodal imaging systems such as PET/CT (Charron, Beyer et al. 2000, Townsend, Beyer et al. 2003, Nehmeh, Erdi et al. 2004), SPECT/CT (Kalki, Blankespoor et al. 1997, Tang, Brown et al. 1997, Iwata, Macdonald et al. 2002, Weisenberger, Wojcik et al. 2003), PET/MRI (Cherry, Louie et al. 2008, Judenhofer, Wehrl et al. 2008, Schlemmer, Pichler et al. 2008, Ng, Bading et al. 2012) PET/FOT (Li, Yang et al. 2011) and FMT-XCT (Ale, Ermolayev et al. 2012) have been developed and reported in various publications. However, these systems exhibit potential health hazards imposed by the ionizing radiations involved during their operation requiring longer imaging time (typically minutes to hours). Currently, there are no imaging schemes or very little reported works which can employ only non-ionizing radiations with reduced interrogation time that are capable of providing multi-scale and multi-level information from the diagnosed sample. A proposed approach is to combine and integrate selected individual modalities of non-ionizing radiations such as ultrasound and optical energies together to help realise this goal. This would necessitate using ultrasound imaging which can structurally map various acoustic heterogeneities along the depth of the tissue of mesoscopic (sub-millimetre) spatial resolution together with optical imaging providing structural and molecular mapping of various optical heterogeneities of sub-micron resolution across the surface of the tissue. Further, the inherent penetration depth limitations for conventional optical imaging modalities could be surmounted by adopting novel photoacoustic imaging concepts

which maps optical absorption heterogeneities at ultrasound resolution along the tissue depth.

This thesis details various numerical and experimental investigations performed towards the realization of a multimodal imaging scheme based on an integrated photoacoustic, ultrasound, fluorescence imaging system (PAUSFI) (desktop version and flexible version) which can perform near-simultaneous fluorescence (FI), photoacoustic (PA) and ultrasound (US) imaging. This would thereby enable the multi-modal imaging system to derive and assimilate complementary information from the targeted site for diagnostic purposes where the inherent limitations of an individual imaging modalities are surmounted by an associated imaging modality. In this context this research has the following objectives and scopes.

1.2 Objective

The main objectives of this experimental research were directed towards tapping the potential advantages offered by integrating ultrasound (US), photoacoustic (PA) and fluorescence (FL) imaging modalities. These include

- Experimental investigations into the enhancements in imaging capabilities of optical and ultrasound imaging systems in terms of novel instrumentation concepts and contrast enhancement methodologies.
- Experimental investigations into the establishment of a novel multi-modal imaging system to map multi-level and multi-scale complementary information.

1.3 Scope

The methodology of the research is outlined as follows:

- Establishment of design axioms and characterisation of the inverted fluorescence microscopy system based on experimental studies so as to characterise and derive fluorescence images from sample surface at microscopic resolution.
- Conceptualisation, configuration and experimental characterisation of the fluorescence micro-endoscope supported with experimental studies to enhance the imaging capabilities of the system for fluorescence imaging from tissue surface at microscopic resolution.
- Configuration and experimental characterisation of the multi-element transducer based ultrasound imaging system and experimental studies to evaluate and enhance its imaging capabilities for performing ultrasound imaging studies along the depth of the tissue at mesoscopic resolution.
- Numerical investigations to determine the photoacoustic signal generation mechanism from spherical and planar absorbers under delta pulse excitation.
- Numerical investigations to determine the effect of dimension and shape on the optical properties of gold nanoparticles for photoacoustic applications.
- Experimental investigations into the development of a single element transducer based high frequency photoacoustic system for selective photoacoustic detection for multiple targeting.
- Conceptualisation, configuration and experimental development of the multi-element transducer based photoacoustic imaging system and experimental

studies to evaluate and enhance its imaging capabilities for conducting deep tissue photoacoustic imaging at mesoscopic resolution.

- Theoretical and experimental studies to investigate into novel contrast enhancement mechanisms for photoacoustic imaging studies.
- Conceptualisation, configuration and experimental development of novel dual-optical modality detection and imaging scheme for simultaneous fluorescence and photoacoustic studies.
- Establish experimental methodologies for the formulation of the principles, concepts and imaging capabilities for the bench-top and fiber-optic microendoscope based multi-modal imaging system. Experimental studies to determine the salient features of the system for multi-scale and multi-level imaging are also to be made.

A block diagram, describing the research roadmap of the proposed investigation is given in Figure 1.1.

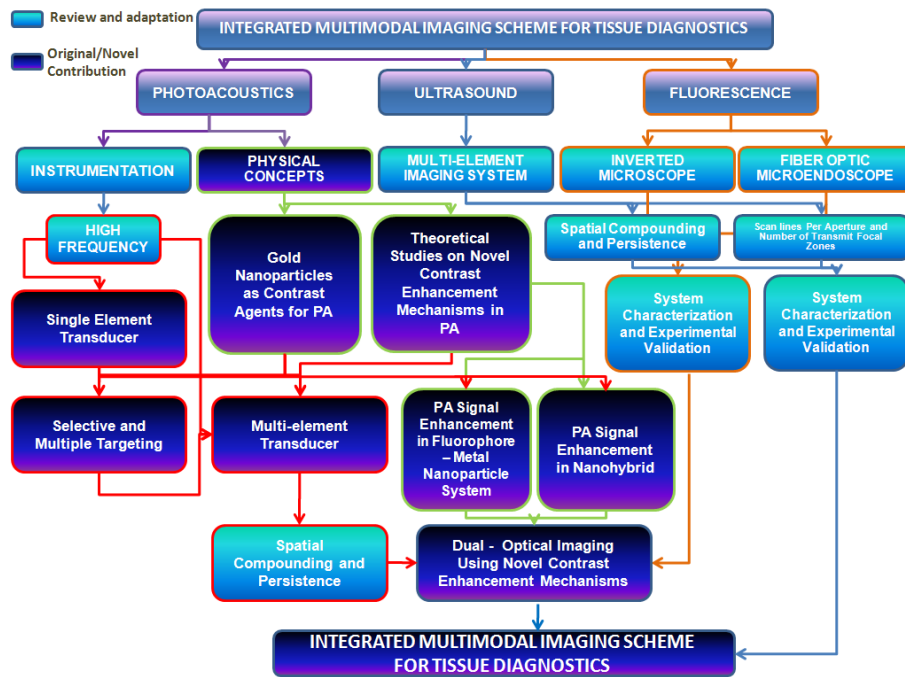


Figure 1.1 Research road map

1.4 Organization of the Thesis

The thesis is organised into seven chapters including the current one. Chapter 2 reviews the significant topics related to the derivation of the proposed research framework. A brief review on the tissue anatomy and morphology is presented at the beginning followed by a brief description on the various imaging modalities for tissue diagnostics. Further, a review on the different multi-modal imaging schemes is performed to derive the research framework depicted in the following section. Based on the proposed research framework, a review on the various aspects of fluorescence, photoacoustic and ultrasound imaging was performed and an outcome of the review is given at the end of the chapter.

Chapter 3 describes the various fluorescence microscopy investigations carried out with the view of further translation into the proposed multi-modal imaging system. Two variants of fluorescent microscopy systems are characterised and compared demonstrating their imaging capabilities to operate with micron or sub-micron spatial resolution. Experimental studies on inverted fluorescence microscope are depicted initially followed by the experimental investigations performed in relation to fluorescence microendoscopy.

Chapter 4 describes the configuration and experimental methodologies to realise the multi-element based ultrasound imaging system. The chapter begins with the physics of ultrasound imaging systems and details the relevant fundamental concepts. The configuration and characterisation of the ultrasound imaging system for deep tissue imaging at mesoscopic resolution is then detailed with the experimental results. Later sections of the chapter describe the implementation of advanced ultrasound imaging concepts such as spatial

compounding and followed by investigations performed to study the effects of scan lines per aperture and number of focal zones on the imaging speed. The chapter concludes with the results obtained from B-mode imaging of the silicone phantom.

Chapter 5 describes the various research areas related to high frequency photoacoustic system. The fundamental theoretical concepts of photoacoustic effect and theoretical simulations performed to study the photoacoustic wave characteristics generated with delta pulse excitation of a spherical and planar absorber are described. A detailed theoretical study based on FDTD simulations to determine the optical properties of gold nanoparticles is then given. This is followed by a detailed description on the various experimental investigations performed such as photoacoustic signal generation for selective multiple molecular targeting, establishment of the multi-element transducer based photoacoustic imaging system, implementation of spatial compounding and persistence techniques for photoacoustic imaging, novel methodologies for enhancing photoacoustic image contrast and implementation of a novel dual-optical modality detection and imaging scheme.

Chapter 6 describes the experimental investigations performed to establish the proposed multi-modal imaging system based on the integration of the fluorescence (FL), photoacoustic (PA) and ultrasound (US) imaging modalities for multi-scale and multi-level imaging. The initial part of the chapter illustrates the various investigations performed to establish and characterise the desktop version of the system. This will be followed by the detailed description of the various investigations performed to establish flexible microendoscope based multi-modal

system. The chapter concludes by discussing the salient features and imaging performance of the two variants of the proposed multi-modal imaging system.

Chapter 7 concludes the thesis by summarizing each of the principal experimental investigations and their results. The major contributions of the research are then outlined and a brief discussion on the various research areas that would naturally follow from those described herein is provided.

CHAPTER 2: LITERATURE REVIEW

This chapter reviews the significant topics related to the derivation of the proposed research framework. A brief review on the tissue anatomy and morphology is presented at the beginning followed by a brief description on various imaging modalities for tissue diagnostics. Further, a review on the different multi-modal imaging schemes is performed to derive the research framework depicted in the following section. Based on the proposed research framework, a review on the various aspects of fluorescence, photoacoustic and ultrasound imaging was performed and the outcomes from the review are detailed towards the end of the chapter.

2.1 Tissue Anatomy and Morphology

A tissue is composed of a group of cells with similar structures working together to perform a common function in an organism. Animal tissues can be classified into four basic types such as epithelial tissue, connective tissue, muscle tissue and nervous tissue. All these four types of tissues can be modelled as a system of discrete structures with varying sizes, shapes and chemical composition (Tuchin 2007). The simplest way to model cellular structures would be to induce a system of non-interacting spherical and cylindrical particles (Tuchin 2007). The epithelial tissue which forms the outer lining in most of the organs is primarily composed of spherical structures with varying diameters. In healthy tissues, the epithelium is composed of cellular structures with an enface diameter of 10-20 μm

(Tuchin 2007). Therefore, by inducing spherical structures onto the surface of phantom tissue, it can emulate or approximate those structural features of an epithelial tissue. Connective and muscle tissues are mostly composed of microfibrils and/or microtubules of cylindrical geometry whose lengths vary from 10-25 μm to few millimetres (Tuchin 2007). However, nervous tissues are a mixture of spherical and cylindrical geometries where the dendrites and axons exhibit cylindrical geometry and the soma has spherical geometry.

To detect possible initiation or offset of a potential disease state in the tissue, any anomalies in terms of variations and shifts in the sizes or molecular compositions of these cellular components can serve as useful indicators. These potential indicators can be effectively monitored and studied by examining the physical, mechanical, thermal, optical and other tissue properties. Several diagnostic procedures should be performed ex-vivo, in-vitro or in-vivo to detect such anomalies (Health 2012). Although many of the tissue diagnostic procedures are able to ascertain various tissue properties, they often fail to provide an accurate localization of the targeted traits. As a result, image based approach is preferred over the conventional assay based approach (Ntziachristos, Ripoll et al. 2005). Image modalities are better able to handle the size heterogeneities of the different types of tissue and their cellular constituents with varying spatial resolution scales. Furthermore, the molecular heterogeneities in the tissue composition demand the use of various forms of input energy in order to obtain and elucidate the multi-level (structural and molecular) information from it. An imaging system with multi-scale and multi-level imaging capabilities could possibly map the structural and

molecular heterogeneities of the tissue components of dimensions ranging from a few nanometres to millimetres at varying depths (Tuchin 2007).

2.2 Medical Imaging Modalities

Various diagnostic imaging techniques are currently used for tissue diagnostics. These techniques can be benchmarked based on the type of energy used (X-rays, Sound waves, Photons or Positrons) to derive the visual information, the degree of spatial resolution (mesoscopic and microscopic) and the level of information that can be obtained (Physiological, Anatomical, Molecular) (Weissleder and Pittet 2008). All medical imaging modalities in the past and present are realised with some form of external electromagnetic energy ranging from radio waves to x-ray radiations that interacts with the tissue. In the context of the potential health hazards imposed by the type of energy used, medical imaging modalities can be classified as ionizing imaging modalities and non-ionizing imaging modalities. The following section briefly reviews the commonly used imaging modalities as well as their relative merits and demerits.

2.2.1 Brief Overview of Ionizing Medical Imaging Modalities

Ionizing medical imaging modalities involve the use of high energy ionizing radiations such as X-rays or gamma rays to perform various imaging procedures. This imposes serious limitations for repeated and frequent imaging procedures owing to the restricted amount of dosage that can be applied. The most widely used ionizing imaging modalities include X-ray computed tomography (XCT) and nuclear imaging modalities such as positron emission tomography (PET) and

single-photon emission computed tomography (SPECT). XCT is a diagnostic procedure that uses x-ray equipment to obtain cross-sectional pictures of the tissue under study. XCT based imaging techniques primarily rely on intrinsic differences in X –ray absorption between bones, water, fats and air. The imaging technique is able to provide high resolution structural images of about 50 μm (Weissleder 2002). However, considering early disease diagnostic interrogation, XCT modality is not able to provide molecular information. XCT also suffers from poor soft tissue contrast and involves health risks due to the usage of ionizing radiations (Thomasson, Gharib et al. 2004). In contrast, nuclear imaging modalities such as PET and SPECT are highly sensitive imaging modalities that are capable of providing functional and molecular mapping of the tissue. However, these techniques suffer from poor spatial resolution (1 - 2 mm), longer imaging time (minutes to hours) and involve the use of radioactive isotopes that can be hazardous to the tissue. Furthermore, the radiotracers used in nuclear imaging modalities require complex synthesis procedures, have short half-lives and can trace only a single molecular species at a given time (Thomasson, Gharib et al. 2004).

2.2.2 Brief Overview of Non-Ionizing Medical Imaging Modalities

In contrast to ionizing medical imaging modalities, non-ionizing imaging techniques make use of harmless low energy input radiations which are safer to image the targeted subjects. Further, they also support repeated imaging procedures with increased energy dosage levels for image clarification and verification. The most widely used non-ionizing imaging modalities include magnetic resonance imaging (MRI), ultrasound and optical imaging modalities.

MRI is based on the emission of an electromagnetic wave by nuclear resonance effect. Detectable signals are produced when powerful magnets are used to polarize the hydrogen nuclei in water molecules in human tissue. MRI based techniques have been reported to offer excellent soft tissue contrast and are devoid of ionizing radiations. In functional MRI (fMRI), activation charts are established and used to capture the image activity involvement or changes of a particular process. The imaging procedures can also be performed with sub-millimeter resolution (10 – 100 μm) using a smaller receiver coil of high magnetic field strength. This however increases discomfort to the subject as well as results in large amounts of redundant image features or information. MRI based techniques are also challenged with long interrogation time typically between minutes to hours and cannot be used in patients with implants.

Ultrasound imaging makes use of non-ionizing acoustic radiations. Structural imaging capabilities with good spatial resolution scales (50 μm) and shorter imaging time (seconds to minutes) can be achieved through this technique (Weissleder and Pittet 2008). However, ultrasound imaging systems are challenged with poor soft-tissue contrast and can only offer limited capabilities for functional and molecular imaging as reported by Wells (Wells 2006).

In optical imaging, the techniques are reported to be able to transcend wide spatial and temporal imaging scales with non-ionizing radiations (Solomon, Liu et al. 2011). In the context of biomedical imaging, the spectral ranges for optical imaging can be from microwave regime to ultra-violet (UV) regime. However, considering the amount of optical absorption and scattering by various tissue chromophores, deep penetration of optical energy in biological tissues can be

achieved only at the near-infrared region (700-1000 nm) (Wang and Wu 2007). Based on the various tissue parameters such as absorption, scattering, and fluorescence together with physical principles of laser-tissue interaction, optical imaging can be used to better harness useful structural, functional and molecular information from a specific tissue site. Further, when optical imaging techniques are melded with bio-conjugated exogenous chromophores, it is plausible to selectively enhance the imaging contrast for molecular targets and also provide functional information on dynamic processes inside the body. Considering the physical principles of laser-tissue interaction and principles of optical imaging, it is therefore noteworthy to conclude that optical imaging has the potential of providing multi-level and multi-scale information. Thus optical imaging modalities offer significant capabilities to extract valuable signatures on physiological anomalies long before any anatomical changes are visible.

Nevertheless, optical imaging of deep structures is limited by the transport mean free path of photon which is about 1 mm into the tissue (Wang and Wu 2007). This is due to the multiple scattering of photons prior to reaching a photo-detector. Therefore, conventional optical imaging techniques are often challenged with either achieving good penetration depth (mm to cm) at the expense of poor spatial resolution (> 1 mm) or high spatial resolution (microns or sub-microns) but shallow penetration depth (μm to mm). An example is that of fluorescence molecular tomography where it can achieve imaging depths close to 10 cm but with lower spatial resolution scales on the order of 1 mm (Weissleder and Pittet 2008). On the other hand, optical imaging modalities such as optical coherence tomography and time gated techniques that relies on ballistic and near ballistic

photons provides good spatial resolution ($< 10 \mu\text{m}$), but are suitable for imaging only the low scattering or thin layers of tissues due to its limited penetration depth ($< 1.2 \text{ mm}$). Though, high resolution imaging ($< 1 \mu\text{m}$) modalities such as confocal and intravital microscopy imaging modalities offer structural, functional and molecular imaging, they are challenged with poor penetration depth ($< 0.2 \text{ mm}$).

Therefore, owing to inherent limitations in optical imaging modalities, potential prospects to develop novel optical hybrids which combine optical imaging with other forms of input energies are being explored. An example is that of photoacoustic imaging which relies on the strengths of both ultrasound and optical imaging techniques. As reported by Wang (Wang 2008), photoacoustic imaging is capable of performing structural, functional and molecular imaging with good lateral resolution of less than $400 \mu\text{m}$ with a penetration depth of up to 6 cm .

In summary, most of the current imaging modalities primarily offers anatomical mapping of the tissue micro-structure and architecture. They do not necessarily provide sufficient information about the functional, genetic or proteomic makeup of the tissue. This is highlighted in Table 1 where the various capabilities of individual imaging modalities are depicted in terms of their spatial resolution, imaging depth, imaging time and target level (Rudin, Beckmann et al. 1999, Phelps 2000, Beckmann, Mueggler et al. 2001, Jain, Munn et al. 2002, Weissleder 2002, Weissleder and Ntziachristos 2003, Ntziachristos, Ripoll et al. 2005, Weissleder and Pittet 2008). From Table 1, MRI and nuclear based techniques are found to require long imaging time which limits their ability to effectively use or deal with real-time imaging requirements. X- ray imaging techniques are able to offer high resolution and faster imaging capabilities.

Modality	Resolution	Depth	Time	Target
PET	1–2 mm	whole body	Minutes to hours	Functional, Molecular
SPECT	1–2 mm	whole body	Minutes to hours	Functional, Molecular
MRI	10-100 μm	whole body	Minutes to hours	Structural Functional, Molecular
X-ray CT	50 μm	whole body	Minutes	Structural Functional,
FMT	1 mm	< 10 cm	Minutes to hours	Functional, Molecular
UM/UI	50 μm -500 μm	mm - cm	Seconds to minutes	Structural Functional
FRI	2-3 mm	< 1 cm	Seconds to minutes	Functional, Molecular
PAM/PAT	1 μm -500 μm	mm - cm	Seconds to minutes	Structural Functional, Molecular
BLI	Several mm	cm	Minutes	Molecular
Fluorescence Microscopy	250 nm – 2 μm	< 2 mm	Seconds to minutes	Structural Functional, Molecular

Table 1 Review of Imaging Modalities

PET – Positron Emission Tomography, SPECT - Single-photon Emission Computed Tomography, MRI - Magnetic Resonance Imaging, CT – Computed Tomography, FMT - Fluorescence Molecular Tomography, UM – Ultrasound Microscopy, UI – Ultrasound Imaging, FRI – Fluorescence Reflectance Imaging, PAM- Photoacoustic Microscopy, PAT – Photoacoustic Tomography, BLI – Bioluminescence Imaging.

They, however, make use of ionizing radiations which limit the amount and repeated number of dosage that can be applied. Considering the optical imaging modalities, the review highlights that these techniques are potentially able to image the structural, functional, and molecular states of the tissues at varying spatial and temporal resolutions. However, owing to the scattering of light in tissues, conventional optical imaging techniques fail to offer the penetration depth and spatial resolution as required in this research. Table 1 also highlights that, to derive structural, function and molecular states of the tissue at adequate penetration depth

and spatial resolution, multiple imaging schemes with optical being the primary imaging technique needs to be employed. This aspect would be further deliberated in the ensuing sections.

2.3 Sequential Multi-Modal Imaging

Sequential multi-modal imaging involves the sequential imaging of the subject with manifold imaging platforms. The procedure primarily involves the movement of the subject across multiple imaging platforms to extract multi-scale and multi-level information. Some of the commonly adopted clinical sequential imaging approaches include MRI-optical biopsy, XCT-optical biopsy, XCT-Ultrasound and MRI- XCT. Although, initial stages of such sequential diagnostic imaging approaches were primarily based on the visual synthesis of the imaging dataset, lately powerful image registration techniques (technique to fuse and co-register images from multiple imaging machines) were employed to enhance their diagnostic capabilities. Towards this direction several robust image registration algorithms were developed which led to the evolution a better sequential imaging approach such as in PET and CT (Shekhar, Walimbe et al. 2005), Doppler ultrasound and MR angiography (Slomka, Mandel et al. 2001), echo planar imaging (EPI) and MRI (Studholme, Todd Constable et al. 2000).

Though this approach satisfied certain imaging requirements in terms of the multi-level and multi-scale imaging capabilities, they often failed to provide an accurate registration of the multi-modal images obtained from moving structures which change its shape dynamically(Hill, Batchelor et al. 2001). Further, owing to the distinct interrogation capabilities of each imaging modality and the translation

time across multiple imaging systems, such approaches could not measure two different parameters simultaneously as well as correlate the dynamic changes in those parameters as reported by Cherry et.al; (Cherry 2006). For these reasons, significant research interests were drawn towards integrating two or more imaging modalities to greater or lesser extent into a single imaging unit. Such systems which are classified as synchronous multimodality imaging systems are briefly reviewed in following section.

2.4 Synchronous Multi-Modal Imaging Systems

In synchronous multi-modal imaging systems, the approach is to integrate the strengths of two or more imaging modalities into a single unit to image the target simultaneously and thereby eliminating the non-synchronous registration problem. Based on the type of radiation involved, the multimodality systems can be grouped under two main approaches namely: ionising multimodality imaging systems and non-ionising multimodality imaging systems.

2.4.1 Ionising Multimodality Imaging Systems

An ionising multimodality imaging system is deemed to involve the usage of ionising high energy radiations in one or more of the imaging modalities involved. The following sub-sections reviews the various ionising multimodality imaging systems that are currently being used.

2.4.1.1 *XCT/PET or SPECT*

Pioneering works in multimodality imaging have been concentrated towards integrating modalities that involve the usage of high energy electromagnetic

photons such as PET or SPECT with XCT (Townsend and Cherry 2001, Hasegawa, Iwata et al. 2002). The approach was initially meant in conjunction with transmission scanning (collection of transmission data) where the radiotracer accumulation was to be localised. Its capabilities were then extended to determine the depth-dependent attenuation of emission photons (Malko, Van Heertum et al. 1986). This aspect of the transmission scan was rarely used as a pure diagnostic tool as reported by Cherry et.al; (Cherry 2006). With the advent of emission/transmission system (Hasegawa, Iwata et al. 2002), the CT system was then able to perform structural mapping of the diagnosed site in addition to photon attenuation mapping. Due to the higher spatial resolution of CT images, the localisation of radiotracers became more accurate and enabled the quantification of radiotracer uptake from a relatively smaller region (Tang, Brown et al. 1997, Da Silva, Tang et al. 2001). Whole body PET/CT and SPECT/CT systems are now commercially available and similar systems have been widely adopted for preclinical imaging in small animal imaging studies. Such systems are typically used for anatomical localization (obtained from XCT) by examining the uptake level of radiotracers in oncology (Beyer, Townsend et al. 2000) where increased amount of radiotracers would point to suspicious lesions in the tissue. However, this particular multi-modal combination is challenged with the usage of ionizing radiation for its operation and is not capable of providing molecular information.

2.4.1.2 MRI/PET or SPECT

Another promising intense research avenues in multimodality imaging was directed towards integrating MRI with PET or SPECT (Cherry 2009). PET/MRI imaging systems were initially used on small animal imaging (Catana, Wu et al.

2006, Judenhofer, Wehrl et al. 2008) and human brain imaging (Schlemmer, Pichler et al. 2008) with reasonable success. By combining MRI with PET or SPECT, radiotracer assays can be used to correlate with several kinds of functional MR measurements. Such combinations can progressively lead to clinical applications that combine structural and functional MRI with molecular PET or SPECT imaging with lesser radiation doses. Nevertheless, one significant drawback of such system is that MRI does not provide information on nuclear signal attenuation correction which inhibits their capability to map the radiotracers efficiently. Several novel designs have been proposed to rectify MRI based attenuation correction. This involves making modifications to the MRI system such as in field-cycled systems (Hofmann, Steinke et al. 2008) and split- magnet (Lucas, Hawkes et al. 2006) designs. In spite of the modifications, the spatial resolution of such systems is in the mesoscopic scale (mm). It does not have real-time imaging capabilities as well as the ability to provide microscopic information from the diagnosed site.

2.4.1.3 XCT/MRI

Research efforts were also devoted towards integrating two structural imaging modalities such as X-ray and MRI imaging systems together. Significant work was reported towards the development of a hybrid X-ray/MRI imaging system used for interventional applications wherein, a prototype X-ray fluoroscopy system has been used to obtain two dimensional (2D) images with higher spatial and temporal resolutions and MRI providing three dimensional (3D) images for accurate localization (Fahrig, Ganguly et al. 2008). Research is also actively being carried out for enhancing the capabilities of such systems, specifically to explore its

potential when integrated with MR systems with higher field strengths so as to enhance the spatial resolution capabilities. However, the high energy X-ray radiation emitted from the XCT component in the multimodal imaging system poses potential health hazards.

Further, significant works have also been reported towards developing optical-nuclear imaging hybrids where optical imaging modalities were coupled with PET or SPECT to perform multimodal molecular and functional imaging. Introduction of single detectors for both optical and nuclear imaging system (Prout, Silverman et al. 2004) opened up new avenues for the realisation of such novel optical-nuclear imaging systems. Recently a simultaneous PET and multispectral 3D fluorescence optical tomography system (Li, Yang et al. 2011) was also reported to show the potential capabilities of such combinations. Hybrid X-ray and FMT systems have been also reported very recently (Ale, Ermolayev et al. 2012) and significant research is being carried out towards the realization of novel optical hybrids.

2.4.2 Non-ionising Multimodality Imaging Systems

This section briefly reviews the significant works reported in relation to the various non-ionising multi-modal imaging schemes. To overcome the constraints of limited amount of information obtained from depths of tissue and the potential health hazards due to ionising radiations, increasing research efforts have put towards developing systems that combine optical imaging systems with non-ionising imaging systems such as MRI (for whole body imaging). Initial works were reported in concurrent optical and MR imaging, where an optical fiber based near infrared (NIR) imager was placed inside the bore of a 1.5T MR imaging

system (Ntziachristos, Yodh et al. 2000). The system could typically perform contrast enhanced diffuse optical tomography (DOT) of the breast (Ntziachristos, Yodh et al. 2000) and MR- guided optical spectroscopy of breast lesions (Ntziachristos, Yodh et al. 2002). As MR element is employed in the system, longer imaging times (minutes to hours) are required which greatly restrict their use where quick response imaging capabilities are needed. Furthermore, the spatial resolution scales of both DOT and MR modalities operate at the mesoscopic scale rather than at microscopic scale.

In summary, there have been significant research works in the development of ionising multimodality imaging systems using nuclear, MRI or X-ray modalities. The key challenges involve the repeated use and the limited level of dosage (the current mean effective dose is 4.6 mSv per diagnostic Procedure) that can be applied to the target subject owing to the use of ionizing radiations. This gives rise to serious health concerns. Such systems are also not capable of performing simultaneous or near- simultaneous imaging coupled with other imaging modalities. Both MR and nuclear imaging based techniques are also challenged as they require long interrogation times (minutes to hours) which restrict their real-time imaging capabilities.

The above reviews also highlight that current sequential multi-modal imaging modalities and synchronous multi-modal imaging systems are not capable of performing multi-level imaging with the spatial resolution scales spanning from microscopic to mesoscopic scales and along the depths of the tissue using non-ionising radiations. It was however found that to provide multi-level and multi-scale information, data from the individual imaging modalities need to be

integrated in such a way that they could provide complementary information from the diagnosed site. It was also established that optical and ultrasound techniques are capable of providing near real-time imaging capabilities with non-ionizing radiations and scalable resolutions. Further, these techniques are also capable of providing multi-level information. Considering the capabilities of various optical imaging techniques in terms of their spatial resolution and penetration depth, the preferred optical imaging modalities to be further examined would be fluorescence microscopy for surface imaging with photoacoustic imaging for deep tissue optical interrogation.

Fluorescence microscopy in the targeted perspective should offer micron or sub-micron spatial resolution from the tissue surface whereas photoacoustic imaging should typically map optical absorption heterogeneities across the depth of the tissue at mesoscopic spatial resolution. Further, complementary structural information based on the acoustic heterogeneities along the depth of the tissue can also be derived using ultrasound imaging at mesoscopic spatial resolution. It is foreseen that, the proposed multi-modal imaging scheme will offer unique imaging capabilities to provide structural and molecular level information at varying spatial resolution scales. The following section reviews the significant works reported in the field of fluorescence, photoacoustic and ultrasound imaging.

2.5 Fluorescence Imaging

This section reviews the significant works reported in the field of fluorescence imaging as well as to investigate the potential use of fluorescence microscopy in the targeted perspective of offering micron or sub-micron spatial

resolution from the tissue surface. Fluorescence imaging has gained considerable interest and significance in the field of biomedicine owing to the potential capabilities in providing functional and molecular visualization of cellular machineries. The approach attempts to exploit the various physical properties of light in several photophysical and photochemical mechanisms at molecular level where several bio-molecular activities in living organisms can be visualised. This can be achieved where certain kinds of molecules are made to absorb light at a specific wavelength and emit light of a higher wavelength after a brief interval (Weissleder and Pittet 2008).

Fluorescence imaging can be performed with the aid of both exogenous as well endogenous chromophores. Autofluorescence from endogenous chromophores such as flavin adenine dinucleotide (FAD) and reduced nicotinamide adenine nucleotide (NADH) are widely used towards the classification of normal, benign or malignant areas within a tissue. Identification of disease biomarkers can also be done by preparing molecular probes that are created by conjugating targeting moieties with a fluorescent dye of interest. Enhanced detection capabilities are also possible with plasmonic enhancement of fluorescent dyes. These techniques can certainly pave the way for the early diagnosis, prognosis and staging of several types of diseases.

2.5.1 Reporter Strategies

Fluorescence imaging involves the usage of several reporter strategies to visualize several molecular processes in-vivo. The two major fluorescence reporter strategies are classified as 1) direct and 2) indirect methods (Ntziachristos 2006). Direct imaging which targets a specific moiety such as a receptor or an enzyme

involves the administration of engineered fluorescent probes that are categorized as active or activatable probes. Active probes are fluorochromes that are bound with a specific affinity ligand for a certain target. However, active probes fluoresce even if they are not bound to the intended target results in nonspecific background signals (Ntziachristos 2006). Activatable probes are molecules which carry quenched fluorochromes ranged in proximity to each other which results in self-quenching (Weissleder, Tung et al. 1999), or by placing next to a quencher using enzyme-specific peptide sequence (Tung 2004) which gets cleaved in the presence of the enzyme. Unlike active probes, activatable probes exhibit lower background signals since they remain dark in the absence of the target thereby increasing the contrast and detection sensitivity. Indirect fluorescence imaging is the strategy adopted for studying gene expression and gene regulation. This technique primarily involves the usage of transgene (called reporter gene) (Ntziachristos 2006) that encodes for a particular fluorescence protein whereby the gene transcription leads to the production of the fluorescent protein. This enables the visualization of gene expression and regulation mechanisms using various fluorescent imaging techniques. Researchers have also developed strategies to study gene expression while maintaining the protein of interest intact (Mohrs, Shinkai et al. 2001).

2.5.2 Fluorescence Imaging Modalities

Fluorescence visualization capabilities are very much dependent on the optical instrumentation employed in conjunction with the various fluorescent probes. Though several new technologies have been developed for fluorescence visualization in living tissues, all these techniques can be broadly classified into

two categories, namely 1) mesoscopic fluorescence imaging and 2) microscopic fluorescence imaging.

2.5.3 Mesoscopic Fluorescence Imaging

Mesoscopic imaging refers to the imaging systems that rely on photographic principles to collect images in low light (Weissleder and Pittet 2008). This technique involves mainly two different approaches such as fluorescence reflectance imaging and fluorescence tomography. Fluorescence reflectance imaging involves the usage of excitation source, filters and a charge coupled device (CCD) camera to obtain two dimensional planar images of various surface features. However, this modality does not provide quantitative data and the spatial resolution scales are beyond 3-5 mm. Fluorescent tomography systems provide quantitative information together with three dimensional maps of fluorochromes using sophisticated algorithms (Ntziachristos, Schellenberger et al. 2004). A detailed description on the theoretical basis of these techniques can be obtained from some prominent reviews (Arridge 1999, Gibson, Hebden et al. 2005).

2.5.4 Microscopic Fluorescence Imaging

Microscopy refers to the technique of viewing features that cannot be directly visualized by human eye. Microscopy forms to be one of the critical tools in current biomedical community and several forms of light microscopy have been widely employed in several biological settings. The first work in this area was reported in 1839 by Rudolph Wagner where he utilized bright field illumination to image the rolling of leukocytes in blood vessels within membranous translucent tissues (Wagner 1839). With the advent of various fluorescence microscopy

modalities including the super-resolution techniques, it is now possible to visualize several cellular processes in-vivo with unprecedented resolution and contrast. The simplest and cost effective way to perform this would be to use a conventional optical microscope with specific fluorescence excitation and emission filters. However, a greater level of interest has been also devoted towards adapting these technologies into flexible probes that can be used for performing high resolution endoscopic examinations of hollow organs and inaccessible areas.

Over the last decade fiber-optic based devices have gained in functionality at greater levels which enhanced the capabilities of fiber-optic fluorescence imaging much more prominent and versatile. Several factors including the applications and manufacturability of such devices provided the primary motivations to pursue high end research in the area of fiber-optic imaging. Fiber-optics based imaging modalities provide high resolution cellular images for basic research on biological and disease processes where conventional microscopy techniques are challenged. Fiber-optics imaging enables the imaging of inaccessible areas within hollow organs and moving subjects with improved flexibility where conventional optical imaging techniques often fail to thrive. Fiber-optics imaging also aids to perform minimally invasive diagnosis and surgical procedures and opens several avenues for performing long term imaging studies in live subjects by implanting fiber-based devices within them. The introduction of novel bio-compatible fluorescent probes and advancements in optical instrumentation has equipped fiber-optic based imaging systems with higher imaging and spectroscopic capabilities in microscopy, endoscopy and microendoscopy. In all these modalities, fiber-optic structures are used for light delivery and collection of fluorescence emissions where specific

focusing and scanning mechanisms are also used to alter the axial and lateral imaging planes.

Fiber – optic based imaging modalities have found its typical applications in the imaging of superficial tissues as well as hollow tissue cavities (Swindle, Thomas et al. 2003, Kiesslich, Burg et al. 2004, Ota, Fukuyama et al. 2005). Fiber-optic based endoscopes have also demonstrated its potential capabilities in cellular imaging within solid tissues of live subjects (Jung, Mehta et al. 2004, Levene, Dombeck et al. 2004, Flusberg, Jung et al. 2005). When an array of parallel optical fibers are bundled together, they are capable of guiding pixelated imaging across the two faces of the fiber bundle. Such image guides can be integrated with conventional magnification optics to provide microscopic images of an object under investigation. However, the performance of such a system is highly determined by the physical properties of the fiber bundle.

The proximal end optics determines the magnification of the system, nevertheless the magnification will be limited by the size of the individual fiberlets of the image fiber. However, the pixelation introduced in the fiber bundle degrades the lateral optical resolution of system about twice the average core to core distance between adjacent fiberlets divided by the optical magnification of the imaging lens (Flusberg, Jung et al. 2005). The thin cladding layer between adjoining cores leads to leakage of light among neighbouring pixels leading to optical cross talk between adjacent cores which reduce the contrast. By the precise positioning and adoption of specific post processing of the images can substantially improve the image quality. In such systems the image quality is primarily determined by the numerical aperture of the fiber, the relative spot size and light

gathering ability which are primarily governed by the focusing element at distal end. Since, this particular research adapts fluorescence imaging concepts for obtaining images with micron or sub-micron spatial resolution from tissue surface, investigations were only performed to establish fluorescence microscopy schemes.

Imaging deeper than few hundred micrometers with sub-millimetre resolution becomes challenging for conventional fluorescence imaging techniques. Apparently, this necessitates further investigations into the usage of novel optical imaging schemes that can provide high contrast images from greater depths with microscopic spatial resolution. Over the recent years, photoacoustic imaging (PAI) has been evolved as one of the promising optical imaging modalities that offers scalable spatial resolution capabilities beyond the optical diffusion limit (~ 1 mm) (Wang and Hu 2012). Further, PAI also offers potential capabilities to provide multi-level information (structural, functional and molecular) from the diagnosed site (Wang and Hu 2012).

2.6 Photoacoustic Effect (PA)

This section seeks to review photoacoustic imaging techniques with the view of mapping optical absorption heterogeneities across the depth of the tissue with mesoscopic spatial resolution. The generation of acoustic waves by the absorption of electromagnetic energy is referred to as photoacoustic (PA) effect (Bell 1880). The history of this phenomenon dates back to 1880 where Alexander Graham Bell reported the observation of sound generated by light (Bell 1880). However, due to the lack of appropriate light sources, there was only little progress for the research on photoacoustics. Photoacoustics regained its interest with the investigation performed by L B Kruezer where PA effect was applied in detecting gas

constituents by using laser-induced PA effect (Kreuzer 1971). Photoacoustics has since been widely employed in various areas pertaining to physics, chemistry, biology, engineering and medicine. Particularly, since the past decade the field of photoacoustics has gained considerable attention in biomedicine where much interests have been devoted towards its applications in various bio-imaging applications (Ntziachristos, Ripoll et al. 2005, Zhang, Maslov et al. 2006, Li and Wang 2009, Razansky, Distel et al. 2009) .

The motivation that drove the development of PAI was to overcome the poor spatial resolution of optical imaging at greater depths and poor soft tissue contrast of ultrasound imaging. Further enhancement in penetration depth can be achieved by adopting radiofrequency (RF) or microwaves for photoacoustic excitation (Kruger, Reinecke et al. 1999, Wang, Zhao et al. 1999) which falls under thermoacoustic imaging (TAI). PAI primarily involves the irradiation of the biological tissue with pulsed lasers where the absorption of the electromagnetic energy leads to local heating of the absorbers and the subsequent thermoelastic expansion results in the generation of broadband pressure waves (ultrasound). The initial distribution of absorbed photons should have exactly the same profile as the stress distribution when the generation of heat is fast enough so that both heat sources and acoustic sources do not move (Xu and Wang 2006). The pressure waves generated from the energy absorbing centers propagate outside the tissue where they are detected by ultrasound transducers. Considering the speed of sound in biological media and the temporal scales of the time –resolved PA signals, an accurate localization of the optical absorber (PA signal source in this case) can be performed along the depth of the sample. Further, by 2D transverse scanning or by

mathematical reconstruction of the time-resolved PA signals from multiple transducers, 3D PA images are formed.

Based on the frequency of the generated photoacoustic wave, photoacoustic methodologies reported in literature can be broadly classified into two main forms;

1) Low frequency photoacoustics and 2) High frequency photoacoustics.

2.6.1 Low Frequency Photoacoustics

This particular form of photoacoustic investigation primarily involves the generation, detection and analysis of low frequency photoacoustic waves whose frequency often ranges in the range of Hertz to kilo Hertz. Low frequency photoacoustic investigations are widely employed in performing various kinds of measurements in solids, liquids as well as gaseous samples. More recently, photoacoustic spectroscopic techniques are employed due to their versatility and compatibility in obtaining the valuable information from the targeted area. They are used mainly in trace gas detection (Sigrist, Bohren et al. 2000), measuring the thermal diffusivity of the samples (Chardon and Huard 1982), depth profiling and analysis of biological materials (Bednov, Savateeva et al. 2003) where both qualitative and quantitative analysis can be performed using the PA technique. Photoacoustic spectroscopy (PAS) which is a non-ionising and non-destructive technique has important applications in research and analysis of inorganic, organic and biological samples (Lim, Mahmood Mat Yunus et al. 2009).

PAS constitutes a simple and reliable experimental (Adams and Kirkbright 1977) tool that can perform investigations with minimal sample preparation and has the capability to perform depth profiling experiments on opaque and scattering

samples in measuring thermal diffusivity and proves as a method which provides direct measurement of energy absorbed by the sample (Sathiyamoorthy, Vijayan et al. 2007). Rosencwaig, Patel and Tam (Patel and Tam 1979, Tam and Patel 1979, Rosencwaig 1980, Patel and Tam 1981) have well established the basic principles of PA effect. Further, James (James Joseph 2010, James Joseph 2012) had also conducted explorations into low frequency photoacoustics. Their research found that low frequency PA is not well suited for high resolution imaging studies. Experimental studies using with open photoacoustic cell (OPC) configuration was conducted to determine the thermal diffusivity of colon phantom tissue and phantom tissue administered with gold nanoparticles. From the experimental investigations, it was observed that this particular technique can be effectively utilized for determining the thermal diffusivity of solid samples. A detailed analysis of the fundamental theoretical concepts of low frequency photoacoustics as well as a description of the OPC based photoacoustic investigations for thermal diffusivity measurements are given in appendix F.

2.6.2 High Frequency Photoacoustics

High frequency photoacoustic investigations primarily involve the generation, detection and analysis of high frequency photoacoustic waves whose frequency often ranges in the ultrasonic range (> 20 KHz). More comprehensive information about the sample under study can be obtained using this technique when compared to low frequency photoacoustic investigations. Majority of the works under this type of investigation falls under PAI which gives cross-sectional or three dimensional imaging of the sample. PAI combines ultrasound resolution with high contrast due to light absorption. The initial distribution of absorbed

photons should have exactly the same profile as the stress distribution when the generation of heat is fast enough so that both heat sources and acoustic sources remain equitable (Xu and Wang 2006). As long as the photons excitation is relaxed thermally, photoacoustic signals are produced, and they depend on any absorbed photons that are either scattered or unscattered (Wang 2008).

Photoacoustic imaging involves three main aspects. They are optical excitation, acoustic detection and image reconstruction. According to the mode of the optical excitation of target specimen, the broad scope of PAT can be categorized and labelled into two as time domain PAT (TD-PAT) (Wang 2008) and frequency domain PAT (FD-PAT) (Telenkov and Mandelis 2006). In TD-PAT acoustic waves are generated by short optical pulses with high peak power whereas in FD-PAT, acoustic waves are generated by a continuously modulated optical source with relatively low mean power and high modulation frequency (Telenkov and Mandelis 2006). The former technique emerged over the years as a preferable way of producing acoustic transients of large magnitude while the later technique was originally employed in the discovery of the photoacoustic effect and is being frequently used in spectroscopic studies as well as thermal diffusivity studies (Rosencwaig 1973, Tam and Patel 1979, Valvano, Cochran et al. 1985, Telenkov, Youn et al. 2001, Qiu, Zhang et al. 2008). Regardless of the mode of optical excitation of acoustic waves, PA signal generation is a multistage process that involves modelling of the photon transport in the tissue under investigation, heat conduction processes and elastic wave generation. Moreover, in order to obtain the physical nature of PA effect in biological tissue, it is required to have a complete three dimensional analysis applied to the specimen with complicated geometrical

shapes (Kruger, Reinecke et al. 1999). Further, much interests have also been devoted towards the usage of pulsed multispectral (Razansky, Buehler et al. 2011) and broadband (hyperspectral) radiation sources.

Photoacoustic detection can be effectively carried out at the surface of the samples based on piezoelectric, capacitive, electromagnetic or laser interferometric principles (Paltauf, Nuster et al. 2007). Laser interferometers or piezoelectrics which have a flat response less than 1 up to 100 MHz are the most suitable sensors for PA tissue imaging. From a sensitive point of view, piezoelectric detection seems to be more favourable but their poor acoustic impedance match between the tissue and detector leads to a non-uniform frequency response, giving a poor representation of the detected signal. Laser interferometric detection is also a preferred option for achieving good lateral resolution and proves to be a noncontact method for remote and backward mode photoacoustic signal detection. However, the sensitivity of this particular technique is often challenged under lower excitation energies. Hence, piezoelectric detection schemes with lead zirconate titanate (PZT) transducers are the most preferred detectors (Wang 2008).

Image reconstruction in PAI involves the mapping of the optical energy absorbing centres which acts as the acoustic sources. Active research is being carried out in this area to enhance the capabilities of various image reconstruction algorithms. Numerous algorithms have been developed and applied successfully for obtaining high quality photoacoustic images with reduced image artefacts. These algorithms can be found in the literatures (Burgholzer, Hofer et al. 2005, Burgholzer, Bauer-Marschallinger et al. 2007, Burgholzer, Matt et al. 2007, Jaeger, Schüpbach et al. 2007, Kunyansky 2007, Modgil, Anastasio et al. 2009). Delay and

Sum beam forming based algorithms are one of the preferred image reconstruction approaches which mainly involves the usage of commercial ultrasound transducers for photoacoustic imaging (Xu and Wang 2006).

Based on the fundamental physical principles of the optical and acoustic wave propagation in biological tissue, PAI is restricted to operate within specific spatial resolution scales and penetration depths. As a consequence, often there are trade-offs between imaging depth and spatial resolution where application specific PAI modalities were developed that offers high resolution or deep penetration imaging capabilities. Towards this direction various forms of PAI have been evolved to image both microscopic and mesoscopic features from the surface as well as along depths of the tissue (Li and Wang 2009). Based on the level of achievable spatial resolution and penetration depth, PAI modalities can be broadly classified into two major forms of implementation: photoacoustic microscopy (PAM) and photoacoustic tomography (PAT). PAM techniques primarily involve the usage of high frequency transducers supported with focused or unfocused optical excitation and adequate 2D transverse scanning mechanisms to construct 3D PA images. Axial resolution is primarily governed by the time-resolved detection of PA signals and pulse width of the optical excitation. Time-resolved detection of PA signals are directly dependent on the frequency of the ultrasound detector (higher the frequency better the localization of the PA signal source) and the operating frequency of the receiver electronics (higher the sampling frequency finer the time-resolved detection of PA signals). Further, the pulse width of the optical excitation should satisfy the conditions of thermal and stress confinements for the targeted size of the optical absorber. Lateral resolution in PAM is

determined by the quality of the optical and acoustic focusing or by the overlap of the optical and acoustic foci. Significant works have been reported in relation to multi-level PAM which involve lateral resolution scales varying from micrometers to few hundred nanometers (Zhang, Maslov et al. 2006, Maslov, Zhang et al. 2008, Rao, Maslov et al. 2011). However, considering the fundamental principles of high frequency ultrasound propagation and optical focusing in biological media, the penetration depths in PAM are limited to few millimeters in biological tissue.

Nevertheless, to perform deep tissue imaging and to accelerate the imaging speeds, near-infrared (NIR) optical excitation and signal detection using ultrasonic transducer arrays are widely used at the expense of sacrificing the spatial resolution. PAT primarily involves the irradiation of the entire region of interest (ROI) by an expanded optical beam to generate the PA signals. The ultrasound detectors coupled at multiple locations around the ROI performs the time-resolved detection of the PA signals and further subjected to mathematical reconstruction routines to form 2D or 3D PA images. Axial resolution in PAT is again dependent on the time-resolved detection of PA signals and pulse width of the optical excitation. However, lateral resolution is primarily governed by the physical dimensions and positioning of the ultrasound detectors. Depending on the excitation wavelengths, the penetration depth of PAT varies from few millimeters to several centimeters. By capitalizing on the low optical attenuation at the biological optical window and low ultrasonic scattering, deep tissue PAI studies were performed with mesoscopic spatial resolution (Ku and Wang 2005, Manohar, Vaartjes et al. 2007, Kim, Erpelding et al. 2010).

In summary, PAT forms the most versatile PA imaging modality in which numerous detectors and system designs have been developed. PAT is also suitable for large area interrogation since PA signals emerging from a wide region can be captured by each ultrasonic detector. Real-time imaging can also be possible in PAT by employing an array of ultrasonic transducers. Current PAT imaging has its challenges in producing high quality images due to the influence of detection geometry, reconstruction algorithms and the inhomogeneous nature of the tissue. Unlike PAT, PAM does not suffer from image artefacts. PAM employs only a single element ultrasonic transducer, which makes it less expensive when compared with array based PAT. However, PAM requires large amount of mechanical scanning making it difficult for real-time interrogation of large area. Therefore, in order to perform near real-time imaging capabilities without scanning, PAI based on transducer arrays should be preferred. Further, to meet the targeted research objectives, the photoacoustic imaging system based on transducer arrays should typically map optical absorption heterogeneities across the depth of the tissue at mesoscopic spatial resolution.

2.7 Nanoparticle Assisted Optical Imaging

The field of biomedicine has also witnessed an increased interest in the use of various kinds of nanomaterials during the past decade. Although tissue contains endogenous sources of signatures for most biomolecules, it is not specific within the tissue milieu which can give a positive identification of the targeted molecule species or protein. An alternative strategy is to use exogenous materials that can access and intervene the molecular world of living cells and their machinery which are of similar size to the targeted molecules. These exogenous particles can be

either used to ‘report’ the presence of a molecule or to ‘intervene’ and therapeutically change a process within a cell.

Recently researchers have started using exogenous contrast agents to enhance the contrast of optical images (Agarwal, Huang et al. 2007). However, the outcomes of these imaging procedures would depend on the fundamental operating parameters (spatial resolution and penetration depth) of each optical technique. Some examples of nanotechnology currently under development for optical imaging applications adapted from (Moghimi and Kissel 2006) are given in Table 2.

Technology	Typical Size	Applications
Quantum Dots	1-10 nm	In-vitro and in-vivo fluorescence based molecular imaging (Alivisatos 1996, Chan and Nie 1998, Gao, Chan et al. 2002)
Plasmonic Nanoparticles	15-200 nm	Photothermal ablation of cells and reflectance and MRI, optical and XCT molecular imaging (Oldenburg, Averitt et al. 1998, Oldenburg, Hale et al. 1999, Loo, Lin et al. 2004, Loo, Lowery et al. 2005, Popovtzer, Agrawal et al. 2008, Moriggi, Cannizzo et al. 2009)
Carbon Nanotubes	1-100 nm diameter and 20-1000 nm length	NIR Photoablation (Kam, O'Connell et al. 2005, Liu, Cai et al. 2007) and Fluorescent sensor (Barone, Parker et al. 2005, Heller, Baik et al. 2005, Heller, Jeng et al. 2006)

Table 2 Nanoparticles in imaging applications

By capitalizing on the unique optical response of these nanoplatforms in terms of their enhanced scattering and absorption properties, the imaging capabilities of a particular optical modality can be further enhanced with the aid of the listed exogenous contrast agents. The advent of novel bio-conjugated nanoplatforms has pushed the limits of molecular level to greater levels. Therefore, molecular information with enhanced sensitivity and specificity can be obtained from targeted site by attaching functional moieties to the surface of the specified nanoparticle.

The development of hybrid multimodality imaging systems with optical based modalities as one of the modes has also generated much research interests. In milieu, significant amount of research is being carried out towards developing nanoparticle based molecular probes for multi-modal systems and a few have been already reported (Kim, Park et al. 2007, Alric, Taleb et al. 2008, Wang, Liao et al. 2012, Wilson, Homan et al. 2012).

The fundamental building blocks in majority of these nanoprobess are plasmonic metal nanoparticles such as gold nanoparticles (Alric, Taleb et al. 2008, Popovtzer, Agrawal et al. 2008, Moriggi, Cannizzo et al. 2009, Wang, Liao et al. 2012, Wilson, Homan et al. 2012). Plasmonic nanoparticles synthesised from noble materials such as gold with or without combinations of a dielectric material are less toxic and are spectrally tunable (Oldenburg, Averitt et al. 1998, Schultz, Smith et al. 2000, Lyon, Fleming et al. 2004). They do not photobleach (Schultz, Smith et al. 2000) and have higher optical cross-section than quantum dots (Yguerabide and Yguerabide 2001). Plasmonic nanoparticles also exhibit an interesting phenomenon called ‘plasmon coupling’ wherein the presence of other resonant scatterers in the

near field induce a shift in the optical properties of the plasmonic particles (Elghanian, Storhoff et al. 1997, Krenn, Weeber et al. 1999, Yguerabide and Yguerabide 2001, Sönnichsen, Reinhard et al. 2005).

Enhancement of the optical signal and image contrast can also be achieved with plasmonic assisted imaging and signalling schemes which in turn acts as one of the future exploratory areas in this research. Plasmonic nanoparticles such as gold nanoparticles possess potential capabilities in the field of optical imaging due to its large surface to volume ratio, tailorable size, shape and composition, structural robustness and its target binding capabilities. Owing to significant technological advancements in the synthesis, fabrication and characterization of nanomaterials, it is now possible to tailor the size, shape and composition of the gold nanoparticle according to specific imaging applications. These capabilities will offer tremendous potential in various areas of optical imaging and photonics in general. Gold nanoparticles have provided significant contributions to various fields of biomedicine such as in genomics (Shim, Lim et al. 2008, Panyala, Peña-Méndez et al. 2009), biosensors (Stewart, Anderton et al. 2008), immunoassays, clinical chemistry (Dykman and Bogatyrev 2007), detection and control of microorganisms (Luo and Stutzenberger 2008), cancer cell photothermolysis (Liu, Dai et al. 2008) and targeted delivery of drugs or other substances (Han, Ghosh et al. 2007). Literatures (Alric, Taleb et al. 2008, Popovtzer, Agrawal et al. 2008, Moriggi, Cannizzo et al. 2009) also show that gold nanoparticles are extensively used in conjugation with various non-optical imaging modalities. Hence, nanoprobes based on gold nanoparticles can be effectively tailored for several

promising multimodal imaging applications comprising of optical, MR or X-ray based imaging modalities.

Various forms of gold nanoparticles have found potential applications in PAI where they are used to enhance PAI contrast and to provide molecular specificity (Mallidi, Luke et al. 2011). However, there is more room for contributions towards this aspect of study wherein efforts can be directed towards studying the absorptive and scattering properties of gold nanoparticles with varying sizes, shape and compositions over a range of wavelengths and to determine a way to tailor their contributions for the selected application. It is thus paramount to determine the optical properties of gold nanoparticles for its efficient in photoacoustic imaging where the PA signal augmentation is directly derived from the optical absorption of gold nanoparticles and this forms one of the major work areas in this research.

2.8 Ultrasound imaging

To complement the optical imaging modalities, this section reviews on the ultrasound imaging technology and the existing work done to obtain structural information based on mapping acoustic heterogeneities along the depth of the tissue with mesoscopic spatial resolution. Ultrasound imaging accounts for one fourth of the clinical imaging procedures around the world and has become matured over the past (Wells 2006). Ultrasound imaging which employs acoustic waves with frequencies above 20 kHz is one of the most widely employed diagnostic imaging modalities in current biomedical settings. This particular modality employs non-ionizing and safe acoustic energy radiation and has been widely used in cardiology, gynaecology, obstetrics and abdominal imaging. Unlike

optical techniques, ultrasound imaging primarily maps the various acoustic heterogeneities present throughout the tissue. Non-invasive and minimally invasive ultrasound imaging can provide high resolution images of the diagnosed site and also aids in performing a multitude of image guided surgeries. Majority of the ultrasound imaging systems use acoustic frequencies in 3 - 20 MHz range for their operation and high frequency modalities like bio-microscopy operates within 20 MHz - 40 MHz.

Ultrasound imaging has been progressed rapidly over the years and the state of the art ultrasound imaging principles based on linear acoustic propagation has been thoroughly reviewed by Wells about 30 years ago (Wells 1977). In ultrasound imaging, images are constructed from scanning the input ultrasound beam, either by the mechanical raster scanning of the transducer or by the electronic control of ultrasound transducer array. The electronic beamforming in transducer array system facilitates the focussing and steering of the ultrasound beams across a specified interrogation area thereby offering dynamic focussing and receiving capabilities. Several advancements in beamforming have been made recently which offer significant capabilities to enhance the quality of ultrasound images (Brown and Lockwood 2005). Further, significant progresses have been also reported in various domains of ultrasound imaging such as electronics and instrumentation, signal and image processing (Wells 2006). Significant works were also reported in the area of ultrasound transducer fabrication namely; lead zirconate titanate (PZT), polyvinylidene difluoride (PVDF) and capacitive micromachined ultrasonic transducer (CMUT). Amongst these, the mostly widely used clinical and pre-clinical transducers are based on PZT array transducers (Wells 2006).

The basic operation of ultrasound imaging involves the application of acoustic energy from the ultrasound transducer into the sample and depending on the acoustic impedance mismatch, the acoustic energy is reflected back to form the images. The depth information of the sample is obtained from the time of arrival of the echo and the characteristic tissue density will be mapped from the intensity of the echo (Christensen 1988). Thus, by capitalizing on the fundamental principles of beamforming and ultrasound propagation in biological media, ultrasound imaging can be used to map the acoustic heterogeneities along the depth of the tissue and thereby aims to provide complementary information from the diagnosed site.

2.9 Summary of Literature Review Findings

A brief review on the four types of tissues showed that, each of the tissue types is composed of complex cellular machineries with a wide range of sizes and molecular compositions where a shift in these cellular parameters indicates a potential disease state of the tissue. Currently, much of the tissue diagnostic procedures are performed with the aid of imaging systems that have been widely employed in both clinical and pre-clinical applications. However, the size and molecular heterogeneities of the different types of tissue and their cellular constituents necessitate an imaging system tailored for early disease diagnostics to provide multi-level information with scalable spatial resolutions. Further, the level of obtainable information and achievable spatial resolutions are directly linked to the type of energy input used for the imaging procedure.

A review on the capabilities of existing imaging systems shows that the information typically gleaned from current imaging modalities are challenged with

their fundamental physical limitations, usage of ionizing radiations, long interrogation time, lack of sufficient spatial resolution and level of obtainable information. Therefore, the inherent limitations of each of the imaging techniques impose fundamental challenges for a single imaging modality to extract all aspects of structural and molecular states of the tissue with adequate spatial resolution. Although sequential imaging of the subject with manifold imaging platforms satisfies certain imaging requirements in terms of the multi-level and multi-scale imaging capabilities, they often fail to provide an accurate registration of the multi-modal images obtained from moving structures as well as fail to measure and correlate two different tissue parameters simultaneously. For these reasons, significant research interests were drawn towards integrating two or more imaging modalities to greater or lesser extent into a single imaging unit. Such systems which are classified as synchronous multimodality imaging systems seek to integrate the strengths of two or more imaging modalities into a single unit to image the target simultaneously or near simultaneously and thereby eliminating the non-synchronous registration problem.

Though majority of the significant research works on synchronous multi-modal imaging systems are based on nuclear, MR or X-ray modalities, they are still challenged with their incapability to perform simultaneous or near- simultaneous imaging. Further, X-ray and nuclear imaging based techniques also involve the usage of ionizing radiations which induce potential health hazards to the subjects. Apparently, this necessitates exploration into novel multi-modal imaging schemes that employ only non-ionizing radiations for obtaining multi-level and multi-scale information. The review on various imaging modalities shows that optical and

ultrasound techniques are capable of providing near real-time imaging capabilities using non-ionizing radiations. Further, the unique capabilities of optical and ultrasound techniques to provide multi-level information supplements the potential of combining these two techniques as an effective multimodal combination. Therefore, high resolution fluorescence microscopy concepts for surface imaging and photoacoustic imaging across the depth with mesoscopic spatial resolution would be an excellent combination. Further, complementary structural information based on acoustic heterogeneities located along the tissue depths can also be derived from ultrasound imaging.

In this perspective, it was found that two forms of fluorescence microscopy can possibly be used to provide micron or sub-micron spatial resolution from the tissue surface namely; conventional optical microscope based and fiber-optic based. Further, the inherent penetration depth limitations for fluorescence microscopy techniques can be overcome by adopting investigating on an imaging schemes based on photoacoustic effect. High frequency photoacoustic imaging can be performed at a faster rate with adequate spatial resolution by using multi-element transducers together with robust image reconstruction algorithms such as delay and sum algorithm. Thus, the proposed photoacoustic imaging system based on transducer array could map optical absorption heterogeneities along the depth of the tissue with mesoscopic spatial resolution. Further, the potential capabilities of photoacoustic imaging can be enhanced by administering the tissue with exogenous contrast agents such as gold nanoparticles. In addition, acoustic heterogeneities along the depth of the tissue can be effectively mapped at mesoscopic spatial resolution with the aid of multi-element ultrasound imaging system equipped with

dynamic focusing and steering capabilities. Experimental investigations are therefore to be conducted towards exploring on how the three distinct imaging systems were to be configured in terms of their excitation sources, detectors and associated optical, mechanical and electronic configurations with the view of integrating them together to form the proposed multi-modality imaging system.

The proposed non-ionizing multimodal imaging system should therefore map multi-level optical and acoustic heterogeneities (complementary information) along the depth of the tissue at multi-scale resolution. Further, investigations using a combination of these three imaging modalities are therefore needed to characterise them accordingly so as to establish a methodology that can derive structural and molecular level information regarding the optical and acoustic heterogeneities (complementary information) along the depth of the tissue at multi-scale resolution (microscopic to mesoscopic).

Chapter 3: PROPOSED INSTRUMENTATION SCHEMES FOR FLUORESCENCE MICROSCOPY SYSTEMS

This chapter describes the various experimental investigations carried out to establish novel instrumentation schemes for fluorescence microscopy systems in the view of future integration with the proposed multi-modal system. The experimental investigations were fundamentally directed towards establishing the fluorescence microscopy systems to obtain fluorescent signatures with micron or sub-micron spatial resolution. Two variants of fluorescence microscopy systems are compared: 1) Inverted fluorescence microscope 2) Flexible fluorescent microscope based on image fiber bundle (fluorescence endoscope). Experimental studies on inverted fluorescence microscope are depicted initially and this will be followed by detailing the experimental investigations performed in relation to fiber-optic fluorescence microscope. The investigations show that both these forms of fluorescence microscopy systems can provide high resolution fluorescent signatures from the phantom tissue surface with the targeted spatial resolution.

3.1 Introduction

In this chapter, the proposed instrumentation methodologies and related system features of an inverted fluorescence microscope and an image fiber assisted microscope would be discussed. The findings would be incorporated and later integrated with the proposed main objective of the system which is a multi-modality imaging system. Investigations into the visualization of fluorescent signatures from

the tissue surface at microscopic spatial resolution are also made to determine the appropriate set of imaging parameters and their relationships. The experimental investigations were fundamentally directed towards establishing the fluorescence microscopy systems to obtain fluorescent signatures with micron or sub-micron spatial resolution with the view of integrating the fluorescence imaging schemes into the proposed multi-modal imaging system. Two common variants of fluorescent microscopy systems are experimentally investigated which involve the establishment of the novel system configurations, calibration, evaluation and characterisation of the imaging systems.

3.2 Fluorescence Microscopy Instrumentation Schemes for Multimodality Imaging

3.2.1 Inverted Fluorescent Microscope

The proposed inverted fluorescence microscope was configured on the Olympus UIS2 optical system (infinity-corrected) and involved systematic formulation and adaptation of the various optical elements required to establish a fluorescence microscopy system. The infinity corrected optics established a system in which the light rays from the specimen were passed through the system without forming any image before the tube lens. This particular optical configuration, therefore, facilitates the mounting of prisms and sliders in the optical path and maintained the image size without any magnification and aberrations throughout the optical path.

The fluorescent microscope for performing video rate fluorescence imaging was configured by careful selection of the suitable optics, filters, mounts, adaptors and the imaging camera. The most critical optical element of any microscope is the objective lens as they are responsible for the primary image formation and determine the quality of the images. Therefore, in order to obtain high quality images with sufficient resolution and brightness, key consideration was made to minimize the spherical and chromatic aberrations with flat field corrections. The objective lens used in conventional metallurgical microscopes would not be suitable as they impose potential spherical and chromatic aberrations if used in fluorescence microscopy applications. Olympus UMPlanFl objective lens which are categorized under Plan Fluorites (Plan Semi-Apochromats) are therefore used in this proposed microscope setup. This is for the UMPlanFl series of microscope objectives had additional spherical aberration and chromatic aberration corrections when compared to Plan achromats that are used in typical metallurgical microscope.

The beam size passing through the objective lens is restricted by the rear aperture or exit pupil whose diameter varies between 5 mm for the highest power objectives and up to 12 mm for the low magnification objective lens. In the proposed epi-illumination experimental configuration, the exit pupil also acted as the entrance pupil making the objective lens to behave as an imaging system as well as a condenser. Therefore, the aperture size and pupil filling was highly critical to obtain high quality images. Larger source image on the pupil would result in the reduction of illumination intensity whereas smaller source image will introduce vignetting of the viewfield. Hence, to produce uniform illumination

across the viewfield, the rear aperture of each of the objectives was optimally filled with the image of the light source using a variable aperture mounted at the laser entrance port of the microscope. Further, adequate optics, filters and optomechanics for direct viewing and to facilitate digital imaging were also integrated into the microscope as detailed in Appendix A.

Once the optomechanics for mounting the camera were configured, the scientific imaging camera (Neo sCMOS. Andor Technology) with complementary metal–oxide–semiconductor (CMOS) sensors was mounted over the camera mount adapter. The sCMOS camera had 2560 x 2160 (5.5 Megapixel) active pixels with a pixel size 6.5 μm and the front illuminated scientific CMOS had a sensor size (width x height) of 16.6 x 14.0 mm (21.8 mm diagonal). The pixel size was determined to provide ideal over-sampling of the diffraction limit in the current fluorescent microscopy applications with 20x and 50x objectives. The following set of calculations ensured that the camera was capable to operate with the maximum possible spatial resolution of the system.

For the perfectly aligned system with objective lens acting as the imaging system and condenser, the maximum possible optical resolution was calculated according to Rayleigh criteria as,

$$\Delta R = \frac{0.61\lambda}{NA} \quad 3-1$$

Where ΔR is the minimum resolvable distance between two points, λ is the illumination wavelength and NA is the numerical aperture of the microscope objective. Assuming an excitation wavelength of 519 nm and numerical aperture of 0.8, the optical resolution was calculated to be 395.74 nm. Considering the 50X

magnification of the objective lens and no additional magnification along the optical path, the image size projected on the sensor was determined to be $19.79\mu\text{m}$. Further, to conform to Nyquist sampling criterion, the image size should be sampled with 2.5 to 3 pixels of the detector. Based on Equation 3.1 and considering the 50X magnification from the 0.8 NA objective lens, the sensor pixel size of $6.5\mu\text{m}$ was adopted as it was adequate to satisfy the Nyquist criterion for imaging the smallest airy disk unit formed in the microscopy system. Further, line pairs per millimeter (LP/mm) and lines of horizontal resolution (LoHR) were determined to be 50.53 and 1414.86 respectively. Considering the aspect ratio (1.19) of the sensor array, the maximum resolution of the sensor array was calculated to be 1683.68. Therefore, the minimum number of pixels required to match the optical resolution of the microscopy system was determined as 2.4 million pixels. This means that a 5.5 megapixel camera when operated at full resolution would be appropriate for such investigations.

Another key configuration consideration is the effective operation of the sensors. A thermoelectric cooling mechanism of the camera is essential to enable the sensors to operate at -30°C to reduce the sensor dark current to 0.07 e-/pixel/sec. The operational efficiency of these sensors would also improve at 50% or greater and within the desired 480 nm – 700 nm range thereby utilizing the high quantum efficiency of the camera. Thus, by incorporating all these factors, the device was transformed into a high sensitive imaging apparatus that can operate with extremely low fluorescence signal. The schematic of the experimental set-up is shown in Figure 3.1.

The experimental set-up, shown in Figure 3.1, consists of a tunable nanosecond pulsed laser (Vibrant 355 II, Opotek Inc., USA) as the excitation source. The signal from the Nd:YAG laser pumped optical parametric oscillator (OPO) enabled the laser to operate in the wavelength range of 410 nm – 720 nm. The pulse width was 5 ns and the pulse repetition rate was 10 Hz. The fluorescent signatures were generated by focussing the excitation beam with the microscope objective lens. The emission signals collected by the objective lens were further propagated along the optical path to the imaging camera. The emission filter mounted along the optical path blocked unwanted wavelengths and ensured that only the fluorescence emission signals are imaged.

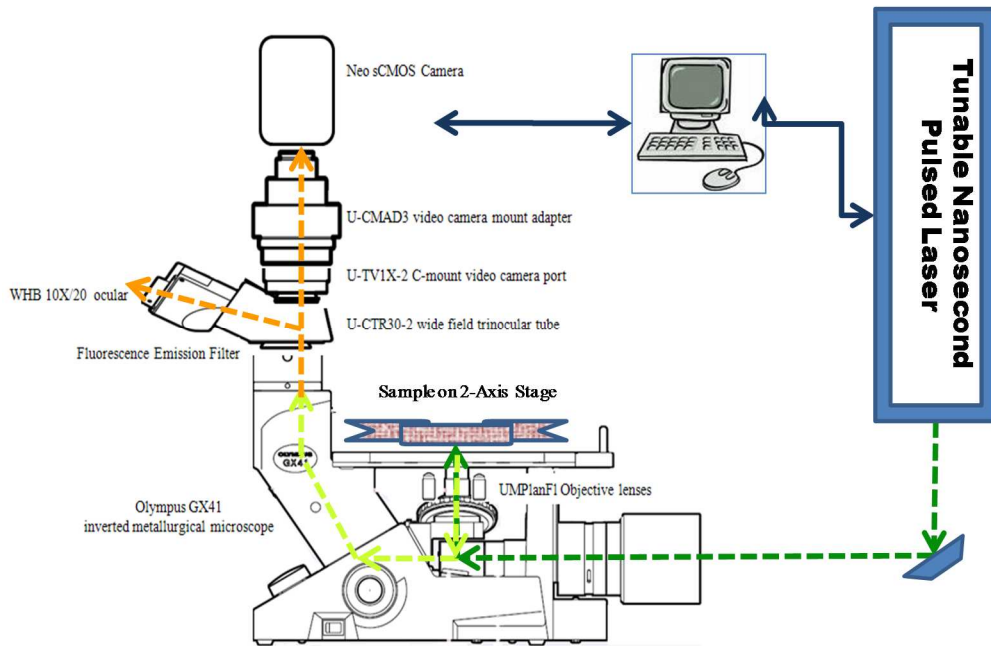


Figure 3.1 Schematic of the proposed experimental set-up for fluorescence microscopy

Fluorescence microscopy was performed with four different types of objective lens whose specifications are listed in Table 3 for fluorescence imaging studies. Prior to the imaging studies, the lateral resolution capability of the system

needs to be characterised. In this research, a standard United States Air Force test target (1951 USAF- resolution test chart) is used for spatial resolution measurements having an illumination wavelength of 519 nm.

Objective Lens	Magnification	Numerical Aperture NA	Working Distance WD (mm)	Focal Length f (mm)	Field of View FOV (mm)
UMPlanFl 5X	5X	0.15	20.0	36.0	3.20
UMPlanFl 10X	10X	0.30	10.1	18.0	1.60
UMPlanFl 20X	20X	0.46	3.1	9.00	0.8
UMPlanFl 50X	50X	0.80	0.66	3.60	0.32

Table 3 Specifications of the microscope objective lens

3.2.1.1 *Results and Discussion*

Figure 3.2 highlights the sixth element of the seventh group of the USAF chart being imaged using the 0.3 NA objective. The sixth element was found to have line-widths of 2.19 μm . Hence, the achievable lateral resolution will be less than 2.19 μm . Higher lateral resolution scales can be further achieved using higher NA objectives and would be essential for mapping fine structures that are less than 2 μm .

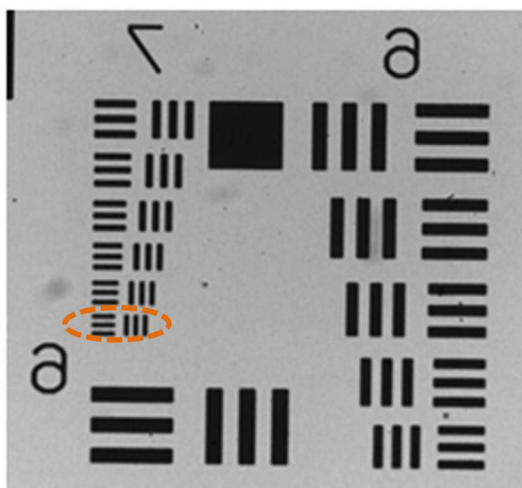


Figure 3.2 USAF test target imaged with 0.3 NA microscope objective lens. The region inside the dotted lines shows the sixth element of the seventh group

Further, fluorescent polystyrene spheres were imaged at an excitation wavelength of 519nm. The carboxylate-modified polystyrene microspheres (F8819, FluoSpheres[®], Molecular Probes[®], Life Technologies) coated with Nile red had an average diameter of $\approx 1 \mu\text{m}$ and an emission peak at 623 nm for 519 nm excitation. The excitation and emission spectra of the fluorescent bead are given in Figure 3.3.

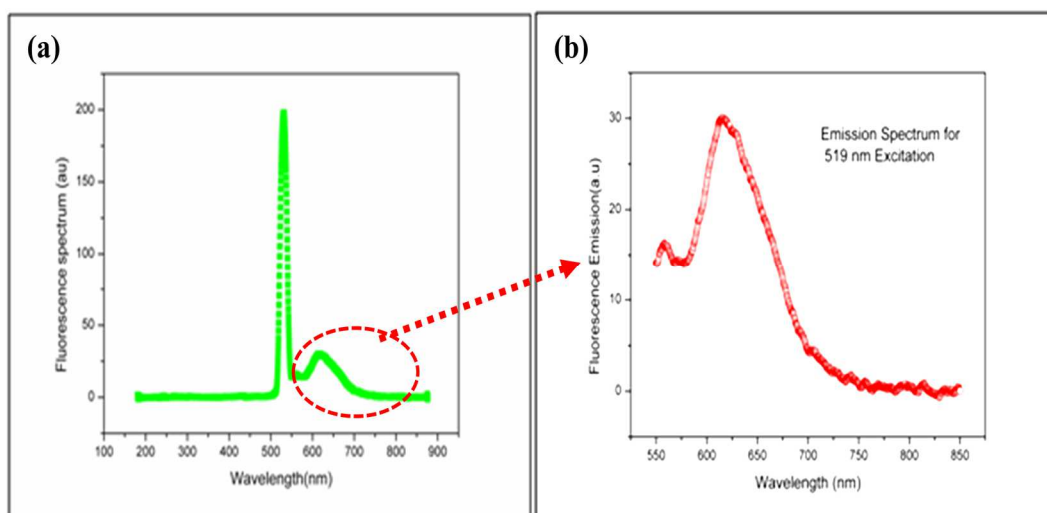


Figure 3.3 a) Absorption and b) Emission spectra of the fluorescent microsphere, the red arrow indicates the zoomed in view of the encircled region in the fluorescence emission spectrum

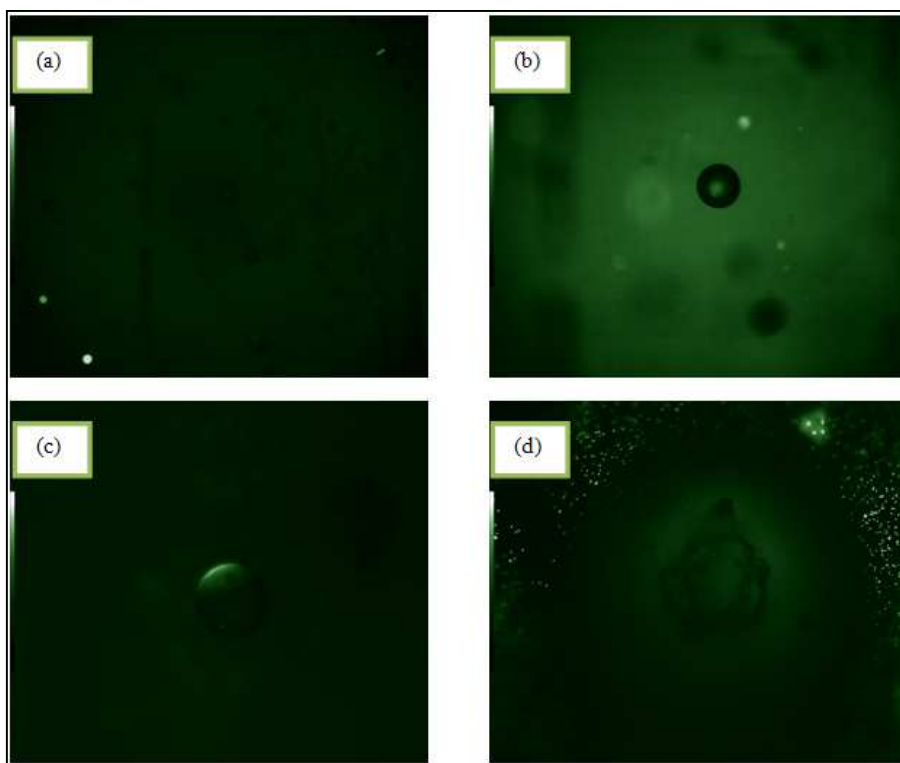


Figure 3.4 Fluorescence images obtained using different microscope objective lens: a) 0.15 NA, b) 0.3 NA, c) 0.46 NA, d) 0.80 NA

Figure 3.4 shows the images obtained with 0.15 NA, 0.3 NA, 0.46 NA and 0.80 NA objective lens respectively. The central portion of the image shows the presence of a bubble located on the surface of the sample and the images of the chosen bubble are illustrated under different magnification scales (Figure 3.4). Though the fluorescent images were not evident under the low NA objective, traces of fluorescent signatures became apparent from 0.3 NA objective. Further, the fluorescent beads were clearly visible under 0.80 NA as shown in Figure 3.4d. It was also observed that the high energy density formed from the tight focus of the laser beam through 0.80 NA objective lens resulted in the bursting of the bubble as shown in Figure 3.4d.

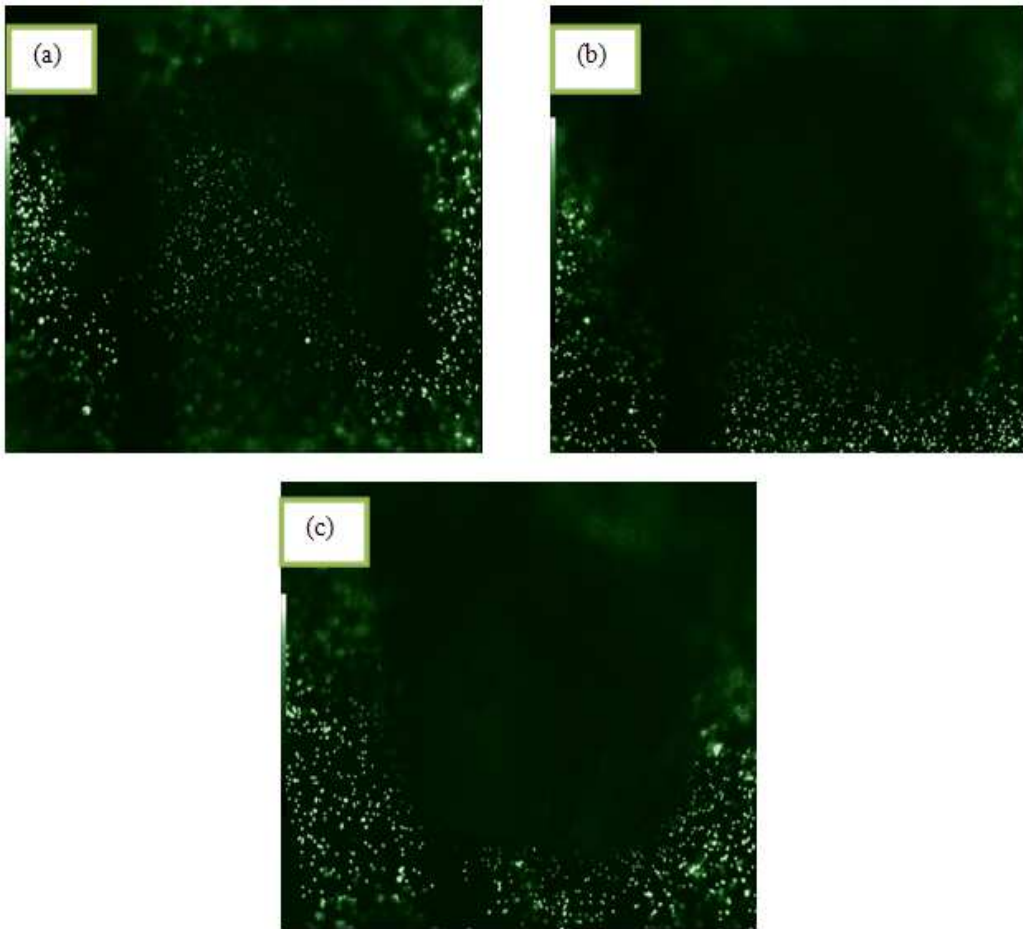


Figure 3.5 Fluorescence images obtained with 0.8 NA objective lens at varying focal planes with a step resolution of $2 \pm 0.4 \mu\text{m}$ across each focal planes

The sample was further imaged using the 0.80 NA objective lens at different focal planes by translating the sample along the depth axis using a micron-precision translation stage with a step movement of $2 \pm 0.4 \mu\text{m}$. The resultant fluorescent images obtained at three different focal planes are shown in Figure 3.5.

However, the larger footprint of the microscope imposes potential challenges for imaging within hollow tracts and deep within organ systems or tumors. Nevertheless, advances in fiber-optic based imaging have enabled biologists to overcome these challenges. Fluorescence microendoscopes (FME) built on the lensed fiber bundles provides images with cellular resolution from complex and

inaccessible three dimensional structures. In this context, the research was also extended towards the realization of a fiber-optic based fluorescence microscopy system. The following section details the proposed experimental configuration and various investigations performed towards this direction.

3.2.2 Fiber-Optic Fluorescence Microendoscope

The experimental set-up shown in Figure 3.6 used a fiber-optic imaging bundle (Sumitomo Electric, Japan), composed of 50,000 multimode fibers with an active area of 0.99 mm and outer diameter 1.2 mm. The GRIN (Gradient-index) lens mounted at the distal end of the fiber bundle imaged a plane within the sample onto the distal end face of the fiber-optic bundle. The GRIN lens (GT-IFRL-100-cus-50-NC, GRINTECH GmbH) was 1.0 mm in diameter and had a working distance 0.3 mm @ 532 nm in air and 0.5 NA. The microendoscopy system built under the epi-illumination configuration, used a microscope objective lens with NA of 0.80 (UMPlanFl 50X, Olympus Corp, Japan) for coupling the excitation laser beam into the fiber. In order to operate under epi-illumination mode, the laser beam was steered into the objective lens using a dichroic beamsplitter (LM01-552-25, Semrock, Inc.). The image formed at the distal end of the fiber was transmitted as pixelated images to the proximal end of the fiber which got coupled through objective lens into the sCMOS camera (Neo sCMOS, Andor Corp, Japan). The emission filter (HQ560/50m, Chroma Tech Corp.) mounted along the optical path blocked unwanted wavelengths and ensured that only the fluorescence emission signals are imaged.

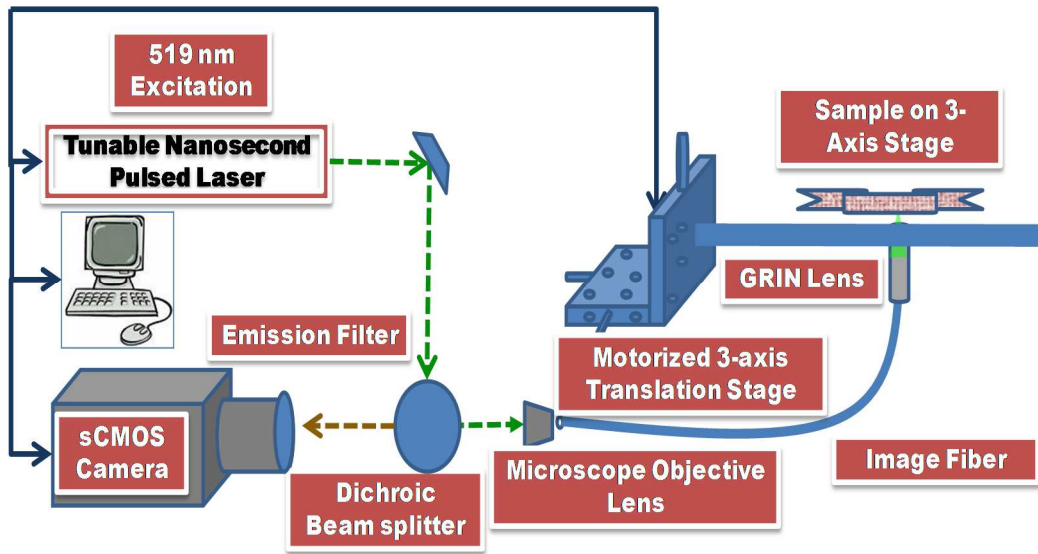


Figure 3.6 Schematic of the fiber-optic fluorescence microendoscope

The objective lens provided 50 times magnification to the imaged object and a variable magnification lens mounted in front of the sensor array was used to maintain the image size so as to satisfy Nyquist sampling criterion for the targeted sensor pixel size of $6.5 \mu\text{m}$. Initially, the lateral resolution of the system was characterized using USAF resolution target and the axial response was measured by scanning a reflective mirror across the focal plane of the system.

3.2.2.1 Results and Discussion

The lateral resolution of the microendoscope system was determined by imaging the seventh group on the USAF resolution test target as shown in Figure 3.7a. However, the quality of the images was found to be degraded with pixelation effects induced by the presence of fiberlets as evident in Figure 3.7a. The pixelated structures were formed from the opaque cladding layer for each of the individual fiberlets, where the cladding thickness was deliberately induced to reduce cross-talk between adjacent fiberlets. Nevertheless, the image degradation introduced by the pixelation effects can be significantly reduced by adopting several image

processing routines. Towards this direction, the current research adopted a frequency domain image processing technique to improve the image quality.

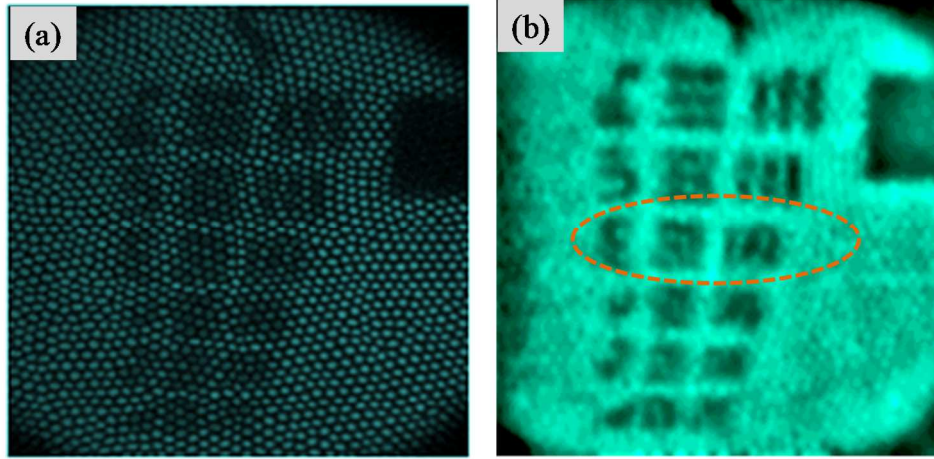


Figure 3.7 USAF test target imaged with GRIN lensed image fiber a) Raw image, b) Post processed image – The region inside the dotted lines shows the third element of the seventh group in USAF chart

The raw image was subjected to Fourier transformation followed by low pass filtering in order to remove the high frequency pixelated appearance in the image. The low pass filtered image was then inverse Fourier transformed to obtain the final processed image as shown in Figure 3.7b. From Figure 3.7b, the derived line resolution can be reasonably restored as evaluation of the second element of the seventh group revealed that the image registered a line density of 144 line pairs/mm that corresponded to a line-width or lateral resolution of $3.47\mu\text{m}$.

Modulation transfer function (MTF) which defines the contrast ratio of the image obtained by an optical system was also determined to be approximately 38% according to

$$MTF(f) = 100\% \times C(f)/C(0) \quad 3-2$$

where, $C(0) = (V_W - V_B)/(V_W + V_B)$ and $C(f) = (V_{\max} - V_{\min})/(V_{\max} + V_{\min})$, V_B and V_W denotes the average luminance for black areas and white areas at the imaged portion. V_{\min} and V_{\max} represent the minimum and the maximum luminescence for a pattern of maximum resolvable spatial frequency of the current system (2nd element of group 7 in the current system) respectively.

Further, due to the presence of the focussing lens (GRIN Lens) at the distal end, the fiber-optic microendoscope imaging assembly can be considered to be operating in a quasi-confocal mode. Therefore, the system was expected to offer optical sectioning capability to a certain extent. The axial response of the system was characterised using the axial response of a planar mirror surface as recommended by Zucker (Zucker 2006). The characterisation methodology involved axial resolution measurements performed by scanning a high reflectance mirror with an average reflectivity greater than 99% (NB1-K12, Thorlabs USA). The mirror was scanned across the focal plane of the GRIN lens with an incremental step-size of 0.5 μm . The corresponding reflection intensities were detected and recorded using a scientific-grade spectrometer (QE6500, Ocean Optics Inc.). The full width at half maximum (FWHM) of intensity profile was then estimated from the theoretical fit of the Gaussian profile according to equation 3-2. The axial resolution (Figure 3.8) of the micro-endoscopy system was determined to be approximately $16 \pm 0.65\mu\text{m}$.

$$y_0 + \left(A / \left(W \times \sqrt{\pi/2} \right) \right) \times \exp \left(-2 \times \left((x - x_c) / W \right)^2 \right) \quad 3-3$$

where A is the intensity at the centre of the beam waist, W is the radius at which the intensity drops to $1/e^2$ of its axial value and $(x-x_0)$ is the radial distance from the center axis of the beam waist.

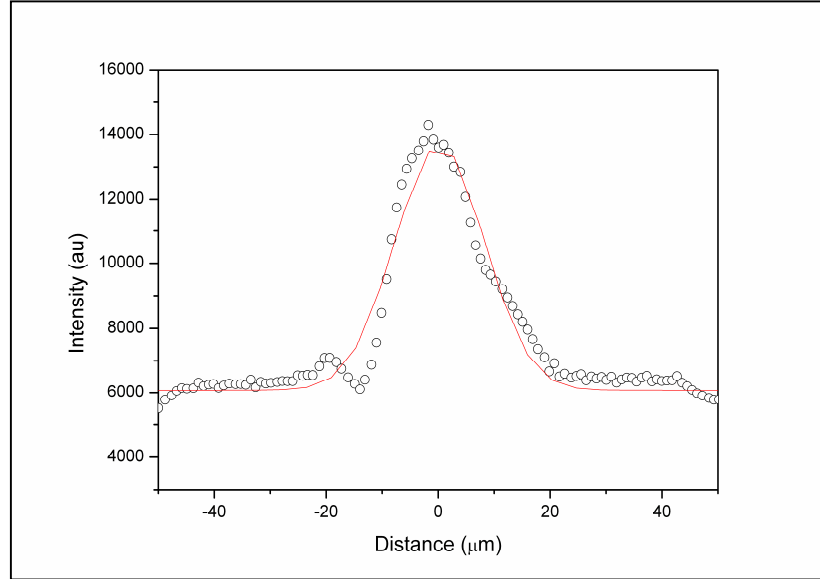


Figure 3.8 Profile of the axial response of the fiber-optic microendoscope

Further, the fluorescence imaging capability of the microendoscope system was tested by imaging the carboxylate-modified polystyrene microsphere coated with Nile red fluorescent material which had an emission peak at 613 nm for 519 nm excitation as given in Figure 3.3. The fluorescence image of the polystyrene microsphere (Figure 3.9) was obtained at an excitation wavelength of 519 nm.

The polystyrene microsphere with an average diameter of $1\mu\text{m}$ was imaged through the fiber-optic bundle. However, the structure of the ordered set of fibers introduced pixelation effect as seen in Figure 3.9, which was removed by post-acquisition image processing as described earlier and shown in Figure 3.10.

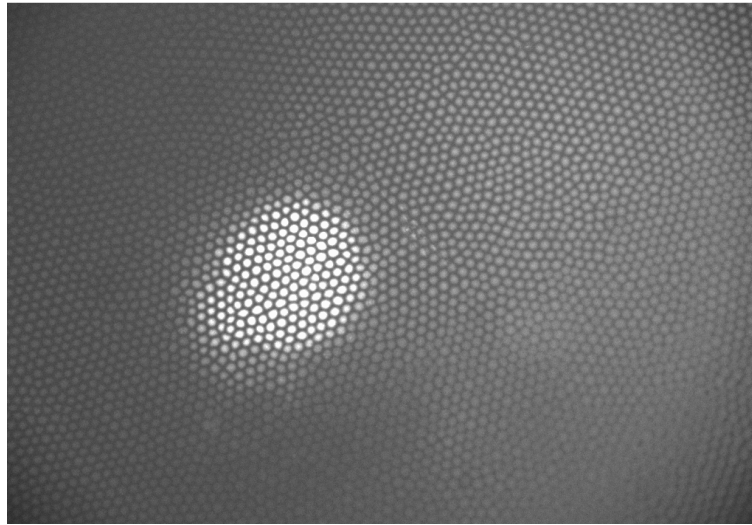


Figure 3.9 Fluorescence image of the polystyrene microsphere imaged using fiber-optic microendoscope

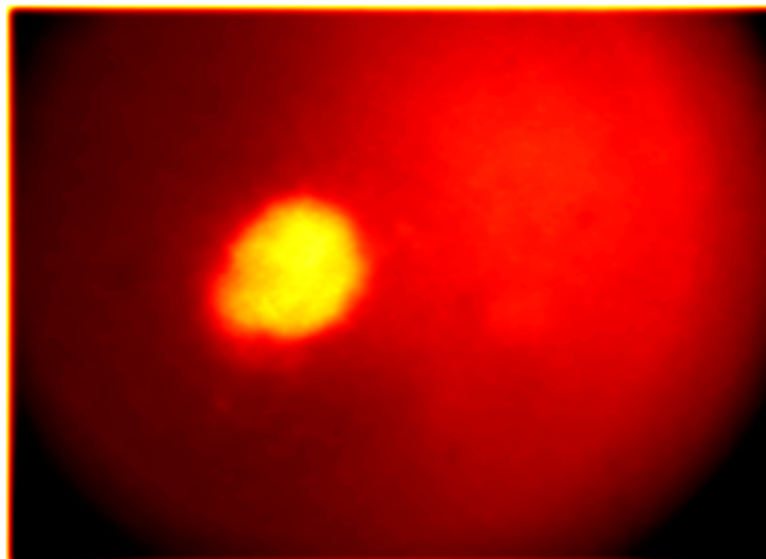


Figure 3.10 Post processed fluorescence image of the polystyrene microsphere

The results obtained illustrated the potential capability of the fiber-optic microendoscope system to perform flexible high resolution ($< 3.47 \mu\text{m}$) fluorescence imaging of various fluorescent samples such as biological tissues. The proposed system can therefore be extended towards imaging and illuminating inaccessible biological samples. This can have potential applications especially in

simultaneous remote light delivery and imaging. A broad spectrum of coherent light can be remotely delivered at relatively higher energies to perform specific therapeutic and imaging procedures. One of the major avenues towards this direction would be to provide sufficient optical energies for photoacoustic (PA) imaging applications. This concept primarily involves the remote delivery of PA excitation energy to deep or inaccessible areas of the organs or organ systems. Owing to the higher propagation length of the photoacoustic waves, the generated PA signals can propagate towards the tissue surface which can be detected with conventional ultrasound transducers for PA imaging.

3.3 Summary of Findings

Two forms of fluorescence imaging configurations namely; Inverted fluorescence microscope and fiber-optic fluorescence microendoscope were investigated and characterised. The proposed instrumentation methodologies and related system features of an inverted fluorescence microscope and an image fiber assisted microendoscope would be incorporated and later integrated with the proposed main objective of the system which is a multi-modality imaging system. Both systems used tunable nanosecond pulsed laser as their excitation source and a sCMOS camera as the detector. The proposed inverted microscope configuration was capable of performing high resolution fluorescence imaging of submicron features from the surface of the sample with sub-micron resolution at varying focal planes along the surface. However, the larger footprint of the system imposed serious limitations for its usage in space constraint applications. Nevertheless, investigations performed with fiber-optic based fluorescence imaging offered

potential capabilities to overcome this limitation with its smaller footprint and flexibility. The microendoscope based on a fiber-optic imaging bundle composes of 50,000 multimode fibers and a GRIN lens mounted at the distal end. Both the lateral and the axial resolution of the system were characterised and the measurements showed that the microendoscope exhibited a lateral resolution of $3.47\text{ }\mu\text{m}$ and axial resolution of $16 \pm 0.65\text{ }\mu\text{m}$. The newly configured system can be used for both imaging purposes as well as for remote delivery of light during its independent operation as well with the proposed multi-modal imaging system. Therefore, the fluorescence microscopy systems satisfy the targeted research objective of providing micron or sub-micron spatial resolution along the tissue surface for its future integration with the proposed multi-modal system.

However, due to the limited penetration depth of light, the fluorescence microscopy techniques are restricted to operate only within the ballistic regime of the photons in biological tissues (which is typically $< 1\text{ mm}$). Hence, their applications cannot be extended towards imaging thick and turbid bio-samples. Nevertheless, hybrid optical imaging technique such as photoacoustic modalities can overcome this limit for high resolution imaging. Details of this aspect and how fluorescence imaging systems were extended towards integrating with the photoacoustic imaging system to provide multi-scale and multi-level information along the depth of the tissue will be discussed in the ensuing chapters of this thesis.

The following chapter discusses about the ultrasound imaging system which forms one of the imaging modalities in the proposed integrated multi-modal imaging system. Characterisation aspects of ultrasound imaging system and

relevant details which actually led to establishment of the proposed multi-modality imaging approach will also be elaborated.

CHAPTER 4: ULTRASOUND IMAGING USING MULTI-ELEMENT TRANSDUCER

This chapter begins with the physics of ultrasound imaging systems and details the relevant fundamental concepts. Building on the fundamental ultrasound imaging principles an ultrasound imaging system was established and characterised so as to map acoustic heterogeneities along the depth of the tissue with mesoscopic spatial resolution. Implementation details of various advanced ultrasound beamforming and signal processing routines will be described followed by the illustration of various aspects of system characterisation such as signal-to-noise ratio and spatial resolution. Further, investigations performed to illustrate multi-transmit and spatial compounding capabilities and their effects on frame rate are described. The chapter concludes with the results obtained from B-mode imaging of the silicone phantom.

4.1 Fundamental Theoretical Concepts of Ultrasound Imaging

This section describes the fundamental theoretical concepts that govern the imaging capabilities of an ultrasound imaging system. The instrumentation and signal processing schemes of the proposed multi-element ultrasound imaging system were designed, configured and characterised based on these theoretical concepts.

4.1.1 Ultrasound Reflection

Imaging of biological tissues using ultrasound depends on two important factors; ultrasound reflection and ultrasound scattering. As ultrasound waves are longitudinal mechanical waves, the acoustic energy propagation is primarily governed by the density of the propagating medium. A change in density results in a shift in the acoustic speed. This results in a portion of the acoustic energy to be reflected from the boundary of the two mediums where the density or acoustic impedance mismatch occurs and the rest of the acoustic beam gets transmitted across the boundaries. The acoustic impedance is governed by the density of the medium as well as the speed of sound in the medium. Acoustic impedance ' I ' is given by ' $I = \rho c$ ', where ' ρ ' and ' c ' denote the medium density (kg/m^3) and speed of sound in the medium (m/s). Since each of the tissue types is of different density, any organ can be defined as an acoustically heterogeneous medium which results in ultrasound reflection and scattering. Ultrasound images are also formed from diffuse ultrasound scattering from the particles smaller than acoustic wavelength. These scattering events termed as Rayleigh scattering, results in speckle formations in the ultrasound image due to the constructive and destructive interference of multiple scattered waves from different directions.

4.1.2 Ultrasound Attenuation

When ultrasound propagates in a heterogeneous medium such as biological tissues, it experiences a loss in the energy as a function of distance. The pressure wave, ' $P(d)$ ' propagating across a distance ' d ' in a medium exhibits the following exponential behaviour (Christensen 1988).

$$P(d) = P(0)e^{-\alpha d} \quad 4-1$$

Where ' $P(0)$ ' is the initial acoustic pressure and ' α ' is the acoustic attenuation in the medium (nepers/cm).

Various factors such as reflection, scattering and absorption contribute to the attenuation of the ultrasound energy. However, the attenuation is mainly due to the absorption by several tissue constituents such as water which further leads to local heating. Therefore, the attenuated ultrasound energy is converted into heat energy and the amount of absorption has a power law dependence on ultrasound frequency.

4.1.3 Ultrasound Transducer

Ultrasound transducer which generates and detects ultrasound is one of the core functional units of any ultrasound imaging system. Piezoelectric transducers based on piezoelectric effect are the most commonly used ultrasound transducers. The piezo crystals convert the applied high voltage signals into acoustic waves that are transmitted into the area to be diagnosed and the echoes are converted back as voltages for further processing. Current technology permits transducers to be tailored into a variety of shapes which can hold a specified number of piezoelectric transducer elements. Depending on the specific application, transducers can be classified into three different categories namely; linear, curved and sector. Linear transducers are mainly employed for performing high resolution imaging at shallow depths. As the elements are arranged linearly, the resultant images are rectangular. Curved transducers are primarily used for typical applications that demand large field of view (FOV) and higher depth. Sector transducers are mainly

used for applications which require large field of view at a smaller footprint. Ultrasound beam from all these transducers can be focused or steered using a process known as beamforming. Further, multiple scan lines can also be formed without the mechanical scanning. Beamforming allows a multi-element transducer to perform dynamic focusing without mechanical scanning. This is achieved by applying suitable delays to individual transducer elements using an electronic beamformer and the number of transmit foci can be varied dynamically from single focus to multiple focus. The resultant detected echoes are also subjected to suitable delays by the beamformer, and the beamformed signals are further subjected to envelop detection and scan conversion.

4.1.4 Linear Arrays

Development of multiple-element transducers with the capability of electronic steering and focusing enables the technique to produce high quality images with higher line density and frame rates. This research employs a 128 element linear transducer where the scan lines were formed using sub-apertures comprising varying number of transducer element combinations. Linear array transducers form rectangular image field by combining a set of scan lines, each formed by a sub-aperture.

4.1.5 Focusing

Electronic focusing of ultrasound beam involves the superposition of ultrasound waves produced by each element with a particular wave pattern where the resultant pattern is formed from the summation of individual wave patterns. This is done by offsetting the excitation of individual elements of a group by a

small time delay (few ns to tens of ns) using a special electronic timing firmware. The timing firmware holds the pulser according to a timing sequence that is generated with respect to the element position and focal zone depth. In transmit focusing, the focal plane can be electronically altered by varying the timing sequence to give high resolution images with multiple focal zones throughout the image. However, data acquisition must be performed for all the line of sights in a single focal zone depth before they are repeated for different focal zone depths. This results in a slow frame rate because images from all the different focal zones are to be combined to a single image prior to the display. The maximum frame rate in this case is given as (Christensen 1988, Hedrick, David L. Hykes et al. 2005)

$$FR_{max} = \frac{C}{2 Z N N_Z} \quad 4-2$$

Where, Z is the depth of interest, N_Z is the number of focal zones, C is the velocity of ultrasound and N is the number of line of sights per focal zone.

Electronic focusing during transmission can be accomplished by varying the beam aperture where the number of elements excited in a group is varied to change the depth of near field and beam width. Aperture focusing is determined by the *f-number* (ratio of focal length (F) to the aperture size (W_a) which is given by (Christensen 1988, Hedrick, David L. Hykes et al. 2005),

$$f - number (f\#) = \frac{F}{W_a} \quad 4-3$$

An *f-number* of 2 is used for optimal focusing and the focusing must occur in the near field of the excited group of elements wherein the depth of near field (NFD) is

determined by the acoustic wavelength (λ) and the dimensions of active elements (Christensen 1988).

$$NFD = \frac{Wa^2}{4\lambda} \quad 4-4$$

The beam width in the region around the focal point is narrowed and the extent of this focal point is given by the depth of field which is determined by the aperture size (W_a), acoustic wavelength (λ) and the focal length (F) and is given by (Christensen 1988),

$$Depth\ of\ field \propto \frac{F^2}{W^2} \quad 4-5$$

Therefore, to maintain the depth of field at various focal lengths, the aperture has to be varied and this can be performed by electronically selecting a small group of elements (small aperture size) at short focal lengths and a large group of elements (large aperture size) at longer focal lengths. Thus, a tighter focus can be achieved by increasing the aperture size with an improvement of the lateral resolution. However, in order to optimize and leverage on the focusing capabilities of transmit or aperture focusing, the received beam should also record the echo from the focal zone. This is performed by a technique called dynamic focusing where the echo signals are subjected to adequate time delays using a delay circuitry in the receiver. This circuitry provides sufficient delays (in nanoseconds) to each element so that the elements of a specific aperture size are made to record the echo signals emerging from a focal zone. Focusing at a particular depth is achieved by adjusting the number of receiving elements in the aperture and a tighter focus can be achieved by increasing the number of elements in the aperture.

Owing to the finite dimension and mechanical property of each individual element and due to their periodic arrangement in the transducer array, the transmitted energy beam will not exhibit a clean beam profile. Undesirable beam profiles called side lobes and grating lobes are also formed when the transducer elements are excited and this leads to the formation of image artefacts. Side lobes generated due to the radial expansion of piezo crystals result in the formation of multiple beams of low ultrasound energy that project radially across a linear array transducer. These energy lobes create unwanted reflections from its propagation path and manifest itself as arising from the main energy lobe. A technique known as apodization is adopted to reduce the effect of side lobes where variable – strength voltage pulses are applied to each element of the aperture during the delay line focusing. Grating lobes are formed by the constructive interference between the acoustic fields emitted by adjacent transducer elements and they can be determined by the pitch of the array. Sub-dicing is then employed to eliminate or minimise the grating lobes. In sub-dicing, a single element in a transducer array is divided into sub elements which are electronically wired together to form a single element. This enables one to effectively reduce the center to center distance between each element and thus directs the grating lobes to occur at an angle greater than 90 degrees.

4.1.6 Beamforming

The beamforming process can be categorized into two different aspects: focusing and steering. Beam focusing and beam steering using a linear multi-element transducer can be performed by applying appropriate pulse emission

delays to each of the transducer elements. Corresponding delays are also applied to the individual echo signals to compensate for differences in the echo arrival time and make the echoes in phase. The acoustic propagation time from aperture to target point determines the amount of delay for each of the transducer elements. The concept can be further elaborated with the following illustration.

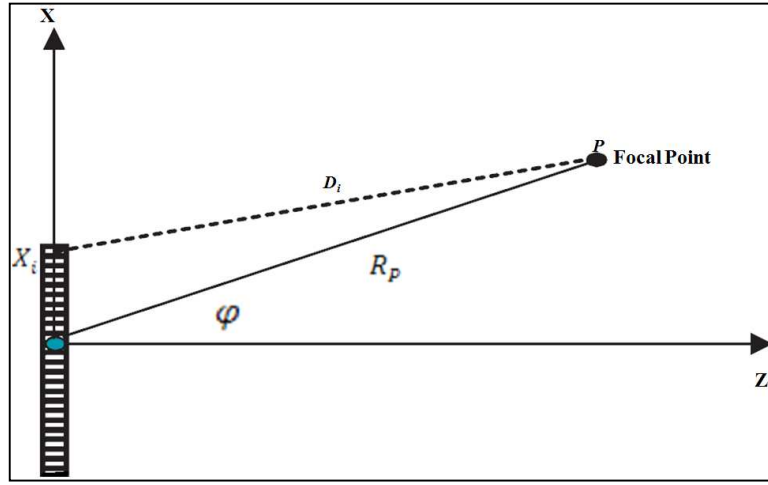


Figure 4.1 Representation of the ultrasound focal point

Considering the origin of the transducer as the center element in Figure 4.1, the propagation time T_i from the i^{th} element to focal point P through acoustic line D_i is given by

$$T_i = \frac{\sqrt{X_i^2 + R_P^2 - 2 X_i R_P \sin(\varphi)}}{c} \quad 4-6$$

Where, R_P is the radial distance from the origin to the focal point P , X_i is the x-axis co-ordinate of the i^{th} transducer element. X_i can be calculated as $X_i = i\Delta X$, where ΔX is the element to element spacing (termed as kerf). φ is the focal point angle with respect to z-axis which defines the scan line of interest and C is speed of sound in medium. When multiple focuses across a single line is being performed,

R_P becomes a function of time. From equation 4-6, the maximum ultrasound propagation time for a given (R_P, φ) combination to achieve an optimum focus can be derived as

$$T_{max} = \frac{\sqrt{X_{max}^2 + R_P^2 + 2 X_{max} R_P \sin(\varphi)}}{c} \quad 4-7$$

Based on the above expression on the appropriate time-delay bias, this will be applied to each of the transducer elements. The pulse waveform $P_i(t)$ will then become

$$P_i(t) = P(t - \tau_i) \quad 4-8$$

Where $\tau_i = T_{max} - T_i$

The same concepts can be adopted in addressing the echo reception procedure where the ultrasound waves reflected from a focal point have to be effectively decoded. Assuming the origin of the ultrasound wave is from the focal point and each of the transducer elements records the resultant ultrasound waves, the time-delay bias that is to be applied for each transducer element during reception can be derived. The propagation time T_i from the focus to the i^{th} element is given by

$$T_{ri} = \frac{\sqrt{X_{ri}^2 + R_P^2 - 2 X_{ri} R_P \sin(\varphi)}}{c} \quad 4-9$$

Where X_{ri} is the co-ordinate in the x-axis of the i^{th} receiver element.

And the time aligned signal $R(t)$ received from the given focal point can be derived as

$$R(t) = \sum_{i=1}^N A_{ri} \sum_{i=1}^N A_{ti} P(t - \tau_{ri} - \tau_{ti}) \quad 4-10$$

Where A_r the apodization applied to each receive signal, A_t is the apodization applied to each transmit signal, τ_r is the amount of time-delay applied to the receive signal and τ_t is amount of time-delay applied to the transmit signal and subscript i denotes the transducer element number.

Beam steering is performed by tuning the direction of the beam across each scan lines and this can be achieved by adjusting the focal point angle φ . Therefore, to account for this, equation 4.6 can be approximated with a Taylor series expansion with peak expansion error less than 1/8 of the ultrasound wavelength and is given by

$$T_i = \frac{R_P - \sin(\varphi)X_i + \frac{\cos^2(\varphi)}{2R_P}X_i^2}{c} \quad 4-11$$

From the above equation it can be noted that component $\frac{-\sin(\varphi)X_i}{c}$ is independent of R_P and dependent on focal point angle φ . Hence, this component is fixed across all the focal planes along a particular scan line and only varies with the focal point angle. This is often referred to as beam steering component. However, the quadratic term $\frac{\cos^2(\varphi)}{2R_P}X_i^2$ is dependent on the focal point and it can be used to adjust the focal point of the received data from the transducer elements. Hence it is also referred to as dynamic focusing component. By accounting for the total round trip of the signal, we have $Ct = 2R_P$, the focusing component can be expressed as

$$\frac{\cos^2(\varphi)}{c^2t}X_i^2 \quad 4-12$$

The following sections detail the system configuration methodologies and its implementation based on the above mentioned theoretical concepts. Various advanced signal processing routines are used to formulate the configuration schemes for the ultrasound imaging system relevant to this research.

4.2 Instrumentation and Configuration Schemes of the Proposed Ultrasound Imaging System

This section gives a detailed methodology for the establishment of a suitable ultrasound imaging system configuration for its future translation into the proposed multi-modality imaging system. The block diagram of the proposed ultrasound imaging system is shown in Figure 4.2 with beamformer controller as the starting point.

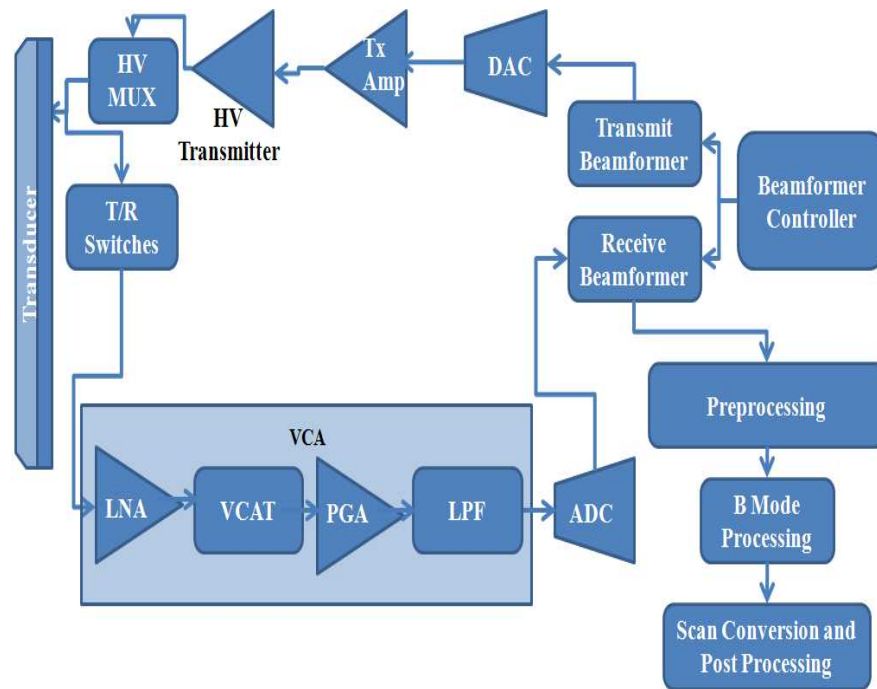


Figure 4.2 Block diagram of the ultrasound imaging system

Beamformer controller synchronized the generation of ultrasound waves with the echo reception. Based on the width and depth of region of interest (ROI), transducer specifications, specified resolution and number of focal points, the beamformer translates the ROI into the required number of scan lines and number of focal points per scan line. Based on the theoretical concepts outlined in section 4.1.6, the transmit beamformer first excites the transducer elements with appropriately time delayed signals so that ultrasound waves are focused and steered to the desired focal point. The excitation signals were typically provided by a sequence of high voltage (HV) pulses generated through HV transmitter and further transmitted through the HV multiplexer unit (HV Mux).

The transmit/receive (Tx/Rx) switch seeks to protect the receiver electronic circuits from unwarranted disturbances or damage by high voltage pulses from HV transmitter. The echo signals were coupled back to the receiving electronics through Tx/Rx switch. In the developed ultrasound system, a linear amplifier is used to initiate an analog front-end processing chain then through a voltage controlled amplifier (VCA) that ends at ADC. The received low voltage signals were fed through the VCA which included low noise amplifier (LNA), voltage controlled attenuator (VCAT), programmable gain amplifier (PGA) and low pass filter (LPF). LNA could be programmed at 12/18/24 dB to provide appropriate pre-amplification to the received echo signals with a very low noise figure. VCAT further attenuated the signal from 0 to -40 dB to improve the overall signal-to-noise ratio (SNR) and was expected to be highly useful while performing near field imaging and TGC. PGA was used to make up for the attenuation of signal along the depths of the tissue which provided specific gains of either 24 dB or 30 dB.

Typically, the raw echo signals were subjected to a total front end gain of about 35 - 60 dB. To filter the signals within the sampling frequency of the analog-to-digital converter (ADC), the amplified signals were passed through the programmable Nyquist filter (LPF) set at 10/15/20/30 MHz.

To avoid any aliasing effects, the Nyquist filter rolled off higher frequency signals in the analog domain before they were fed into the 12-bit, 40 MHz ADC. The overall function parameters for VCA was determined from the signal sampling time where signals from higher depth were subjected to higher gain. The digital signals reaching the Rx beamformer were further subjected to appropriate scaling and delays to perform coherent summation of the echo signals. Beamformed echo signals were also subjected to the various pre-processing routines as described in section 4.2.1. VCA, digital Tx, HV MUX and beamformer controller (FPGA based) were all 64 channel systems with the corresponding multiplexers (1:2) scaled to 128 transducer elements. The transducer array operated at center frequency (-6 dB, average) of 7.699 MHz supported the 128 elements having an element pitch of 300 μm , 19 mm elevation focus, 6 mm elevation aperture and had -6 dB fractional bandwidth of 80.88% . Azimuth length of the transducer was 38.40 mm and -20 dB ring-down time (average) was 0.171 μs .

Two families of Xilinx field programmable gate arrays (FPGA) were used namely; Virtex (digital side) and Spartan (analog side). Appendix B shows a screen shot of the layout of the printed circuit board (PCB) with the joint test action group (JTAG) programming of the Spartans from iMPACT and Xilinx programming cable (DLC 10). At the digital front end side, the echo channels were delayed,

windowed (apodized), summed, filtered and then Hilbert transformed to the sum of the squares before compressed to 8 bits for display as detailed in section 4.2.1.

4.2.1 Signal Processing

In order to extract and provide quality images from the echo signals, the radio frequency (RF) echo signals have to undergo specific signal processing routines. These include band-pass filtering, envelop detection, log compression and time gain control (TGC). The following section details their significance and how these signal processing routines were implemented in the envisaged ultrasound imaging system

4.2.1.1 Band-pass Filtering

Band-pass filtering was performed to reduce noise outside bandwidth of the transducer and signal receiving electronics circuitry. In this research, a set of 16 finite impulse response (FIR) filters were implemented individually or as a sliding filter, where each of the filters was applied across every $1/16^{\text{th}}$ point of the full image over selected field of view. Sliding filters were implemented in the ascending order of their 3 dB cut-offs so that higher frequency components from near-field and lower frequency components from far-field were more efficiently processed. The 79 tap FIR filter utilized predefined Matlab coefficients. Filter coefficients were also generated from Matlab with varying filter configurations. Much of the investigations in this work were implemented with 1 MHz- 12 MHz frequency band as the two 3 dB frequency cut-offs.

4.2.1.2 Envelop Detection

Envelop detection was typically done non-coherently to construct the ultrasound image. This work primarily involved the use of Hilbert transform to extract a complex signal from the received RF signal which was of 18 bit acoustic line. The magnitude of this complex signal was further subjected to low pass filtering and decimation.

4.2.1.3 Log compression

Log compression was done in order to compress the processed RF data to fit the dynamic range for display and can be also used for brightness correction. In this work, the magnitude of the complex RF signal is compressed into 8-bit for gray scale image display where the maximum gray value assigned is 255. The beamformed data from the ultrasound system typical outputs 36-bit value $[12\text{-bit (ADC)} + 6\text{-bit (64 element)}]^2$ which will be compressed to 8-bit.

4.2.1.4 Time Gain Control (TGC)

Time gain control (TGC) or time gain compensation was performed by a variable gain amplifier (VGA) to compensate for the ultrasound signal attenuation across the depth of travel. The TGC was spread over the selected depth of interrogation with each of the nine potentiometers capable of providing a gain of 40dB across the image.

The following subsections briefly describe the implementation of various advanced signal processing routines such as spatial compounding and persistence for enhancing the imaging capabilities of the system.

4.2.2 Implementation of Advanced Signal Processing Routines

4.2.2.1 *Spatial (Angle) Compounding*

Coherent interference from acoustic scatterers induced ultrasound speckles that degraded the image quality, particularly while imaging low contrast structures. Spatial compounding was performed to reduce the effects of ultrasound speckles during the image formation. This process involved taking multiple views of an object from different angles which was further transformed into a composite image by obtaining the weighted sum of each of the views. The composite image was devoid of speckles to a great extent as each of the views provided an uncorrelated speckle pattern with which multiple beam angle data was averaged to improve the presentation of boundaries throughout the field of view.

Spatial compounding improved the signal significantly, though it was mostly for a speckle signal to noise ratio, the improvement was estimated to be the square root of the number of angles used. The conceived system supported up to 9 angles (-4 to +4) with an angle offset up to 4 degrees. However, it was observed that the current transducer specifications do not allow more than 9 angles as the side lobes induced image artefacts at more than ± 15 degrees. Therefore an angle offset of 4 degrees was the maximum allowed value while employing all the 9 angles.

4.2.2.2 *Persistence*

Though spatial compounding could reduce speckle effects to certain extent, improved imaging capabilities were offered by incorporating temporal averaging techniques such as persistence. With persistence, ultrasound speckles were reduced

by taking the weighted average of the sample points in two successive image frames. Mathematically the persistence function is defined as (Li and Liu 2009)

$$i'_k = \alpha i'_{k-1} + (1 - \alpha)i_k \quad 4-13$$

Where $0 \leq \alpha \leq 1$ is the persistence coefficient, i'_k and i_k denotes the persisted and unprocessed pixel (sample point) of frame K , respectively. For persistence, the current frame was averaged over x number of frames and the resultant frame was collected and stored in the memory. This was followed by making another identical frame made from the same pulse patterns send through the same locations. The sample points in this frame were not the same if anything was moving or if there were speckles. The frames were then averaged to form the new frame (e.g. (line 34 sample 356 + line 34 sample 356) / 2). This may be done with many frames, and the limitation here was in the memory capacity of the graphic processing unit and how much data it could hold onto at any given point. Further, the total number of frames to be averaged was also dependent on all the added samples from spatial compounding, multiple lines per aperture, multi transmit etc, where in the memory did actually add up rather quickly. The current system could hold on to 10 frames at a time with 4 angle spatial compounding from 4 focal planes. The persistence could also help with any stray noise, though it did not really have any, so long as the power supply was on a clean feed.

4.3 Characterization of the Proposed Ultrasound Imaging System

This section describes the experimental procedures and results for evaluating the signal-to-noise ratio (SNR) and spatial resolution of the proposed ultrasound imaging system.

4.3.1 Signal-to-Noise Ratio (SNR) Measurement

Signal-to-Noise Ratio (SNR) of the system assessed the ability of the system to effectively detect the lowest level of signal at the frequency of interest within the system noise floor. Noise gets introduced into the signal at several stages and then cascaded along the signal flow. Electromagnetic interference introduced within the laboratory from laser, motion controller, PC, oscilloscope and mains supply contributed to various levels of noise into the imaging system. Therefore, to enhance the detection sensitivity of the system, the echo signals had to be effectively isolated from the noise which was a critical factor of consideration for the ultrasound system performance. The following section details various investigations performed to evaluate the system sensitivity (signal to noise) within the operating environment of the system.

4.3.1.1 *Materials and Method for SNR Measurements*

Investigations performed to evaluate the system SNR are according to the guidelines imposed by American institute of ultrasound in medicine (AIUM) (Committee 1984). Ultrasound test interface with a known reflection coefficient with respect to the perfect planar reflector (ultrasound reflection coefficient value of 1; e.g. water-air interface) was used for SNR measurements. This work involved the usage of a water-stainless steel interface which had a reflection coefficient of 0.58 dB below the perfect reflector.

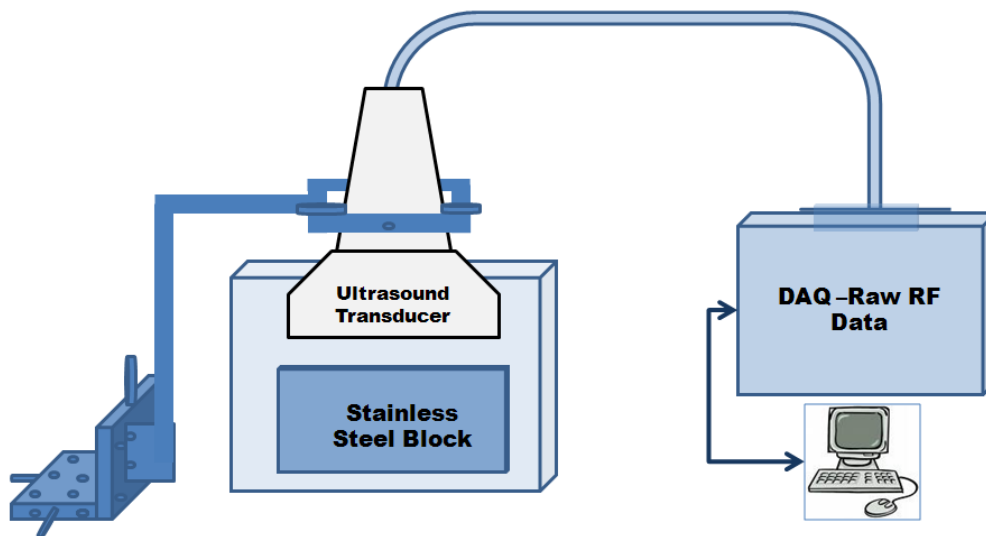


Figure 4.3 Schematic of the signal-to-noise ratio (SNR) measurement set-up

The chosen stainless steel block was initially subjected to surface profile measurements to ensure that the test specimen had the required surface quality. The surface roughness of the stainless steel block test specimen of size 3 cm x 3 cm x 2 cm (W x L x H) was determined to be approximately 0.3 μm . To perform the SNR studies, the stainless steel block was positioned inside an acrylic water tank filled with degassed water at 22 °C as shown in Figure 4.3. The transducer was positioned perpendicular to the planar test surface of the reflector block where the transducer movements were controlled using a manual three axis stage. The distance between the transducer surface and the planar reflector were maintained within the pulse echo focal distance of the transducer. This task was achieved by translating the focal distance of the transducer with micron precision step movements until the maximum echo signal was recorded in the A-mode display. Once the optimum pulse echo focal distance was determined, the transducer elements were initially pulsed according to a +- pulse sequence with 40 V positive and negative high voltage settings and the corresponding amplitude of the echo

signal was recorded for each of the 128 elements. The A-mode signals from each of the 128 transducer elements were analyzed independently to determine the exact element located right across the lateral plane of the test target.

To obtain the maximum echo signal to within the electronic safety limits, the HV settings for the pulsed transmitters were limited to a maximum value of ± 70 V and the TGC settings were set to the maximum value. The resultant echo amplitude was measured and recorded for the maximum echo amplitude. Once the echo measurements were performed, the HV settings and TGC values were turned down to zero to perform the noise measurements. The resultant signal formed to be the broadband background noise introduced into the system owing to various electronic components inside the system and the operating environment. The SNR measurements were performed for both single channels and the whole system having 68 dB and 110 dB respectively and therefore expected to offer good imaging capabilities.

4.3.2 Characterisation of the System Resolution

Both the axial and lateral resolutions of the imaging system were characterised. Axial resolution is defined as the minimum resolvable spacing between two reflectors along the propagation axis of the ultrasound beam where the two reflectors remain resolved for all greater distances between them. Lateral resolution is defined as the minimum resolvable spacing between two reflectors perpendicular to the propagation axis of the ultrasound beam where the two reflectors remain resolved for all greater spacing. The resolution of the ultrasound system was determined by analyzing the ultrasound beam properties which was

given by the point spread function (PSF) of the system. The lateral and axial profiles of the system were studied by varying the transducer focal length as well as the position of the point test target.

4.3.2.1 *Materials and Methods for Resolution Measurements*

Axial and lateral measurements (in-plane) were performed with the aid of the experimental set-up shown in Figure 4.4. Ultrasound test interface with a known reflection coefficient with respect to the perfect planar reflector was employed for the spatial resolution measurements. The investigations involved the use of a water-stainless steel interface which had a reflection coefficient of 0.58 dB below the perfect reflector. A stainless steel wire of diameter 90 μm was used as the test target. The thin metal wire was stretched and fixed across the acrylic tank filled with water as shown in Figure 4.4.

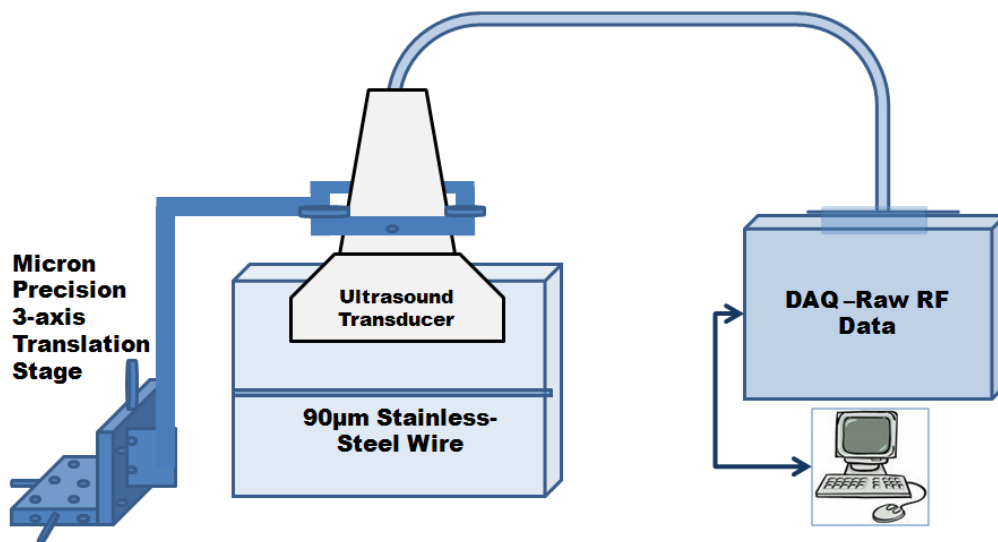


Figure 4.4 Schematic of the resolution measurement set-up

The transducer was positioned perpendicular to the metal wire and the distance between the transducer surface and the metal wire was fixed exactly at the

pulse echo focal distance of the transducer. This was due to the ultrasound beam that diverged rapidly away from the focal point which resulted in the degradation of spatial resolution. Once the focal point and the transducer element that formed the right acoustic line was determined, the ultrasound pulser was subjected to the voltage sequence of ± 40 V. The transducer was then translated across the plane perpendicular to the metal wire until the peak amplitude in the acoustic line was obtained in the A-mode display. A set of 12 readings was taken and the mean value of the resultant signal profile gave the PSF across the axial plane with the -3 dB attenuation point of the PSF profile shown in Figure 4.5. The axial resolution of the system was measured of 151 ± 2.24 μm .

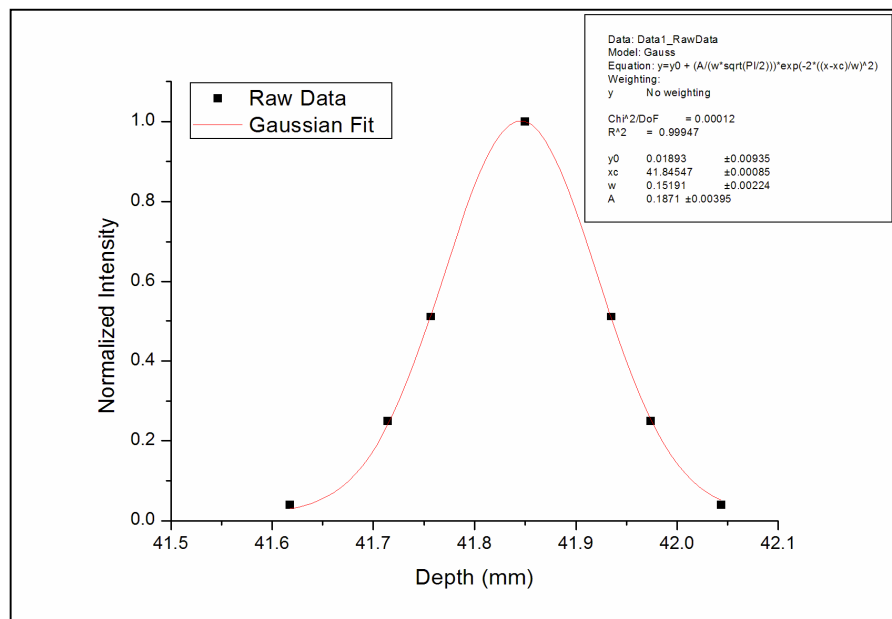


Figure 4.5 Profile of the axial response of the ultrasound imaging system

Axial resolution could be further improved to a certain extent by increasing the number of samples per line (decimation) that were displayed on screen. The decimation took specific number of samples down the acoustic line and this would

then be directly averaged. So every set of 8 samples was averaged to have 512 samples which were subsequently displayed on the screen. However, this will provide only an improvement in a highly zoomed image as the number of pixels the samples spread over will dominate or “saturate” the display. To mitigate this, one would need to determine what the center frequency of the transducer, pulse repetition frequency and the sampling rate should be.

The in-plane lateral resolution was also measured in a similar way by translating the transducer across the plane perpendicular to the metal wire with a step resolution of 20 μm along a range of 500 μm . The peak amplitudes of the obtained echo signal were recorded with 12 repetitions for each step movement to derive the resolution profile across the lateral plane as shown in Figure 4.6. The -3 dB attenuation point of the PSF profile was measured and found to be 345 ± 2.53 μm . This formed the in-plane lateral resolution of the developed ultrasound imaging system.

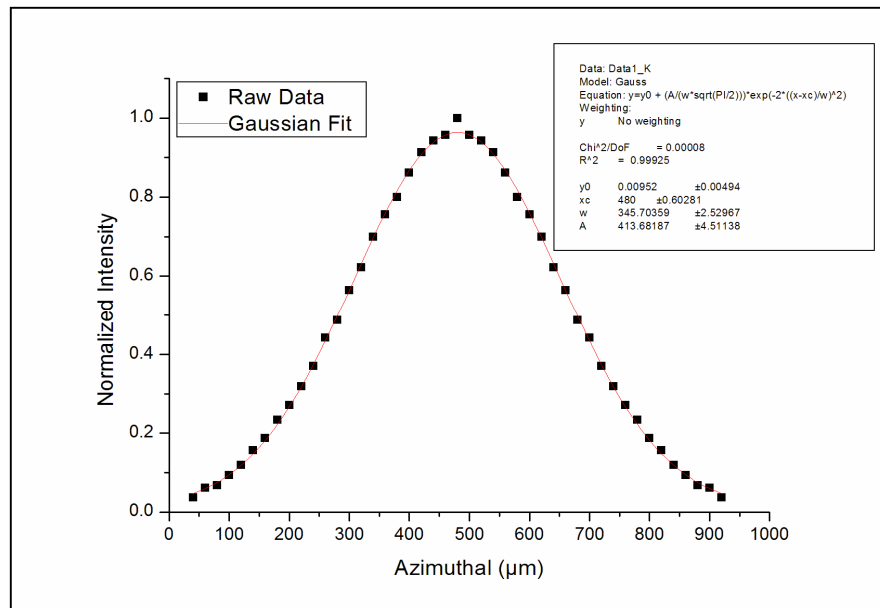


Figure 4.6 Profile of the in-plane response of the ultrasound imaging system

To enhance the lateral resolution across the azimuth plane (in-plane), one way was to increase the number of acoustic lines. This however does not improve the resolution as the lateral resolution was a theoretical limitation of the aperture size, element size, number of elements and electronic focusing in transmit and receive modes. Hence, the following section details the investigations performed to determine the effect of number of scan lines per aperture in the current system.

4.4 Investigations into the Effect of Scan Lines per Aperture

A scan line can be defined as a straight line in the imaging space in which sample points of an image are present. Ultrasound images were thus composed of multiple scan lines which make each scan line to be a sample of the tissue under investigation. The experiments performed were based on 64 element receive aperture, unless otherwise stated explicitly. The number of scan lines (line density) formed in an aperture determined the lateral resolution in the azimuth plane to a great extent. A higher line density provides better in-plane lateral resolution and leads to better images (due to reduction in speckles and unwanted reflections). However, it was observed that increasing the line density inherently reduces the frame rate.

Theoretically, if the number of scan lines is increased by twice, it reduces the frame rate by half. Therefore, in order to determine the optimal imaging parameters, it was required to evaluate the acceptable frame rates and number of scan lines for the proposed imaging system. A series of investigations were performed with f-number 2 (since f-number 2 gives optimal focussing) so as to realize this effect and the results obtained are depicted in Table 4 and Figure 4.7.

Table 4 shows that an increase in the number of scan lines increased the frame time (time to make a frame). In effect, this operation aided in reducing the effect of reflections formed from the first reflector along the depth of the image.

Number of Scan lines	Frame Rate (frames/second)
1	67
2	33
3	17
4	8

Table 4 Number of scan lines versus frame rate

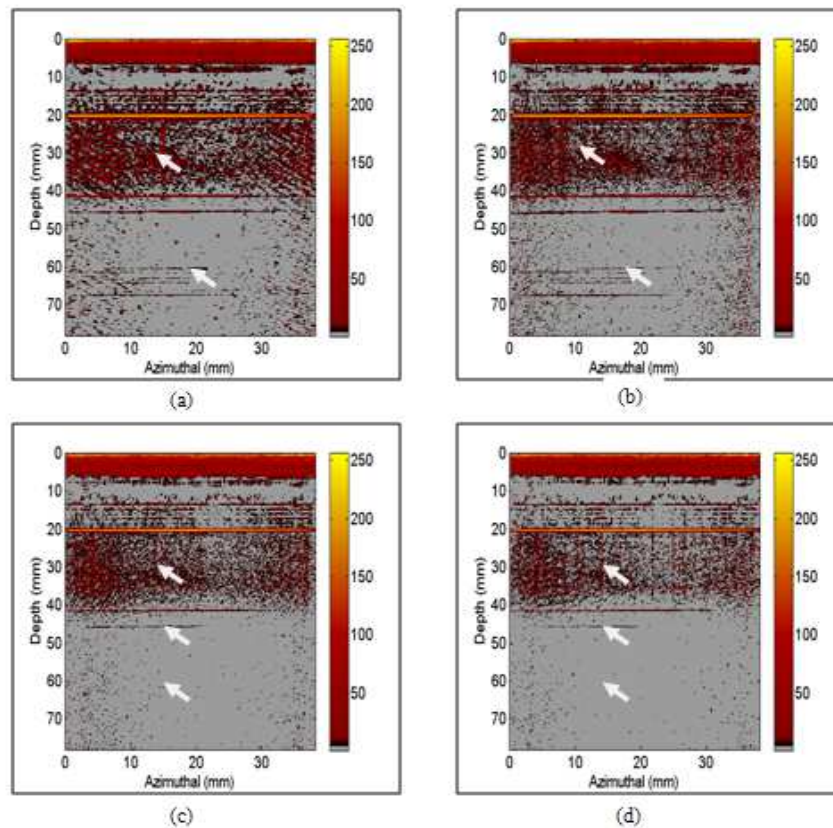


Figure 4.7 Effect of acoustic lines per aperture on the image quality and frame rate; The white pointers denote the regions of interest where a reduction in speckles and reflections were observed with an increase in number of scan lines; (a) 1 line, (b) 2 lines, (c) 3 lines, (d) 4 lines

Figure 4.7 also highlights that speckles and unwanted reflections (denoted by the pointers) are reduced with an increase in the number of scan lines per aperture. This can be attributed owing to the increase in the amount of time taken to form an image which results in the attenuation of echoes and speckles formed along the scan line. The results (Table 4) also show that the frame rate reduced by half with an increase in the number of acoustic lines per aperture.

For an f-number of 1, the aperture size was equal to the distance from the transducer. So at 2 cm from the transducer surface, the aperture size would be 2 cm. However, the transducer was only 38 mm wide having a 64 element transmit and receive aperture. Therefore, the maximum aperture size in this case was limited to 19 mm. It should be noted that increasing the number of scan lines above 16 lines per aperture resulted in a much higher density than the resolution power of the transducer. This resulted in the formation of the samples for every individual beamformed point at $19.25 \mu\text{m}$ $((1540/40 \text{ MHz})/2)$ for a speed of sound of $\sim 1540 \text{ m/s}$.

4.5 Implementation of Multi-Transmit Focal Zones and its Effect on Frame Rate

The optimization of lateral resolution across the long-axis (azimuth) was enhanced over depth by multiple transmit focal zones along the depth. The beam width in this case was improved to about 5 - 10% by the addition of electronic focusing during transmit and dynamic electronic focusing during receive respectively. Therefore, providing multiple transmit focal zones significantly improved the imaging capabilities of the system. In this method, multiple transmit

focal points were selected and the same acoustic line was excited once for each focal point. A linear interpolation was then performed on the weighting to average the lines together in between focal points to form the final image. However, an increase in the number of transmit focal zones decreases the frame-rate and the resultant effect of this phenomenon was observed to be more at greater depths. Hence, the total number of transmit focal zones in the conceived system were limited to four focal zones. A series of investigations was performed to test this capability and to study its influence on the frame rate. The results obtained are depicted in Figure 4.7.

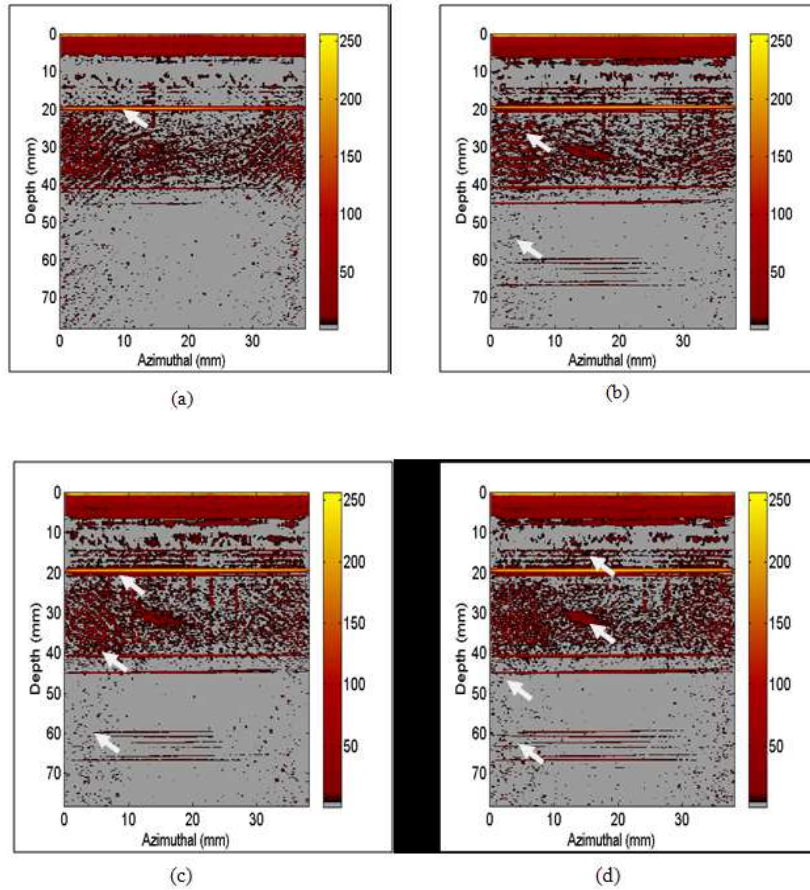


Figure 4.8 Images with multi-transmit focal zones, The white pointers denote the position of different focal zones; (a) 1 focal zone, (b) 2 focal zones, (c) 3 focal zones, (d) 4 focal zones

Figure 4-8 shows the B-mode images obtained with multi-transmit focal zones ranging from 1 to 4 focal zones. The pointers indicate the depth at which the focal zones were formed. The results show that features located in the close proximities of the focal zones were imaged clearly.

Number of Transmit Focal Zones	Focal Zone Depths (mm)	Frame Rate (frames/second)
1	Focal Zone 1 = 21	67
2	Focal Zone 1 = 27 Focal Zone 2 = 54	33
3	Focal Zone 1 = 21 Focal Zone 2 = 40 Focal Zone 3 = 60	22
4	Focal Zone 1 = 17 Focal Zone 2 = 33 Focal Zone 3 = 48 Focal Zone 4 = 64	16

Table 5. Number of focal zones versus frame rate.

The results also found that with an increased number of acoustic lines per aperture, the reflections of the echoes from the perfect reflector located at the depth of 20 mm were imaged more clearly when multiple focal zones were formed. This is because the same acoustic line is excited along multiple focal points at once leading to the capture of all the reflections formed along that particular scan line. This process ultimately enabled the system to record all the multiple reflected echoes along the scan line before they attenuate. A decrease in the frame rate

(Table 5) was also observed with an increase in the number of focal zones due to the increase in the amount of time taken to form the images from the larger number of focal zones.

The investigations carried out so far illustrated the characterization and the advanced capabilities of the conceived ultrasound imaging system. The evaluations have enabled the system capability and performance to be benchmarked. The following section demonstrates the potential of this system in imaging the silicone based phantom tissue fabricated with acoustic heterogeneities within their layers. A detailed description on the phantom fabrication procedure is given in Appendix C.

4.6 B – Mode Imaging of Silicone Phantom

Brightness mode (B – mode) imaging capabilities of the proposed ultrasound imaging system was studied by mapping the acoustic heterogeneities present within the phantom tissue. The tissue mimicking structure fabricated with silicone - intralipid matrix consisted of hollow polymer tubes and optical fibers along the depth as the ultrasound reflectors. The acoustic reflectors and their locations inside the silicone – intralipid phantom tissue are shown in Figure 4.9.

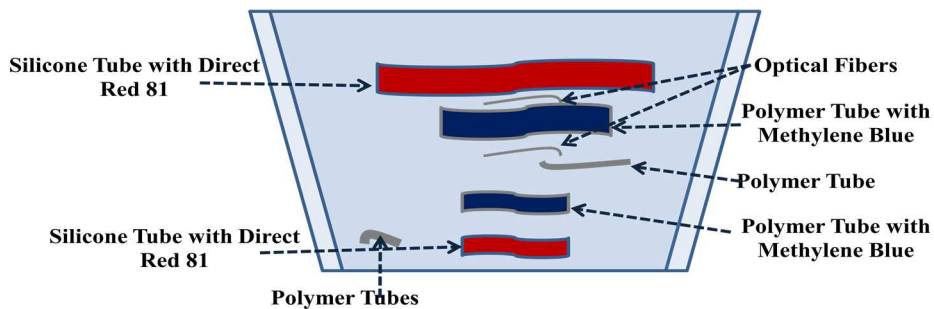


Figure 4.9 Schematic of the silicone phantom

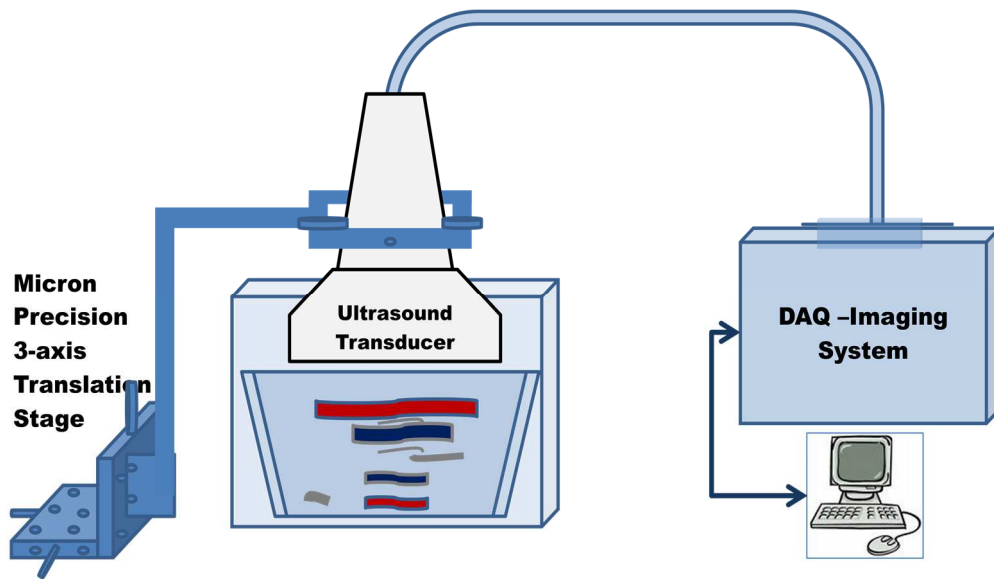


Figure 4.10 Schematic of the experimental set-up for B - mode imaging

Ultrasound imaging of the phantom tissue (Figure 4.9) was performed with the 128 element ultrasound imaging system described in the section 4.2. The phantom tissue was placed inside the acrylic tank filled with de-ionized water and the ultrasound transducer was mounted over the phantom surface (Figure 4.10).

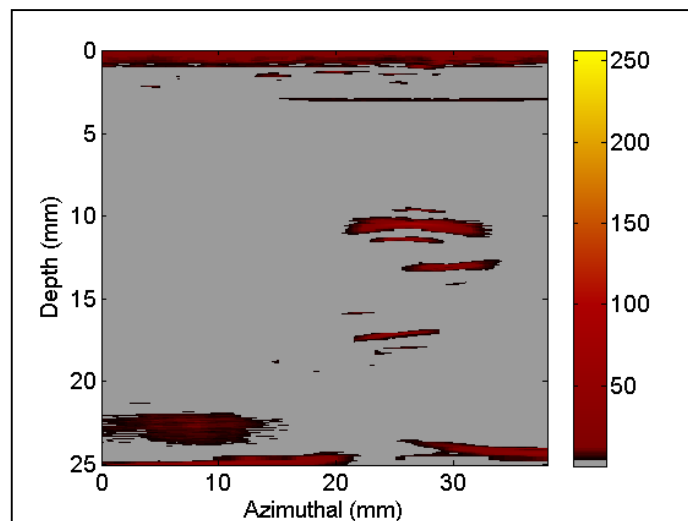


Figure 4.11 B- mode image of the silicone phantom

B- mode image (Figure 4.11) of the phantom was then obtained at a frame rate of 67 frames per second (fps) with 1 scan line per aperture resulting in 128 acoustic lines in the frame. Single transmit focal zone at 19 mm down the acoustic line was selected so as to match the elevation focus of the transducer. The imaging capability of the ultrasound imaging system was examined by performing 2D mapping of the acoustic reflectors located inside the tissue mimicking material. The B-mode shows that the system was capable of mapping the acoustic reflectors placed along different depths of the phantom tissue with mesoscopic resolution. All of the six acoustic reflectors were mapped with ± 0.03 mm accuracy and the results exhibit good imaging continuity.

4.7 Summary of Findings

Ultrasound imaging is one of the mostly widely used clinical imaging modalities across the globe. Although this is a matured and well established imaging modality, the capabilities of the ultrasound imaging system can be enhanced to derive better diagnostic outcomes. A brief description on the fundamental physics and theory of ultrasound lays the foundation blocks to configure a 128 element ultrasound imaging system. Incorporation of high end firmware and advanced post processing concepts into the system supplemented the capabilities of the system to provide ultrasound images from various depths of the tissue. The SNR measurements show that the single channel and the whole system exhibited a SNR of 68 dB and 110 dB respectively. The resolution measurements showed that the system is able to operate with in-plane resolution of 345 ± 2.53 μm

and $151 \pm 2.24 \mu\text{m}$ along the axial plane which meets the desired mesoscopic spatial resolution.

Further, number of scan lines per aperture and number of transmit focal zones were benchmarked against the acceptable frame rates. It was observed that an increase in the number of scan lines per aperture or number of transmit focal zones resulted in a reduction in the frame rate. However, enhancements in the image quality were observed with more number of scan lines per aperture and transmit focal zones. Incorporation of various advanced techniques such as altering the number of acoustic lines per aperture, decimation, spatial compounding and multiple transmit focal zones enabled the imaging system to generate high quality ultrasound images. The investigations performed with silicone based phantom and perfect reflectors showed that the system was capable of providing ultrasound images at frame rate of 68 fps (frames per second).

As mentioned in the literature review, it was established that both ultrasound and photoacoustic imaging exhibits similar physics and instrumentation concepts at the receiver end. Therefore, the potential capabilities of the proposed ultrasound imaging system can be further extended towards performing photoacoustic imaging. The proposed photoacoustic system should therefore operate with the receiving with the post processing hardware and software routines used in conjunction with the ultrasound imaging system. The following chapter discusses these aspects and relevant details of the various works performed to establish the proposed photoacoustic imaging system which was built on the developed ultrasound imaging system.

CHAPTER 5: DUAL-MODALITY PHOTOACOUSTIC IMAGING WITH ENHANCED CONTRAST

This chapter begins with a detailed description of the fundamental theoretical concepts of photoacoustic effect. Further, theoretical simulations performed to study the photoacoustic wave characteristics generated with delta pulse excitation of a spherical and planar absorber is illustrated. This will be followed by the theoretical simulation and experimental investigations into the optical properties of gold nanoparticles and photoacoustic signal generation for selective and multiple targeting. Further, the establishment of the multi-element transducer based photoacoustic imaging system is discussed. Various investigations to map optical absorption heterogeneities along the depth of the phantom tissue with mesoscopic spatial resolution were performed. Implementation of spatial compounding and persistence techniques will be then described and illustrated. Towards the end, novel methodologies for enhancing photoacoustic image contrast are discussed. The section culminates with the implementation of a novel dual-optical modality detection and imaging scheme where simultaneous fluorescence and photoacoustic signals and images of various samples were obtained.

5.1 Introduction

Generation and detection of high frequency photoacoustic waves can be used to perform high resolution imaging of thick and turbid samples with ultrasonic resolution and optical contrast. This approach can therefore be used to derive

anatomical, structural and functional mapping of various biological samples (Wang 2008) and as one of the associated imaging modalities of the proposed multi-modality imaging system. The following sections outline the fundamental theoretical concepts of high frequency photoacoustic imaging and lay the foundation blocks to realize a photoacoustic imaging system.

5.1.1 Theoretical Formulations and Concepts of Photoacoustic Imaging

Photoacoustic signal generation inside the tissue involves the generation of acoustic waves by the successive transformation of light energy into heat leading to mechanical stress which is referred to as thermo-optical mechanism of stress generation. However, the irradiation of pulses should be under the conditions of temporal pressure confinement and temperature confinement which demands the pulse width of the excitation source to be shorter than the stress relaxation time and thermal relaxation time. Laser energy is transformed to heat energy by the fast non-radiative relaxation of the excited states due to the absorption of the laser radiation by the medium. Subsequently, a pressure rise is formed owing to the thermal expansion of the instantaneously heated tissue (Oraevsky, Jacques et al. 1997). This leads to pressure wave propagating in omni-directionally as acoustic waves throughout the tissue.

The photoacoustic pressure waves, induced via local heat deposition by optical energy absorption, can be described with the photoacoustic wave equation (Wang and Wu 2007).

$$\nabla^2 p(\vec{r}, t) - \frac{1}{V_s^2} \frac{\partial^2 p(\vec{r}, t)}{\partial t^2} = -\rho_m \beta \frac{\partial^2 T(\vec{r}, t)}{\partial t^2} \quad 5- -1$$

where, $p(\vec{r}, t)$ denotes the acoustic pressure at location \vec{r} and time t , $T(\vec{r}, t)$ denotes the local temperature rise due to optical energy absorption, V_s the speed of sound and ρ_m the mass density. β represents the isobaric thermal expansion coefficient that describes the relative increase in tissue volume per unit rise of temperature under constant pressure (isobaric condition). The wave propagation is represented by the left hand side of the equation and the source term is represented by the right hand side (Lihong V. Wang 2007).

Under thermal confinement condition, the source term (thermal equation) can be represented in terms of the heat energy generated by optical energy deposition.

Therefore,

$$\rho_m C_V \frac{\partial^2 T(\vec{r}, t)}{\partial t^2} = S(\vec{r}, t) \quad 5-2$$

Where C_V represents the specific heat capacity at constant volume, describing the energy required by a unit mass of tissue to raise its temperature by a temperature unit and $S(\vec{r}, t)$ is the spatiotemporal distribution of instantaneous optical power absorption density. Equation 5-1 can therefore be rewritten as

$$\frac{\partial^2 p(\vec{r}, t)}{\partial t^2} - c^2 \Delta p(\vec{r}, t) = \Gamma \frac{\partial}{\partial t} S(\vec{r}, t) \quad 5-3$$

where, c is the speed of sound and Γ is the Grueneisen coefficient

The time dependence of the laser pulse can be approximated by the use of temporal Dirac function $\delta(t)$ as the source term is non-zero during laser pulse duration.

Therefore, the source term can be expressed as,

$$S(\vec{r}, t) = Q(\vec{r}) \delta(t) \quad 5-4$$

Thus equation 5-1 becomes,

$$\frac{\partial^2 p(\vec{r}, t)}{\partial t^2} - c^2 \Delta p(\vec{r}, t) = \Gamma \frac{\partial}{\partial t} Q(\vec{r}) \delta(t) \quad 5-5$$

Initial pressure distribution from the above equation can therefore be derived as,

$$\begin{aligned} p_0(\vec{r}) &= \Gamma Q(\vec{r}) \\ &= \Gamma H \mu_a \end{aligned} \quad 5-6$$

where, H is the laser fluence and μ_a is the optical absorption co-efficient.

It is to be noted that an increase in pressure is directly proportional to the absorbed energy density E_{abs} which is determined by the product of the absorption coefficient of the medium μ_a (cm^{-1}) and the laser fluence H (J/cm^2). Hence, a change in the optical absorption can be effectively derived from analysing the photoacoustic signal obtained under same fluence conditions. This forms the basis of photoacoustic imaging.

The general photoacoustic wave equation given in equation 5-1 can be solved by the Green function approach (Lihong V. Wang 2007). Green's function for photoacoustic wave is defined as the response to a spatial and temporal impulse. The source term is given as

$$\left(\nabla^2 - \frac{1}{c^2} \frac{\partial^2}{\partial t^2} \right) G(\vec{r}, t; \vec{r}', t') = -\frac{\beta}{c^2} \frac{\partial^2 T(\vec{r}, t)}{\partial t^2} \quad 5-7$$

where \vec{r}' and t' denote the source location and time.

Solving equation 5-1 by the Green's function gives (Lihong V. Wang 2007),

$$p(\vec{r}, t) = \frac{1}{4\pi c^2} \frac{\partial}{\partial t} \left[\frac{1}{ct} \int d\vec{r}' p_0(\vec{r}') \delta\left(t - \frac{|\vec{r} - \vec{r}'|}{c}\right) \right] \quad 5-8$$

Upon laser irradiation and at the onset of heat generation, the PA wave propagates in two opposite directions as planar waves along the axis of the laser beam (assuming single dimension propagation). The amplitude of the pressure waves propagating in each of the directions is therefore equal to half of the initial amplitude of the pressure wave which is at the time of stress generation.

In order to realize the concepts discussed, theoretical simulations were formulated and performed based on delta pulse excitation of PA signal generation and wave propagation from a planar slab and a sphere (Lihong V. Wang 2007). The objects were modelled considering the physical and optical properties of human colon tissue layers obtained from the literature (Marchesini, Pignoli et al. 1994, Huang Z 2004, Hidović-Rowe and Claridge 2005). The response of point absorber to step heating or delta heating is adopted as the principle behind delta pulse excitation and subsequent generation of photoacoustic signals.

5.1.2 Numerical Simulations of Photoacoustic Signal Excitation

5.1.1.1 *Delta Pulse Excitation of Slab*

Photoacoustic wave generation from a slab was simulated based on the theoretical concepts derived. A delta excitation pulse irradiated the homogenous slab of thickness l . This leads to an initial pressure p_0 to be built up within the slab. The pressure formed is propagated outwards in both positive and negative z directions. Using Equation 5-8, the pressure distribution can be obtained. The integral over the volume is expressed as integral over a solid angle as shown in Figure 5.1. From Figure 5.1, it can be observed that a part of the spherical shell of radius ct subtends a solid angle from the observation point $r = (0, 0, z)$.

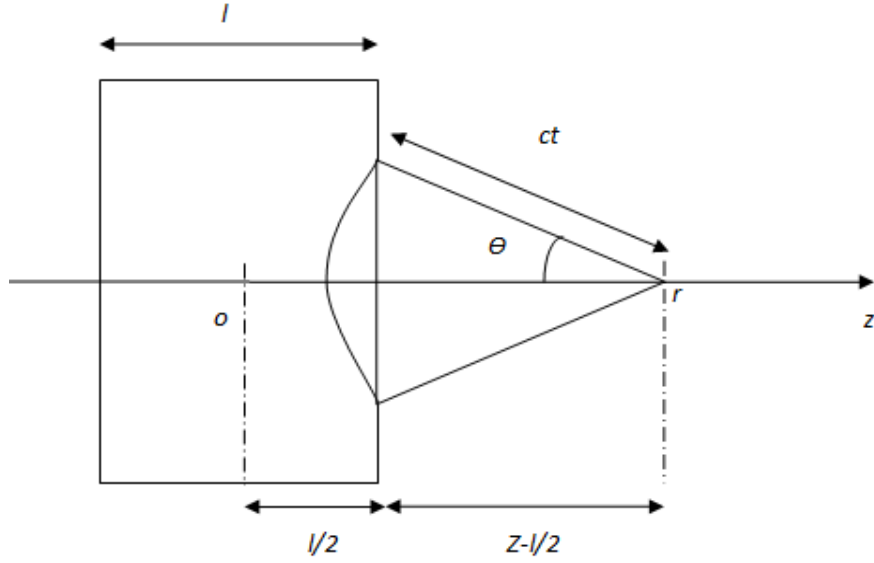


Figure 5.1 Slab Object

With regard to the observation point, two cases are considered.

1. Observation Point on the positive z axis ($z \geq 0$)

When the observation point is outside the slab, three cases could arise in terms of the propagation time

a. $ct < z - l/2$

Under this condition, the spherical shell does not touch the slab. Therefore, using Equation 5- 8 this gives,

$$p(z, t) = 0 \quad 5 - 9$$

b. $z - l/2 \leq ct \leq z + l/2$

For this condition, the spherical shell intersects the near edge of the slab at polar angle θ w. r. t (with respect to) the negative axis. Therefore Equation 5- 8 becomes

$$p(z, t) = \frac{1}{4\pi c^2} \frac{\partial}{\partial t} \left[\frac{1}{ct} \int d\vec{r} p_0(\vec{r}) \delta(t - \frac{|\vec{r} - \vec{r}|}{c}) \right]$$

$$p(z, t) = \frac{p_0(\vec{r})}{4\pi c^2} \frac{\partial}{\partial t} \left[\frac{1}{t} \int d\vec{r} \delta(ct - |\vec{r} - \vec{r}|) \right]$$

$$p(z, t) = \frac{p_0(\vec{r})}{4\pi c^2} \frac{\partial}{\partial t} \left[\frac{1}{t} \int_0^{2\pi} \int_0^\theta (ct)^2 \sin \theta d\theta d\varphi \right]$$

$$p(z, t) = \frac{p_0(\vec{r})}{4\pi c^2} \frac{\partial}{\partial t} \left[\frac{1}{t} (ct)^2 \int_0^{2\pi} 1 - \cos \theta d\varphi \right]$$

$$p(z, t) = \frac{p_0(\vec{r})}{4\pi} \frac{\partial}{\partial t} [2\pi t (1 - \cos \theta)]$$

$$p(z, t) = \frac{p_0(\vec{r})}{2} \frac{\partial}{\partial t} [t (1 - \cos \theta)] \quad 5 - 10$$

From Figure 5.1, $\cos \theta$ can be determined from,

$$\cos \theta = \frac{z - \frac{l}{2}}{ct}$$

Substituting the value of $\cos \theta$ into Equation 5-10 this gives,

$$p(z, t) = \frac{p_0(\vec{r})}{2} \frac{\partial}{\partial t} \left[t \left(1 - \frac{z - \frac{l}{2}}{ct} \right) \right]$$

$$\text{Therefore } p(z, t) = \frac{p_0(\vec{r})}{2} \quad 5 - 11$$

$$c. \quad ct > z + l/2$$

The third condition relates to the spherical shell intersecting the far edge of the slab at polar angle θ' w. r. t the negative axis. Equation 5-8 would therefore be given as

$$\begin{aligned} p(z, t) &= \frac{1}{4\pi c^2} \frac{\partial}{\partial t} \left[\frac{1}{ct} \int d\vec{r} p_0(\vec{r}) \delta(t - \frac{|\vec{r} - \vec{r}|}{c}) \right] \\ p(z, t) &= \frac{p_0(\vec{r})}{4\pi c^2} \frac{\partial}{\partial t} \left[\frac{1}{t} \int d\vec{r} \delta(ct - |\vec{r} - \vec{r}|) \right] \\ p(z, t) &= \frac{p_0(\vec{r})}{4\pi c^2} \frac{\partial}{\partial t} \left[\frac{1}{t} \int_0^{2\pi} \int_0^\theta (ct)^2 \sin \theta d\theta d\phi \right] \\ p(z, t) &= \frac{p_0(\vec{r})}{4\pi c^2} \frac{\partial}{\partial t} \left[\frac{1}{t} (ct)^2 \int_0^{2\pi} \cos \theta' - \cos \theta d\phi \right] \\ p(z, t) &= \frac{p_0(\vec{r})}{4\pi} \frac{\partial}{\partial t} [2\pi t (\cos \theta' - \cos \theta)] \\ p(z, t) &= \frac{p_0(\vec{r})}{2} \frac{\partial}{\partial t} [t (\cos \theta' - \cos \theta)] \quad 5 - 12 \end{aligned}$$

From Figure 5.1, the values of $\cos \theta$ and $\cos \theta'$ would be

$$\begin{aligned} \cos \theta &= \frac{z - \frac{l}{2}}{ct} \\ \cos \theta' &= \frac{z + \frac{l}{2}}{ct} \end{aligned}$$

Substituting the value of $\cos \theta$ in Equation 5-12 this gives

$$p(z, t) = \frac{p_0(\vec{r})}{2} \frac{\partial}{\partial t} \left[t \left(\frac{z + \frac{l}{2}}{ct} - \frac{z - \frac{l}{2}}{ct} \right) \right]$$

$$\text{And } p(z, t) = 0$$

5 - 13

2. Observation point inside the slab

When the observation point is inside the slab, the three conditional cases in terms of the propagation time would be

a. $ct < l/2 - z$

In the first condition, the spherical shell is totally within the slab. The function in Equation 5- 8 would be

$$p(z, t) = \frac{1}{4\pi c^2} \frac{\partial}{\partial t} \left[\frac{1}{ct} \int d\vec{r} p_0(\vec{r}) \delta(t - \frac{|\vec{r} - \vec{r}|}{c}) \right]$$

$$p(z, t) = \frac{p_0(\vec{r})}{4\pi c^2} \frac{\partial}{\partial t} \left[\frac{1}{t} \int d\vec{r} \delta(ct - |\vec{r} - \vec{r}|) \right]$$

$$p(z, t) = \frac{p_0(\vec{r})}{4\pi c^2} \frac{\partial}{\partial t} \left[\frac{1}{t} \int_0^{2\pi} \int_0^\pi (ct)^2 \sin \theta d\theta d\varphi \right]$$

$$p(z, t) = \frac{p_0(\vec{r})}{4\pi c^2} \frac{\partial}{\partial t} \left[\frac{1}{t} (ct)^2 \int_0^{2\pi} 2 d\varphi \right]$$

$$p(z, t) = \frac{p_0(\vec{r})}{4\pi} \frac{\partial}{\partial t} [4\pi t]$$

$$p(z, t) = p_0(\vec{r})$$

5 - 14

b. $l/2 - z \leq ct \leq l/2 + z$

In the second condition, the spherical shell intersects the near edge of the slab at polar angle θ wrt the negative axis as in Equation 5 -11. The $p(z, t)$ function would give

$$p(z, t) = \frac{p_0(\vec{r})}{2} \quad 5 - 15$$

c. $ct > l/2 + z,$

In the third condition, the spherical shell will intersect the far edge of the slab at polar angle θ' wrt the negative axis as in Equation 5–13. Thus this gives

$$p(z, t) = 0 \quad 5 - 16$$

3. *Observation point on the negative z axis ($z < 0$)*

For this analysis, the results obtained are similar to the cases discussed as above when the observation point is on the positive z axis. This is owing to the slab object being symmetrical.

Therefore, the initial pressure distribution can be written as,

$$p_0(z) = p_0 U\left(z + \frac{l}{2}\right) U\left(-z + \frac{l}{2}\right) \quad 5 - 17$$

Where U is the Heaviside function defined as,

$$U(z) = \begin{cases} 1 & \text{for } z \geq 0 \\ 0 & \text{for } z < 0 \end{cases}$$

The pressure distribution at any time t would be

$$p(z, t) = \frac{1}{2} p_0(z - ct) + \frac{1}{2} p_0(z + ct) \quad 5 - 18$$

From the equation 5–18, it can be observed that the first term represents a right propagating plane wave along the positive z axis and the second term represents the left propagating plane wave along the negative z axis. The physical phenomenon of the equation 5–18 would be that of, when the slab is excited using delta pulse, the pressure is first created within the slab and further gets split into two plane waves each having half the magnitude of the initial pressure and propagating in opposite directions.

In order to prove this concept and the fundamental parameters governing the photoacoustic signal generation in a tissue, a series of simulations was performed based on the delta excitation of a slab with the optical and physical properties of human colon tissue. Simulations for the pressure generation were performed with a delta pulse excitation on a slab on three different layers of the human colon tissue model. The input parameters adopted for each of the colon layers and their respective simulation results are shown in Figure 5.2 – Figure 5.4. Each of these layers had varying thickness ($395\ \mu\text{m}$ – $500\ \mu\text{m}$) and absorption coefficients ($2.3\ \text{cm}^{-1}$ - $3.3\ \text{cm}^{-1}$) with muscle layer having the highest value followed by mucosa and then submucosa. The fluence rate was considered to be $10\ \text{mJ}/\text{cm}^2$. The acoustic velocity was assumed to be $1500\ \text{m/s}$. The detector was set at two times half the thickness of the slab (Figure 5.1).

1. Mucosal Layer (Figure 5.2)

Thickness: 395 μm

Absorption coefficient: 2.7 cm^{-1}

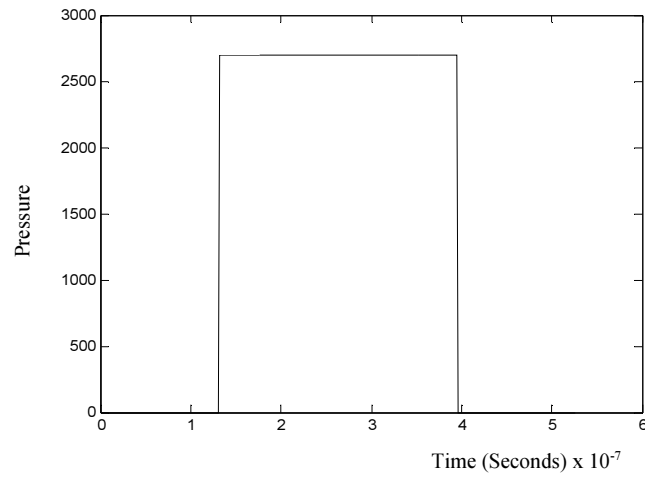


Figure 5.2 Pressure propagation in mucosal layer for slab

2. Submucosal Layer (Figure 5.3)

Thickness: 415 μm

Absorption coefficient: 2.3 cm^{-1}

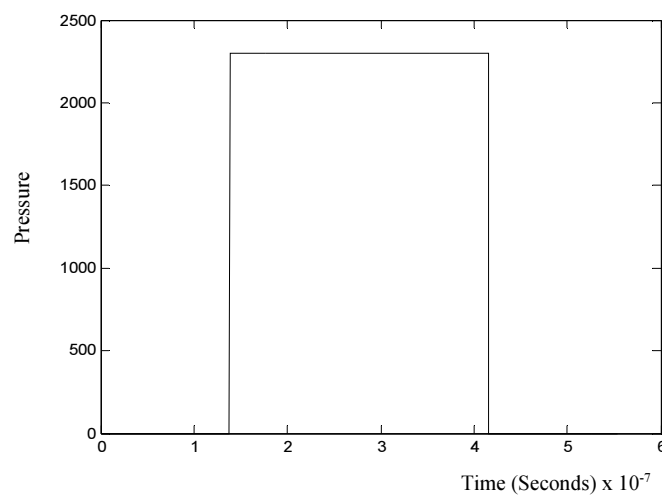


Figure 5.3 Pressure propagation in submucosal layer for slab

3. Muscle Layer (Figure 5.4)

Thickness: 500 μm

Absorption coefficient: 3.3 cm^{-1}

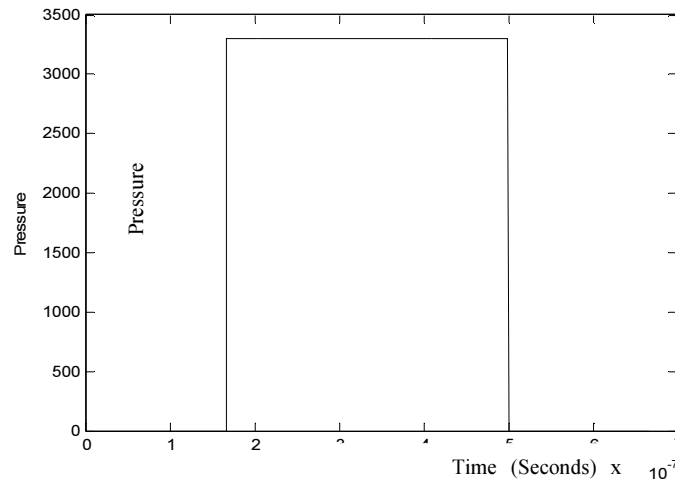


Figure 5.4 Pressure propagation in muscle layer for slab

Analyzing Figure 5.2 –Figure 5.4, it can be noted that the amplitude of the pressure wave increases with an increase in the absorption coefficient of the medium. It was also observed that the muscle layer had the highest pressure amplitude followed by mucosa and then submucosa which was in agreement with the theory. The simulation results obtained (Figure 5.2 –Figure 5.4) in the form of rectangular waves generated from the slab for delta pulse excitation was also in agreement with theoretical profiles of the generated PA wave given in the reference (Chen and Diebold 1995). The pressure signal detected at the transducer surface is computed to be half of the initial pressure where the generated pressure propagates in two opposite directions. The following simulation results substantiated the theoretical basis of this argument. Simulations were performed where the initial pressure was assumed to be a constant value of one and the velocity of the sound in the medium (c) to be 1500 m/s. The thickness of the slab (l) was considered to be 1 mm.

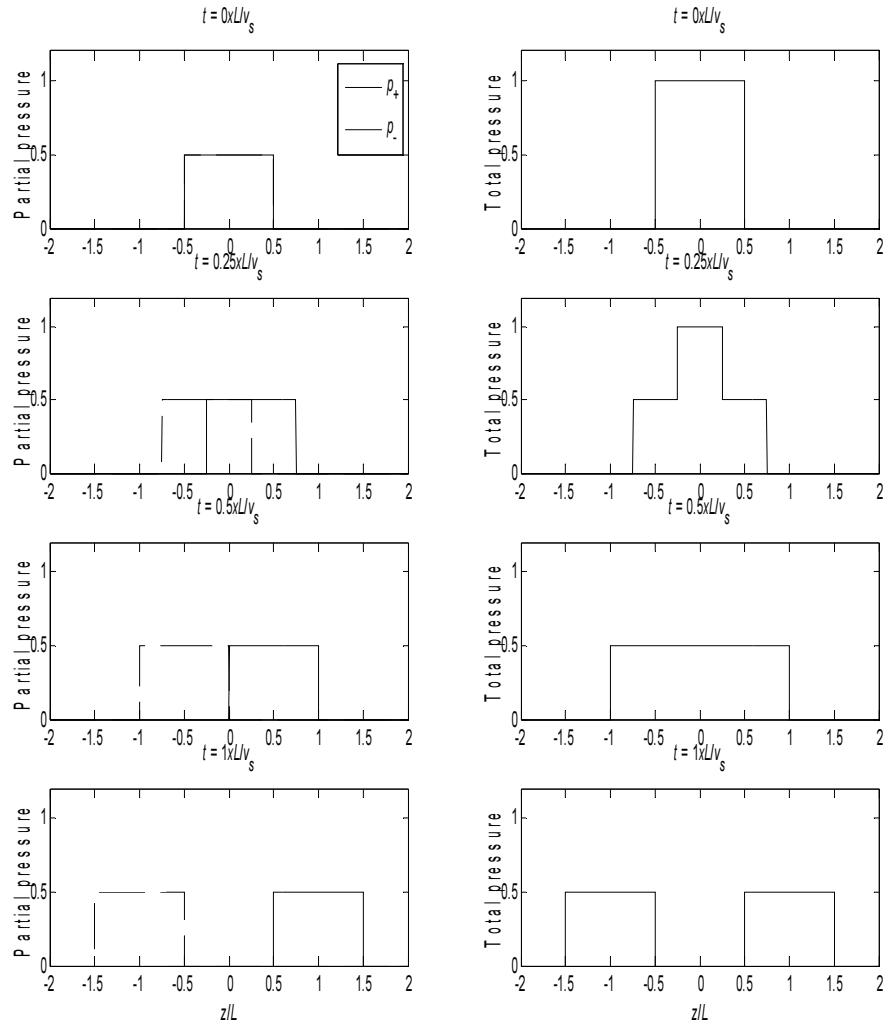


Figure 5.5 Pressure propagation from irradiated slab

Figure 5.5 illustrates the generation of the pressure wave and how the generated pressure propagates across the medium. From Figure 5.5, it was evident that the generated pressure propagated in two opposite directions as plane waves with half the amplitude of the initial pressure which is consistent with the theory. However, as detailed in section 2.1, most of the tissue constituents exhibit spherical geometry. Further, various plasmonic nanoparticles used for molecular imaging and PA contrast enhancement can be also approximated with spherical geometry. Numerical simulations were therefore performed to study PA generation within a

spherical geometry. This would enable one to better understand how the pressure wave is being generated from a cylindrical structure on delta heating.

5.1.1.2 *Delta pulse excitation of sphere*

The theoretical concepts of photoacoustic wave generation from a sphere were derived under delta pulse excitation of a sphere. This is considered in Figure 5.6 where a delta excitation pulse heats up the homogenous sphere of radius (R_s) leading to an initial pressure generation p_0 inside the sphere. As in the case of delta pulse excitation of the slab described in section 5.1.1.1, the pressure distribution was derived from Equation 5- 8.

The integral over the volume is converted into an integral over a solid angle as shown in Figure 5.6. From Figure 5.6 , it can be observed that a part of the spherical shell of radius ct subtends at a solid angle from the observation point $r = (0, 0, z)$.

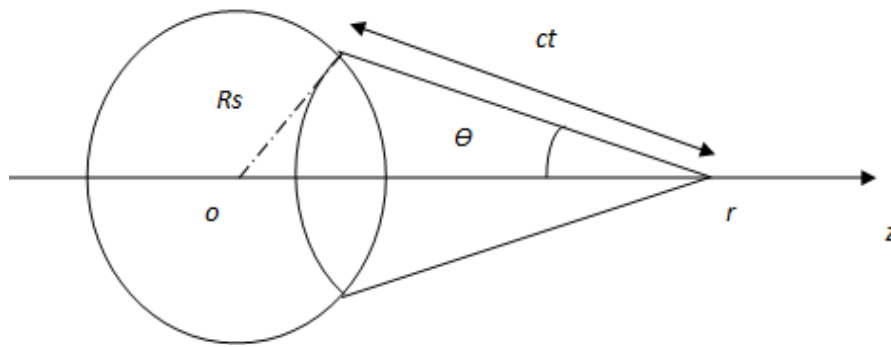


Figure 5.6 Sphere Object

With regard to the observation point, two cases are considered.

1. **Observation point outside the sphere ($r \geq R_s$)**

When the observation point is outside the sphere, three situational cases could arise in terms of its propagation time.

a. $ct < r - R_s$

In the first condition, it is observed that the spherical shell does not touch the heated sphere. Equation 5- 8 would be,

$$p(r, t) = 0 \quad 5 - 19$$

b. $r - R_s \leq ct \leq r + R_s$

In this condition, the spherical shell would intersect the near edge of the heated sphere at polar angle θ wrt the negative axis. The function in Equation 5-8 would become,

$$p(r, t) = \frac{1}{4\pi c^2} \frac{\partial}{\partial t} \left[\frac{1}{ct} \int d\vec{r} p_0(\vec{r}) \delta(t - \frac{|\vec{r} - \vec{r}|}{c}) \right]$$

$$p(r, t) = \frac{p_0(\vec{r})}{4\pi c^2} \frac{\partial}{\partial t} \left[\frac{1}{t} \int d\vec{r} \delta(ct - |\vec{r} - \vec{r}|) \right]$$

$$p(r, t) = \frac{p_0(\vec{r})}{4\pi c^2} \frac{\partial}{\partial t} \left[\frac{1}{t} \int_0^{2\pi} \int_0^\theta (ct)^2 \sin \theta d\theta d\varphi \right]$$

$$p(r, t) = \frac{p_0(\vec{r})}{4\pi c^2} \frac{\partial}{\partial t} \left[\frac{1}{t} (ct)^2 \int_0^{2\pi} 1 - \cos \theta d\varphi \right]$$

$$p(r, t) = \frac{p_0(\vec{r})}{4\pi} \frac{\partial}{\partial t} [2\pi t (1 - \cos \theta)]$$

$$p(r, t) = \frac{p_0(\vec{r})}{2} \frac{\partial}{\partial t} [t (1 - \cos \theta)] \quad 5 - 20$$

From the figure, $\cos \theta$ would be

$$\cos \theta = \frac{(ct)^2 + r^2 - R_s^2}{2rct}$$

Substituting the value of $\cos \theta$ into Equation 5 – 20, this gives,

$$p(r, t) = \frac{p_0(\vec{r})}{2} \frac{\partial}{\partial t} \left[t \left(1 - \frac{(ct)^2 + r^2 - R_s^2}{2rct} \right) \right]$$

$$p(r, t) = \frac{p_0(\vec{r})}{2r} (r - ct) \quad 5 - 21$$

c. $ct > r + R_s$,

In the third condition, the spherical shell passes at the far edge of the heated sphere and does not intersect with the sphere.

Using Equation 5- 8, the function would be,

$$p(r, t) = 0 \quad 5 - 22$$

2. Observation point inside the slab ($r \leq R_s$)

For observation point inside the slab, the analysis of three conditions in terms of the propagation time would be

a. $ct < R_s - r$

In this condition, it is found that the spherical shell is totally enclosed by the heated sphere. Equation 5- 8 would give,

$$p(r, t) = \frac{1}{4\pi c^2} \frac{\partial}{\partial t} \left[\frac{1}{ct} \int d\vec{r} p_0(\vec{r}) \delta(t - \frac{|\vec{r} - \vec{r}|}{c}) \right]$$

$$p(r, t) = \frac{p_0(\vec{r})}{4\pi c^2} \frac{\partial}{\partial t} \left[\frac{1}{t} \int d\vec{r} \delta(ct - |\vec{r} - \vec{r}|) \right]$$

$$p(r, t) = \frac{p_0(\vec{r})}{4\pi c^2} \frac{\partial}{\partial t} \left[\frac{1}{t} \int_0^{2\pi} \int_0^\pi (ct)^2 \sin \theta \, d\theta \, d\varphi \right]$$

$$p(r, t) = \frac{p_0(\vec{r})}{4\pi c^2} \frac{\partial}{\partial t} \left[\frac{1}{t} (ct)^2 \int_0^{2\pi} 2 \, d\varphi \right]$$

$$p(r, t) = \frac{p_0(\vec{r})}{4\pi} \frac{\partial}{\partial t} [4\pi t]$$

$$p(r, t) = p_0(\vec{r}) \quad 5 - 23$$

$$b. \quad R_s - r \leq ct \leq R_s + r$$

In second condition, the spherical shell emerges out of the sphere as in Equation 5 – 21 giving,

$$p(r, t) = \frac{p_0(\vec{r})}{2r} (r - ct) \quad 5 - 24$$

$$c. \quad ct > R_s + r,$$

In the third condition, the spherical shell encloses the heated sphere and no longer intersects with the sphere. The function in Equation 5- 8 would be expressed as,

$$p(r, t) = 0 \quad 5 - 25$$

The initial pressure can therefore be written as,

$$p_0(r) = p_0 U(r) U(-r + R_s) \quad 5 - 26$$

Where U is the Heaviside function defined as,

$$U(z) = \begin{cases} 1 & \text{for } z \geq 0 \\ 0 & \text{for } z < 0 \end{cases}$$

The pressure distribution as a function of time t can therefore be derived as,

$$p_0(\vec{r}, t) = \frac{r + ct}{2r} p_0(r + ct) + \frac{r - ct}{2r} p_0(-r + ct) \quad 5 - 27$$

$$+ \frac{r - ct}{2r} p_0(r - ct)$$

From Equation 5–27, it can be observed that the first term denotes a converging spherical wave with the second term denoting a diverging spherical wave that originates from the initially converging wave propagating through the center of the sphere and the third term highlighting a diverging spherical wave. From Equation 5 – 27, the wave behaviour characteristics can be explained as follows; when the sphere is excited using delta pulse, the pressure splits into two equal parts, each initiating a spherical wave, with one propagating inwards as a converging spherical compression wave (first term in Equation 5–27) and the other propagating outwards as a diverging spherical compression wave (third term in Equation 5 – 27). When the converging spherical compression wave (first term in Equation 5 – 27) reaches the center of the heated spherical object, it gets translated into a diverging spherical rarefaction wave (second term in Equation 5–27).

In order to prove this concept and the fundamental parameters governing the photoacoustic signal generation in tissue, numerical simulations were further performed. Pressure versus time was plotted by considering the optical absorption coefficient and the thickness of the human colon layers used in section 5.1.1.1. The fluence rate was considered to be 10 mJ/cm^2 to ensure the laser safety conditions.

The acoustic velocity was assumed to be 1500 m/s. The input parameters adopted for each of the colon layers and their respective simulation results are shown in Figure 5.7 – Figure 5.9.

1. Mucosal Layer (Figure 5.7)

Radius: 197.5 μm

Absorption coefficient: 2.7 cm^{-1}

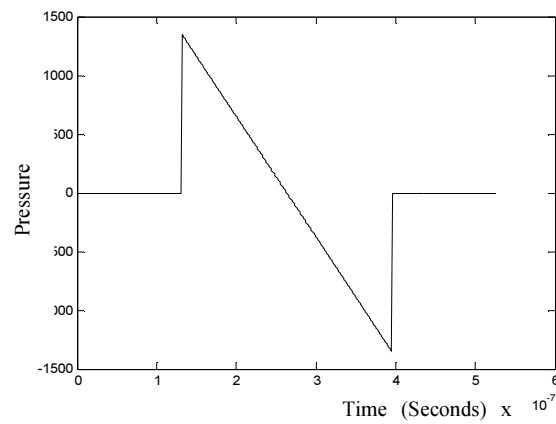


Figure 5.7 Pressure propagation in mucosal layer for sphere

2. Submucosal Layer (Figure 5.8)

Radius: 207.5 μm

Absorption coefficient: 2.3 cm^{-1}

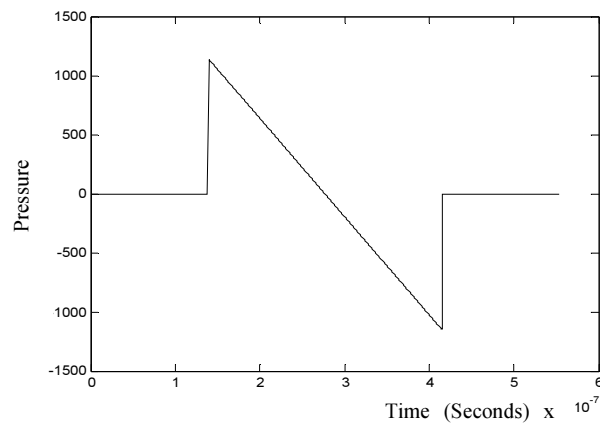


Figure 5.8 Pressure propagation in submucosal layer for sphere

3. Muscle Layer (Figure 5.9)

Radius: 250 μm

Absorption coefficient: 3.3 cm^{-1}

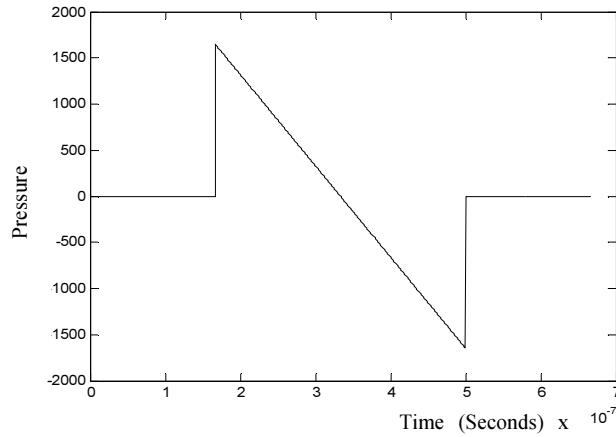


Figure 5.9 Pressure propagation in muscle layer for sphere

Figure 5.7 – Figure 5.9 show that the amplitude of the pressure wave varies with the absorption coefficient of the medium. Muscle layer had the highest pressure amplitude followed by mucosa and then submucosa as the amplitude of photoacoustic signal is directly proportional to the absorption coefficient of the absorber. The results also showed that an ‘N’ shaped bipolar wave was generated from a sphere on delta pulse excitation. The simulated results are consistent with theoretical explanation highlighted by Chen and Diebold’s work on the generated PA wave (Chen and Diebold 1995). Looking into the characteristic time scale duration for each of the bipolar signals, it was evident that smaller absorbing spheres will generate PA signals with larger frequency components. The PA signal generated from the irradiated tissue is therefore expected to be a broadband signal whose frequency spans across a wide bandwidth depending on the size of the absorbing structures.

In summary, the basic theory of photoacoustic wave generation and the nature of the generated waves with advance in time and change in the source geometry was reviewed. An attempt to realize the theoretical concepts of photoacoustic signal generation and propagation were performed with the model simulations in two distinct geometries with varying optical properties. Various experimental investigations performed in relation to high frequency photoacoustics were also made.

5.2 Investigations into High Frequency Photoacoustic Signal Enhancement Using Plasmonic Nanoparticles

Recently, various kinds of plasmonic nanoparticles were used to enhance photoacoustic signals for molecular photoacoustic imaging (Wang 2008). The primary source of the photoacoustic signal is to be induced by the enhanced optical energy absorption of nanoparticles which results in rapid heating of the particle. The heat from the particle will be further diffused into the surrounded medium leading to the generation of PA signals from their rapid expansion and contraction of the medium. Another source of PA signal generation would be the nanoparticle itself, where high frequency ($>$ MHz depending on the size of the particle) PA signals are generated. However, the amplitude of these signals would be relatively smaller when compared to PA signal generated from surrounding medium.

5.2.1 Nanoparticles as Contrast agents for Photoacoustic Imaging

Nanoparticles when melded with the PAI can serve as multifunctional and highly sensitive diagnostic tools for deep tissue imaging applications. Amongst the

various types of nanoparticles used, metal nanoparticles have found profound applications in disease diagnostics. Amongst the various kinds of metal nanoparticles, gold nanoparticles have provided significant contributions towards various fields of biomedicine such as in genomics (Shim, Lim et al. 2008, Panyala, Peña-Méndez et al. 2009), biosensors (Stewart, Anderton et al. 2008), immunoassays, clinical chemistry (Dykman and Bogatyrev 2007), detection and control of microorganisms (Luo and Stutzenberger 2008), cancer cell photothermolysis (Liu, Dai et al. 2008) and targeted delivery of drugs or other substances (Han, Ghosh et al. 2007). Owing to their unique optical responses due to surface plasmon resonance (SPR), gold nanoparticles exhibit enhanced absorption cross-sections across the visible to NIR wavelength region.

5.2.1.1 Surface Plasmon Resonance

When noble metals such as gold and silver are reduced to nanoscale dimensions, restrictions are imposed towards the spatial confinement of the electrons, which induces restrictions to the electron motion. However, these freely moving electrons of the metal nanoparticle will be periodically displaced with respect to the lattice ions when it is driven by the electric field of an incident optical beam. Depending on the nanoparticle composition, size, shape and the dielectric properties of the surrounding medium, the periodic electron displacement creates charges separated by a distance at opposite surfaces of the particle. However, the displaced charges will attract each other and contribute to a restoring Coulomb force. This phenomenon results in an electron oscillator with specific frequency and the quantum of the electron oscillator is called surface plasmon (SP) and the collective coherent oscillation in resonance with the frequency of the

incident light is called the surface plasmon resonance (SPR). Due to plasmonic confinement, all radiative and non-radiative properties of the metal particle are enhanced by orders of magnitude. Nevertheless, the plasmon oscillations will be subjected to dephasing due to the number of processes that damp their collective oscillations and this result in the decay of plasmon oscillation leading to a decrease in their optical efficiencies.

5.2.1.2 Absorption, scattering and optical tuning

Many original concepts related to nanoplasmonics were initially built on the theoretical and experimental studies with gold nanospheres as explained by Mie theory (Mie 1908). However, for non-spherical nanoparticles such as nanorods, the theoretical SPR band intensity can be explained based on Gans theory (Gans 1915). According to Gans theory, two SPR bands are generated when the shape of the gold nanoparticle is changed from spheres to rods namely; (1) a strong band tunable in the visible to NIR region that corresponds to electron oscillations along the long axis referred to as longitudinal band, and (2) a weak band in the visible region that corresponds to electron oscillations along the short-axis referred to as transverse band,. The longitudinal band is tunable where the SPR peaks can be red-shifted by increasing the aspect ratios (length/width) of the nanoparticle whereas the transverse band is insensitive to size changes. Besides altering the shape, optical tuning into NIR region can be also achieved by introducing structural variation into the nanoparticle such as in core-shell nanoparticles. The most commonly used particles are silica core/gold shell and gold core/silica shell nanoparticles with the former exhibiting the best optical tuning property. However, silica core/gold shell nanoparticles are more widely used due to its inherent optical tuning property owing

to the higher level of red shift of the SPR band from visible to NIR region by varying the core-shell thickness ratio. The red shift is attributed to the increased coupling between surface plasmons of the inner core and outer shell (Jain and El-Sayed 2007) of the nanoparticle. Therefore, for the efficient usage of gold nanoparticles for photoacoustic applications, it is desirable to explain and quantify these optical behaviors using computational models. Recently, there have been considerable interests towards performing FDTD based theoretical studies for determining the interaction of light with nanoscale structures such as metal nanoparticles (Futamata, Maruyama et al. 2003, Tanev, Tuchin et al. 2006, Liu, Guyot-Sionnest et al. 2007, Chu, Schonbrun et al. 2008). In this context, theoretical studies were conducted to address and develop FDTD method based computation models for gold nanospheres (radius ' r '), core-shell nanoparticles (core radius ' R_1 ', shell radius ' R_2 ') and gold nanorods (aspect ratio ' AR ' = length('L')/width('W')). The geometry of these particles are shown in Figure 5.10.

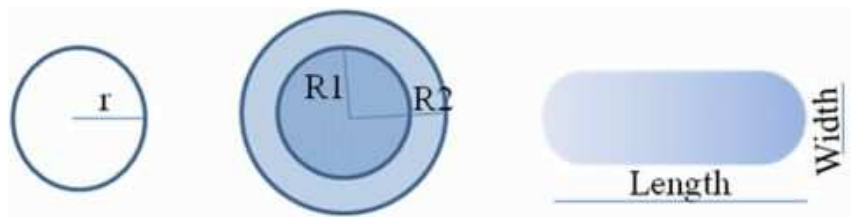


Figure 5.10 Geometry of simulated nanoparticles a) Nanosphere, b) core-shell nanoparticle, c) nanorod

5.2.1.3 Finite-difference time-domain method

In this method, the electromagnetic fields can be quantified as a function of frequency or wavelength by performing Fourier transforms as a function of time. The FDTD technique which is discrete in both time and space make use of fine

mesh called Yee cells to describe the electromagnetic fields and materials under investigation. In order to solve the Maxwell's equations in discrete time steps, the mesh size is related to each of the time steps through the speed of light. By employing a light source into the computational model, it is possible to determine the propagation of electromagnetic field through the structure of interest until the electromagnetic fields are vanished from the computation region. The frequency dependence of the power flow at any point or group of points can be also deduced from the Fourier transform of the time domain information obtained. In addition, the scattering properties of the investigating structure can be derived from the far field projection of the near field data.

5.2.1.4 Novel FDTD Models for Determining the Optical Properties of Gold Nanoparticles

Three dimensional FDTD computation models were formulated in FDTD Solutions 7.5 for gold nanospheres, nanoshells and nanorods within a volume of $8\mu\text{m}^3$. The models involved the use of a total field scattered field (TFSF) source surrounding the defined nanoparticle, one power monitor in the total field region and one in the scattered field region to calculate the absorption and scattering cross-sections respectively. The analysis group placed inside the TFSF source calculated the absorption cross section whereas the analysis group located outside the TFSF source calculated the scattering cross section. In order to accurately resolve the electromagnetic interactions at the curved surfaces of the nanoparticles, a mesh override region of 0.7 nm was employed within a volume of 170nm^3 encompassing the nanoparticle as well as the TFSF source. The TFSF source spanned within a wavelength range of 380 nm to 1064 nm with the three frequency monitors each

computing the discrete Fourier transforms of the time domain fields that were placed around the nanoparticle. The embedding dielectric medium was assumed to be water with a refractive index of 1.33, often used to approximate the in-vivo conditions. The optical constants for gold and silica were taken from Johnson and Christy (Johnson and Christy 1972) and Palik (Palik 1985) respectively. The models were tested for accuracy by comparing the optical efficiencies of each of the models with its equivalent reported in the literature and the results are explained in the following sections.

5.2.1.5 FDTD Simulations to Determine the Optical Properties of Spherical Gold Nanoparticles

The following sections illustrate the FDTD method and further describe the various simulations performed to determine the optical properties of spherical and rod shaped gold nanoparticles. Three dimensional FDTD computation models were formulated in FDTD Solutions (Lumerical Inc.) for gold nanospheres, nanoshells and nanorods within a volume of $8\mu\text{m}^3$. The models were tested for accuracy by comparing the optical efficiencies of each model with its equivalent as reported in the literature. The results are explained in the sub-sections that follow.

5.2.1.6 Gold Nanosphere

The proposed simulation model for the gold nanosphere was tested for its accuracy prior to running the required computations. This was done by comparing the FDTD results with Mie-theory based computations. FDTD method based computations were performed for determining the absorption and scattering cross-

sections as a function of size parameter of the gold nanosphere and the Mie efficiency comparison with its equivalent analytic solution is given in Figure 5.11.

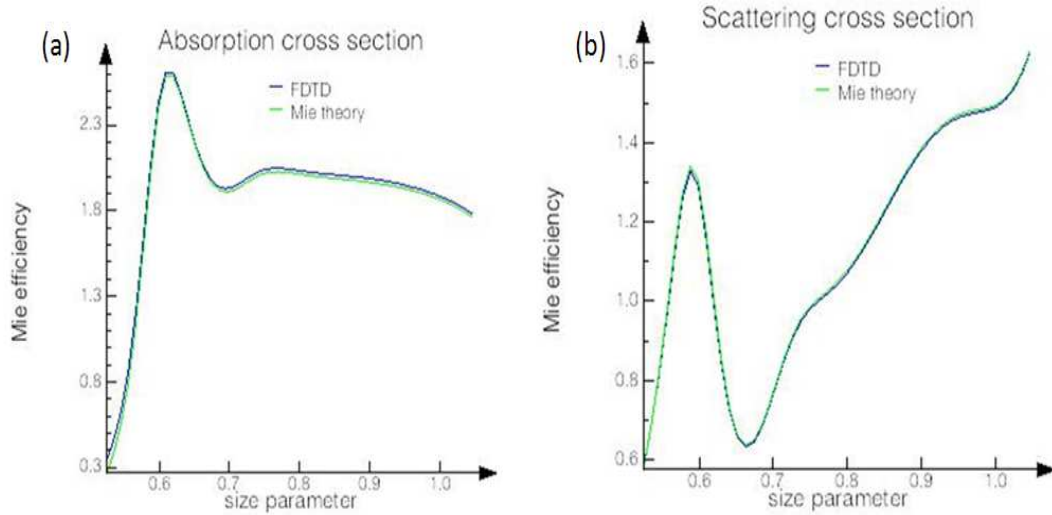


Figure 5.11 Comparison of FDTD result with analytic solution, a) Absorption cross-section b) Scattering cross-section

Figure 5.11 a and Figure 5.11 b, it can be observed that the results of the FDTD computation model agreed well with the analytical solutions for both absorption and scattering cross-sections. The developed model was therefore adopted for further studies to determine optical properties and behavior for various nanosphere sizes.

5.2.1.7 Core-Shell Nanoparticles

The proposed FDTD model for the core-shell nanoparticle was developed within the earlier mentioned computational environment and the nanoshell was modeled as a two layer system consisting of two overlapping nanospheres. In the region where the nanospheres overlap, the mesh orders were set to two distinct values to ensure that only the optical constants of the particular material were used in the core with R_1 as its radius and R_2 as the shell radius. The credibility of the

developed model was determined by comparing the optical efficiency values obtained from the model with the reported work (Jain, Lee et al. 2006).

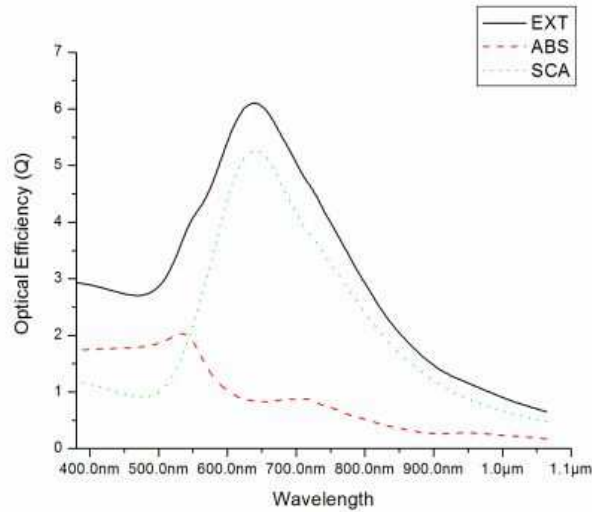


Figure 5.12 Calculated spectra of the optical efficiencies from the FDTD model; $R_1=40\text{nm}$ and $R_2=70\text{nm}$.

Optical efficiencies and optical trends, as shown in Figure 5.12, were in excellent agreement with the results reported by El –Sayed Group (Jain, Lee et al. 2006). The developed model was therefore adopted for further studies.

5.2.1.8 Gold Nanorods

Though there have been prior investigations on the optical properties of nanorods with varying morphologies (Lee and El-Sayed 2005, Prescott and Mulvaney 2006), this research made use of a novel approach which involved a hemispherically capped cylinder to approximate the nanorod. The proposed FDTD model of the nanorod was composed of a solid cylinder whose ends were capped with solid hemispheres with a radius equivalent to the radius of the solid cylinder. The developed model was validated by comparing the optical efficiencies obtained

from the model (Figure 5.13) with the reported work (Ungureanu, Rayavarapu et al. 2009) for an aspect ratio (AR) of 2.26.

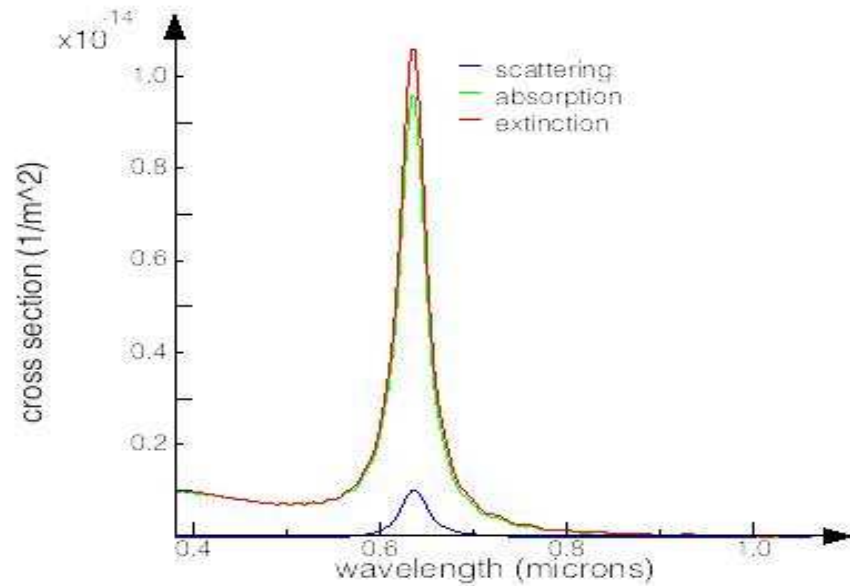


Figure 5.13 Calculated spectra of the optical cross-sections of gold nanorod from the FDTD model; $L=44.8$ nm and $W=19.8$ nm, $AR=2.26$.

Figure 5.13 shows that the SPR maximum was obtained at 634 nm from the FDTD model for gold nanorod with an aspect ratio of 2.26. The results were consistent with other reported works; 633 nm (Ungureanu, Rayavarapu et al. 2009) and the theoretical relationship (634.7 nm) derived by Link and El-Sayed (Link, Mohamed et al. 1999, Link and El-Sayed 2005).

5.2.2 Results and Discussion

5.2.2.1 Gold Nanospheres

Simulations were performed for gold nanospheres within a radius range of 10 nm - 60 nm with the proposed model. Extinction, absorption and scattering

efficiencies for each of the nanospheres were recorded and the results are given in Figure 5.14.

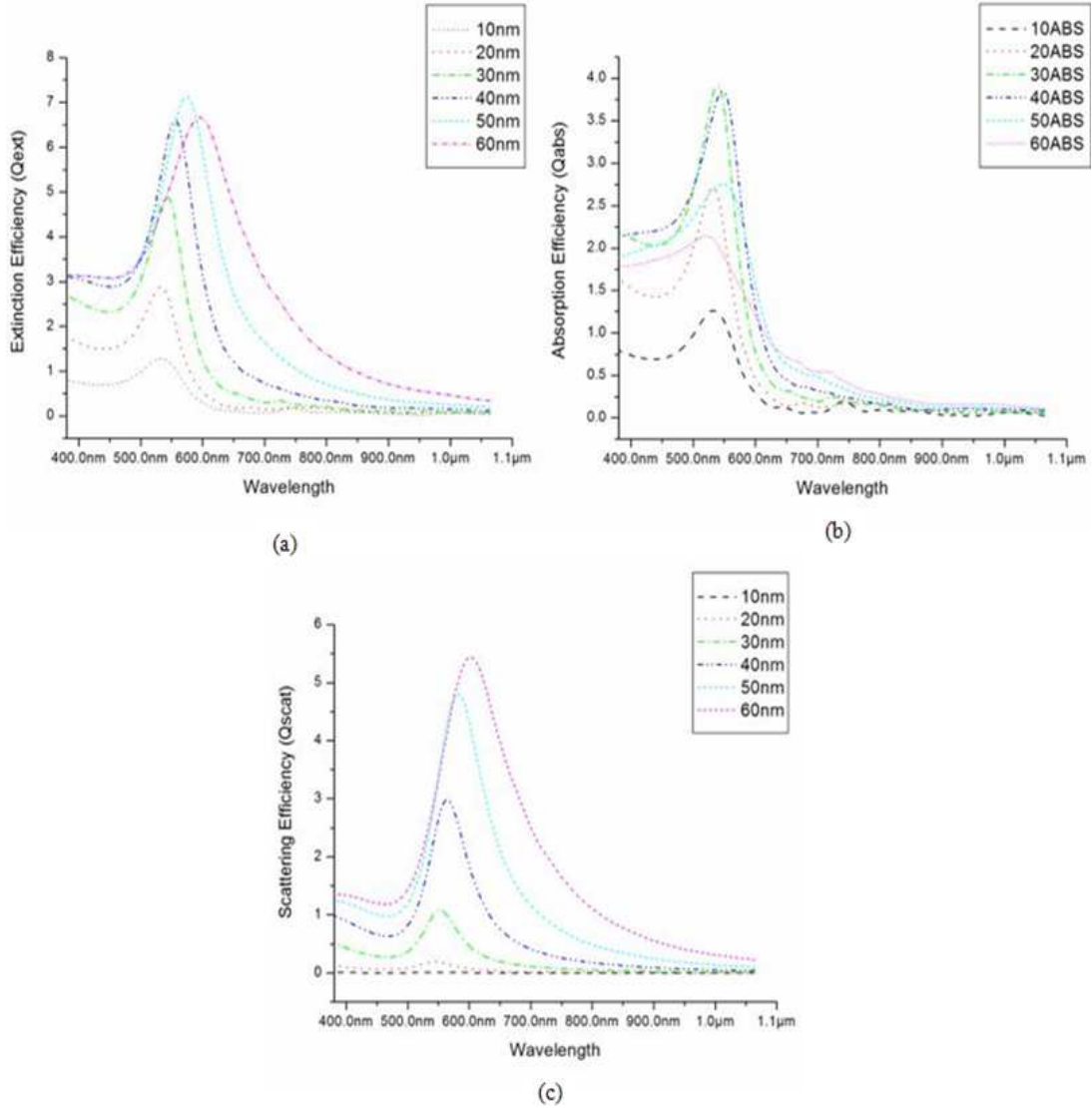


Figure 5.14 Optical efficiencies of gold nanospheres; a) Extinction, b) Absorption, c) Scattering

Peak extinction wavelengths (λ_{\max}), peak absorption efficiency (Q_{abs}) and its corresponding wavelength (λ_{abs}), peak scattering efficiency (Q_{scat}) and its corresponding wavelength (λ_{scat}), absorption to scattering ratio at λ_{abs} and scattering to absorption ratio at λ_{scat} were also computed as given in Table 6.

Dimension	λ_{ext}	Qabs (λ_{abs})	Qscat (λ_{scat})	Qabs/ Qscat @ λ_{abs}	Qscat/ Qabs @ λ_{scat}
r=10nm	532.8nm	1.26 (531.60nm)	0.01 (550.20nm)	126.38	0.01
r=20nm	532.8nm	2.71 (531.60nm)	0.19 (545.12nm)	15.06	0.08
r=30nm	541.36nm	3.91 (538.89nm)	1.08 (552.78nm)	4.07	0.31
r=40nm	555.38nm	3.85 (547.65nm)	2.99 (564.69nm)	1.51	0.89
r=50nm	574.32nm	2.75 (547.65nm)	4.80 (582.83nm)	0.84	2.22
r=60nm	594.59nm	2.14 (521.03nm)	5.44 (602.18nm)	1.08	4.61

Table 6 Calculated peak optical efficiencies Qabs, Qscat and corresponding wavelengths λ_{ext} , λ_{abs} , λ_{scat} , absorption to scattering ratio at λ_{abs} and scattering to absorption ratio at λ_{scat} for nanospheres

From Figure 5.14 and Table 6, the findings revealed that the extinction efficiency for nanospheres improved with an increase in the nanoparticle size. The results obtained exhibited similar trends with those reported in experiments (Link, Mohamed et al. 1999, Link and El-Sayed 2000). This reflected the direct dependence of the nanosphere extinction cross-section with respect to the nanosphere volume as detailed in Mie theory. A red-shift in the extinction peak with an increase in the radius of the nanosphere can also be found in Figure 5.14. Besides that, an increase in the relative contribution of scattering to the total extinction spectra was observed with an increase in the particle size. These nanospheres were therefore more suited for scattering based optical modalities.

However, as the particle size further increased, the extinction peak decreased with a broadening of the peak due to an increase in radiative damping for the larger particle. If the particle size is further increased, higher order modes in the field expansion will become more significant which can result in quadrupole or higher multipole resonances thereby inhibiting the tunability properties of the nanoparticle.

5.2.2.2 Core/Shell Nanoparticle

FDTD computation models were developed for two types of core/shell nanoparticles; one having silica core and gold shell and the other with gold core and silica shell. Calculation of the optical efficiencies for two different dimensions ($R_1=20$, $R_2=50$ and $R_1=30$, $R_2=50$) of silica-gold nanoshells are shown in Figure 5.15 a and Figure 5.15 b respectively.

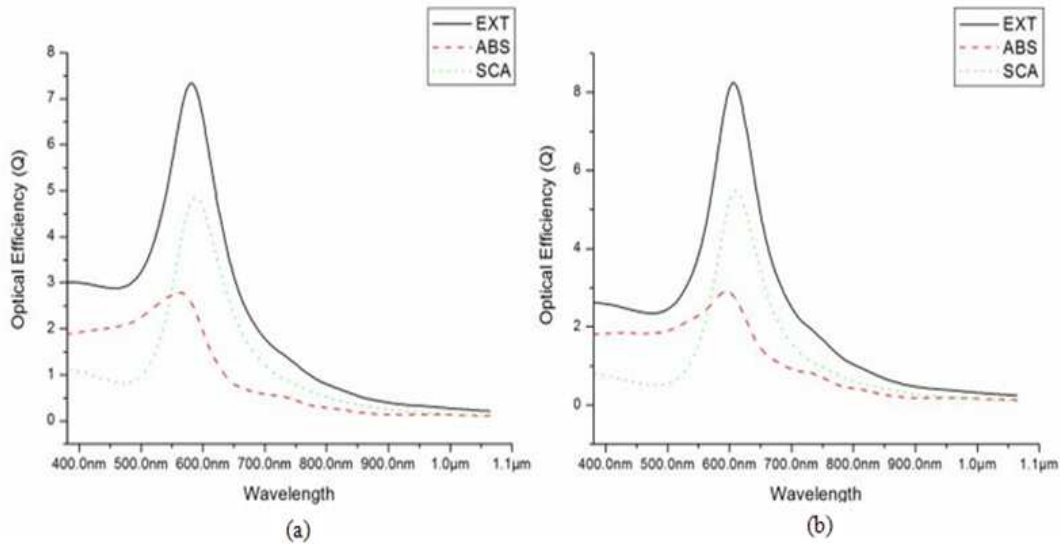


Figure 5.15 Optical efficiencies of core-shell (Silica core- Gold Shell) nanoparticles radius; a) $R_1=20$ and $R_2=50$, b) $R_1=30$ and $R_2=50$

Figure 5.15 shows that the core-shell ratio of the nanoshells controls the position of the SPR. From the simulation results, it was evident that the extinction peak red-shifts from visible to near-infrared region in relation to changes in the core radius

to shell radius (R1 to R2) ratio for a constant total nanoparticle size (which is the shell size R2). In other words, the extinction peak red-shifts when the shell thickness was reduced. This is attributed to the increased coupling between surface plasmons of gold shell with silica core which resulted in a change in the effective dielectric constant of silica. This facilitates the usage of these nanoparticles in the near-infrared optical window where optical absorption is minimal and favourable for optimal light penetration. Optical efficiencies shown in Figure 5.15 also exhibited an increase in the extinction peak when the shell thickness was reduced. This showed that a decrease in the core-shell ratio can be effectively used to tailor the scattering properties of the nanoparticle as in Figure 5.15, where the configuration R1=30nm R2=50nm exhibited higher scattering when compared to R1=20nm R2=50nm. The increase in extinction peaks with the thinning of shell layer was due to the increase in polarization at the sphere boundary. The nanoshell also exhibited optical efficiencies that were comparable or even larger in magnitude when compared to solid nanospheres thus making it more favourable for various biomedical imaging applications.

Table 7 shows λ_{\max} , Q_{abs} with its corresponding λ_{abs} , Q_{scat} with its corresponding λ_{scat} , absorption to scattering ratio at λ_{abs} and scattering to absorption ratio at λ_{scat} for R1=20, R2=50, R1=20, R2=60 and R1=30, R2=50, R1=30, R2=60. From Table 7, it was found that an increase in the total nanoparticle size (R2) alone resulted in little red-shift exhibiting lower absorption and higher scattering properties.

Dimension	λ_{ext}	Q_{abs} (λ_{abs})	Q_{scat} (λ_{scat})	$Q_{abs}/$ Q_{scat} @ λ_{abs}	$Q_{scat}/$ Q_{abs} @ λ_{scat}
R1=20nm R2=50nm	582.00nm	2.79 (562.00nm)	4.86 (588.00nm)	0.750	2.07
R1=30nm R2=50nm	607.00nm	2.91 (596.00nm)	5.49 (610.00nm)	0.59	2.03
R1=20nm R2=60nm	597.00nm	2.14 (524.00nm)	5.40 (605.00nm)	1.13	4.43
R1=30nm R2=60nm	609.00nm	2.11 (528.00nm)	5.59 (616.00nm)	1.34	4.27

Table 7 Calculated peak optical efficiencies Q_{abs} , Q_{scat} and corresponding wavelengths λ_{ext} , λ_{abs} , λ_{scat} , absorption to scattering ratio at λ_{abs} and scattering to absorption ratio at λ_{scat} for Silica core – Gold shell nanoparticles

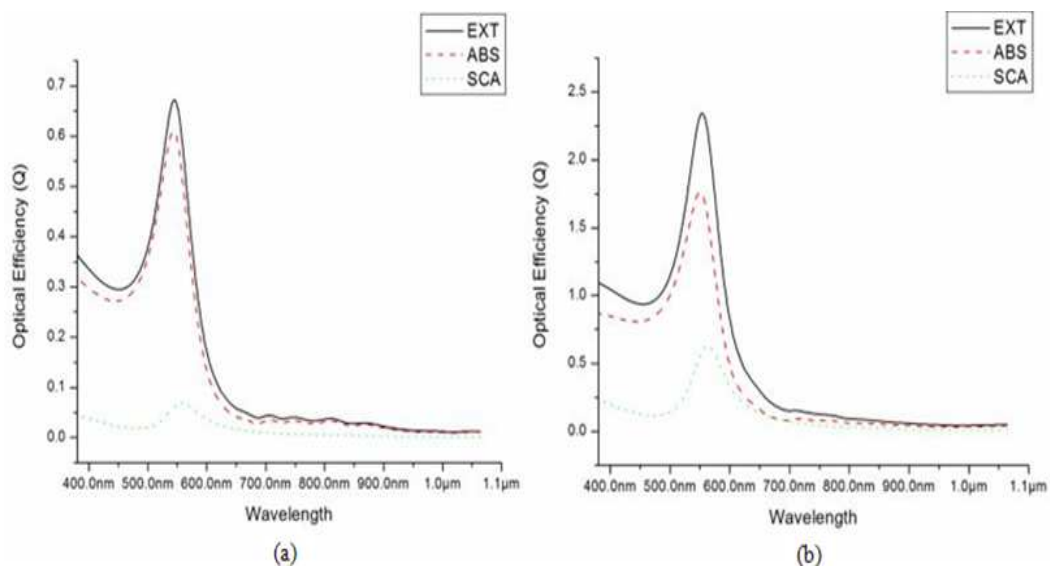


Figure 5.16 Optical efficiencies of core-shell (Gold core- Silica Shell) nanoparticles: a) R1=20 and R2=50, b) R1=30 and R2=50

Figure 5.16 and Table 8 show that when the thickness of the silica shell was decreased, the intensity of the extinction peak increased with a red-shift in the SPR peak due to increased coupling between surface plasmons of gold core with silica

shell. This resulted in a change in the effective dielectric constant of silica as well as leading more plasmons to be trapped within the silica shell. However, the magnitude of the shift was much smaller than the equivalent gold shell-silica core particle due to the reduced interactions of gold plasmons with the surrounding medium. The magnitude of the optical efficiencies was also significantly lower than the silica-gold nanoshells and the solid nanospheres.

Dimension	λ_{ext}	Q_{abs} (λ_{abs})	Q_{scat} (λ_{scat})	$Q_{\text{abs}}/$ Q_{scat} @ λ_{abs}	$Q_{\text{scat}}/$ Q_{abs} @ λ_{scat}
R1=20nm R2=50nm	543.99nm	0.61 (543.99nm)	0.07 (557.35nm)	9.96	0.13
R1=30nm R2=50nm	553.00nm	1.76 (550.00nm)	0.63 (563.00nm)	3.16	0.39
R1=20nm R2=60nm	546.00nm	0.44 (544.00nm)	0.06 (558.00nm)	8.42	0.16
R1=30nm R2=60nm	556.00nm	1.28 (552.00nm)	0.50 (565.00nm)	2.93	0.44

Table 8 Calculated peak optical efficiencies Q_{abs} , Q_{scat} and corresponding wavelengths λ_{ext} , λ_{abs} , λ_{scat} , absorption to scattering ratio at λ_{abs} and scattering to absorption ratio at λ_{scat} for Gold core – Silica shell nanoparticles

Computations were further extended towards determining the trends in optical properties of the rod shaped gold nanoparticles with varying dimensions. As discussed earlier, gold nanorods offered excellent tuning capabilities for the SPR wavelength by tailoring the aspect ratio. Results, shown in Figure 5.17, affirm that the red shift of SPR peak in gold nanorods with an increase in the aspect ratio by

altering the width of the nanorod. The peak optical efficiencies and corresponding wavelengths are shown in Table 9.

Dimension	λ_{ext}	Q_{abs} (λ_{abs})	Q_{scat} (λ_{scat})	$Q_{\text{abs}}/$ Q_{scat} @ λ_{abs}	$Q_{\text{scat}}/$ Q_{abs} @ λ_{scat}
AR=2.26 Reff = 13.10	633.00nm	24.00 (633.00nm)	1.18 (634.00nm)	20.33	0.049
AR=3.1 Reff = 14.25	721.00nm	45.10 (721.00nm)	3.33 (721.00nm)	13.54	0.07
AR=3.4 Reff = 14.62	756.00nm	60.10 (756.00nm)	5.55 (756.00nm)	10.82	0.09
AR=3.6 Reff = 14.85	778.00nm	68.20 (778.00nm)	6.87 (776.00nm)	9.92	0.10
AR=3.9 Reff = 15.19	810.00nm	78.50 (810.00nm)	8.44 (810.00nm)	9.30	0.10
AR=4.1 Reff = 15.41	833.00nm	85.90 (833.00nm)	9.63 (833.00nm)	8.92	0.11
AR=4.3 Reff = 15.62	854.00nm	92.10 (854.00nm)	10.60 (852.00nm)	8.68	0.11

Table 9 Calculated peak optical efficiencies Q_{abs} , Q_{scat} and corresponding wavelengths λ_{ext} , λ_{abs} , λ_{scat} , absorption to scattering ratio at λ_{abs} and scattering to absorption ratio at λ_{scat} for nanorods

It was observed that the total extinction spectrum of the gold nanorods not only depends on the wavelength of the incident light, but also on the aspect ratio

and the effective radii (R_{eff}), where $R_{\text{eff}} = (3V/4\pi)^{1/3}$ for nanorod with volume ‘V’. Figure 5.17 shows that as the width of the nanorod increases (hence R_{eff}), the line width of the SPR peak broadens due to the increased radiative damping associated with the larger volume of the nanoparticle.

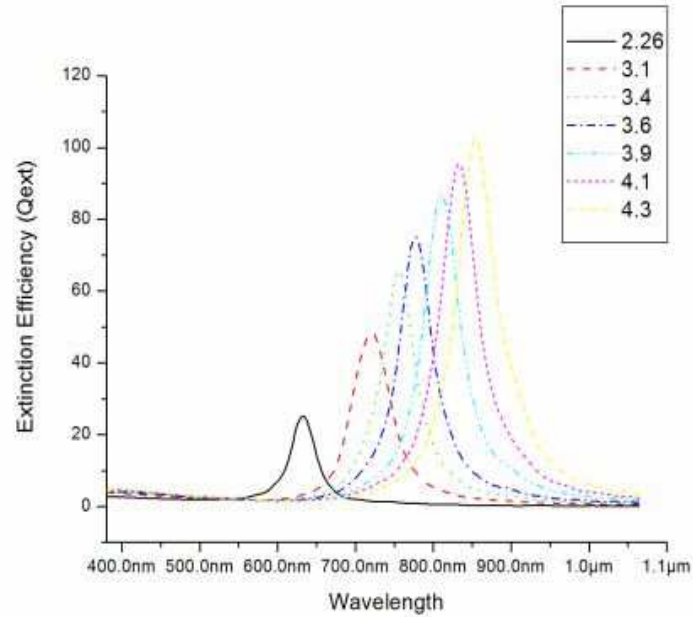


Figure 5.17 Extinction efficiencies of gold nanorods with varying aspect ratios

Figure 5.18 shows the absorption and scattering efficiencies of the gold nanorods with varying aspect ratios where enhancements in their optical properties were also observed. This phenomenon can be explained from the effective radius of the particle where a higher effective radius results in higher levels of optical scattering and absorption. A more detailed study to validate this phenomenon will be illustrated in section 5.2.2.3. It is noteworthy that the absorption scales of the nanorods are much higher compared to its spherical counter parts. Great tunability towards near-infrared range can also be achieved by precisely varying the aspect ratio of the nanorod.

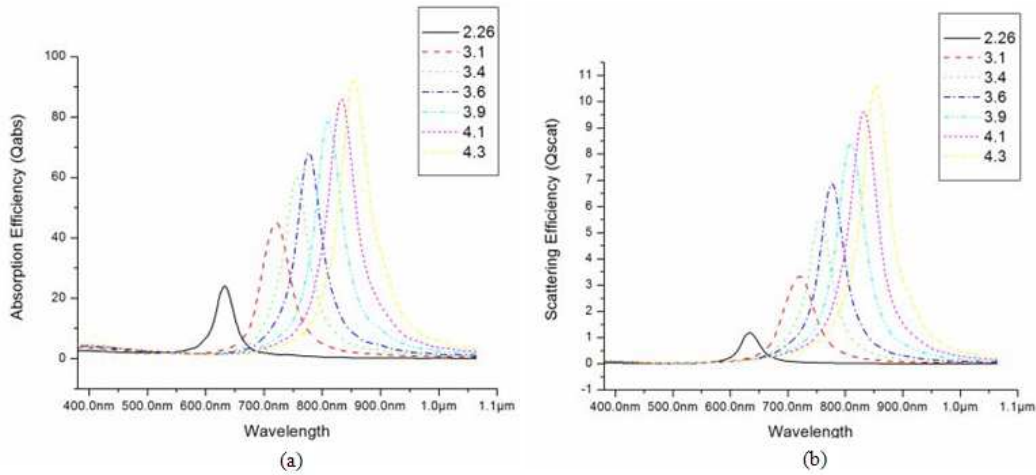


Figure 5.18 Optical efficiencies of gold nanorod with varying aspect ratios:
(a) Absorption, (b) Scattering

An increase in the optical efficiencies towards higher aspect ratios is attributed to the increased size (R_{eff}) of the nanorod. This would be explained in the ensuing section. When compared to nanospheres, the scattering quantum yield of the nanorod which is the ratio of scattering efficiency (Q_{scat}) to the total extinction efficiency (Q_{ext}) at the resonance maxima was found to increase dramatically as aspect ratio increases. This might be due to the significant reduction of plasmon dephasing in nanorods when compared to nanospheres.

5.2.2.3 Dependence of optical efficiencies on nanorod size

Investigations were further carried out to determine the dependence of the nanorod volume-size ratio on the optical efficiencies by varying the length and width (hence effective radius) at a fixed aspect ratio of 2.26. Figure 5.19 shows the absorption and scattering efficiencies of the gold nanorods with an aspect ratio of 2.26 and varying R_{eff} . The results showed an increasing trend for both absorption and scattering efficiencies with an increase in the R_{eff} .

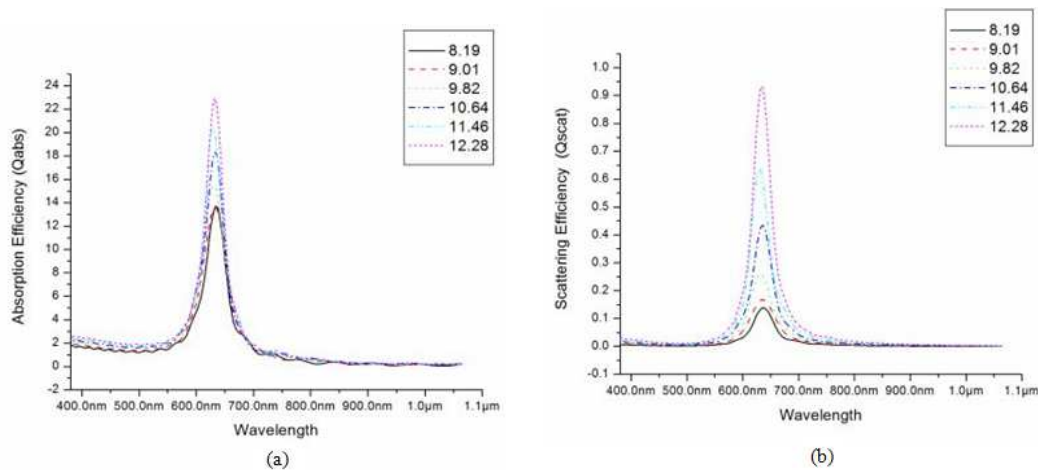


Figure 5.19 Optical efficiencies of gold nanorod with aspect ratio $R = 2.26$ and varying Effective Radius: (a) Absorption, (b) Scattering

The results obtained highlight that when compared to nanospheres and core-shell nanoparticles, gold nanorods offered excellent optical absorption properties that are well suited for optical absorption based photothermal/photoacoustic applications. The suggested approach for its usage in a particular photoacoustic investigation would be to determine the nanorod aspect ratio that offers maximum SPR/extinction value at the preferred diagnostic or therapeutic wavelength. The value can then be used to determine the optimum size (R_{eff}) of the nanoparticle for the specific biomedical application. In this perspective, this research also involved experimental investigations towards exploring the tunability of gold nanorods and their photoacoustic signal generation. The following section details the various works performed towards this direction.

5.3 Investigations into Selective Photoacoustic Signal Generation for Multiple Targeting Using Plasmonic Nanoparticles

Comparison of the molar extinction coefficients for plasmonic nanoparticles with other contrast enhancement tools such as organic dyes shows that plasmonic

nanoparticles exhibit higher absorption cross-sections when compared to organic dyes. Further, gold nanorods exhibit excellent absorption properties due to their higher absorption cross-section. Gold nanorods also offer excellent spectral tunability for its usage across a wide range of excitation wavelengths. Therefore, the NIR spectral response of gold nanorods together with their higher absorption cross-section makes them the most preferred choice for photoacoustic imaging and sensing for biological applications. The geometry of the nanorods induces narrow plasmon resonance bands leading to specific absorption spectral bands and this phenomenon can be effectively used for selective photoacoustic signal excitation. In this context, theoretical and experimental investigations were performed to demonstrate the selective photoacoustic signal excitation from nanorods with varying aspect ratios. FDTD simulations were initially carried out to determine the exact dimensions and aspect ratios for each of the nanorods and the respective methodologies are detailed in the following sub-sections.

5.3.1 FDTD Simulations for Selective Photoacoustic Signal Generation and Multiple Targeting

FDTD simulations were performed to determine the optical properties of gold nanorods with four different aspect ratios. The dimensions of each gold nanorod and their corresponding aspect ratios are given in Table 10. Table 11 and Figure 5.20 show that extinction peaks of FDTD simulation was having comparable agreement with the theoretical predicted values (Huang, Neretina et al. 2009). The FDTD simulation results were also in close agreement with the experimentally observed values as given in section 5.3.2.

Nanorod Type	Height (nm)	Width (nm)	Aspect Ratio
1	64	45	1.42
2	94	22	4.27
3	166	25	6.64
4	67	10	6.7

Table 10 Dimensions and aspect ratios of gold nanorods

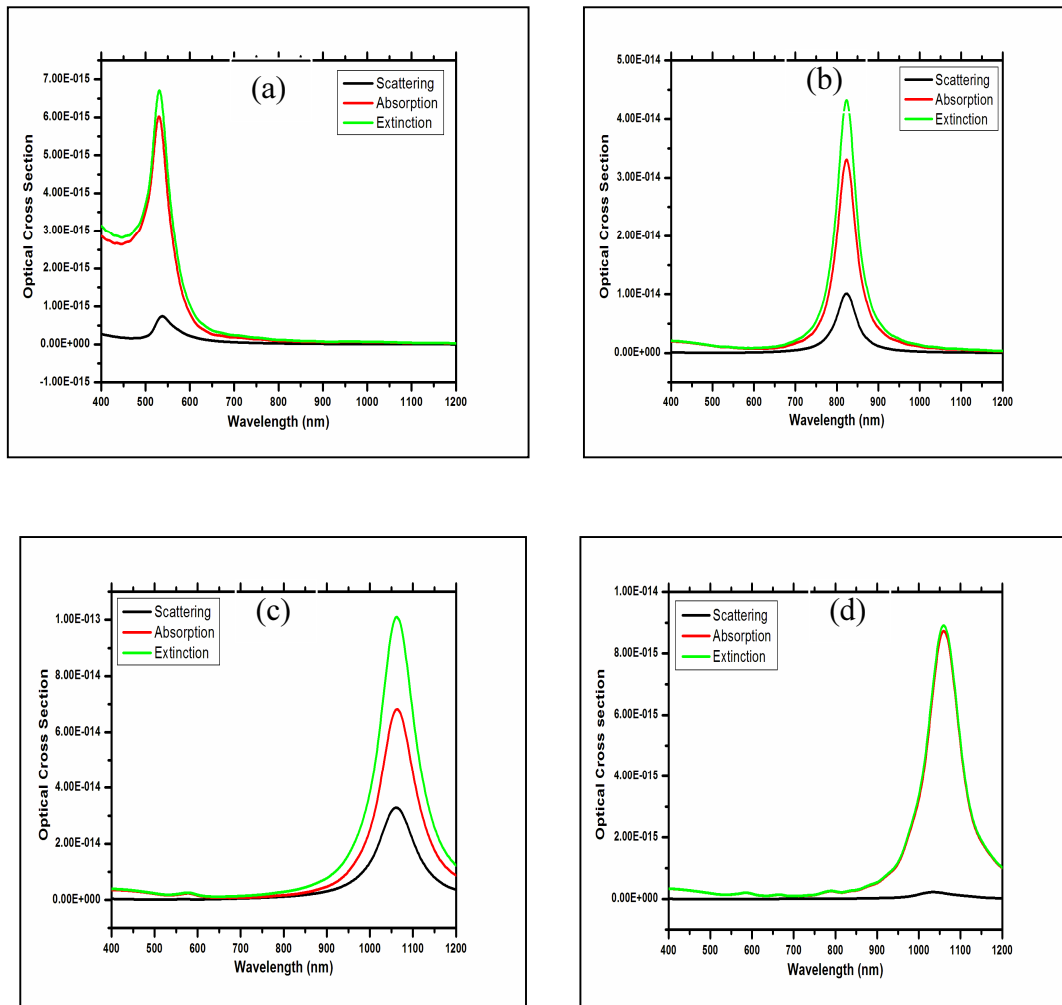


Figure 5.20 Optical cross-sections of gold nanorods determined from FDTD simulations; a) Type 1, b) Type 2, c) Type 3, d) Type 4

Nanorod Type	Height (nm)	Width (nm)	Aspect Ratio	FDTD SPR Peak (nm)	Theoretical SPR Peak (nm)
1	64	45	1.42	530.12	554.9
2	94	22	4.27	824.14	825.65
3	166	25	6.64	1060.76	1050.8
4	67	10	6.7	1062.85	1056.5

Table 11 SPR peaks wavelength of gold nanorods determined from FDTD simulations

Since the theoretical estimation of SPR peak was primarily devised for rod shaped particles, type 1 nanorods which were close to spheroids exhibited the highest degree for variation from the theoretically predicted SPR peak. Simulation results also showed that nanorods exhibited excellent absorption cross-sections which make them highly favourable for photoacoustic applications. Further, analysis of Figure 5.20 showed that the extinction peaks of the four different nanorods were highly dependent on the effective radius or volume of the nanoparticle. Although type 3 and type 4 nanorods had similar aspect ratios, type 3 nanorod exhibited much higher extinction cross-section due to its higher volume and effective radius. Hence, higher photoacoustic signals were expected from type 3 nanorods. Similar trends were also predicted for experimental photoacoustic signals under similar fluence conditions.

5.3.2 Experimental Investigations into Selective Photoacoustic Signal Generation and Multiple Targeting

FDTD simulations showed that the optical absorption cross-section is highly dependent on the volume or effective radius of the nanorod. A corresponding

dependency of the photoacoustic signal amplitude with the optical absorption cross-section was therefore expected. Gold nanorods were custom ordered from Nanopartz™ Inc., USA according to the dimensions used in the FDTD simulations. The cetyl trimethylammonium bromide (CTAB) capped nanorods were initially resuspended by five minutes of sonification followed by a two minute vortex. The transmission electron microscope (TEM) images of the nanorods illustrated in Figure 5.21 show that the nanorods exhibited excellent size uniformity. However, a $\pm 9\%$ size variation was observed with type 4 nanoparticles.

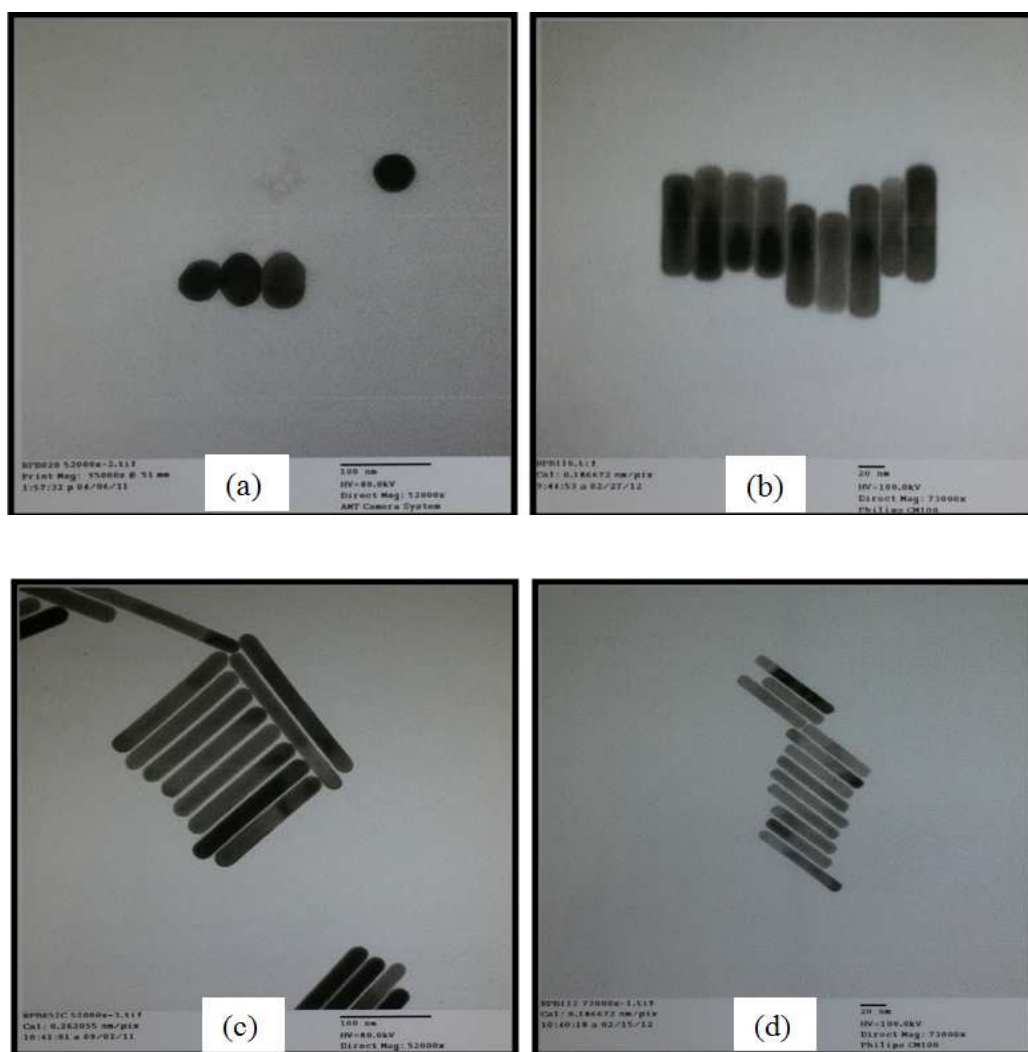


Figure 5.21 TEM images of gold nanorods; a) Type 1, b) Type 2, c) Type3, d) Type 4

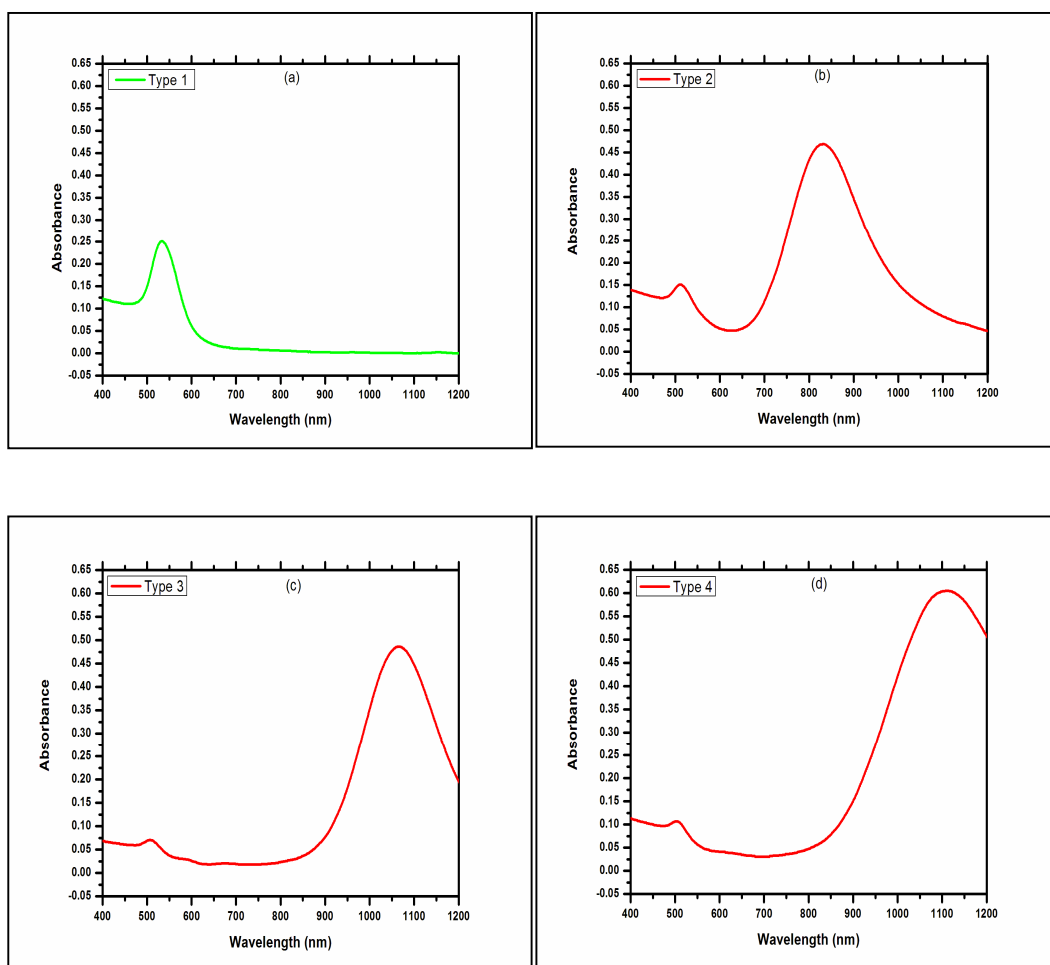


Figure 5.22 UV-VIS absorption spectrum of gold nanorod solution; a) Type 1, b) Type 2, c) Type 3, d) Type 4

Further, in order to maintain same particle concentrations, the nanorod solutions were prepared with similar optical densities. The absorption spectrum of the optimized nanorod solutions are given in Figure 5.22. UV-Vis absorption measurements, illustrated in Figure 5.22, show that gold nanorod solutions exhibited comparable similarities in their optical densities. However, due to its lower concentrations, type 1 nanorod exhibited lesser optical density when compared to others. Similar trend showing lower photoacoustic signal amplitude was therefore predicted from photoacoustic experiments under similar fluence conditions. Further, comparison of the absorption trends between FDTD

simulations and experimental investigations showed similar spectral responses. The simulation results augured well with the experimental results obtained. A deviation in the absorption trend can be observed in Table 12 for type 4 nanorod due to their $\pm 9\%$ size variations induced during the synthesis.

Nanorod Type	Height (nm)	Width (nm)	Aspect Ratio	Absorption Peak from FDTD Simulations (nm)	Absorption peak from UV- VIS Measurements (nm)
1	64	45	1.42	530.12	532
2	94	22	4.27	824.14	827
3	166	25	6.64	1060.76	1064
4	67	10	6.7	1062.85	1107

Table 12 Absorption peaks of gold nanorods from FDTD simulation and UV-VIS absorption measurements

Further, experimental investigations were performed to determine the photoacoustic response of gold nanorods under similar fluence conditions as detailed in the following sub section.

5.3.2.1 *Implementation of single element high frequency photoacoustic system*

The proposed experimental set-up for single element high frequency photoacoustic studies is shown in Figure 5.23. The nanosecond pulses are the most widely used optical excitation sources and single or multi-element piezoelectric transducers are preferred detectors in PA signal detection. An Nd:YAG laser pumped optical parametric oscillator (OPO) based tunable nanosecond pulsed laser

was used to irradiate the sample from the top and the corresponding photoacoustic signals were detected using the spherically focused immersion transducer (V327, Olympus Corp.) positioned along the surface of the cuvette. The transducer operated at center frequency (-6 dB, average) of 9.65 MHz having a -6 dB fractional bandwidth of 57.73% and element size of 9.525 mm.

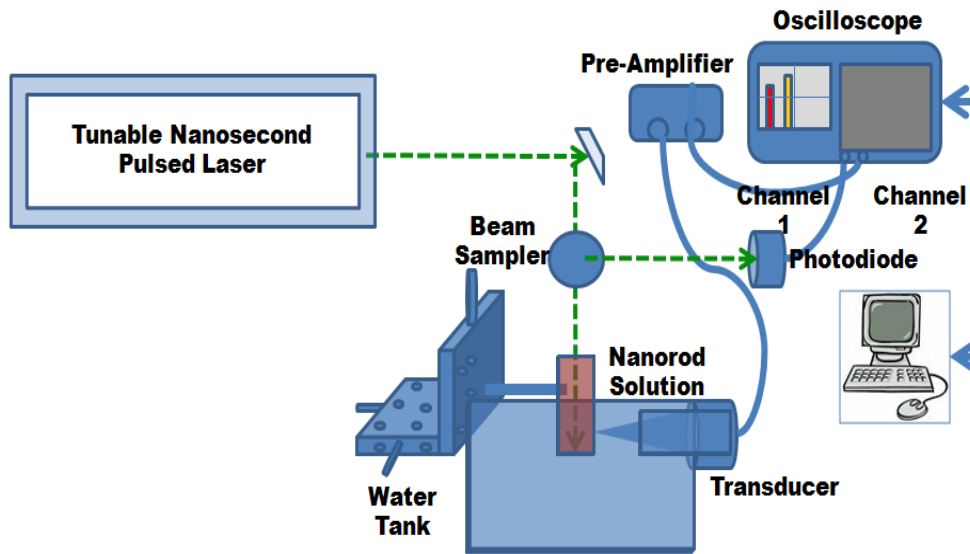


Figure 5.23 Experimental set-up of the proposed single element high frequency photoacoustic system

The cuvette was positioned 19.75 mm away from the transducer surface, which was within the focal length of the transducer. The excitation beam and the ultrasound transducer was positioned perpendicular to each other with the center of the laser beam directing within the focal length of the transducer. The detected photoacoustic signals were amplified by 40 dB using an ultrasonic preamplifier (5678 preamp, Olympus Corp.) prior to its acquisition by the oscilloscope (TDS 3054, Tektronix, Inc.). The beam sampler sampled 5% of the input beam into the photodiode which acted as the trigger source for the photoacoustic system. The photodiode recorded the laser energy fluctuations and its values were used to

compensate the effect of laser energy fluctuations in the photoacoustic signal. The gold nanorod solutions were irradiated with their peak absorption wavelengths (Figure 5.22) under similar fluence conditions and the results obtained are shown in Figure 5.24.

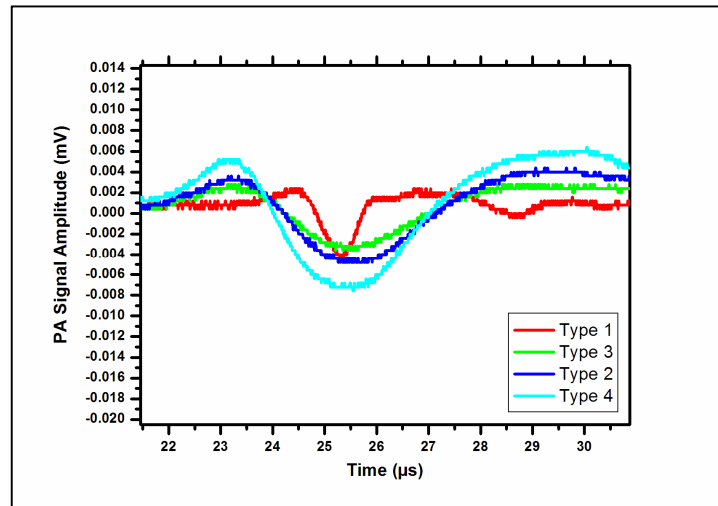


Figure 5.24 Photoacoustic signal amplitude of gold nanorod solution

Figure 5.24 shows the amplitude of the photoacoustic signals obtained from the four types of gold nanorod solutions under similar fluence conditions. As predicted in the previous section, the amplitudes of the photoacoustic signals were directly proportional to absorbance of the sample. As expected from the absorbance measurements performed in section 5.3.2, type 4 exhibited the highest photoacoustic signal amplitude and similar trends were observed with three other types of nanorod solution. This concept can be effectively used for performing multiple molecular targeting in tissues wherein nanorods with distinct SPR peaks can be selectively bio-conjugated and excited to detect specific bio-molecular constituents inside the tissue. Further, the photoacoustic investigations were extended towards realizing high resolution photoacoustic images from phantom tissue as detailed in the following section.

5.4 Investigations into Photoacoustic Imaging using Multi-element Transducers

This section details the various experimental investigations performed to realize the envisaged photoacoustic imaging system. The proposed experimental system comprises of Nd:YAG laser pumped optical parametric oscillator (OPO) based tunable nanosecond pulsed laser and a multi-element linear array ultrasound probe with the associated electronics for synchronization, data acquisition, image reconstruction and image display. Absorbing centers made out of two distinct absorbing dyes and gold nanorods were simulated across different depths of the silicone based phantom tissue. Experimental results from the photoacoustic imaging system were used to map and locate the photoabsorbers located at different depths.

5.5 Photoacoustic Imaging of Optical Absorbers

Photoacoustic imaging involved the reconstruction of optical absorbing centers based on the time-resolved detection of acoustic waves generated in tissue through optical energy absorption. The generated PA signals were detected in analogous with the signal detection and post processing routines performed in a conventional ultrasound imaging system. Hence, the hardware platform used for ultrasound imaging was extended and configured to be used for photoacoustic imaging. However, photoacoustic signals were generated from all parts of the tissue where adequate optical energy was available. Further, the photoacoustic signals were broadband signals arising from multi-sized absorbers. Most of the

reception and post processing techniques involve in photoacoustic imaging were therefore quite different from that of conventional ultrasound imaging. The following section details the experimental set-up and the various investigations carried out to realize the photoacoustic imaging system based on a conventional ultrasound imaging hardware.

5.5.1 Configuration of the Photoacoustic Imaging System

Ultrasound and photoacoustic imaging share almost similar physics and instrumentation concepts at the receiver end. Hence, the proposed photoacoustic imaging set-up involved the usage of the ultrasound imaging hardware described in section 4.2. However, additional firmware capabilities were also incorporated into the basic ultrasound system as shown in Figure 5.25.

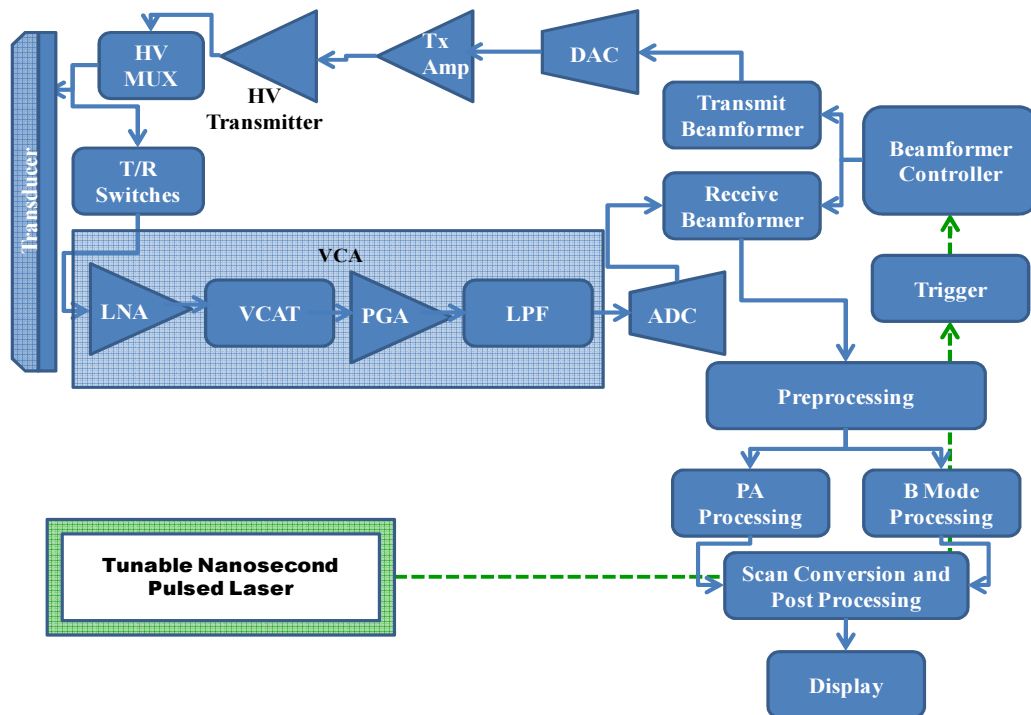


Figure 5.25 Block diagram of the proposed photoacoustic imaging system

The ultrasound system was equipped with a programmable trigger module to integrate and synchronize the pulsed laser of the photoacoustic imaging system. The laser pulses generated photoacoustic signals from the optical absorption centres located in the samples. The generated photoacoustic signals propagated uniformly across the sample and the multi-element transducer coupled with sample acquired the resultant photoacoustic signals with the same theoretical and instrumentation concepts used in the ultrasound imaging system.

The received raw RF data was further subjected to the post processing routines described in section 4.2.1 to form the photoacoustic images. The schematic of the experimental photoacoustic imaging system based on the transmission mode is shown in Figure 5.26. Since the envisaged photoacoustic system was operated with acoustic resolution, the spatial resolution capabilities were solely determined by the ultrasound transducer parameters which were given as $345 \pm 2.53 \mu\text{m}$ across in-plane and $151 \pm 2.24 \mu\text{m}$ along the axial plane.

An Nd:YAG laser pumped optical parametric oscillator (OPO) based tunable nanosecond pulsed laser (Vibrant 355 II, Opotek Inc., USA) operating between 410 nm - 720 nm and emitting 5 ns pulses at a repetition rate of 10 Hz was used as the photoacoustic excitation source. The laser beam was focused on to the surface of the sample using a microscope objective lens (UMPlanFl 5X, Olympus Japan). A variable aperture fixed along the optical path tuned the laser beam diameter to adequately fill the pupil diameter of the objective lens. The trigger signal was tapped from the Q-switch synchro output channel of the laser control unit using a co-axial cable assembly mounted with Bayonet Neill–Concelman (BNC)

connecters at both ends. Further, the delay between the Q-switch synchro output and actual beam output was measured and tuned to the minimum using the experimental measurement set-up as shown in Figure 5.27. The measurement system comprises a beam sampler (BSF10-A, Thorlabs Inc.) that sampled a portion (5%) of the laser beam into the silicon photodiode (SM05PD1A, Thorlabs Inc.). The voltage signals from the photodiode were fed into the channel 1 of the oscilloscope (TDS 3054, Tektronix Inc.) through the co-axial cable. The Q-switch synchro out connected to the channel 2 of the oscilloscope measured the time of arrival of the Q-switch signal. The delay between the two signals (channel 1 and channel 2) was then measured. Further, the delays between the two channels were tuned to 512.34 ps by changing the Q-Switch out delay of the laser controller.

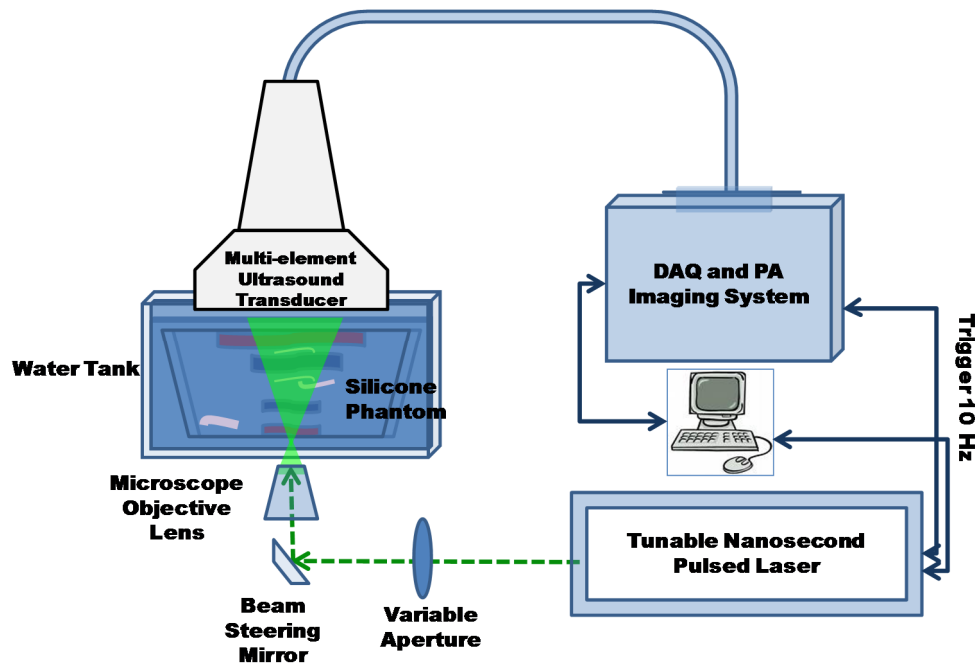


Figure 5.26 Schematic of the experimental set-up for photoacoustic imaging

The tuned Q-switch synchro output signal was then fed to the trigger input of the imaging system which was programmed to trigger the photoacoustic imaging

system. At every rising edge of the trigger, the imaging system performed photoacoustic signal acquisition and further post processing routines to form the photoacoustic images. Advanced ultrasound processing concepts such as spatial compounding and persistence were also adapted into the photoacoustic imaging.

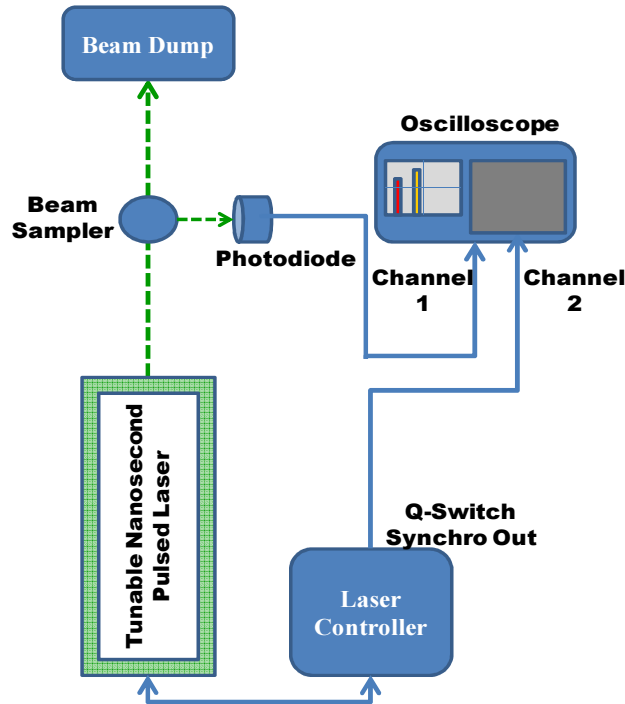


Figure 5.27 Schematic of the experimental set-up to measure timing jitter

5.5.2 Experimental Methodology

Photoacoustic imaging of the silicone phantom simulated with two distinct absorbing dyes (Figure 5.29) were performed with the proposed experimental set-up. Two optical dyes, namely; Direct Red 81 (Sigma Aldrich, Singapore) and Methylene Blue (Merck Millipore, Singapore) with distinct absorption profiles were used to simulate the absorption centers along varying depths of the phantom tissue (Figure 5.28).

The excitation wavelengths for the photoacoustic imaging procedure of the phantom were determined from the optical absorbance spectrum of the two dyes measured using a UV-VIS-NIR spectrophotometer (UV-3101 PC NIR, Shimadzu Corp.). The absorbance measurements, given in Figure 5.29, show that the dyes had very distinct absorbance spectrums. Direct Red 81 had maximum absorbance in 500 nm - 525 nm wavelength range and Methylene Blue had maximum absorbance around 650 nm - 680 nm. The concentrations of both these dyes were tuned to obtain similar optical densities as shown in Figure 5.29.

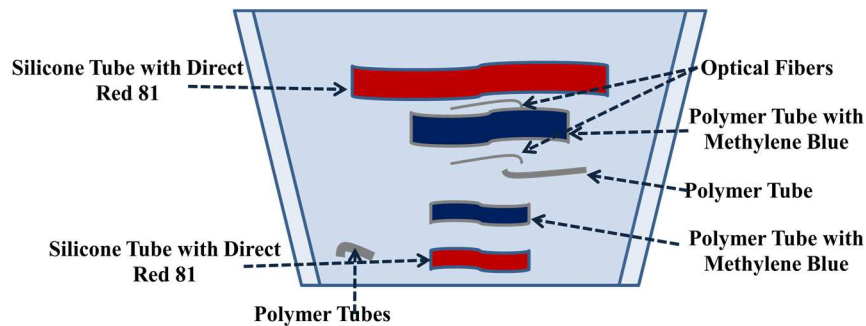


Figure 5.28 Schematic of the silicone phantom with absorbing centers

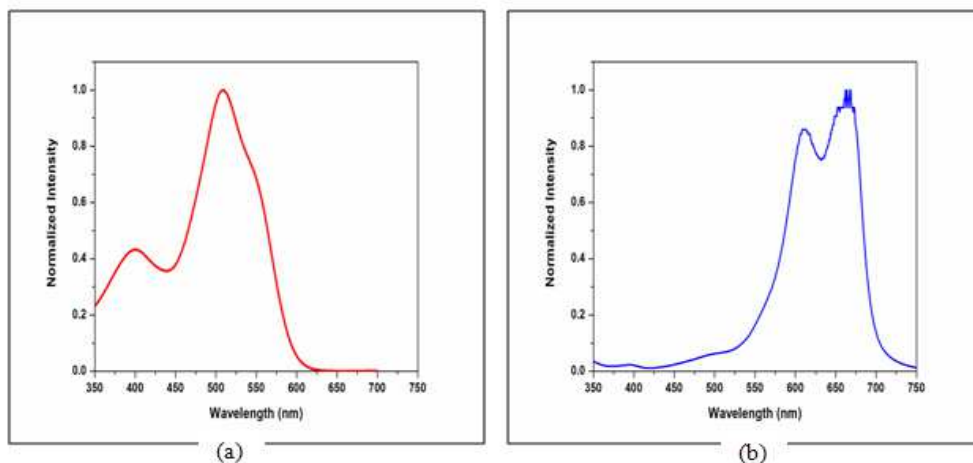


Figure 5.29 Absorption spectra of the absorbing dyes: a) Direct Red 81, b) Methylene Blue

According to the theoretical concepts described in section 5.1, photoacoustic signals are most effectively generated by illuminating the sample with the respective peak absorbance wavelengths. Therefore, photoacoustic imaging experiments were initially designed to map the absorbing centres simulated with the two different dyes. An input laser wavelength of 519 nm was used to image features simulated with Direct Red 81 and input wavelength of 670 nm was used to image the structures made with Methylene Blue. However, initial investigations showed that the laser output energy in 630 nm - 710 nm wavelength ranges did not offer sufficient fluence to generate comparable photoacoustic signals from depths. Therefore, an input wavelength of 570 nm was employed to map the absorbing centers made out of Methylene Blue.

5.5.3 Results and Discussion

Experiments were performed at 519 nm to image the absorbing centers made out of Direct Red 81. According to equation 5.6, the intensity of the photoacoustic signal has a linear relationship to the incident fluence. Therefore, two distinct fluence levels were used to demonstrate the effect of fluence in photoacoustic imaging. The phantom was initially exposed to laser energy of approximately 3 mJ/cm² to excite the photoacoustic signals from the absorbing centers made with Direct Red 81. The resultant image (Figure 5.30a) mapped the silicone absorbing center made with Direct Red 81 located just below the surface of the phantom tissue.

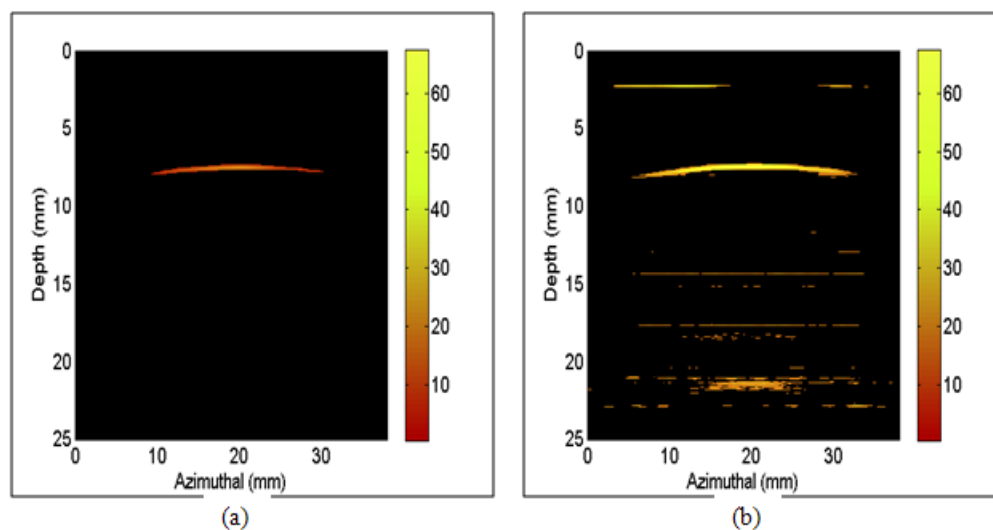


Figure 5.30 Photoacoustic image of the phantom at varying fluence: a) 3 mJ/cm^2 , b) 6 mJ/cm^2

However, the absorbing centers holding Methylene Blue were not mapped since the dye had very low absorption at 519 nm. Although the absorbing center located at the bottom of the sample was made with Direct Red 81, the image failed to map its presence. This was attributed due to the lower fluence available at this depth. However, doubling the fluence resulted in an increase in the photoacoustic signal intensity as shown in Figure 5.30b. From Figure 5.30, the intensity maps clearly showed the difference in the photoacoustic signal intensity at varying fluence levels. Further, the increased fluence level resulted in the generation of satisfactory photoacoustic signals from the absorbing center located at the bottom of the sample as shown in Figure 5.30b.

Experiments were further extended towards imaging the absorbing centers made with Methylene Blue dye. As discussed earlier, the investigations were carried out at 570 nm. At this wavelength, both Direct Red 81 and Methylene Blue registered significant absorption levels (Figure 5.29). Therefore, these absorbing

dyes were expected to generate ample photoacoustic signals located along the depth of phantom tissue. Investigations were performed by exposing the sample surface with incident fluence around 8 mJ/cm^2 .

The experimental results in Figure 5.31 clearly showed all the simulated absorbing centers were located along the depth of the phantom tissue. Optical absorption centers made out of both Direct Red 81 and Methylene Blue dyes were clearly mapped due to adequate optical absorption at 570 nm. As shown in Figure 5.31, higher incident fluence on the top layers of the phantom resulted in the formation of more intense photoacoustic signals from the optical absorbers located along the top layers.

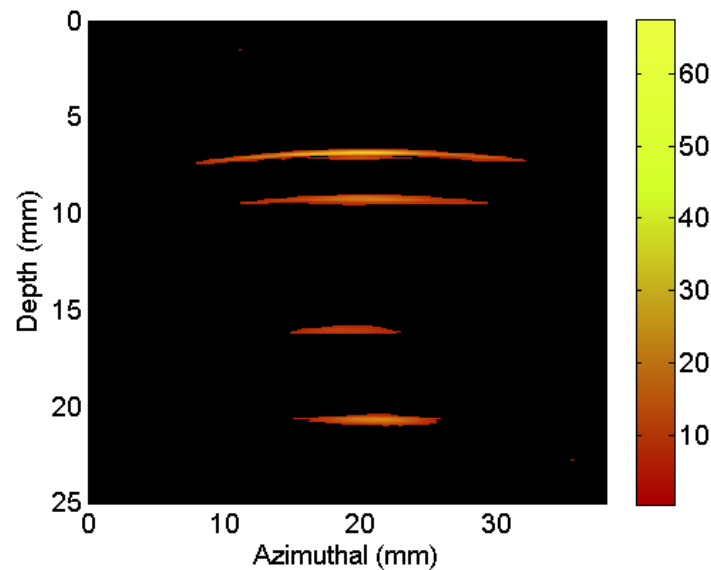


Figure 5.31 Photoacoustic imaging of the phantom tissue

The absorption studies showed that Direct Red 81 had almost double the absorbance at 570 nm when compared to Methylene Blue. The effect of this was very much evident in the photoacoustic image shown in Figure 5.31, where more

intense signals were observed from the absorbers with Direct Red 81 when compared to absorbers made out of Methylene Blue.

5.5.4 Novel Approaches to Enhance Photoacoustic Imaging with Spatial (Angle) Compounding and Persistence

A potential research area that can be contemplated as an extension to proposed photoacoustic imaging system would be to adapt the various advanced ultrasound signal processing routines into PAI. Although spatial compounding and temporal averaging technique such as persistence have been widely used in ultrasound imaging systems to reduce the effect of ultrasound speckles, no works have been reported so far in using these techniques for photoacoustic imaging. Obtaining multiple views of the same absorber from distinct angles and taking the weighted average of the sample points in two successive image frames will result in the enhancement of the imaging capabilities of a PAI system. In this context, the implementation of spatial compounding and persistence techniques (Szabó 2004) in photoacoustic imaging was performed where the specified techniques aided in the effective mapping of boundary features as well as minimizing the effect of laser energy fluctuations in PAI.

5.5.4.1 *Materials and Methods*

Spatial compounding technique involves taking multiple views of an object from different angles which gets further transformed into a composite image by obtaining the weighted sum of each of the views. A detailed theoretical description on the technique can be found in reference (Szabó 2004). Mathematically the persistence function is defined by (Li and Liu 2009)

$$ii'_k = \alpha i'_{k-1} + (1 - \alpha)i_k \quad 5 - 28$$

where $0 \leq \alpha \leq 1$ is the persistence coefficient, i'_k and i_k denotes the persisted and unprocessed pixel (sample point) of frame K , respectively. Thus, an image frame was averaged over x number of frames and the resultant frame was collected and stored in the memory. This was followed by making another identical frame made with similar excitation conditions through the same locations. The sample points in this frame were not the same if movement is present or if there were laser energy fluctuations. The frames were then averaged to form the new frame (e.g. (line 34 sample 356 + line 34 sample 356) / 2).

PAI studies were performed using silicone - intralipid based tissue mimicking phantom having a thickness of ~ 28 mm. Absorbing centers fabricated with Direct Red 81 (Sigma Aldrich, Singapore) dye were introduced along two distinct depths (5 mm and 9 mm) of the phantom tissue. Experiments were performed using the Nd:YAG laser pumped optical parametric oscillator (OPO) based tunable nanosecond pulsed laser (Vibrant II, Opotek Inc.) operated at 519 nm with a pulse repetition rate of 10 Hz and 5-7 ns pulse width as shown in Figure 5.32. The sample was irradiated from the top with an incident fluence of ~ 15 mJ/cm² on its surface. The corresponding photoacoustic signals were detected using the multi-element linear array transducer gel –coupled and mounted on the opposite side of the sample. The laser was tuned to output at 519 nm which delivered an approximate fluence of 15 mJ/cm² on the sample surface.

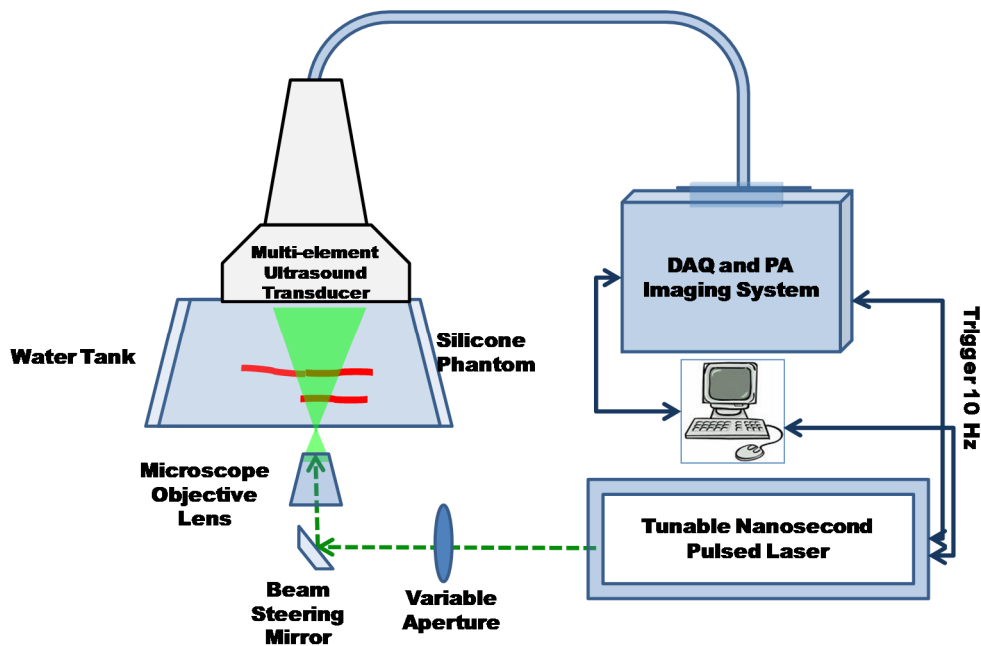


Figure 5.32 Schematic of the experimental set-up for photoacoustic imaging with spatial compounding and persistence

The imaging system was configured to support up to 9 angles (-4 to $+4$) with an angle offset up to 4 degrees and persistence of 2. The proposed experimental system supported up to 9 angles (-4 to $+4$) with an angle offset up to 4 degrees. It was observed that the current transducer specifications do not allow more than 9 angles as the side lobes induced image artefacts at more than ± 15 degrees. Therefore, an angle offset of 4 degrees was the maximum allowed value while employing all the 9 angles. A composite photoacoustic frame (b) was formed from the fusion of the corresponding sample points from 9 angles shown in Figure 5.33.

5.5.4.2 Results and Discussion

Photoacoustic imaging of the phantom tissue with the two light absorbing tubular structures located at different depths were performed at 9 different angles with an offset of 4 degrees as shown in Figure 5.33 (a-i), ranging from angle 1 to angle 9 respectively. The images illustrated in Figure 5.33 clearly showed the dynamic

steering of the receiver across the 9 angles while forming the photoacoustic images. Figure 5.33 shows that each angle mapped the same absorber differently and introduced inaccuracies and image artefacts to the photoacoustic images. However, fusion of the images from few distinct angles was expected to map the absorbers more accurately with minimum image artefacts. Investigations were further performed to fuse these images to demonstrate the effect of spatial compounding in photoacoustic imaging. Figure 5.34a and Figure 5.34b respectively show that the photoacoustic images of the phantom without and with spatial compounding.

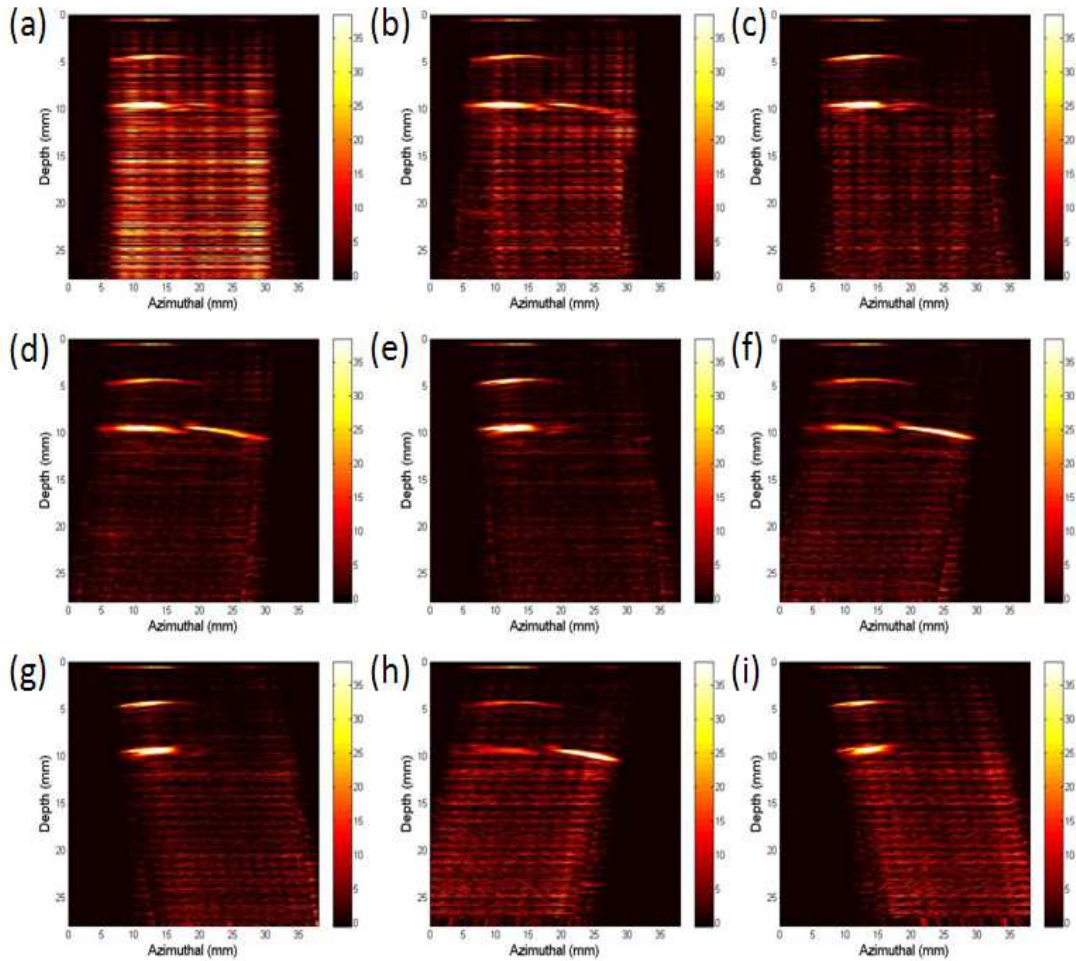


Figure 5.33 Photoacoustic Images of the Phantom at Varying Angles: a) Angle 1, b) Angle 2, c) Angle 3, d) Angle 4, e) Angle 5, f) Angle 6, g) Angle 7, g) Angle 8, i) Angle 9

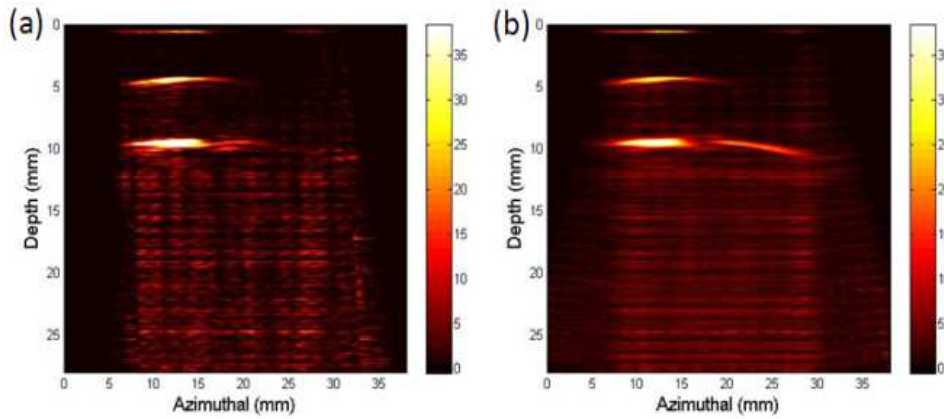


Figure 5.34 Photoacoustic images: a) Without spatial compounding, b) With spatial compounding

Figure 5.34b shows a highly precise mapping of the optical absorbers was obtained with the aid of spatial compounding technique. However, the image formed without the spatial compounding (Figure 5.34 a) failed to map the optical absorbers. Further Figure 5.34b also shows that the effect of laser energy fluctuations were minimised by using persistence in conjunction with spatial compounding.

5.6 Investigations into Photoacoustic Contrast Enhancement Mechanisms Using Novel Dual – Optical Mode Detection and Imaging Scheme

Considering the impending applications and capabilities of multi-modal imaging schemes, a potential multi-modal combination can be contemplated that can offer tremendous potential for the future. The proposed configuration would involve effectively blending the salient features of fluorescence microscopy and PAI. Such system aims to map micron or sub-micron fluorescent features from

tissue surface together with sub-millimetre optical absorption heterogeneities along the depth of the tissue. However, a reduction in the absorption cross-section of gold nanoparticles in the visible region imposes serious limitations for obtaining acceptable levels of PA signal amplitude under visible excitation. Therefore, considering the fluorescence excitation wavelengths, there is huge demand to have contrast enhancement strategies that offers enhanced optical absorption cross-sections across the visible wavelength. Although gold nanospheres and gold-silica core-shell nanoparticles exhibit absorption peaks across the visible region (Jain, Lee et al. 2006, James Joseph 2011) for augmenting PA signal generation, investigation into novel nanoplatforms with enhanced absorption cross-sections while maintaining the overall compact size is of great importance.

Towards this direction two distinct forms of novel contrast enhancement approaches are proposed namely; 1) Photoacoustic signal enhancement using fluorophore - metal nanoparticle system and 2) Synergetic photoacoustic contrast-enhancement via graphene oxide wrapping on plasmonic core shell nanohybrids. Further, by the careful selection of contrast agents, the proposed strategies also open up novel approaches to enhance the photoacoustic signals under any excitation wavelengths. The following sections describe the experimental and theoretical aspects of these studies in detail.

5.6.1 Photoacoustic Signal Enhancement Using Fluorophore - Metal Nanoparticle System

Considering the possible excitation wavelengths in typical fluorescence imaging studies, it is well understood that majority of the fluorescence studies are

performed under visible light excitation. To carry out simultaneous fluorescence and photoacoustic imaging experiments with single excitation source therefore demands the usage of nanosecond pulsed lasers operating in the visible wavelength range. An exciting and significant research avenue in this regard would be to establish possible synergetic contrast enhancement schemes for both fluorescence and photoacoustic imaging. As discussed in section 2.5 and section 2.7, the most preferred class of contrast agents for fluorescence and photoacoustic imaging are organic fluorescent dyes and gold nanoparticles respectively. Though significant works have been reported where molecules close to metal surfaces were observed with either enhancement (Kramer, Trabesinger et al. 2002, Shimizu, Woo et al. 2002) or quenching of fluorescence (Trabesinger, Kramer et al. 2002, Dulkeith, Ringler et al. 2005), no works have been reported so far on photoacoustic signal generation in a typical fluorophore - metal nanoparticle system. Towards this direction, investigations were performed to study the behaviour of photoacoustic signals in a fluorophore – metal nanoparticle system derived from distinct sets of rhodamine 6G (Rh6G) - gold nanorod (GNP) solutions. For the experiments, gold nanorods (Figure 5.35a) having an aspect ratio of 1.4 were selected as AuNP and the UV/Vis absorption spectra of the AuNP (~ 0.05 mg/mL) showed characteristic surface plasmon absorptions at 526 nm and 555 nm in aqueous solution (Figure 5.35b). Further, the fluorescence emissions from the experimental solution sets prepared with varying concentrations (refer to Table 13 for particle concentrations) of AuNP and Rh6G at 526 nm excitation were measured using a spectrofluorophotometer. The peak fluorescence emission spectra measured at 526 nm excitation and the relative AuNP concentrations in the experimental sets are given in Figure 5.35 c and

Figure 5.35 d respectively. The error bar in Figure 5.35 c shows the ± 0.01 standard error in the emission measurements performed using the spectrofluorophotometer. Fluorescence emission spectra of the experimental sets at 526 nm excitation shows a reduction in the fluorescence emission intensities with an increase in the concentration of quenchers as illustrated in Figure 5.35 c and Figure 5.35 d.

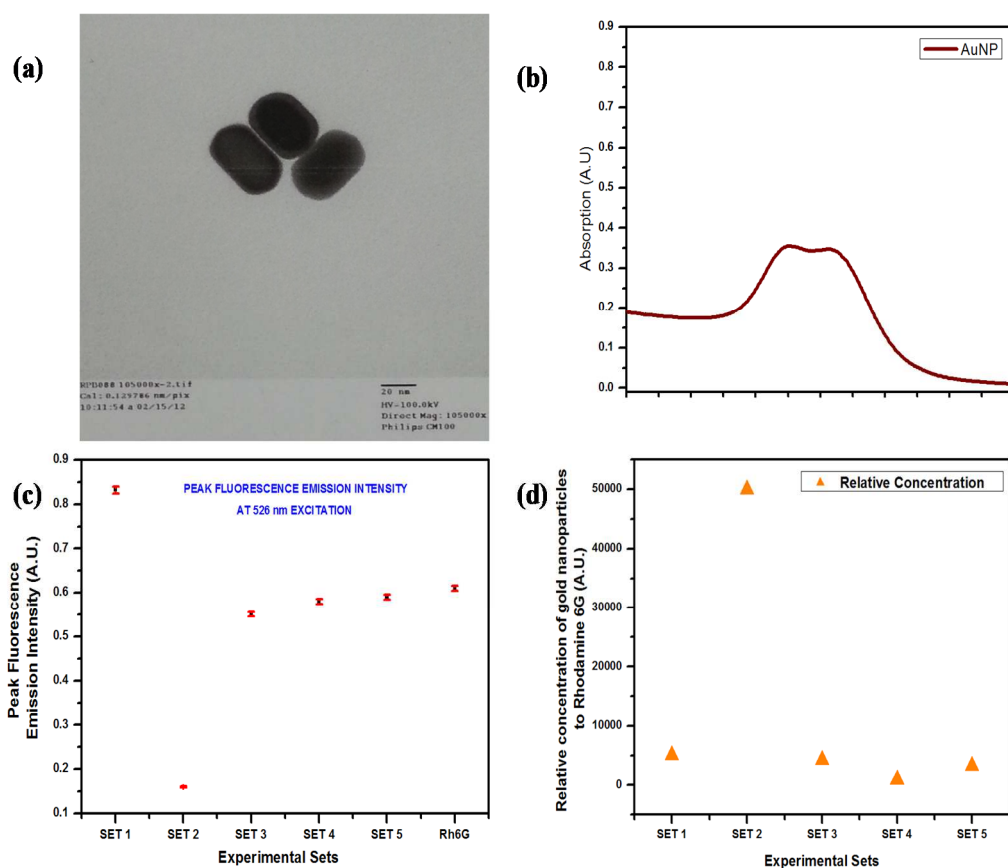


Figure 5.35 (a) Transmission electron microscopy images (TEM) of gold nanorod (AuNP), (b) UV/Vis absorption of AuNP, (c) Peak fluorescence emission intensities measured from the experimental sets, d) Relative AuNP concentrations in the experimental sets.

Experimental Set No	Concentration of gold nanoparticles (~mg/mL)	Concentration of Rhodamine 6G (M)	Relative concentration of gold nanoparticles to Rhodamine 6G (A.U.)
1	0.025	5×10^{-6}	5000.00
2	0.045	0.9×10^{-6}	50000.00
3	0.033	7.8×10^{-6}	4230.77
4	0.0045	5×10^{-6}	900.00
5	0.016	5×10^{-6}	3200.00

Table 13 Particle concentrations in the experimental fluorophore – nanoparticle solution

Maximum fluorescence quenching was observed for experiment set 2, where the concentration of nanoparticles remained the maximum. Supporting to the above argument, fluorescence quenching levels were found to increase for further subsequent additions. However, a tremendous deviation from this trend was observed in set 1 where an unusual enhancement in the fluorescence intensity was seen. Possible causes for this effect could be either the occurrence of resonance energy transfer or due to the amplification of the incident electric field by the gold nanoparticles. Nevertheless, the exact scientific basis that resulted in this phenomenon needs further exploration.

Further, the photoacoustic signal enhancements and subsequent improvements in image contrast for PAI were studied. Simultaneous amplitude mode (A-mode) photoacoustic and fluorescence emission measurements were initially performed with all the distinct sets of aqueous solutions (set 1 to set 5,

Rh6G solution and AuNP solution) using an integrated fluorescence – photoacoustic signal detection scheme as shown in Figure 5.36.

The proposed experimental set-up shown in Figure 5.36 used a tunable nanosecond pulsed laser system (526 nm, 5 ns pulse width, 10 Hz pulse repetition rate, 300 μ J pulse energy) for the simultaneous generation of photoacoustic and fluorescence signals. Photoacoustic signals were detected using the spherically focused immersion transducer (V327, Olympus Corp.) with 10 MHz center frequency. The excitation beam and the beam axis of the ultrasound transducer was positioned perpendicular to each other with the center of the laser beam falling within the focal length of the transducer.

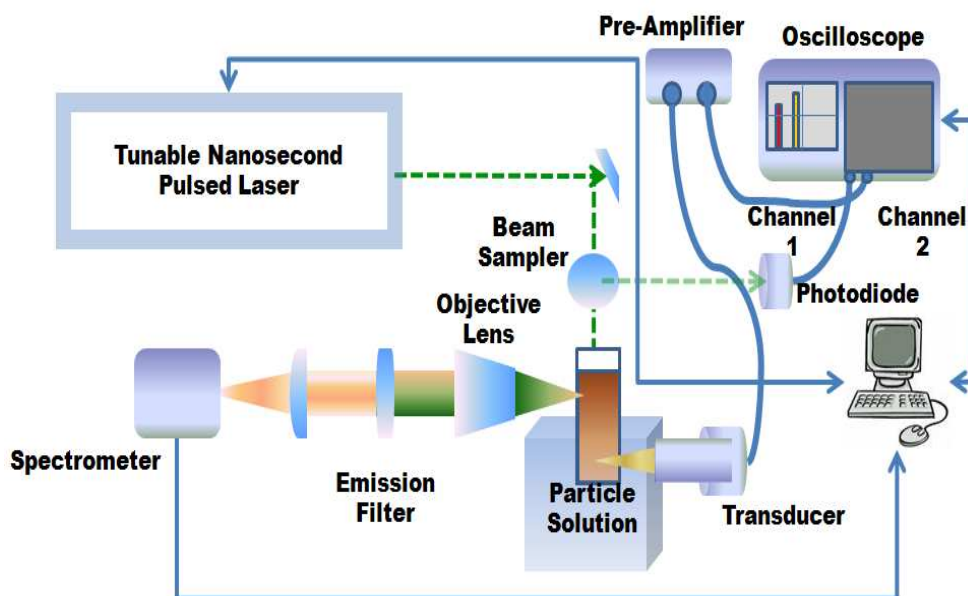


Figure 5.36 Proposed experimental set-up for simultaneous photoacoustic and fluorescence studies

The detected PA signals were further amplified by 40 dB using an ultrasonic preamplifier (5678 preamp, Olympus Corp.). A digital oscilloscope (TDS 3054, Tektronix Inc.) was used as the digitizer and the data acquisition device and the data

was recorded into a PC for further processing. Fluorescence signals were collected using a long working distance, infinity corrected microscope objective (20 X / 0.42 NA, Mitutoyo Corp.) positioned with the center of the laser beam falling at the focus of the objective lens. The emission filter (HQ560/50m, Chroma Tech Corp.) mounted along the emission optical path filtered the signals before it was detected and recorded using the scientific-grade spectrometer (QE6500, Ocean Optics Inc.).

Photoacoustic and fluorescence signals of the seven distinct sets of experimental solutions were performed and the averaged photoacoustic and fluorescence spectral intensities for 100 pulses under study are shown in Figure 5.37.

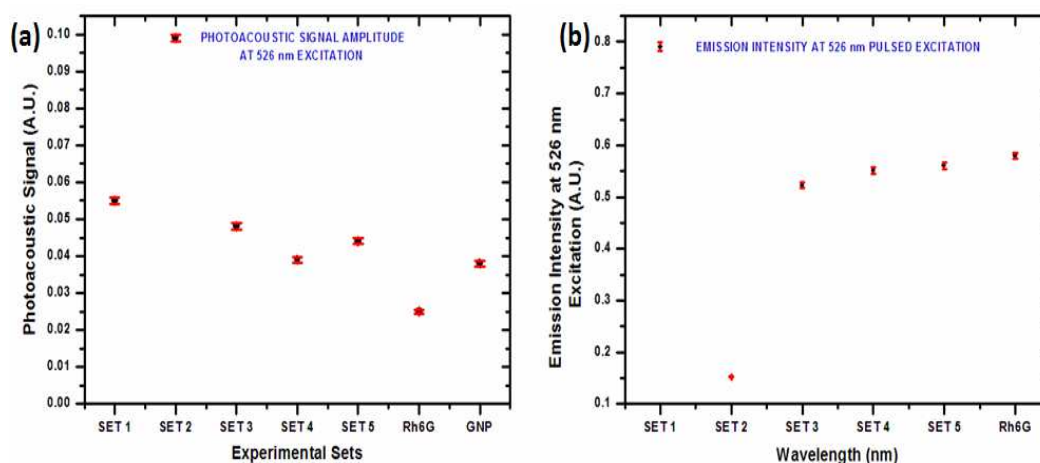


Figure 5.37 Experimental results from simultaneous photoacoustic and fluorescence studies at 526 nm excitation. a) Photoacoustic signal amplitude, b) Fluorescence emission intensity

The error bar shows ± 0.013 standard deviation of the photoacoustic and fluorescence signals measured using 100 laser pulses. Considerable enhancement in photoacoustic signals were observed from set 2 followed by set 1, set 3, set 5, set 4, GNP and Rh6G respectively. The photoacoustic signal from set 2 was observed to be about 2.9 and 4.1 times higher compared to the gold nanoparticle and rhodamine

6G solutions respectively. Correspondingly photoacoustic signals from set 1, set 3, set 4 and set 5 were (1.53, 2.2), (1.34, 1.93), (1.09, 1.56), (1.22, 1.76) higher compared to gold nanoparticle and Rh6G solutions (GNP, Rh6G) respectively.

A consistent enhancement in the amplitude of photoacoustic signals were observed in all the five different sets of solutions when compared to the signals from the aqueous solutions of gold nanoparticle and rhodamine 6G. Further, comparison of photoacoustic signal amplitude with the corresponding fluorescence emission intensity showed an inverse relationship between them with the only exception in set 1. Therefore, the relation of emission intensities with the photoacoustic signal amplitude from a fluorophore – metal nanoparticle system was further investigated.

Considering the fundamental theoretical principles of photoacoustic effect, one could infer that the enhancement in the photoacoustic signal would be due to the corresponding enhancement in the optical absorption of the experimental solutions. To eradicate this possibility, a series of optical absorbance measurements of the seven experimental solutions using the UV-VIS-NIR spectrophotometer (UV-3101 PC NIR, Shimadzu Corp.) was performed.

Figure 5.38a and Figure 5.38b respectively shows the absorption spectrum and relative change of absorption at 526 nm of the seven different sample sets. The absorbance of the seven sample sets at 526nm showed that Rh6G exhibited maximum absorbance followed by set 1, set 5, set 3, GNP and set 2 respectively.

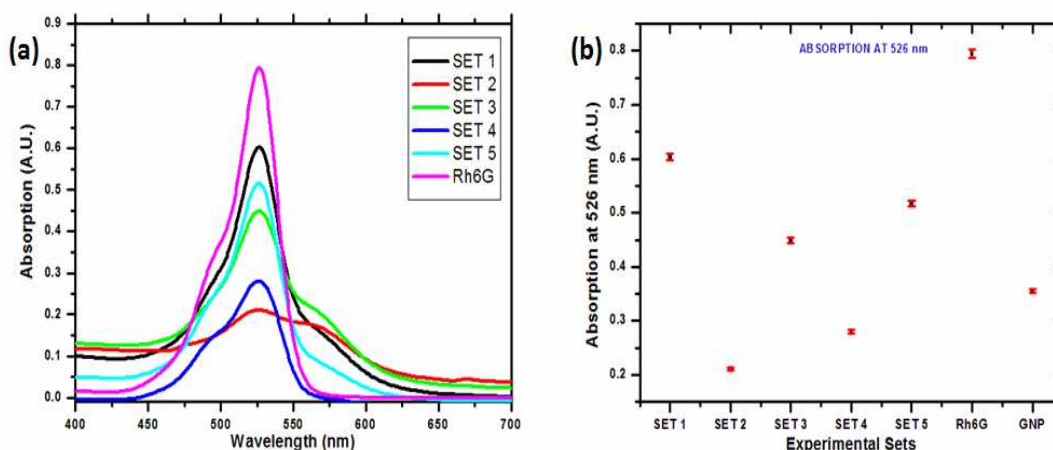


Figure 5.38 Absorption measurements of the experimental sets. a) Absorption spectrum, b) Absorption at 526 nm excitation.

Comparison of the photoacoustic signal amplitudes obtained from each sample sets (Figure 5.37 a) with their corresponding absorption intensities (Figure 5.38 b) showed that the enhancement in the photoacoustic signal amplitudes were not directly linked with their respective absorbance at 526nm. Therefore, the significance of change in absorptive properties of the sample sets as the reason for the enhancement of photoacoustic signal amplitude was excluded. In this context, the only possible source for the observed photoacoustic signal enhancement would therefore be related to certain photophysical interactions in a fluorophore – metal nanoparticle system.

In fluorophore – metal nanoparticle system, the interaction of gold nanoparticles with the fluorescence molecules can be explained based on three main mechanisms (Lakowicz 2001). The first mechanism involves an enhancement in the fluorescence intensity due to the amplification of the incident electric field by the metal nanoparticles, as observed in metal colloids (Sokolov, Chumanov et al. 1998, Hayakawa, Selvan et al. 1999, Selvan, Hayakawa et al. 1999). The second mechanism involves the enhancement of the intrinsic radiative decay rate of the

fluorophore due to the presence of metal nanoparticles (Lakowicz 2001). For the proposed PA signal enhancement, a third mechanism which involves energy transfer quenching to metal nanoparticles due to the damping of the dipole oscillators (excited fluorophore is considered as the oscillating dipole) by the nearby metal nanoparticles (Campion, Gallo et al. 1980) is adopted.

Excited fluorophores are oscillating dipoles which oscillate at higher frequencies and emit short wavelengths. The basic principles of fluorescence and the factors affecting the fluorescence emission such as quenching, environmental effects, resonance energy transfer (RET) and rotational motions are well documented and understood (Lakowicz 2001). Quantum yield of a fluorophore, which describes the fluorescence efficiency of an excited molecule is determined by the ratio of the fluorescence emission (i.e. number of photons emitted) to the sum of all decay rates of the excited state (i.e. number of photons absorbed). These factors are generally governed by the two mechanisms of relaxation, namely radiative decay rate (Γ) and non-radiative decay rate (K_{nr}). Quantum yield of a particular fluorophore in the absence of quenching interactions is hence given by (Lakowicz 2001)

$$Q = \frac{\Gamma}{\Gamma + K_{nr}} \quad 5 - 29$$

Therefore, according to equation 5–29, any change in the quantum yield implies a change in either the radiative or the non-radiative decay rate. Significant works have been reported which show variations in the quantum yield and excited state lifetimes of the molecule (Chance, Prock et al. 1978, Novotny 1996). The studies show variations in the radiative decay rate due to photon emission and variations in the non-radiative decay rate due to energy dissipation. Enhancements in

both the radiative and non-radiative decay rates of atoms or molecules close to metal surfaces were also observed with either enhancement (Kramer, Trabesinger et al. 2002, Shimizu, Woo et al. 2002) or quenching of fluorescence (Trabesinger, Kramer et al. 2002, Dulkeith, Ringler et al. 2005) .

In a fluorophore – metal nanoparticle system, non-radiative decay leads to heat dissipation into the surrounding medium. In this case, the relaxation pathways for non-radiative decay process are dominated by collisional quenching and resonance energy transfer. Assuming negligible resonance energy transfer, collisional quenching with a bio-molecular rate constant K_{nr} and quencher concentration $[Qu]$ decreases the quantum yield according to the following (Lakowicz 2001)

$$Q = \frac{\Gamma}{\Gamma + K_{nr} + K_q[Qu]} \quad 5 - 30$$

According to equation 5 - 30, the quantum yield can therefore be modified by changing the non-radiative decay rate and the concentration of quenchers. Further, a decrease in quantum yield implies a reduction in the number of emitted photons to the number of photons absorbed. Considering the energy conservation principle, the reduction in photon emission from the excited fluorophore will therefore result in an increased level of heat dissipation into the surrounding medium. This phenomenon ultimately leads to an enhancement in the local temperature due to optical absorption. According to the fundamental theory of photoacoustic signal generation, the local pressure rise p_0 immediately after the laser excitation at position r is given as (Wang 2008),

$$p_0(r) = \frac{\beta T(r)}{\kappa} \quad 5 - 31$$

Here, β denotes thermal coefficient of volume expansion κ denotes the isothermal compressibility and T denotes the change in temperature. It is reported that a temperature rise of 1 milliKelvin yields a pressure rise of 8 mbar (Wang 2008). Therefore it is expected that, an increase in the temperature due to increased levels of fluorescence quenching will be translated into a corresponding enhancement in the photoacoustic signal.

5.6.1.1 Dual – Optical Mode Imaging with Combined Fluorescence and Photoacoustic Imaging

Further, the potential capabilities of the proposed approach for contrast enhancement in photoacoustic imaging was demonstrated by performing combined fluorescence and photoacoustic imaging experiments. Experiments were performed with the silicone tissue mimicking phantom shown in Figure 5.39. The phantom tissue was fabricated with fluorescent microspheres over the surface and absorption centers made with experimental set 2 and rhodamine 6G solutions along the depth. A silicone based optical absorption center made with rhodamine 6G solution was simulated at an approximate depth of 4.8 mm from the phantom surface. Further, two distinct types of silicone inclusions made out of experimental set 2 and rhodamine 6G solutions respectively were simulated at an approximate depth of 10 mm from the phantom surface.

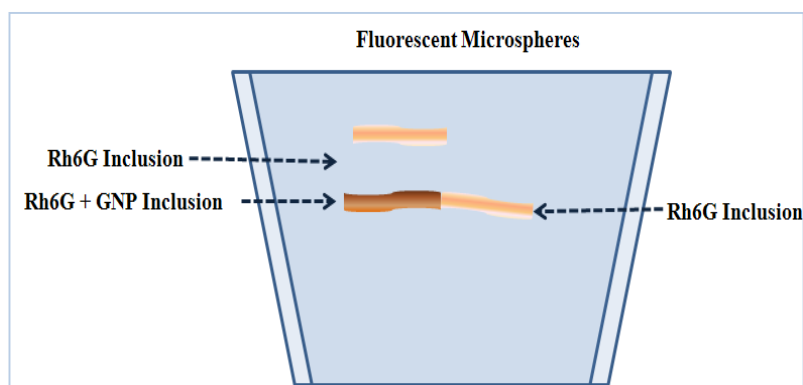


Figure 5.39 Schematic of the fluorophore – gold nanoparticle based phantom tissue

Dual – optical mode imaging of the sample was then performed using a novel experimental set-up shown in Figure 5.40. Fluorescence and PA imaging studies on the tissue mimicking phantom were performed with a tunable nanosecond laser and microscope objective lens as the signal excitation apparatus. A scientific imaging camera supported with optimal sampling optics and linear array ultrasound transducer having compatible electronic instrumentation were used as the detectors for fluorescence imaging and PA imaging respectively. The phantom sample was mounted over a 3-axis translation stage with its fluorescent surface oriented towards the distal end of the microscope objective. The tunable nanosecond laser (Vibrant II, Opotek) operated at 526 nm had a pulse repetition rate of 10 Hz and 5-7 ns pulse width. To produce uniform illumination across the viewfield of the 0.80 NA microscope objective lens (UMPlanFl 50X, Olympus), the rear aperture of each of the objectives was optimally filled with the image of the light source using suitable beam shaping optics.

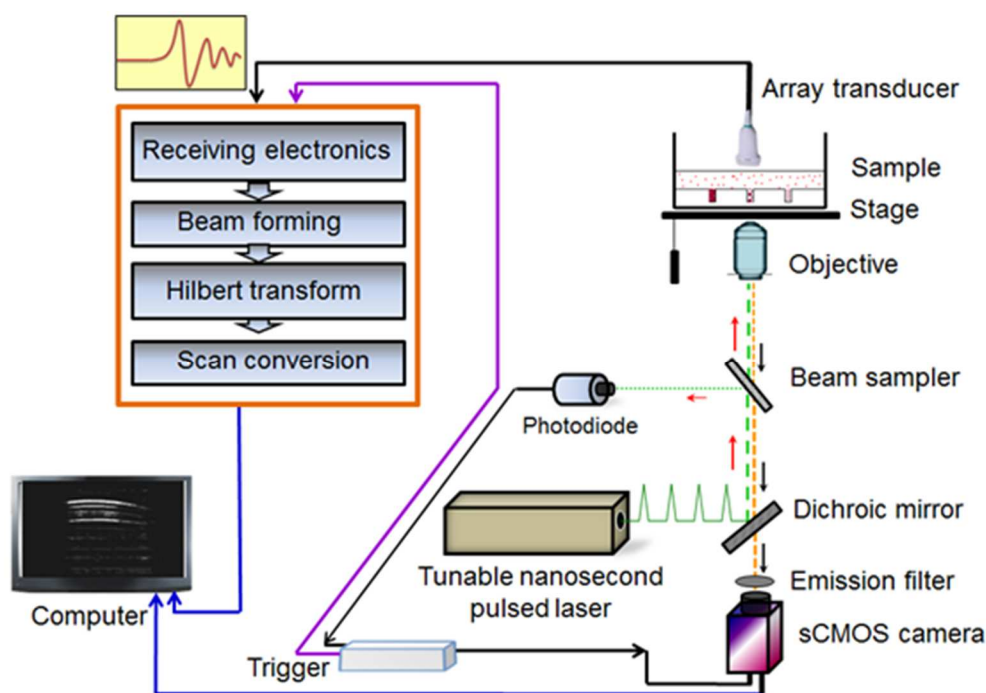


Figure 5.40 Proposed experimental set-up for combined fluorescence and photoacoustic imaging

The fluorescent signatures were generated by focusing the excitation beam through the microscope objective lens. The emission signals collected by the objective lens were further propagated along the emission optical path to the imaging camera (Neo sCMOS, Andor Technology). The sCMOS camera had 2560 x 2160 (5.5 Megapixels) active pixels with a pixel size of 6.5 μm . The front illuminated scientific CMOS had a sensor size (width x height) of 16.6 x 14.0 mm (21.8 mm diagonal). The pixel size was determined to provide ideal over-sampling of the diffraction limited image in the current fluorescent microscopy configuration with the 50x objective. The emission filter (HQ560/50m, Chroma Tech Corp.) mounted along the optical path blocked undesired wavelengths and ensured that only the fluorescence emission signals were imaged. PA signals were acquired using the 8 MHz linear array transducer mounted over the opposite side of the phantom

sample. The transducer array operated at center frequency (-6 dB, average) of 7.699 MHz supported 128 elements with an element pitch of 300 μm , 19 mm elevation focus, 6 mm elevation aperture and had -6 dB fractional bandwidth of 80.88% . Azimuth length of the transducer was 38.40 mm and -20 dB ring-down time (average) was 0.171 μs . Fluorescent and PA signals were generated simultaneously for each laser pulse and the data acquisition process was triggered and synchronized by a fast photodiode – beam sampler unit (SM05PD1A- BSF10-A, Thorlabs Inc.) mounted along the laser beam propagation path. The sCMOS camera set with an exposure time of 500 ms formed the fluorescent images in the PC. The PA signals were Hilbert transformed and further subjected to delay and sum algorithm to form the PA images. Figure 5.41 shows the images obtained from the dual- optical mode imaging system.

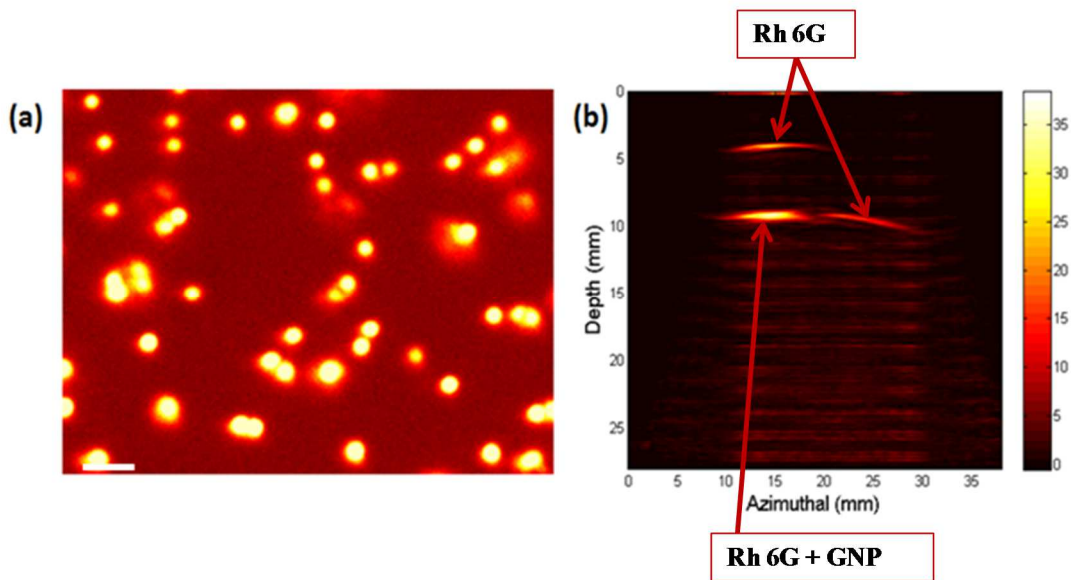


Figure 5.41 Images obtained from the proposed combined fluorescence and photoacoustic imaging system; a) Fluorescence image, b) Photoacoustic image. (Scale bar - 5 μm)

As shown in Figure 5.41 a, fluorescent microbeads were clearly imaged from the surface of the phantom at an excitation wavelength of 526 nm. Although the fluorophore – gold nanoparticle absorption center was located below the rhodamine 6G inclusion, significant enhancements in photoacoustic signal were clearly observed from the fluorophore – nanoparticle inclusion (Figure 5.41 b). Further, visible differences in photoacoustic signal contrasts were also observed from the various absorbing centers as shown in Figure 5.41 b.

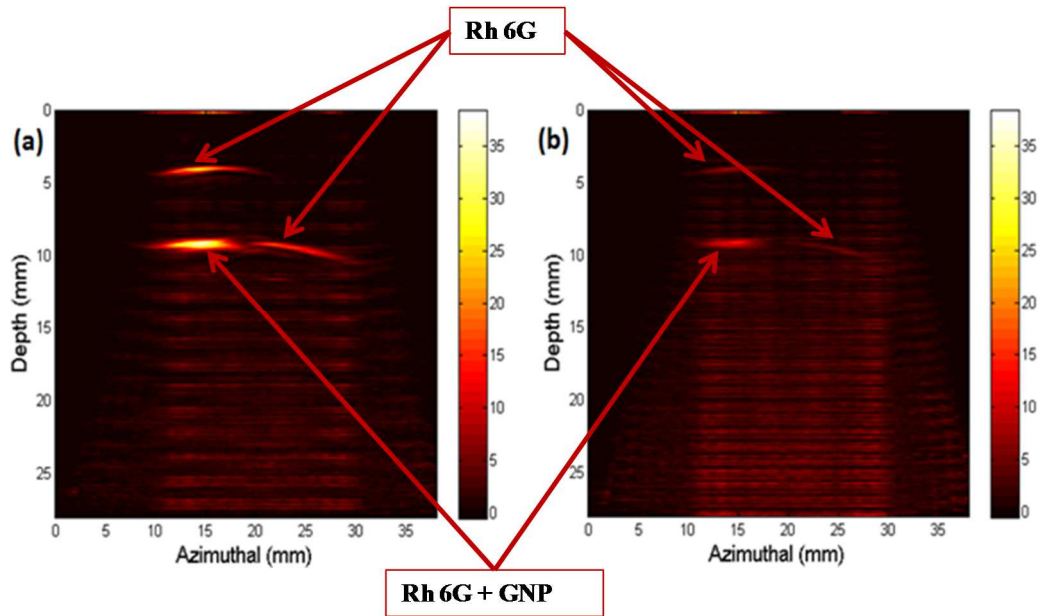


Figure 5.42 Photoacoustic imaging at two distinct excitation wavelengths; a) 526 nm, b) 555 nm

Further to support and validate this effect, photoacoustic imaging studies on the phantom were performed at 526 nm and 555 nm excitation. As shown previously, all the three distinct absorption regions exhibited good photoacoustic signal contrasts at 526 nm excitation (Figure 5.42a). However, at 555 nm excitation, a reduction in the photoacoustic image contrast (Figure 5.42b) was observed. This was owing to the reduced photon absorption by Rh6G together with the reduced

fluorescence emission at 555 nm excitation which ultimately induced a reduction in the photoacoustic signal intensities. Nevertheless, due to the significant optical absorption of gold nanorods at 555 nm, a relative enhancement in the photoacoustic signal was observed at 555 nm excitation from the absorbing region simulated with the Rh6G - AuNP solution.

5.6.2 Synergetic photoacoustic contrast-enhancement via graphene oxide wrapping on plasmonic core shell nanohybrids.

Though the usage of gold nanoparticles such as gold nanorods facilitated deep tissue PAI, increased research interests have been also devoted towards establishing novel nanoplatfroms for multi-modal imaging systems. Towards this direction, gold nanoparticle based multi-modal contrast agents have been widely used for PAI based multi-modal imaging schemes (Jin, Jia et al. 2010, Barrow, Wei et al. 2012). Given the potential capabilities of these multi-modal contrast agents, novel nanoplatfroms for emerging multi-modal imaging combinations are expected to evolve over the years. Although gold nanospheres and gold-silica core-shell nanoparticles exhibit absorption peaks across the visible region (Jain, Lee et al. 2006, James Joseph 2011) for augmenting PA signal generation, investigation into novel nanoplatfroms with enhanced absorption cross-sections while maintaining the overall compact size is of great importance.

Towards this direction, the synthesis of a novel hybrid nanomaterial (GO-SiO₂@AuNP) with enhanced absorption in visible range was developed and performed, by enwrapping graphene oxide (GO) on gold-silica core-shell while maintaining its compact size (please refer to appendix E for the detailed synthesis

procedure). For the experiments, gold nanoparticles (AuNP) with ~ 22 nm diameter and silica shell with thickness ~ 44 nm to get core-shell structure $\text{SiO}_2@\text{AuNP}$ of ~ 100 nm size were selected. The judicious selection of particles with an average size of approximately 100 nm is crucial since the particle size affects the bio-distribution and tumor uptake in a post-angiogenic state. GO was then wrapped around $\text{SiO}_2@\text{AuNP}$ to get the final hybrid GO- $\text{SiO}_2@\text{AuNP}$ shown in Figure 5.43.

5.6.2.1 Synthesis and characterization of AuNP, $\text{SiO}_2@\text{AuNP}$ and GO- $\text{SiO}_2@\text{AuNP}$

The synthesis of the GO wrapped plasmonic core shell nano hybrid GO- $\text{SiO}_2@\text{AuNP}$ involved three main steps as shown in Figure 5.43. In Step 1, freshly prepared gold nanoparticles with size ~ 20 -22 nm were covered with a shell of 4-aminopropyl triethyl silane (APTES) modified silica with c. a. 44 nm thickness. The thickness of silica coating and size of AuNP were fixed based on the approximation that the final fixed size of the hybrid should be ~ 100 nm. Thus, owing to the presence of amino ($-\text{NH}_2$) functional groups a positive charge density was developed around $\text{SiO}_2@\text{AuNP}$ core shell nanoparticles. Next, in step 2 freshly prepared ultrathin GO sheets were allowed to wrap around $\text{SiO}_2@\text{AuNP}$ by making use of electrostatic interaction between positively functionalized silica surface and negative charge on GO surface to get the final plasmonic nanohybrid GO- $\text{SiO}_2@\text{AuNP}$.

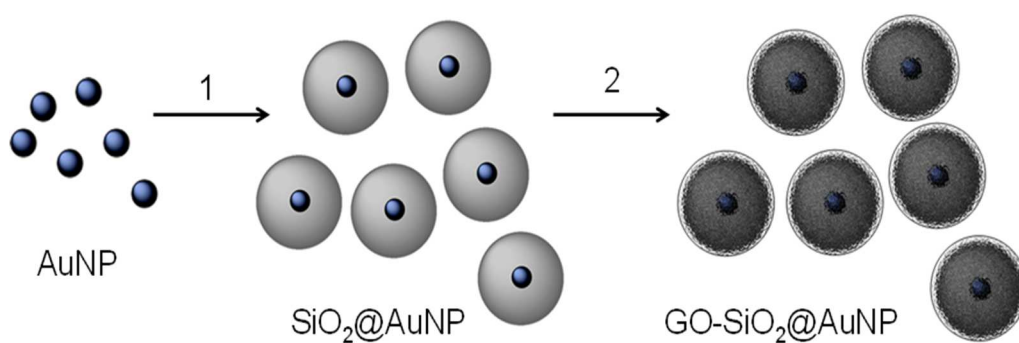


Figure 5.43 Schematic diagram showing synthesis of graphene oxide (GO) enwrapped gold-silica core shell nanoparticles (GO-SiO₂@AuNP). *Step 1*: APTES modified silica coating on AuNP. *Step 2*: wrapping of graphene oxide on the surface of SiO₂@AuNP.

UV/Vis absorption changes

UV/Vis absorption spectra of AuNP (~ 0.5 mg/mL) showed characteristic surface plasmon absorption at 527 nm in aqueous solution (Figure 5.44 a, black curve). Coating with silica shell of average thickness 44 nm, reduced the optical density (by the order of 1.5 times) of SiO₂@AuNP (0.5mg/mL depicted by a red curve in Figure 5.44a) when compared to the bare AuNP's. Also, SiO₂@AuNP exhibited a slightly (5 nm) red shifted absorption maxima at 532 nm. However, the GO wrapped hybrid GO-SiO₂@AuNP with the same concentration of ~ 0.5 mg/mL, exhibited an enhancement in the absorption at 527 nm (Figure 5.44 a, blue curve). Digital image (Figure 5.44 b) showed a clear visible enhancement in the contrast when comparing aqueous solution of all the three particles in separate sample vials.

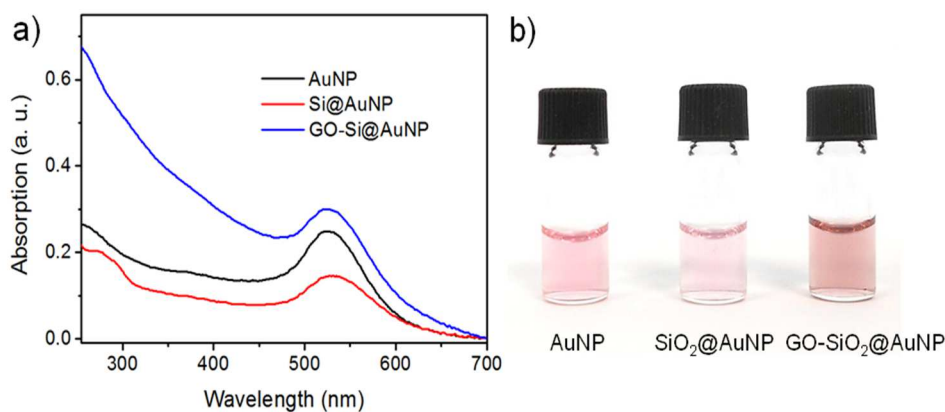


Figure 5.44 (a) UV/Vis absorption changes of AuNP (black curve), SiO₂@AuNP (red curve) and GO-SiO₂@AuNP (blue curve), (b) Digital image of aqueous solutions of ~ 0.5 mg/mL corresponding nanoparticles in aqueous solution at pH 7.2.

Further, a detailed theoretical examination was conducted using finite difference time domain (FDTD) method (FDTD Solutions, Lumerical Inc.) to prove the experimental observation of the optical response of as synthesised nanoparticles. The simulation models involved the usage of total field scattered field (TFSF) source and power monitors across the total field and the scattered field regions. The analysis groups placed inside the TFSF source calculated the absorption cross-sections of the specified nanoparticle and the analysis group located outside the TFSF source calculated the scattering cross-sections. The electromagnetic interactions along the curved surfaces of the nanoparticles were accurately resolved using a mesh override region having a mesh size of 0.7 nm. The mesh override region encompassed the nanoparticle as well as the TFSF source. The TFSF source spanned within a wavelength range of 400 nm to 650 nm and the three frequency monitors positioned around the nanoparticle computed the discrete Fourier transforms of the time domain fields. In order to approximate the in-vivo conditions, the embedding dielectric medium was assumed to be water with a refractive index of

1.33. The optical constants for gold and silica were taken from Johnson and Christy (Johnson and Christy 1972) and Palik (Palik 1985) respectively. The optical constants for graphene oxide were derived using the coefficients of Cauchy functions obtained from the literature (Jung, Vaupel et al. 2008).

The calculated absorption cross-section, shown in Figure 5.45a, revealed that the relative contribution of absorption across the visible region could enhance dramatically upon GO wrapping on SiO₂@AuNP's. It was anticipated that the combined effect of Au plasmon absorption and GO absorption contributed to an enhanced residual electromagnetic field enhancement in GO-SiO₂@AuNP and thereby an enhanced absorption in the visible region, in particular at 527 nm. Therefore the local electromagnetic properties were calculated which allowed to assess the relative contribution of individuals in the nanohybrid to the experimentally observed enhanced absorption intensities.

Contours of electromagnetic near field distribution calculated using FDTD for AuNP, SiO₂@AuNP and GO-SiO₂@AuNP for polarization along X-Z axis is shown in Figure 5.45b-d respectively. Max $|E|^2$ values at the excitation wavelength of 527nm over AuNP, SiO₂@AuNP and GO-SiO₂@AuNP were compared along with the experimentally obtained Stoke intensities of each geometry. $|E|^2$ value of an isolated SiO₂@AuNP was lowered by a factor of 1.2 relative to AuNP's. Upon GO wrapping, $|E|^2$ value was enhanced by a factor of 1.5 in GO-SiO₂@AuNP relative to SiO₂@AuNP's. Thus, the calculated values examined the trends observed in experimental signals and provided a solid justification for the experimental observations.

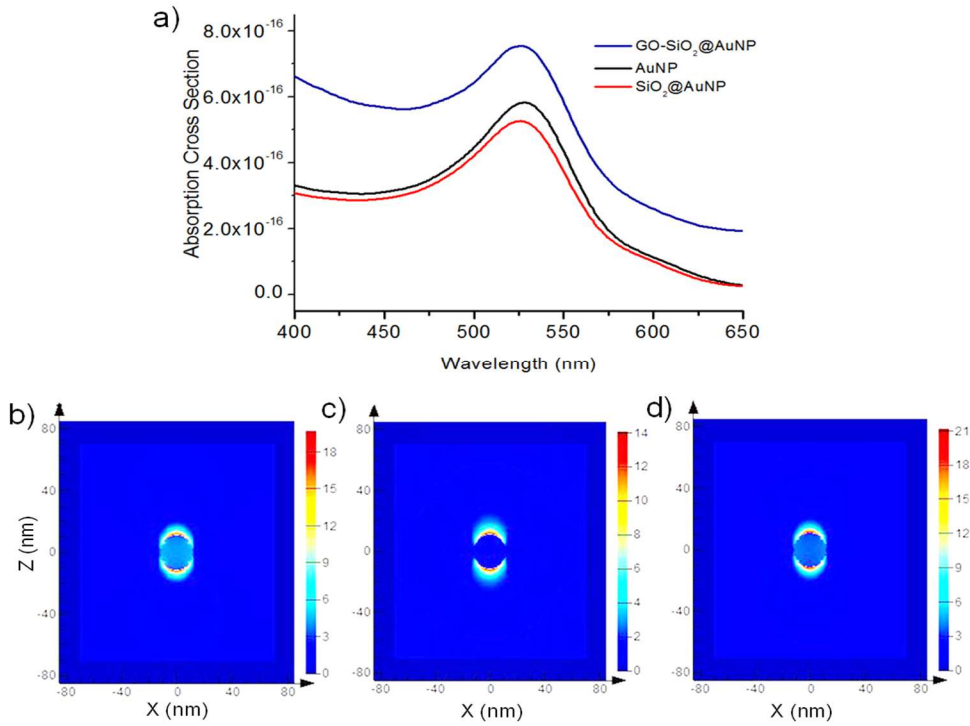


Figure 5.45 a) Absorption cross-section of an isolated AuNP (black curve), SiO₂@AuNP (red curve) and GO-SiO₂@AuNP (blue curve) for the longitudinal polarization of the incident light calculated using FDTD. Contours of the electromagnetic near field enhancement at the excitation laser wavelength 527 nm for b) isolated AuNP, c) SiO₂@AuNP and d) GO-SiO₂@AuNP as a function of X, calculated using FDTD. The colour scale represents the electromagnetic field enhancement ($|E|^2$).

The potential contrast enhancement capability of the GO wrapped hybrid nanoparticle for PAI were further examined using the experimental set-up and methodology detailed in section 5.3.2.1. Amplitude mode (A-mode) photoacoustic studies were initially performed with aqueous solutions of AuNP, SiO₂@AuNP and GO-SiO₂@AuNP (~0.5mg/mL). PA signals were generated using the tunable nanosecond pulsed laser system (527 nm, 5 ns pulse width, 10 Hz pulse repetition rate, 300 μ J pulse energy) and detected using the spherically focussed immersion ultrasonic transducer (10 MHz center frequency). PA signals of the aqueous solutions of three separate nanoparticles are shown in Figure 5.46a.

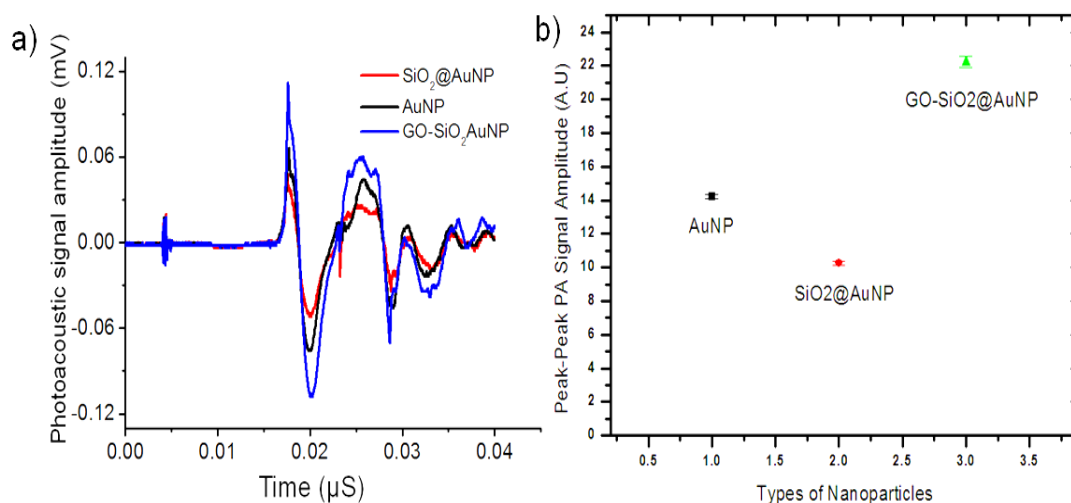


Figure 5.46 a) High resolution scan of photoacoustic signals from AuNP, SiO₂@AuNP and GO-SiO₂AuNP. b) Average peak-to-peak signal intensities of AuNP, SiO₂@AuNP and GO-SiO₂@AuNP nanoparticles

A plot showing the comparison of the averaged PA spectral intensities from 100 laser pulses with three set of particles under study being shown in Figure 5.46b. The error bar shows the standard deviation from the mean value measured for 100 readings. Similar to the variations observed in the absorption spectra, a steady enhancement in signal intensity by a factor of 2.3 was observed for GO-SiO₂@AuNP hybrid nanoparticle when compared to the SiO₂@AuNP's. The findings affirm the effect of higher light absorption and offered an enhancement in thermal conductivity increase via GO wrapping process for an enhanced photoacoustic effect.

5.6.2.2 Combined fluorescence microscopy and PAI using AuNP, SiO₂@AuNP and GO-SiO₂@AuNP

In this section, combined fluorescence and photoacoustic imaging experiments were performed simultaneously to demonstrate the unique capability of the GO-SiO₂@AuNP in providing enhanced PA image contrast at visible excitation

across depths greater than 6 mm. The experiments were performed using the experimental set-up and methodology as described in section 0. Dual-modal optical imaging of samples was performed using Nile red loaded fluorescent microbeads (ex. at 527 nm) embedded in the agar phantom on all the three distinct nanoparticle wells constructed across the sample. Along the first layer agar gel (transparent, air bubble free) of (0.5 cm) with 1 cm total tissue mimic thickness, three separate wells (3×0.1 mm) were created with a horizontal separation of 2 cm from each other. AuNP, SiO₂@AuNP and GO-SiO₂@AuNP (100 μ L each, 0.5 mg/mL) were then dissolved separately in 250 μ L gelatin solution (75 mg/mL) at 55 °C. The gelatin mixtures were gently vortexed to get homogenous solutions. The gelatin mixed nanoparticle solutions were then filled into respective wells inside the agar phantom and allowed to cool to room temperature. After confirming the gelatin solidification inside the wells, further layer of agar solution was carefully added on the top of the wells with a thickness of ~ 0.5 cm followed by the random dispersion of diluted fluorescent microspheres (1 μ m diameter) across the phantom surface. The freshly prepared agar phantom with the fluorescent microspheres and nanoparticles loaded in gelatin matrix were then used for all the imaging studies.

Figure 5.47 shows the photoacoustic image of AuNP, SiO₂@AuNP and GO-SiO₂@Au nanoparticles embedded in gelatin matrix and fluorescent images of microbeads loaded with Nile red. The fluorescent microbeads were clearly imaged from the surface of all the three distinct wells (Figure 5.47 d-f). The weak fluorescent features obtained in the images were from different layers of microbeads embedded in the phantom. However, visible differences in PA image contrast were observed in the PAI experiments. The GO-SiO₂@AuNP exhibited the strongest PA

signal contrast (Figure 5.47 c) followed by the bare gold nanosphere (AuNP) (Figure 5.47 a) and then by gold-silica core-shell nanoparticle ($\text{SiO}_2\text{@AuNP}$) (Figure 5.47 b). In this case, the corresponding enhancement in photoacoustic signals were directly related their respective absorptive properties.

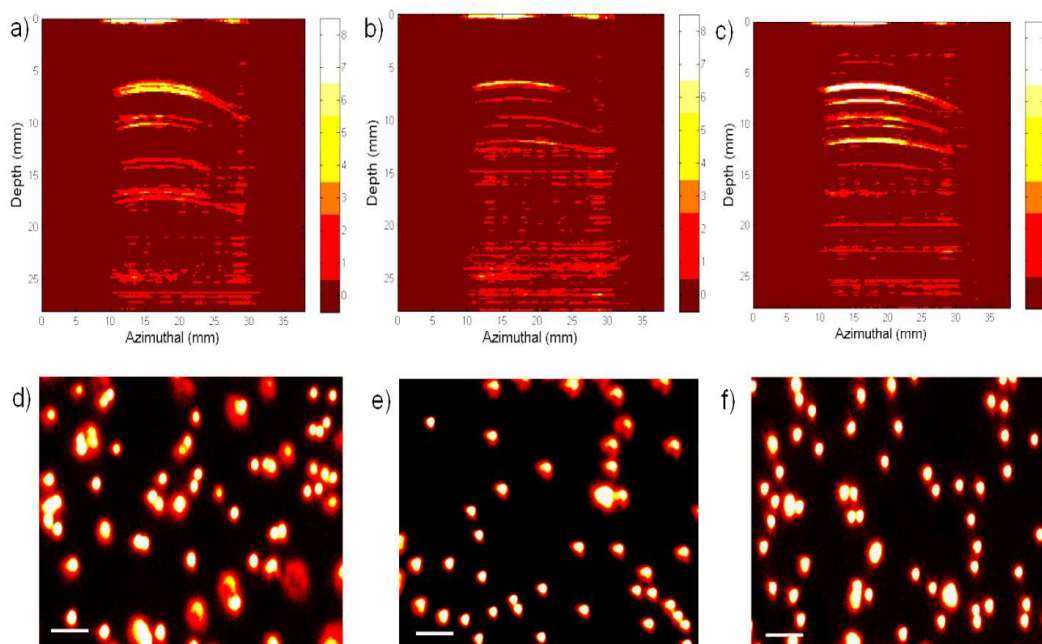


Figure 5.47 Photoacoustic image of a) AuNP, b) $\text{SiO}_2\text{@AuNP}$ and c) $\text{GO-SiO}_2\text{@AuNP}$ embedded in gelatin separate wells in agar phantom. Fluorescent microroscopy images of microbeads (d-f) loaded randomly in the agar phantom (Loaded dye: Nile red) excited with the same laser pulses at 527 nm. (Scale bar 5 μm)

This unique property of the hitherto unreported nanohybrid, $\text{GO-SiO}_2\text{@AuNP}$ makes them excellent candidates for conducting contrast-enhanced PAI studies at depths greater than 6mm under visible excitation. Further, the enhanced absorption of the nanohybrid opens up new avenues for performing simultaneous fluorescence microscopy and PAI with pulsed excitation in the visible range from a single laser.

5.7 Summary of Findings

The theoretical concepts of photoacoustic imaging show that the amplitude of the photoacoustic signal has a linear relationship with absorption coefficient and incident fluence. Further, the theoretical derivations and numerical simulations to investigate the behaviour of photoacoustic signal generation from planar and spherical geometries showed the emergence of rectangular and N-shaped bipolar signals from the slab and sphere respectively. FDTD simulations to determine the optical properties of gold nanoparticles showed gold nanorods as the most suitable contrast agents for photoacoustic imaging due to their higher optical absorption cross-sections and optical tunability. Further, high frequency photoacoustic investigations on gold nanorods with distinct extinction peaks together showed the potential for selective multiple targeting photoacoustic studies. Photoacoustic imaging of phantom tissues show that, the photoacoustic imaging system offers significant capabilities to map optical absorption heterogeneities located along the depth of the tissue. The experimental results also showed that the amplitude of the photoacoustic signal is directly proportional to the absorption coefficient of the sample and the incident laser fluence. Adaptation of spatial compounding and persistence concepts into photoacoustic imaging was proposed and the experimental studies showed a significant improvement in the imaging capabilities of the photoacoustic imaging system. Investigations performed towards establishing two novel photoacoustic contrast enhancing mechanisms showed that the proposed approaches offered significant photoacoustic signal augmentation at visible wavelength excitation. In short, photoacoustic imaging can be used in

conjugation with carefully chosen contrast agents to perform mesoscopic deep tissue optical imaging with excellent optical contrast.

As proposed in chapter 1, to derive and assimilate the complementary information from the targeted site for diagnostic purposes, a multimodal imaging scheme based on an integrated photoacoustic, ultrasound, and fluorescence imaging system needs to be established. The multimodal imaging system would seek to map the multi-level optical and acoustic heterogeneities (complementary information) along the depth of the tissue at multi-scale resolution (microscopic to mesoscopic). The following chapter describes the various aspects and relevant details of the works performed to establish the proposed multi-modal imaging scheme.

CHAPTER 6: AN INTEGRATED MULTI-MODALITY IMAGING SCHEME FOR MULTI-LEVEL AND MULTI-SCALE INFORMATION MAPPING

This chapter proposes a multi-modal imaging scheme using non-ionizing radiations to map the multi-level optical and acoustic heterogeneities (complementary information) along the depth of the tissue at multi-scale resolution (microscopic to mesoscopic). Experimental investigations were performed to establish and characterise the desktop version of the multi-modal imaging scheme. This is then followed by the detailed description of the various investigations performed to establish the imaging capabilities of the flexible fluorescence microscope based multi-modal imaging scheme.

6.1 Proposed Integrated Multi-Modality Imaging System

This section presents the proposed configuration of the integrated multi-modal imaging system comprising of photoacoustic, ultrasound and fluorescence imaging modalities which has the potential to map structural and molecular level information at multi-scale resolution. Novel integrated schemes are established in the proposed configuration that makes use of non-ionizing radiation sources to map multi-level optical and acoustic heterogeneities (complementary information) along the depth of the tissue at multi-scale resolution (microscopic to mesoscopic). The proposed configuration, as shown in Figure 6.1 composes of two different types of hardware level integration, namely at the excitation hardware and at the receiver

hardware. The first approach involved the integration of the fluorescence imaging system with the ultrasound and photoacoustic imaging systems. The integration sought to establish an imaging platform where the signal excitation source comprising the tunable pulsed laser was shared for multi-modal signal generation. The tunable pulsed laser excited both the fluorescence and photoacoustic simultaneously from the phantom tissue. Further, B-mode ultrasound frames were formed between the laser pulses. However, the detection of the corresponding fluorescence and photoacoustic signals were performed with distinct detectors. The sCMOS camera acted as the detector for the fluorescence signals and the multi-element piezoelectric transducer with the associated electronics were used as detectors for the ultrasound and photoacoustic imaging systems. No additional hardware resources were shared and the imaging units operated synchronously based on the trigger signals from the tunable laser.

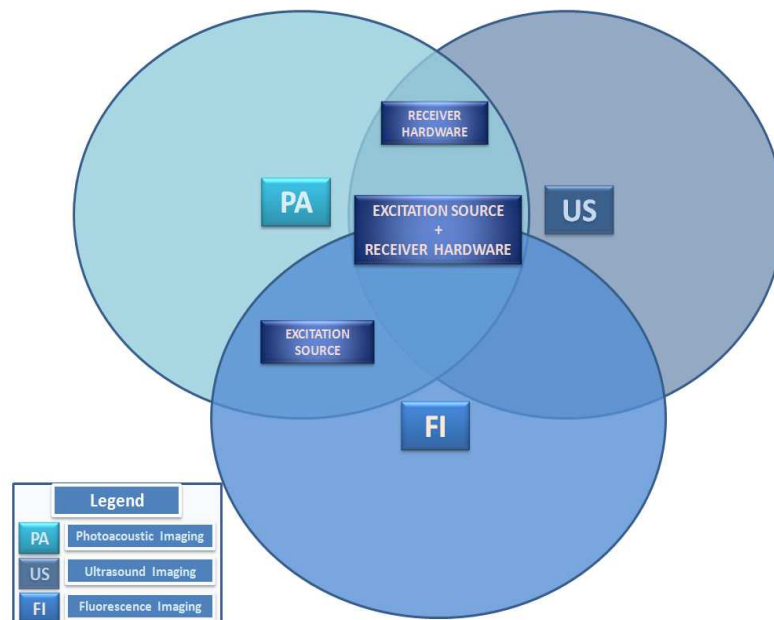


Figure 6.1 Configuration of the proposed multi-modality imaging system

The second type of integration concerns the firmware integration of the ultrasound and photoacoustic modalities. This involved formulating and developing a high level set of hardware and software at the receiver side where the entire receiver firmware was to be shared to generate the ultrasound and photoacoustic images. Since the ultrasound and photoacoustic signals exhibited similar physical principles, the same set of receiving hardware were used to acquire and process both the ultrasound and photoacoustic signals. Figure 6.2 shows the block diagram of the proposed firmware configuration.

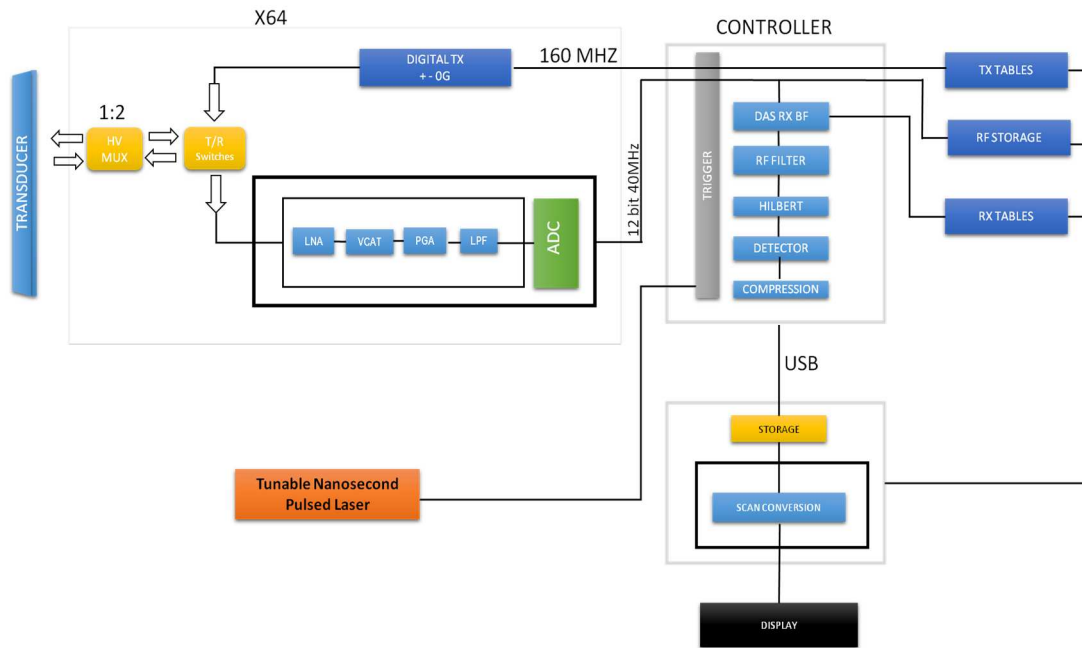


Figure 6.2 Block diagram of the integrated ultrasound and photoacoustic imaging system

The main interface between the ultrasound and photoacoustic modalities in the integrated system was the trigger unit (Figure 6.2). The trigger unit signalled the beamformer controller to switch from the ultrasound mode into the photoacoustic mode. Once the Q-switch synchro out of the laser triggered the

beamformer controller, the transmit controller was disabled and the receiver beamformer was set to acquire the photoacoustic signals generated by the laser pulses. The radio frequency (RF) storage recorded the photoacoustic read out signals for each photoacoustic line it wanted to gather. Each time the photoacoustic data was read out, it was acquired and processed like any other ultrasound RF line. The data process would be apodized, beamformed, filtered, Hilbert transformed or envelope/detected, compressed and scan converted. Photoacoustic signal acquisition and processing worked exactly the same as in the ultrasound imaging with the only differences in the beamformer coefficients (speed of sound is one way in PA mode) and lack of transmit. To support these tasks, the system was equipped with 5 blocks of 36 MB static rams where 3 blocks were used for beamformer coefficients, 1 for the RF data buffer, and the other one for the sampled data going out to the processing and display unit.

Once the two levels of basic system integration were performed and tested, investigations were further carried out to demonstrate the unique capabilities of this multi-modal imaging scheme. Two distinct forms of the proposed multi-modal approach were established, namely an inverted optical microscope based multi-modal imaging system and a fiber-optic microscope based multi-modal imaging system. While the former configuration aims to perform multi-modality imaging of thin and accessible samples, the later configuration typically offers multi-modal imaging capabilities to image inaccessible and inner walls of hollow structures. The following sections detail the investigations carried out to study and characterize the potential capabilities of these two forms of imaging systems.

6.2 Inverted Optical Microscope Based Approach

6.2.1 Experimental Methodology

The schematic of the multi-modal system based on the inverted fluorescence microscope is shown in Figure 6.3. The integration concerns primarily the hardware level integration where the three imaging modalities are to be synchronized and integrated for providing near-simultaneous fluorescence, ultrasound and photoacoustic images. The following section details the basic instrumentation and the results obtained in this regard.

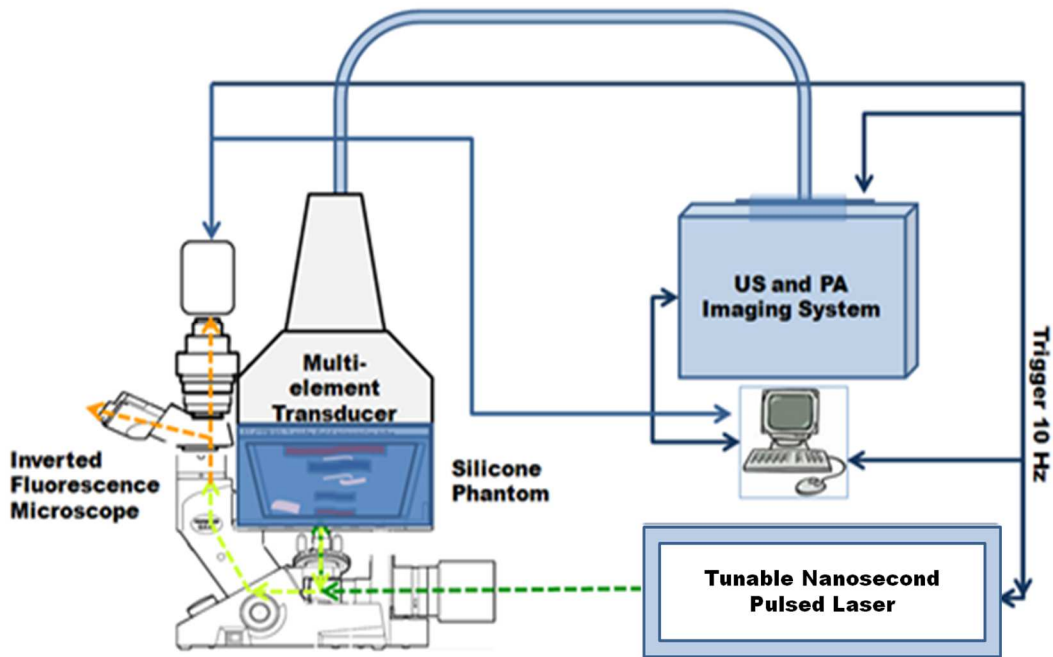


Figure 6.3 Schematic of the multi-modal imaging system based on inverted microscope

The proposed imaging system shown in Figure 6.3 involved the integration of the inverted fluorescence microscope, ultrasound imaging system and the photoacoustic imaging system described in section 3.2.1, 4.2 and 5.4 respectively.

The tunable pulsed laser (Vibrant 355 II, Opotek Inc., USA) acted as the master controller, where the trigger signal from the Q switch synchro out of the laser, initiated the fluorescence, ultrasound and photoacoustic imaging routines. The silicone phantom sample shown in Figure 4.9 and represented in Figure 6.3 (refer to Appendix C for phantom fabrication details) was simulated with fluorescence, ultrasound and photoacoustic signal sources. The phantom sample was then mounted over the imaging platform of the fluorescence microscope with the piezoelectric transducer placed on the opposite side as shown in Figure 6.3. The sample was exposed to an incident pulse energy of approximately 300 μJ at 519 nm to excite both the fluorescence and photoacoustic signals. The 10 Hz trigger signal from the laser triggered the sCMOS camera (Neo sCMOS, Andor Technology) which was set to an exposure time of 100 ms. The same trigger signal was also fed into the PA imaging system to form the photoacoustic images. This ensures the simultaneous generation of fluorescence and photoacoustic images. Further, B-mode ultrasound imaging of the sample was performed between the laser pulses.

6.2.2 Results and Discussion

Multi-modal imaging of the silicone phantom was performed with the inverted fluorescence microscope based system described in section 6.2.1. The surface of the silicone phantom was simulated with the polystyrene fluorescent beads of 1 μm diameter and acoustic and photoacoustic sources simulated along the depth of the phantom as detailed in Appendix C. The results obtained are given in

Figure 6.4(a-c) which shows the fluorescence, photoacoustic and ultrasound images respectively obtained from the multi-modal imaging system.

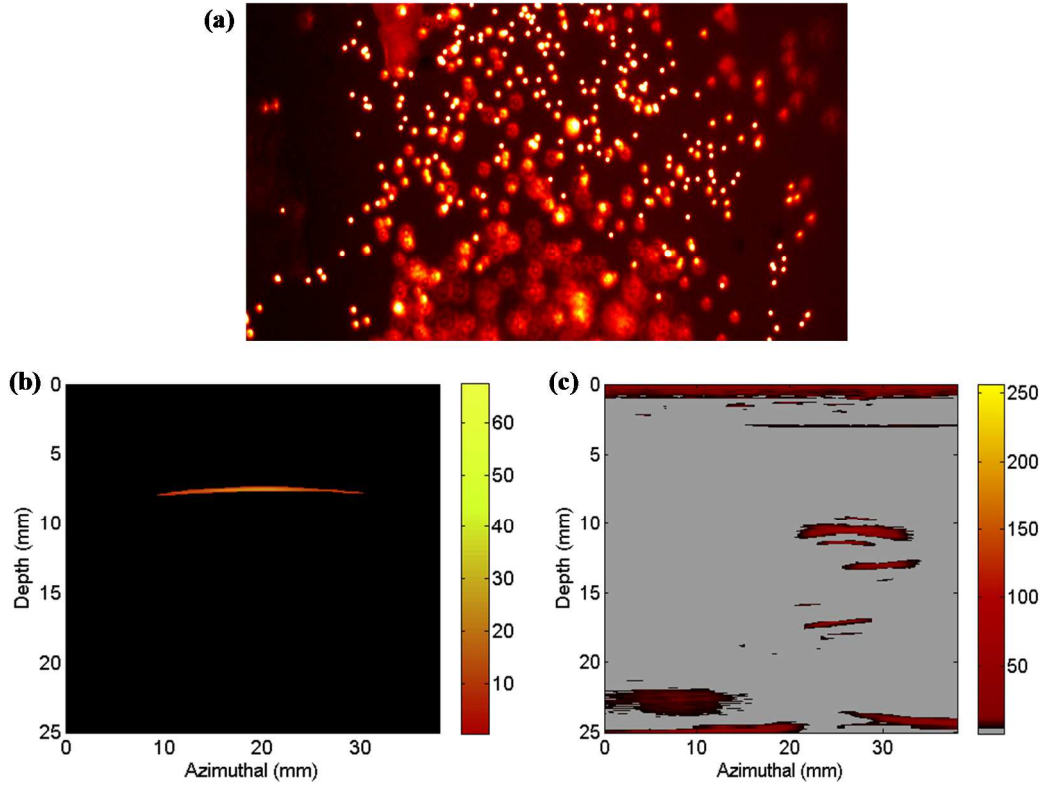


Figure 6.4 Images obtained from the inverted microscope based multi-modal system: a) Fluorescence image, b) Photoacoustic image, c) Ultrasound image

Figure 6.4a shows the images of the fluorescent microbeads present along the surface of the phantom tissue. Micron or sub-micron fluorescent signatures from the sample surface were imaged and mapped accordingly. Further, the photoacoustic image illustrated in Figure 6.4b shows that the image of the optical absorption center simulated with Direct Red 81 dye mapped is of mesoscopic resolution quality. However, the minimal laser energy ($300 \mu\text{J}$ at 519 nm in this case) needed to be regulated and delivered on to the sample to avoid possible photo-bleaching and this imposed limitations to obtain sufficient photoacoustic

signals from depths greater than 10 mm of the tissue. The B-mode image depicted in Figure 6.4c illustrated the potential imaging capability of the multi-modal system to map the acoustic heterogeneities located with mesoscopic resolution along the entire tissue thickness of 2.5 cm. Comparing Figure 6.4c with Figure 4.9 and Figure 4.11 it can be observed that the multi-modal imaging system was capable of mapping the acoustic heterogeneities present along the entire thickness of the phantom tissue.

From the fluorescence, photoacoustic and ultrasound images obtained, it is evident that the proposed multi-modality imaging system can derive the required multi-scale imaging of the optical and acoustic heterogeneities from the surface and along the depth of the phantom tissue. However, the investigations would be limited for ex-vivo imaging particularly due to the larger footprint of the inverted fluorescence microscope. Therefore, further investigations were performed towards establishing the flexible multi-modal system and the following section provides a detailed description of the approach.

6.3 Fiber-Optic Based Approach

Investigations were further channelled towards extending the capabilities of the system for performing the multi-modal imaging from small or inaccessible areas. This was done by swapping the inverted microscope with the fiber-optic based microscope described in section 3.2.2. The experimental scheme for the proposed system is shown in Figure 6.5.

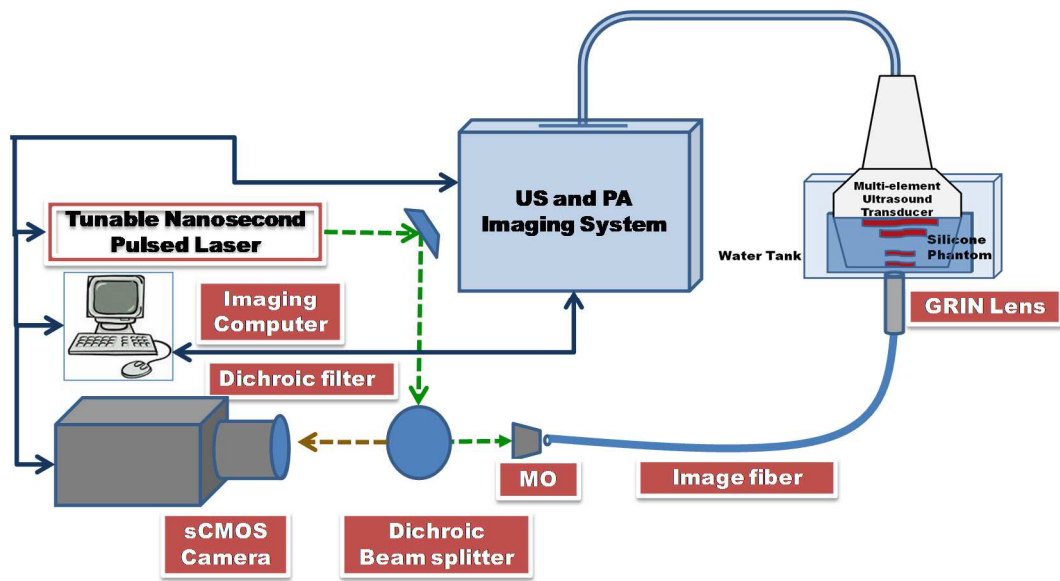


Figure 6.5 Schematic of the multi-modal imaging system based on fiber-optic microendoscope

The flexible multi-modal imaging system depicted in Figure 6.5 comprised an optic-fiber bundle for the delivery of the excitation energy for both fluorescence and photoacoustic signals. Both the fluorescence and photoacoustic signals were generated simultaneously and the fluorescence signals were further collected by the illumination fiber and imaged using the scientific camera. The photoacoustic signals propagated to the surface of the phantom tissue surface were captured using the multi-element piezoelectric transducer coupled to the phantom tissue. The time resolved photoacoustic signals were further subjected to the pre-processing and post-processing routines described in section 5.4. Further, the acoustic heterogeneities present along the phantom tissue were also mapped using the ultrasound imaging apparatus. The ultrasound imaging system performed the ultrasound pulse-echo routines as detailed in Chapter 4: to form the B-mode images in the time frame between the laser flashes. The following section details the results obtained from the flexible multi-modal imaging system.

6.3.1 Results and Discussion

Investigations were performed with 519 nm excitation wavelength and an incident laser energy of approximately 300 μJ . The results obtained are given in Figure 6.6.

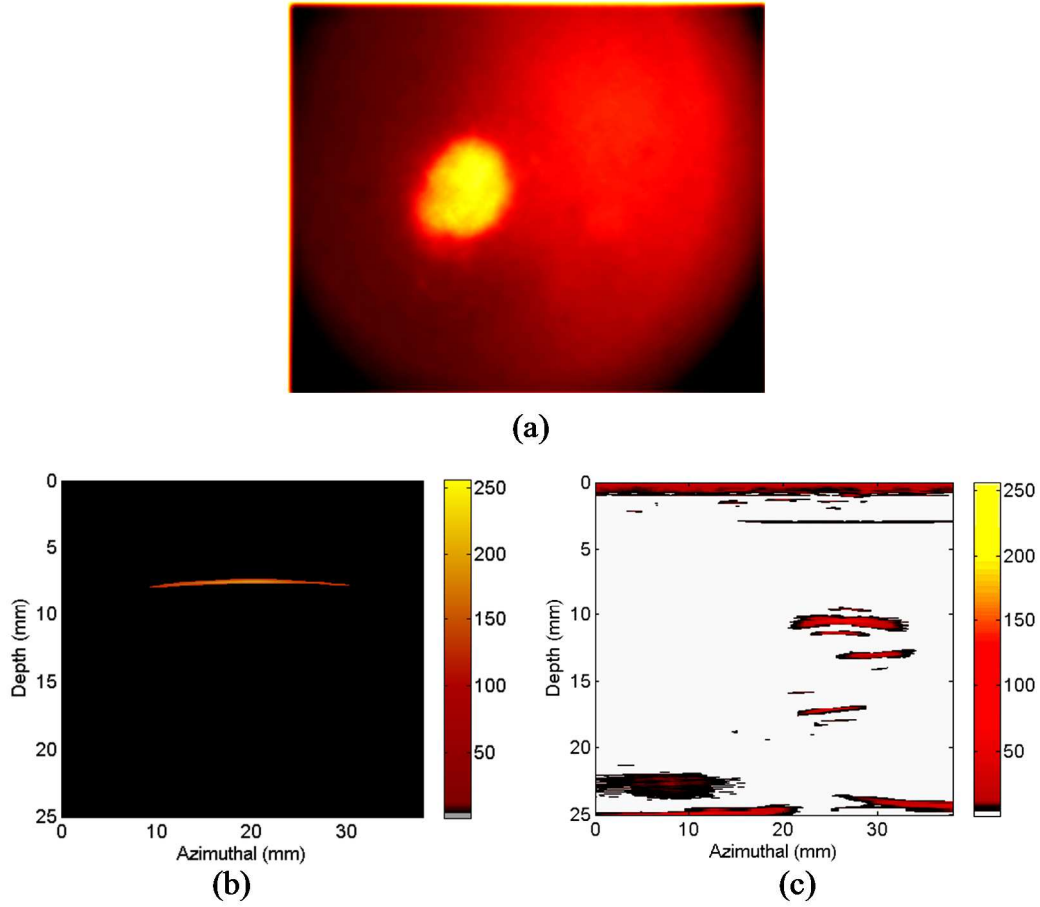


Figure 6.6 Images obtained from the fiber-optic microendoscope based multi-modal system: a) Fluorescence image, b) Photoacoustic image, c) Ultrasound image

Figure 6.6(a-c) shows the fluorescence, photoacoustic and ultrasound images respectively obtained from the fiber-optic microendoscope based multi-modal imaging system. The proposed system was able to obtain the three targeted distinct types of image information. Figure 6.6a shows the image of the fluorescent microbead mapped using the illumination fiber-optic bundle and imaged using the

scientific camera. Comparable image contrast and resolution of similar quality as per an independent operation can be derived. This highlighted that the proposed integrated multi-modal imaging system was able to map micron or sub-micron fluorescent signatures from the sample surface without loss of image quality.

Further, the optical absorptions along the depth of the phantom tissue resulted in the generation of photoacoustic signals. Since photoacoustic signal attenuation is two to three orders magnitude less than optical attenuation in tissue, the photoacoustic signals generated from the top layers of the phantom tissue are propagated towards the opposite side of the tissue surface. These signals are acquired by the ultrasound transducer coupled to the tissue surfaces which are then used to form the photoacoustic images of mesoscopic resolution as shown in Figure 6.6b. However, the lower fluence delivered onto the sample imposed limitations in obtaining photoacoustic signals for image capture from depths greater than 10 mm of the tissue. Further, the mesoscopic acoustic heterogeneities located along the entire tissue thickness of 2.5cm can also be mapped and derived with by ultrasound imaging of the phantom tissue as shown in Figure 6.6c.

6.4 Summary of Findings

A comparison between the images obtained by the multi-modality imaging system and the independent imaging ones was also made. The experimental results in terms of spatial resolution, penetration depth and frame rate could be found in Table 14. From the results, it was observed that each of the individual modalities

exhibited similar imaging capabilities as observed during their independent operation.



Imaging Parameter	Independent Operation			Multi-modal Operation		
	Fluorescence Imaging	Photoacoustic Imaging	Ultrasound Imaging	Fluorescence Imaging	Photoacoustic Imaging	Ultrasound Imaging
Spatial Resolution	<u>Inverted Fluorescence Microscope</u>			<u>Inverted Fluorescence Microscope</u>		
	$< 1 \mu\text{m}$ (Lateral)	$345 \pm 2.53 \mu\text{m}$ (Lateral)	$345 \pm 2.53 \mu\text{m}$ (Lateral)	$< 1 \mu\text{m}$ (Lateral)	$345 \pm 2.53 \mu\text{m}$ (Lateral)	$345 \pm 2.53 \mu\text{m}$ (Lateral)
	<u>Fiber-optic Fluorescence Microendoscope</u>			<u>Fiber-optic Fluorescence Microendoscope</u>		
	$< 3.47 \mu\text{m}$ (Lateral) $16 \pm 0.65 \mu\text{m}$ (Axial)	$151 \pm 2.24 \mu\text{m}$ (Axial)	$151 \pm 2.24 \mu\text{m}$ (Axial)	$< 3.47 \mu\text{m}$ (Lateral) $16 \pm 0.65 \mu\text{m}$ (Axial)	$151 \pm 2.24 \mu\text{m}$ (Axial)	$151 \pm 2.24 \mu\text{m}$ (Axial)
Penetration Depth (mm)	Surface Imaging	>25	>25	Surface Imaging		>25
Frame-rate (Frames/Sec)	1	10	67	1	10	

Table 14 Comparison of imaging parameters of the imaging systems during independent operation and multi-modal operation

All the three forms of imaging modalities in the multi-modal system mapped their targeted imaging features as during their independent operation with the only notable and significant variation in photoacoustic and ultrasound imaging modes as shown in Table 14. The photoacoustic images obtained with the multi-modal system were challenged with limited penetration depth (<10 mm) when compared with its independent counterpart. This was primarily attributed to the low level of

optical fluence induced onto the phantom sample to avoid possible photo-bleaching. However, higher penetration depths (>2 cm) can be obtained through the application of higher fluence at the cost of possible photo-bleaching.

Another significant variation in imaging performance pertained to the frame-rate registered in ultrasound imaging. In the multi-modal system, the frame rate of both the ultrasound and photoacoustic imaging was primarily determined by the repetition rate of the laser. Figure 6.7 shows the process flow of the image formation in the proposed multi-modality imaging system. The laser repetition rate of 10 Hz defined the number of PA frames per second. This value eventually determined the total number of PA frames and the number of B-mode frames made between the laser flashes. Therefore, at 10 Hz laser pulse repetition rate, this would translate to about 4 frames of ultrasound images being made between a single frame of photoacoustic image generated. This frame rate (approximately 40 ultrasound frames per second) by the multi-modal imaging system would be lower to 67 image frames obtained by the independent ultrasound imaging system. Some image quality would be compromised. To increase the number of frame rate, the imaging depth, speed of sound in the medium and the number of lines per aperture would need to be revised accordingly. With spatial compounding, the frame rate was determined by the number of angles in B-mode and PA mode as the frame formation cannot be kept up with the repetition rate of the laser (multiple laser pulses are required to form single PA frame). However, considering the experimental results obtained, it can be observed that the two forms of the proposed multi-modal imaging system could successfully map multi-level optical and acoustic heterogeneities (complementary information) along the depth (>2 cm)

of the tissue at multi-scale resolution ($<1\ \mu\text{m}$ to $<0.5\ \text{mm}$) but with lower penetration depth for photoacoustic imaging and fewer frame rate of ultrasound imaging.

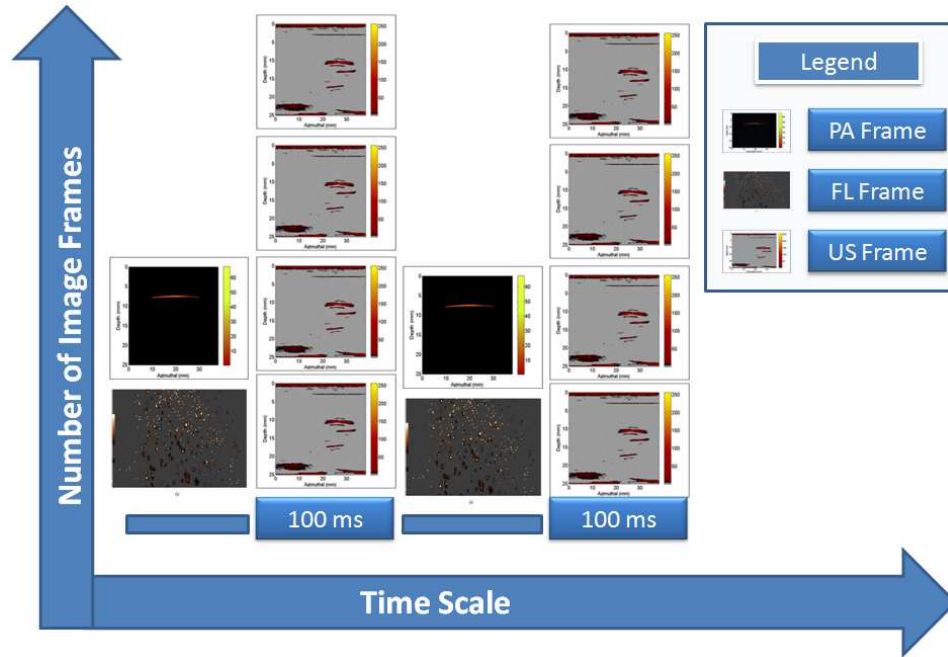


Figure 6.7 Imaging process flow of the proposed multi-modality imaging system

In summary, two forms of a multi-modal imaging system (PAUSFI) (desktop version and flexible version) which can perform near-simultaneous photoacoustic (PA), ultrasound (US) and fluorescence (FI) imaging were established and characterised. The fluorescence imaging modalities offered micron or sub-micron spatial resolution from tissue surface and the photoacoustic and ultrasound imaging modalities mapped optical absorption and acoustic heterogeneities with mesoscopic resolution along the depth of the tissue. The experimental results showed that targeted multi-level imaging along the depth of the tissue with multi-scale resolution (microscopic to mesoscopic) can be obtained.

CHAPTER 7: CONCLUSIONS AND FUTURE WORKS

This chapter begins with the brief descriptions on the outcomes of the various investigations conducted. The salient and original contributions from this experimental research are then highlighted and the chapter concludes by laying the future work directions.

7.1 Conclusion

A novel multi-modal imaging scheme using non-ionizing radiations has been successfully conceptualised, established and experimentally demonstrated. The proposed integrated photoacoustic, ultrasound, and fluorescence imaging (PAUSFI) system could potentially map the optical and acoustic heterogeneities located along the depths of the tissue with multiple spatial resolutions. Relevant and complementary multi-level information from the targeted site for disease diagnostic purposes can be derived and assimilated from the process. Further, two novel photoacoustic signal enhancement strategies and a theoretical methodology to study the optical behaviour of nanoparticles are also formulated capable of performing a variety of deep tissue molecular photoacoustic and various optical imaging studies.

Fluorescence microscopy investigations were carried out to obtain fluorescent signatures with micron or sub-micron spatial resolution. Imaging studies performed using fluorescent microbeads and the proposed inverted fluorescence microscope showed that the system offers excellent capabilities to

image at different focal planes of the sample and the lateral resolution measurements predict a sub-micron resolution scale while working with a 0.8 NA or higher NA objective lenses. Further, the fluorescence microscope based on a lensed coherent image fiber bundle was established and characterised. The fiber-optic microscopy system configured with a GRIN lens assembly at its distal end exhibited lateral and axial resolutions of $3.47\ \mu\text{m}$ and $16 \pm 0.65\ \mu\text{m}$ respectively. Imaging studies performed with the fiber-optic based fluorescence microscope showed that the proposed system can be used for both microendoscopies as well as for remote delivery of light.

On ultrasound imaging, a proposed multi-element transducer having a 128 element linear array transducer supported with high end firmware and advanced post processing concepts was developed and characterised. The characterisation of the proposed system showed SNR of 68 dB and 110 dB for single channel and whole system respectively and in-plane and axial resolution of $345 \pm 2.53\ \mu\text{m}$ and $151 \pm 2.24\ \mu\text{m}$ respectively. Further, enhancements in ultrasound image quality was observed at the expense of frame rate for every change in number of scan lines per aperture and number of transmit focal zones. The investigations performed with silicone based phantom and perfect ultrasound reflectors showed that the system was capable of performing ultrasound imaging at frame rate of 68 fps from depths greater than 2.5 cm.

Theoretical studies to investigate the photoacoustic signal profile generated from spherical and planar geometries upon delta pulse excitation were performed. It was observed that spherical structures generated N – shaped bipolar signals and planar structures generated rectangular pulse shaped signals. FDTD models were

developed and simulations were conducted to determine the optical properties of gold nanoparticles for its future application as photoacoustic contrast agents. It was observed from the simulation that gold nanorods exhibited the highest optical absorption and tuning capabilities and therefore forms to be the most preferred class of contrast agents for photoacoustic applications. Further, UV- Vis absorption measurements of the gold nanorod solutions showed that the nanorods exhibited similar optical properties as predicted from the FDTD simulations. Experimental photoacoustic investigations on gold nanorods having distinct aspect ratios were performed with high frequency single element immersion transducer. The experimental results showed that nanorods can be selectively excited using their SPR peak wavelengths and the amplitude of photoacoustic response is directly related to its optical absorption cross-sections. This approach can be adapted for selective multiple molecular targeting applications where each of the nanorod types is bio-conjugated to target distinct molecular biomarkers.

A multi-element transducer based photoacoustic imaging system was established by integrating a tunable pulsed laser with the receiving and post processing hardware and software routines used in conjunction with the ultrasound imaging system. Dual wavelength excitation of the phantom sample showed that the photoacoustic imaging system was capable of mapping spectral variations along the depth of the tissue. Increased amount of fluence resulted in the formation of photoacoustic signals with correspondingly increased intensities. The investigations performed also demonstrated the linear dependence of absorption coefficient in photoacoustic signal generation. Further, the imaging performance of the PAI system was significantly enhanced by using spatial compounding and

persistence technique. The implementations of these advanced RF data processing algorithms resulted in clear structural boundary images being obtained with reduced image artefacts.

Two novel contrast enhancement mechanisms for photoacoustic imaging were proposed and studied using novel dual – optical mode detection and imaging system. The first approach which involved studies using fluorophore – metal nanoparticle system was performed by varying the concentrations of gold nanoparticles in aqueous solutions of rhodamine 6G. It was observed that the variations in quencher (gold nanoparticle) concentrations resulted in variations in the fluorescence intensities where higher quencher concentrations resulted in lower fluorescence emissions. The photoacoustic investigations performed with these test solutions also showed significant increase in photoacoustic signal amplitude. Correlation of the emission intensities with the photoacoustic signal amplitudes using a dual-optical mode detection scheme showed that the enhancements in photoacoustic signals were due to the increased heat generation from fluorescence quenching.

Synthesis and experimental analysis of a novel hybrid nanoparticle was formulated and performed. A novel hybrid nanomaterial (GO-SiO₂@AuNP) with enhanced absorption in visible range was synthesised by enwrapping graphene oxide (GO) on gold-silica core-shell nanoparticle. FDTD simulations and experimental studies showed that the permanent electrostatic wrapping of two dimensional GO on Au (22 nm)-SiO₂(44nm) core-shell nano structure enhanced the collective residual absorption of the final hybrid (GO-SiO₂@AuNP) in full visible spectrum ranging from 380-700 nm. In particular, GO wrapping enhanced the plasmon absorption at

527 nm in GO-SiO₂@AuNP owing to the total increase in electromagnetic near field intensities as evident from the FDTD calculations. Photoacoustic and fluorescent imaging with tissue mimics embed with both fluorescent microbeads and gelatin fixed nano particles also showed excellent multimodal images, especially where GO-SiO₂@AuNP's showed significant PA contrast enhancement. This unique strategy therefore opens up new avenues for enhancing PAI contrast and combined dual-optical mode imaging using plasmonic nanoparticles with considerably lower cytotoxicity and without any structural modifications

To meet the targeted research objectives, a multimodal imaging scheme based on an integrated photoacoustic, ultrasound, fluorescence imaging system was established. Two forms of a multi-modal imaging system (PAUSFI) (desktop version and flexible version) which can perform near-simultaneous photoacoustic (PA), ultrasound (US) and fluorescence (FI) imaging were established and characterised. The proposed multi-modal imaging system involved hardware integration at the excitation level where the tunable pulsed laser was used for the simultaneous formation of the fluorescent and photoacoustic images. Further, a second type of integration was performed at the receiver firmware where a single firmware platform was used to generate and form the ultrasound and photoacoustic images. All the three forms of imaging modalities in the multi-modal system mapped their specific imaging features with the same level of precision as during their independent operation with the only notable and significant variation in photoacoustic and ultrasound imaging modes. Experimental investigations of the two forms of the multi-modal imaging systems could perform multi-level optical

and acoustic heterogeneity (complementary information) mapping along the depth ($>2\text{cm}$) of the tissue at multi-scale resolution ($<1\mu\text{m}$ to $<0.5\text{mm}$).

7.2 Major Contributions

The major contributions of this research thesis are summarized as follows

- ❖ A novel multimodal imaging platform and related methodologies for multi-level and multi-scale imaging of tissues has been successfully configured and developed. (The outcome of the research is expected to lead into the development of a potential clinical or pre-clinical imaging platform).
- ❖ An integrated image fiber assisted microfluoroendoscopy system has been established and demonstrated for microscopic imaging of fluorescent features from tissue surface.
- ❖ A new methodology incorporating gold nanoparticles for selective and multiple photoacoustic detection has been formulated for selective molecular studies.
- ❖ FDTD based simulation models with related methodologies and algorithms for the determination of the optical properties of gold nanoparticles has been devised and verified.
- ❖ Novel contrast enhancement methodology for photoacoustic imaging using fluorophore – metal nanoparticle solution is established for augmenting photoacoustic signals.
- ❖ A novel nanoparticle based on graphene oxide wrapped gold-silica core-shell nanoparticles has been synthesized and experimentally verified for enhancing photoacoustic image contrast in the visible excitation region.

7.3 Suggestions for Future Work

There exist numerous possibilities for future studies in relation to the proposed multi-modal imaging scheme as well in enhancing the various capabilities of the distinct imaging systems. This section details a brief list of studies that naturally seem to be extensions of the research work described in this thesis.

- ❖ Improvements in the ultrasound/photoacoustic imaging hardware can be also envisaged by which considerable enhancements in the imaging capabilities of the systems can be achieved. Improvements in the imaging speeds can be achieved by enhancing the clocking speeds of the FPGA's and upgrading the data communication channels into state of the art thunderbolt connection between the console and the PC. Further, photoacoustic imaging speeds can be enhanced by integrating the system with high repetition rate pulsed lasers. This would also enable the system to perform Doppler shift based investigations to characterise flowing liquid mediums. Resolution capabilities of the systems can be further enhanced by using high frequency ultrasound transducers and precisely engineered optical illumination schemes. Improvements in PAI performance for imaging moving structures can be achieved by adopting dynamic persistence methods and high repetition rate lasers. The visualisation capabilities of the system can also be enhanced by providing dynamically overlaid ultrasound and photoacoustic images.
- ❖ Although photoacoustic signal enhancements in a fluorophore – metal nanoparticle system was studied based on the fundamental photophysical principles, further tests are necessary to confirm the real physics behind this

observation. A key experimental investigation that can be undertaken would be to perform time resolved studies to investigate the energy transfer mechanisms in the proposed fluorophore – metal nanoparticle system. Considering the distant dependant resonance energy transfer mechanism, it is predicted that photoacoustic based studies are expected to evolve as potential tool as plasmonic molecular rulers in greater depths. Considerable levels of research can be also devoted towards the theoretical and experimental establishment of novel multi-mode or single mode contrast agents based on plasmonic nanoparticles with enhanced optical efficiencies at the desired wavelengths.

- ❖ Considering the unique diagnostic capabilities of the proposed multi-modal imaging system, it is foreseen that that the system can find profound applications in a variety bio-imaging procedures. One typical application in this regard would be for early diagnosis of cancer. The initial step towards the realisation of such an approach would be to investigate into the bio-signatures and imaging parameters that can point out cancer at a very early stage. The best way to do this would be to derive these imaging parameters from the hallmarks of cancer (Hanahan D 2000). More details of a new research area can be found in Appendix G.

APPENDICES

APPENDIX A - Configuration of The Inverted Fluorescent Microscope

The inverted fluorescence microscope employed in this research is built from a compact inverted metallurgical microscope (Olympus GX41). The basic building block of the microscope shown in Figure A. 1 is built on the Olympus UIS2 Optical System (Infinity-corrected) where infinity corrected objective lens are used.

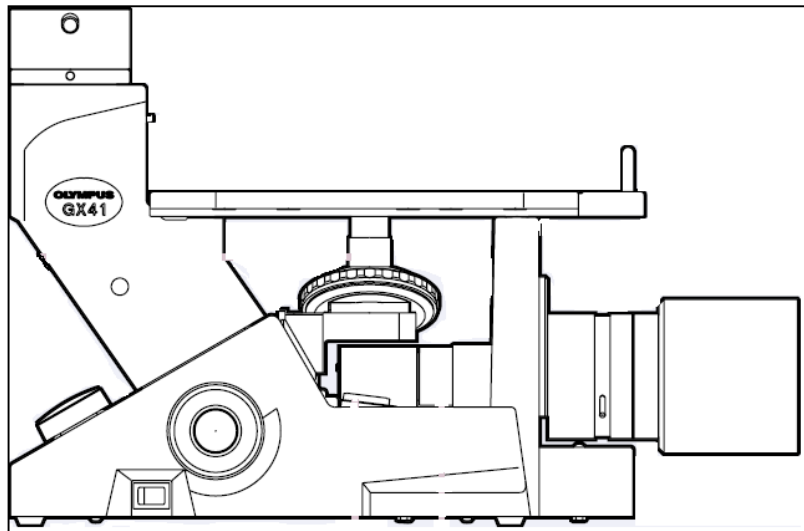


Figure A. 1 Schematic of the Microscope

Direct visualization of the fluorescent signatures is then made possible by mounting a wide-field trinocular tube with a pair of eye pieces (oculars). The system expansion is done by mounting the trinocular tube suitable for the available ocular. For the direct visualization of fluorescence images, Olympus WHB 10X/20 oculars are mated with Olympus U-CTR30-2 wide field trinocular tube as shown in Figure A. 2. Fluorescent images are separated out by mounting suitable emission filter just before the entrance optics of the trinocular.

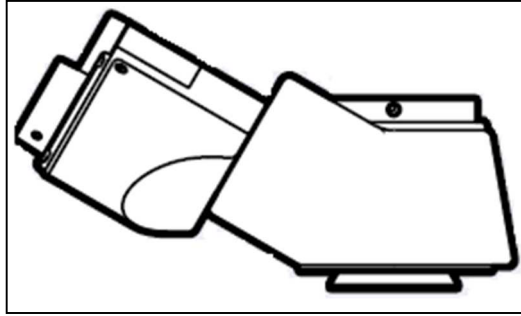


Figure A. 2 Schematic of the Trinocular tube

Further, to facilitate digital recording of the samples, the trinocular tube is mounted with suitable C-mount video camera port (Olympus U-TV1X-2, and video camera mount adapter (Olympus U-CMAD3, Figure A. 3). The focus of the unit is then tuned by adjusting the amount of screwing into the U-TV1X-2.

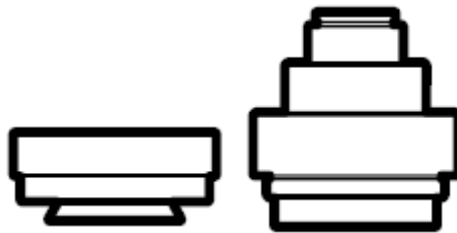


Figure A. 3 Schematic of the C-mount video camera port and video camera mount adapter

Once the camera mounting optomechanics are configured, the scientific camera (Neo sCMOS. Andor Technology) with complementary metal–oxide–semiconductor (CMOS) sensors is mounted over the camera mount adapter. The schematic of the proposed customized fluorescence microscope is shown in Figure A. 4.

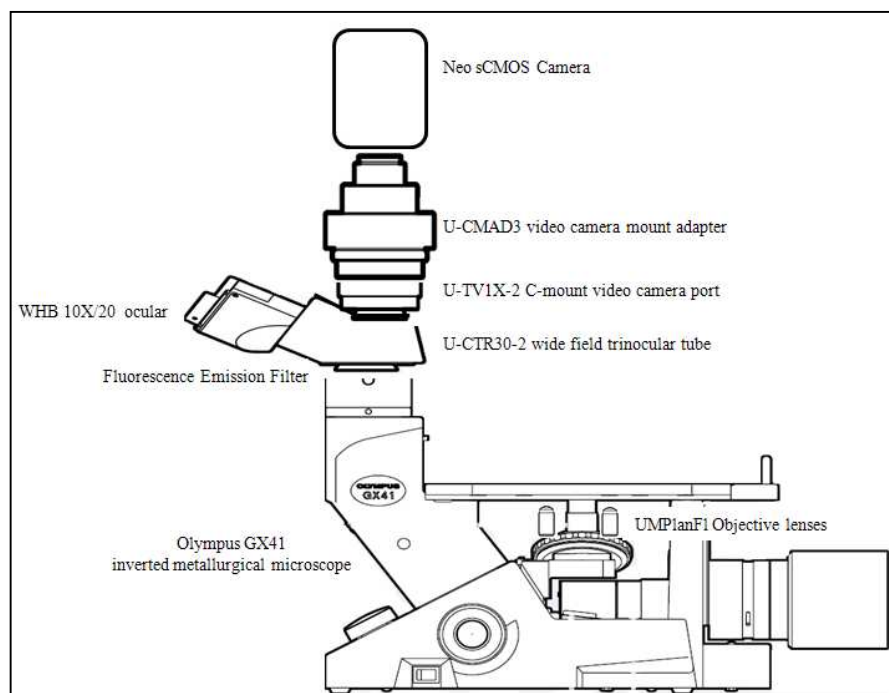


Figure A. 4 Schematic of the Proposed Inverted Fluorescence Microscope

APPENDIX B - Programming Interface for the Integrated Linear Array Ultrasound and Photacoustic Imaging System

Two families of Xilinx Field Programmable Gate Arrays (FPGA) are used, namely; Virtex (Digital Side) and Spartan (Analog Side). Figure B. 1 shows a screen shot of the layout of the Printed Circuit Board (PCB) with the Joint Test Action Group (JTAG) programming of the Spartans from iMPACT and Xilinx programming cable (DLC 10).

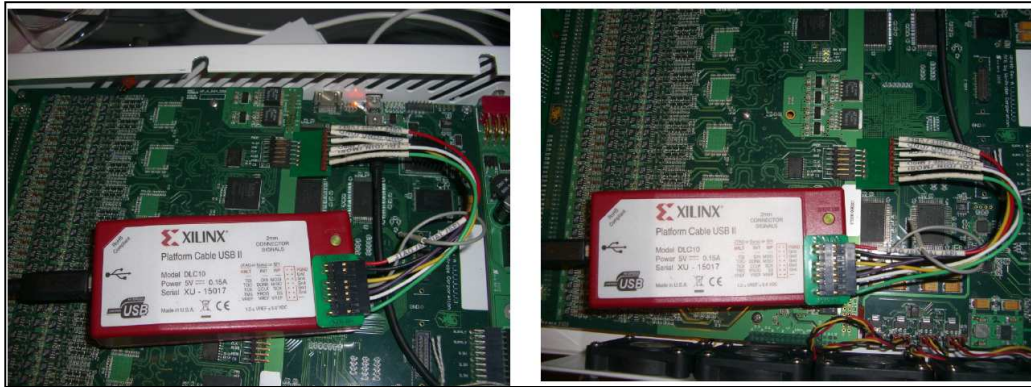


Figure B. 1 Images of the PCB with Spartan Programming Device

APPENDIX C - Phantom Preparation

Introduction

Tissue-mimicking phantoms are objects that replicate the properties of human or animal tissues in the development and optimization of diagnostic imaging systems (Patterson and Pogue 2006),(Zell, Sperl et al. 2007). Due to the relevance in performance validation of systems used in measuring optical, acoustic and even physical properties of tissues, phantoms are required to replicate the properties of human or animal tissues. The applications of the phantoms (Bioud and Bérubé-Lauzière 2008)-(Kim , Garcia-Urbe et al. 2008) are extended but not restricted to the following application areas in equipment characterization such as performance testing, routine quality control, optimization of system designs, system calibration and quantification of various system parameters. Although phantoms are commercially available, the inconsistencies in the status of the phantoms present a major challenge.

Over the last few decades, considerable efforts has been put to develop phantoms for optical imaging and spectroscopy (Srinivasan, Kumar et al. 2002), (Lualdi, Colombo et al. 2001) -(Firbank and Delpy 1993). The diverse spectral and geometrical range of the optical applications has made the establishment of tissue phantoms arduous and fairly complicated. Most of the reported phantoms simulate optical properties at selected wavelengths, are instable over time, or cannot be used to replicate stratified tissues of varying optical properties (Lualdi, Colombo et al. 2001). In addition, optical phantom design is dependent upon the desired optical and physical properties for a specific application. Due to the increasing importance

of precise fabrication of phantoms, a series of fabrication approaches have been experimented and only a few were generally accepted. The main constituents for sample fabrication include a host medium, scattering agents and absorbing agents (Mincu, Brunette et al. 2008). Host medium includes the usage of epoxy resin, polyester or silicone as these materials provide enhanced shaping flexibility and long-term optical stability (Sukowski, Schubert et al. 1996). The three main choices for scatterers are white metal oxide powders (Al_2O_3 or TiO_2), lipid microparticles and polymer microparticles (Patterson and Pogue 2006). To introduce absorption properties into the host material, various kinds of dyes and phospholipid emulsions have been investigated (Patterson and Pogue 2006).

Materials and methods

The main constituents for fabricating an optical phantom includes a host medium, absorbing agents and scattering agents (Mincu, Brunette et al. 2008). The following sections describe the various materials used for phantom fabrication.

Host Medium

Various types of materials have been used as host medium to house scatterers and absorbers: These materials fall principally under three categories such as solid (Firbank, Oda et al. 1995), (Lualdi, Colombo et al. 2001), (Firbank and Delpy 1993), (Tahir and Dainty 2005), aqueous suspension or liquid (Choukeife and L'Huillier 1999) and hydrogels (Kim, Garcia-Urbe et al. 2008), (Viator and Prahl 1999). However, characteristics such as stability, refractive index, cost and ease of fabrication and biological compatibility varies across the choice of materials and should be carefully considered for its usage in the desired investigation modality.

The advantages of solid phantoms over liquid phantoms in fabricating layered phantoms and arbitrary phantom geometries have been reported (Ayers, Grant et al. 2008),(Patterson and Pogue 2006). The most widely used solid host materials that offer improved flexibility and long-term optical stability are composed of epoxy resin, polyester or silicone (Sukowski, Schubert et al. 1996).

Silicone possess mechanical properties to simulate tissue (Moffitt, Chen et al. 2006) with its well defined microstructure, making it insensitive to rough handling (Zell, Sperl et al. 2007) and provides high durability. Therefore this work involves the usage of room temperature vulcanizing (RTV) silicone as the host material (Bays, Wagnieres et al. 1997). RTV silicone consists of two components, namely a silicone base catalyst and a curing agent which are to be weighed and mixed with a ratio of 9:1 (Zell, Sperl et al. 2007) or 10: 1 (Bays, Wagnieres et al. 1997). Refractive index of this phantom is found to be 1.404, which indicate that it is suitable for simulating soft tissue ($n=1.33$ to 1.50) (Bolin and Preuss 1989).

Scattering Agents

The choice of the scatterer hinges upon considerations such as the type of embedding base material, its limitations and stability issues. Powdered particles hold a wide range of particle sizes and shapes which hinders the precise evaluation of the density of scatterers. Therefore lipid emulsions such as Intralipid is preferred to introduce scattering centers inside the optical phantoms (Patterson and Pogue 2006). Intralipid is primarily composed of soybean oil, glycerin, water and egg lipid together with the mixture of undisclosed quantities of certain stabilizing reagents (Michels, Foschum et al. 2008) to adjust the pH between 6 to 8.9 ((FDA)). This work involves the usage of Intralipid-20% which is composed of

20% soybean oil, 2.2% glycerin, 1.2% egg yolk phospholids and water (Michels, Foschum et al. 2008).

Absorbing Agents

In order to deliver the desired absorbance into the host material, various kinds of dyes and phospholipid emulsions can be used. This work involves the usage of three absorbing agents namely Direct Red 81, Methylene Blue and Rhodamine 6G.

Fabrication Methodology

A five layered silicone phantom sample was fabricated and the fabrication methodology adopted for forming each of the silicone layers is as follows. RTV silicone (ELASTOSIL® RT 601 A/B, Wacker Chemicals South Asia Pte Ltd, Singapore) was used to prepare the host material. The desired amount of Elastosil RT601A/B was weighed with a mixing ratio of 0.1 W/W of curing agent (RT601B) for one unit weight of silicone base catalyst (RT601A). 1.5 % (V/V) of Intralipid was further mixed with the curing agent. The base catalyst was then subjected to mechanical blending for approximately 15 minutes. In order to degas the bubbles, the mixture was then placed in the vacuum chamber set at room temperature, 1 KPa, for less than 45 minutes. The sample was then poured into the mold and further subjected to degassing in vacuum chamber under similar conditions for 30-60 minutes. The sample was further allowed to cure in the refrigerator set at 4°C for 24 hours.

Polymer tubes and tubular silicone structures were used to introduce absorption centers inside the silicone phantom. Three different kinds of dyes namely, Direct Red 81, Methylene blue and Rhodamine 6G were used with 1% volume ratio. Prior

to its usage, the absorption spectra of the dyes were measured with a UV/VIS spectrophotometer and 1% dilution with deionized water. Polymer tubes were filled with the Methylene Blue dye. Silicone tubular absorption centers were fabricated by mixing Direct Red 81 with portions of the uncured silicone host material. The absorption centers were then introduced into the different layers of the phantom through a multistage procedure. This involves the creation of multilayered host material consisting of five layers for the inclusion of absorption centers at various layers. Each layer of the host material was fabricated carefully according to procedure described in the previous section. Initially, the base layer of the silicone phantom was fabricated and cured with an approximate thickness of 2.2 mm. Silicone tubular absorption center (0.45 mm diameter) mixed with Direct Red 81 and polymer tubes (1.8 mm outer diameter, 0.45 mm and 0.40 mm outer and inner diameter) were further introduced prior to the addition of the second layer of host material. The second layer of silicone host material was subsequently added to form an additional thickness of approximately 5.4 mm over which polymer tube (0.45 mm outer diameter) filled with Methylene blue dye was placed. Third layer of host material with an approximate thickness of 54 mm was further fabricated to hold the second polymer tube (0.45 mm and 0.40 mm outer and inner diameter) filled with Methylene blue dye. The fourth layer of host material was then fabricated over it with an approximate thickness of 27 mm. Silicone tubular absorption center (≈ 0.45 mm diameter) mixed with Direct Red 81 was then introduced and the fifth layer of host material with an approximate thickness 81 mm was fabricated over it to form the ultrasound-photoacoustic phantom. Additional acoustic heterogeneities were also introduced by placing a small strand of optical fiber (≈ 450 μm) across the fourth and fifth layer and a polymer tube

(0.50 mm and 0.43 mm outer and inner diameter) between the second layer of the silicone host material. Further to exhibit fluorescence, the phantom was administered with fluorescent microspheres. Fluorescent polystyrene spheres with an average diameter of $\approx 1\mu\text{m}$ were used to introduce fluorescent property to the phantom tissue. The carboxylate - modified poly-styrene microsphere coated with Nile red fluorescent material has an emission peak at 641 nm for 532 nm excitation. 1 ml of polystyrene spheres (PS) solution was diluted in 20 ml methanol as a precursor. 0.25 ml of diluted PS sample containing polystyrene spheres was then uniformly spread over the surface of the silicon phantom matrix and subjected to cure for 12 hrs.

APPENDIX D- Design of The Transmission and Reflection Mode High Frequency Photoacoustic Setup

The different configuration setups designed for reflection and transmission mode detection are shown in the next few pages. Besides these setups, few configuration setups using short and long distance objective lens have also been designed for dual – optical imaging. The different parts and components designed to build the high frequency photoacoustic experimental setup is being discussed in this section. Figure D. 1 - Figure D. 4 shows the assembled experimental configurations.

The 3D modelling software Solidworks was used to design the experimental set up. The main design requirement was to model and build a system with the reflection and transmission modes for different sensor positions.

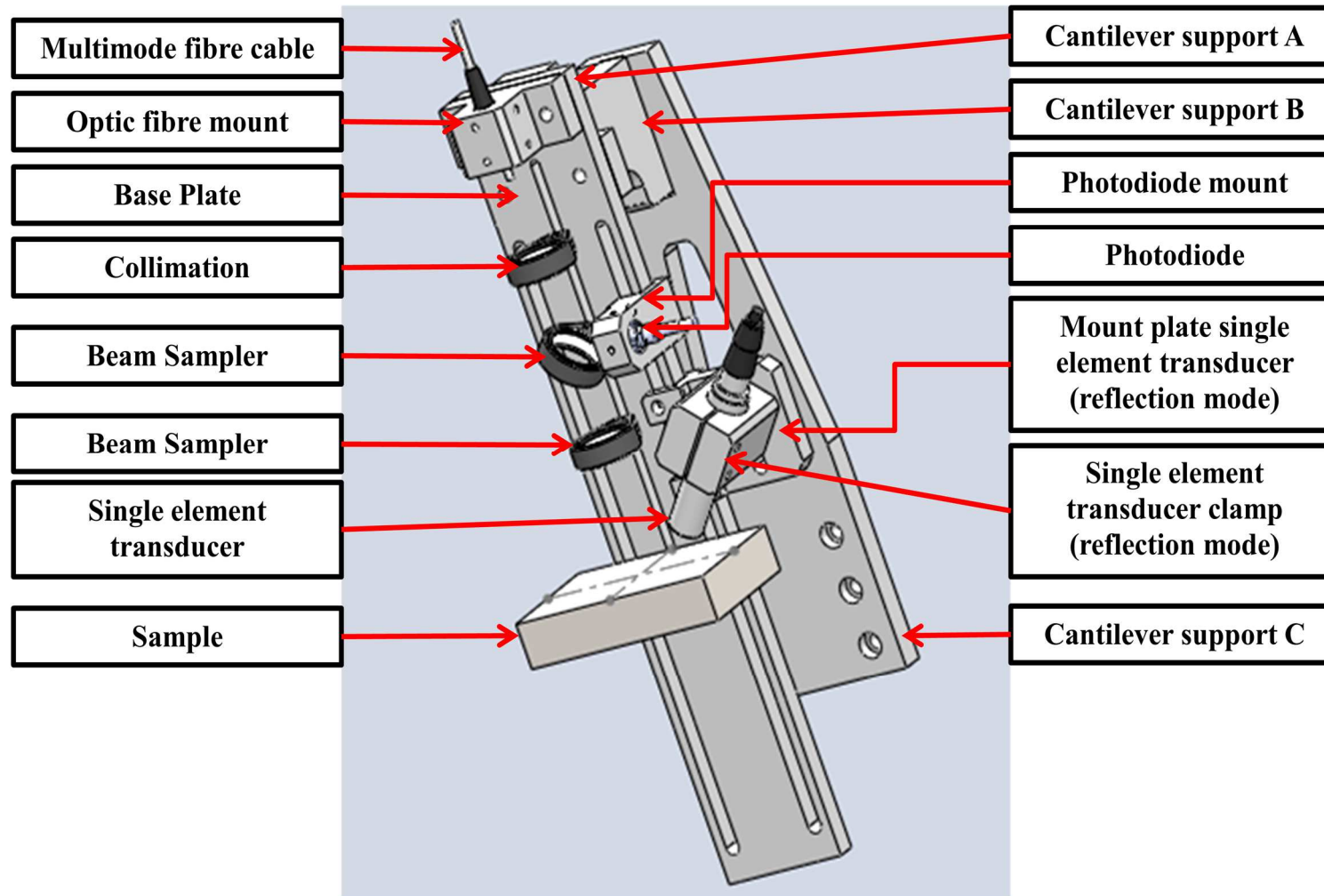


Figure D. 1 Single element reflection mode configuration setup

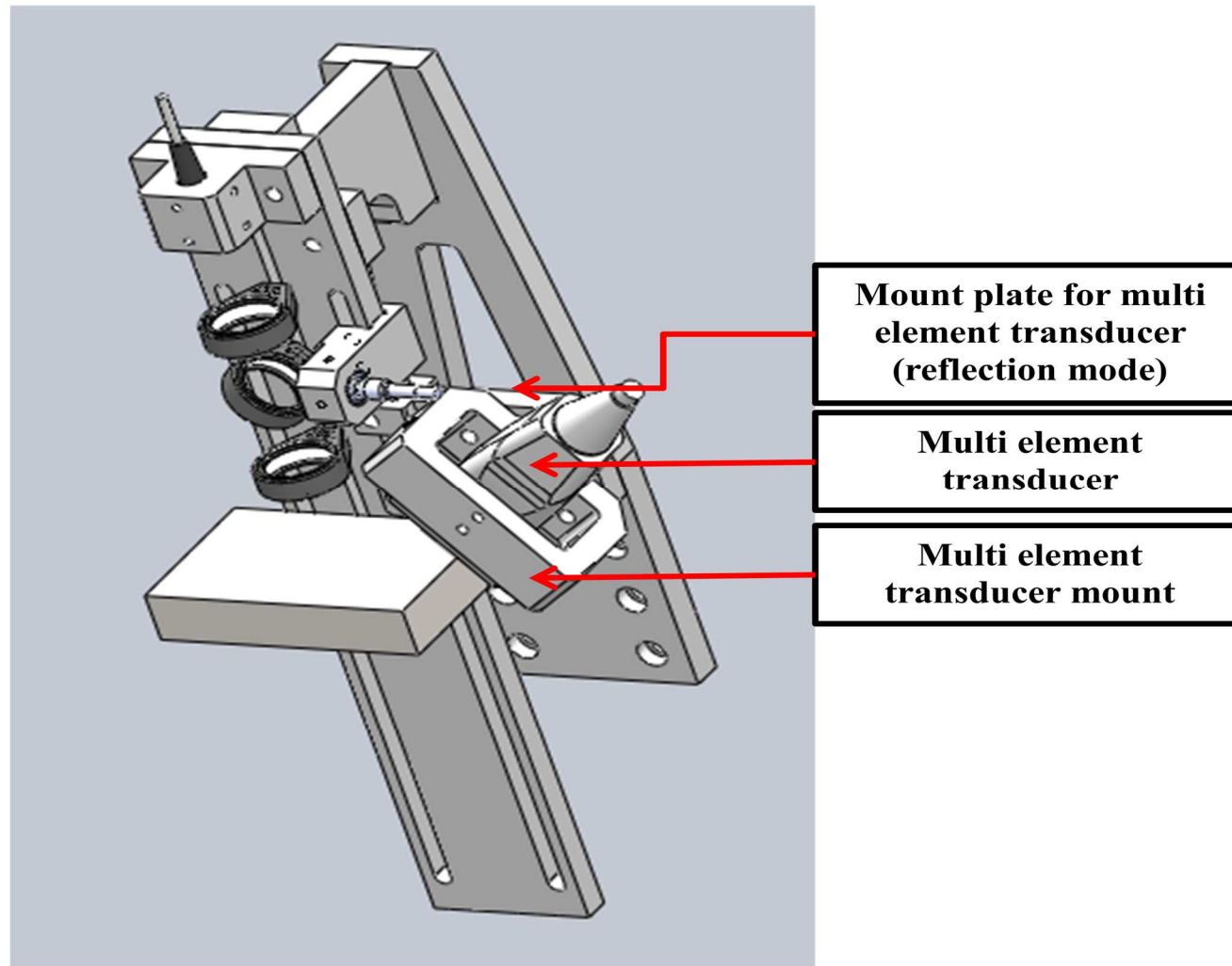


Figure D. 2 Multi element reflection mode configuration setup

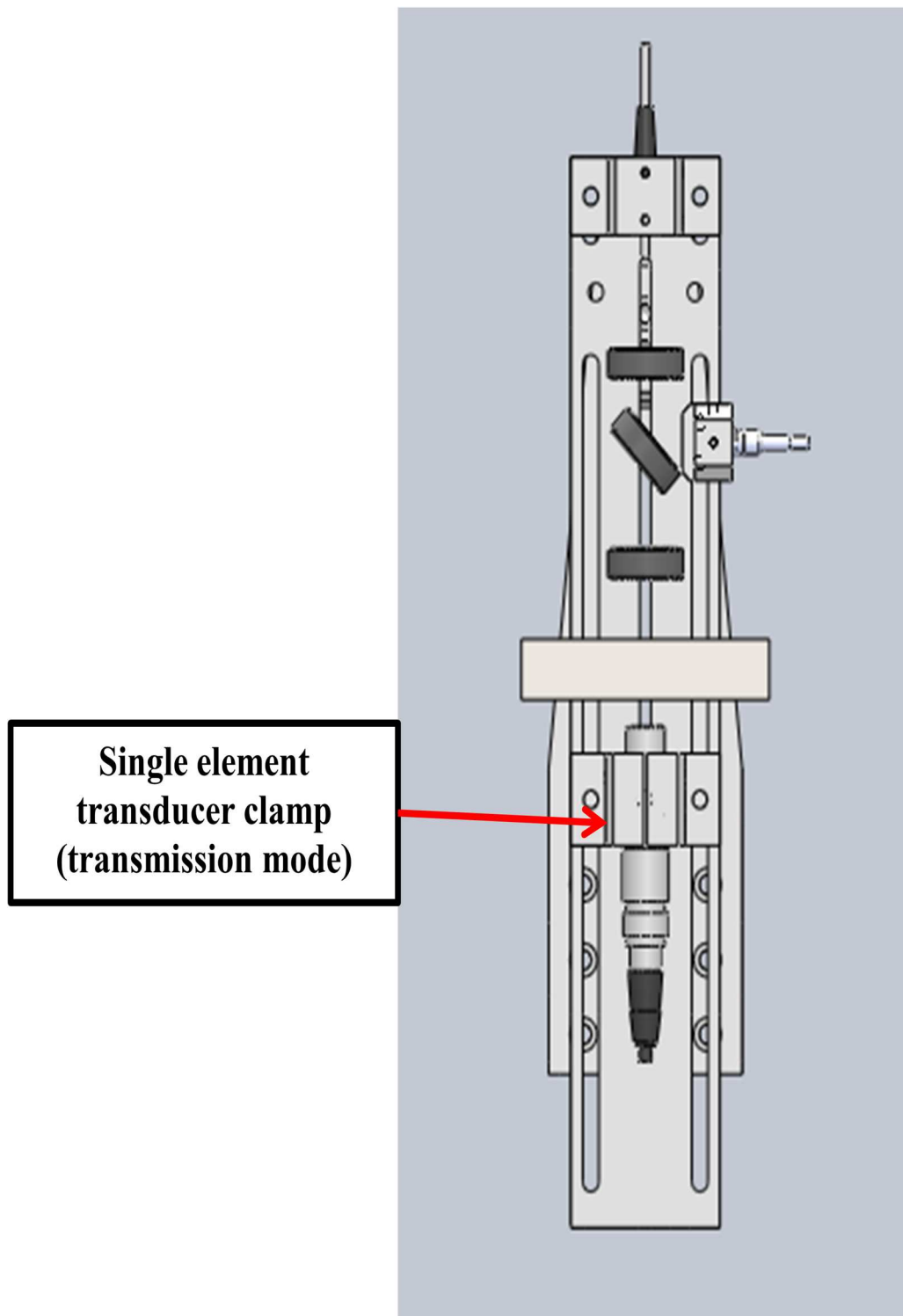


Figure D. 3 Single element transmission mode configuration setup

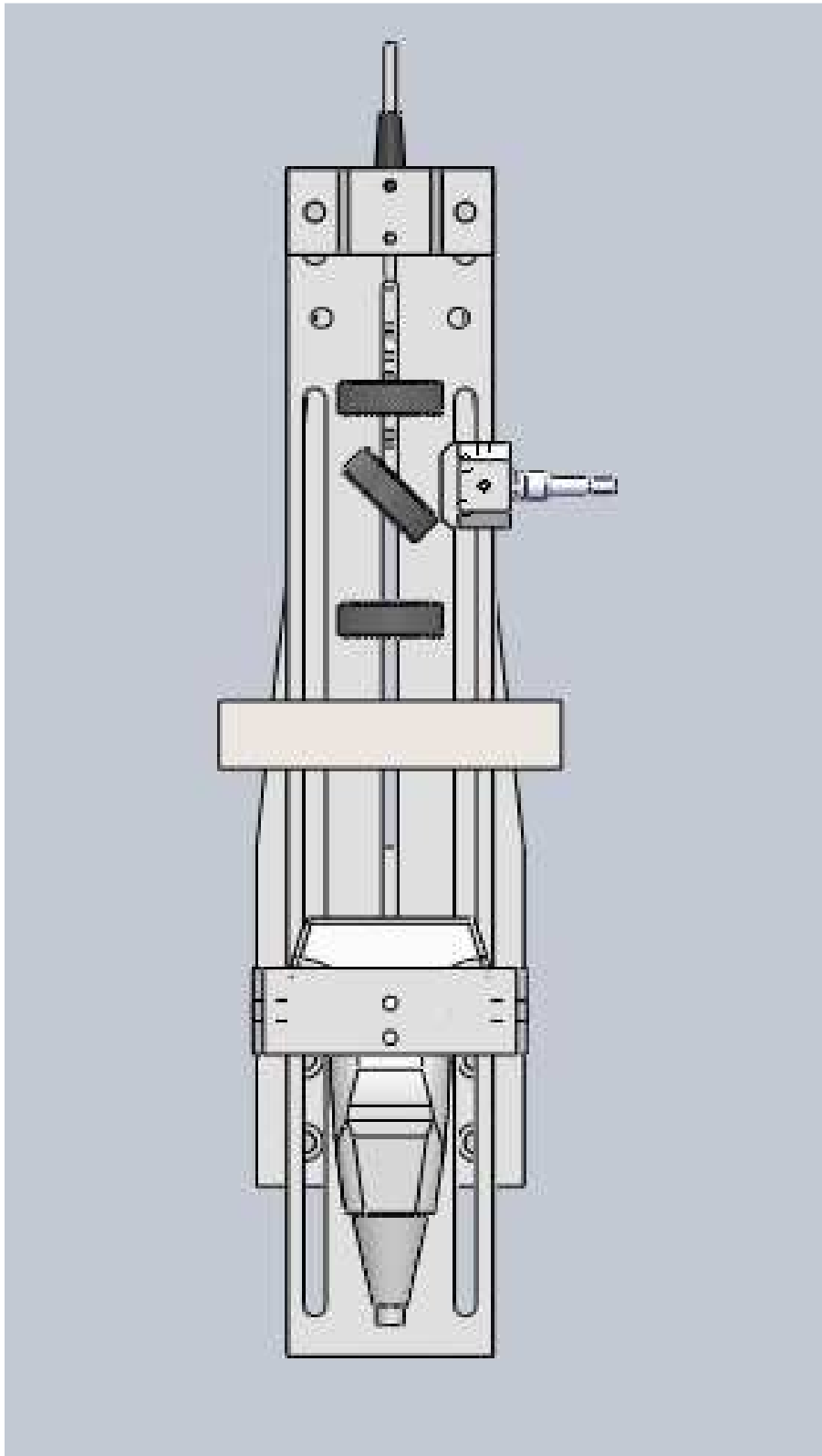


Figure D. 4 Multi element transmission mode configuration setup

Detailed design of the parts and components

The following section introduces the parts and components designed to meet the requirement. Aluminium being light and strong has been chosen for the fabrication of all parts.

Base Plate



Figure D. 5 Base Plate for mounting optical and acoustic components

Figure Figure D. 5 shows the design of the base plate where all the optical and acoustic components are mounted. Features like long slots are given to the design for positioning the optical components within the focal lengths. The overall dimension of the design is 350 x 60 x 10 mm.

Optic fiber mount

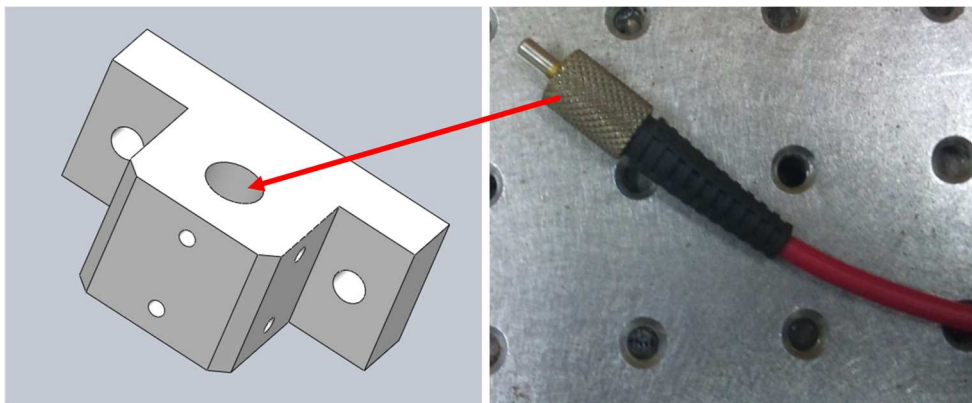


Figure D. 6 Optic fibre mount and cable

Figure D. 6 shows a mount designed for holding the optic fiber cable as a light source in an upright position. This part mounted on to the base plate. M3 tapped holes are drilled to keep the cable tight in position. Sharp edges are chamfered to protect from injuries. The overall dimension for the part is 60 x 35 x 35 mm.

Single element transducer clamp design for transmission mode detection

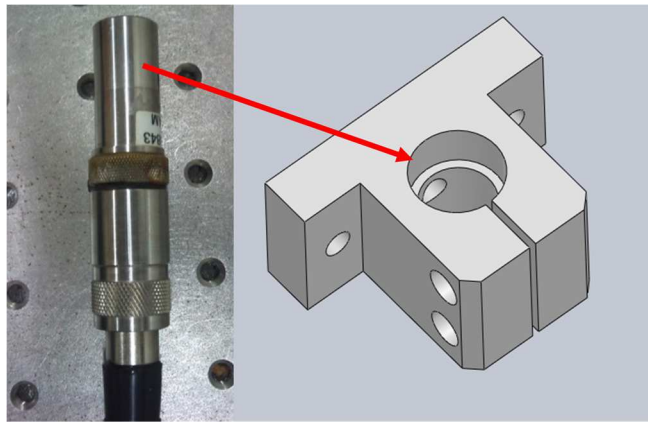


Figure D. 7 Single element transducer and the mount

The clamp design shown in Figure D. 7 holds the single element transducer in the transmission mode detection setup. The part is mounted to the base plate that acts like a clamp when tightened with screws and helps to position the transducer within the focal length of 0.75 inches (19.05 mm). The overall dimension of the part is 60 x 45 x 45 mm.

Short working distance objective lens mount

Figure D. 8 shows the part designed to clamp the short working distance objective lens to the base plate. This part can slide through the slots given in the base plate to adjust the distance between the sample and the objective lens to meet the focal length requirement. The overall dimension of the part is 60 x 48 x 46 mm.

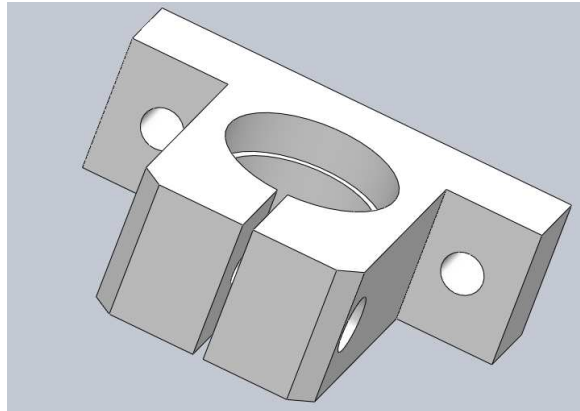


Figure D. 8 Short working distance objective lens mount

Multi element transducer mount for reflective and transmission modes

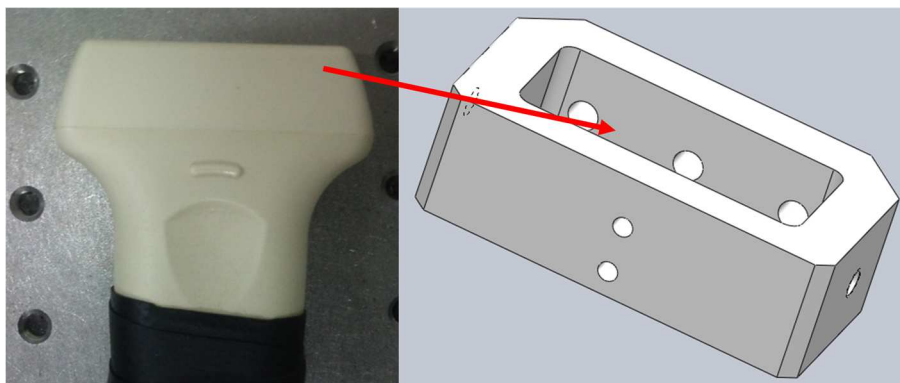


Figure D. 9 Multi element transducer and the mount

The multi element transducer and the holder used to mount it to the base plate are shown in Figure D. 9. The multi element transducer holder is compatible for using in both transmission and reflective mode detection systems. The overall dimension of the part is 80 x 45 x 45 mm.

Photodiode mount

Figure D. 10 shows the photodiode used for detecting the incident light along with the part designed to mount it to the base plate. This part is movable in the vertical axis to adjust the height accordingly for better reception from the beam sampler. The overall dimension of the part is 50 x 20 x 25 mm.

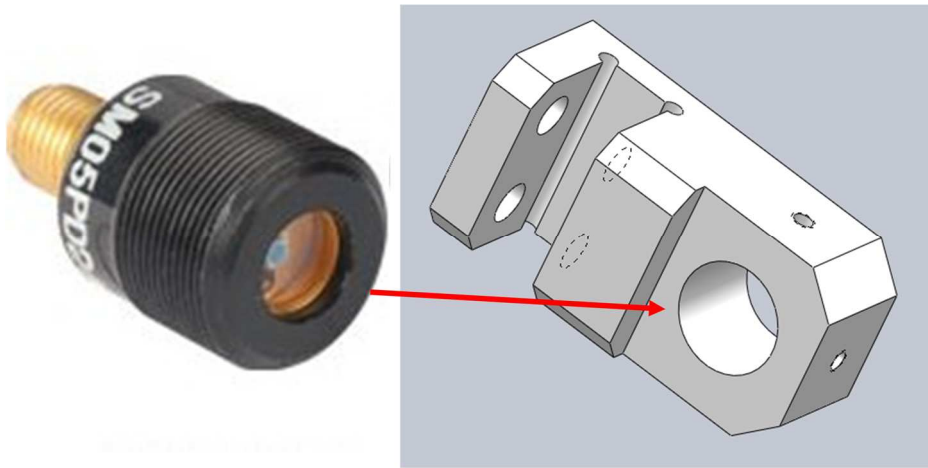


Figure D. 10 Photodiode and the mount

Long working distance objective lens mount

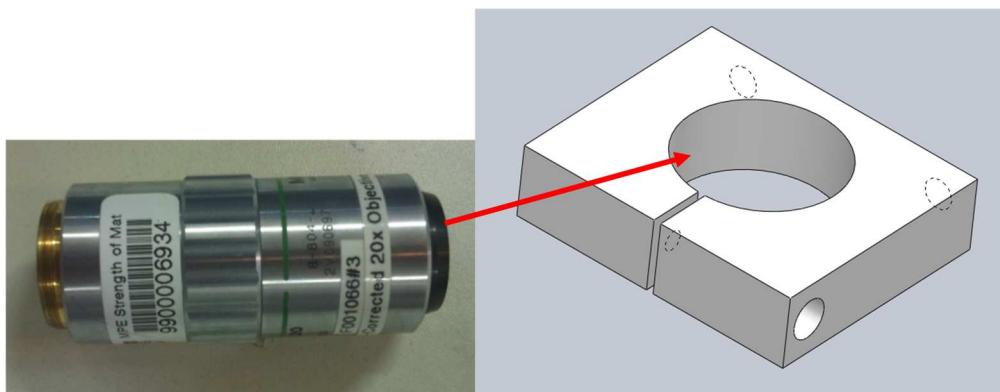


Figure D. 11 Long working distance objective lens and the mount

Figure D. 11 shows the long working distance objective lens and the clamp designed for fixing it to the base plate. The mount is movable in the vertical axis

for adjusting the distance with sample for meeting the focal length requirement of the lens. The overall dimension of the part is 50 x 50 x 15 mm.

Mount plate for single element transducer in reflective mode detection

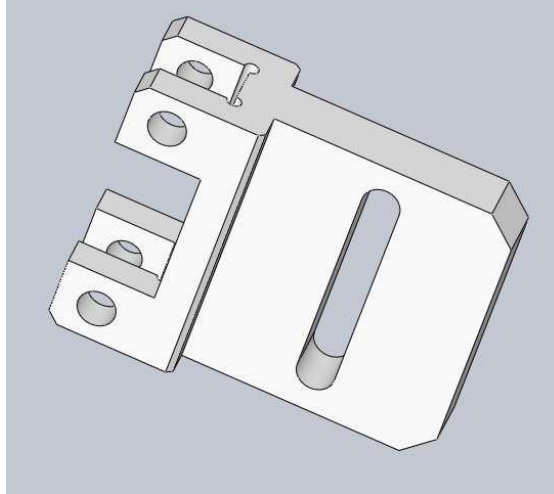


Figure D. 12 Mount plate for single element transducer in reflective mode detection

The part shown in Figure D. 12 is designed for setting the single element transducer in the reflection mode detection. In reflection mode, the single element transducer is held by a clamp design (shown in next section). The clamp is then fixed to this mount plate that is finally mounted to the base plate. The overall dimension of the part is 65 x 22.10 x 50 mm.

Single element transducers clamp for reflective mode detection

Figure D. 13 shows the part designed for clamping the single element transducer for reflective mode detection. This is part is fixed to the mount plate shown in previous section which is finally mounted to the base plate. The design easily allows the transducer to rotate in 360 ° for sensor directionality check. The overall dimension of the part is 45 x 32 x 30 mm.

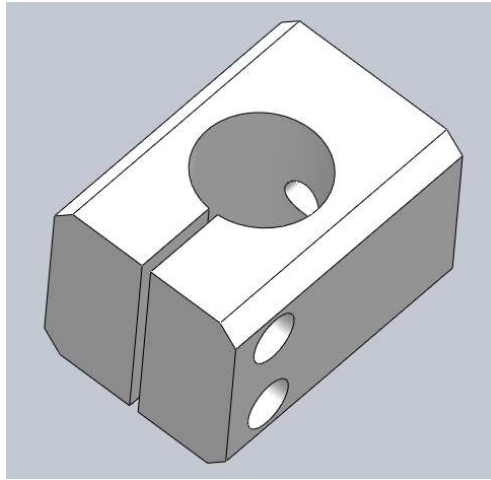


Figure D. 13 Single element transducer clamp for reflective mode detection

Cantilever beam support for base plate

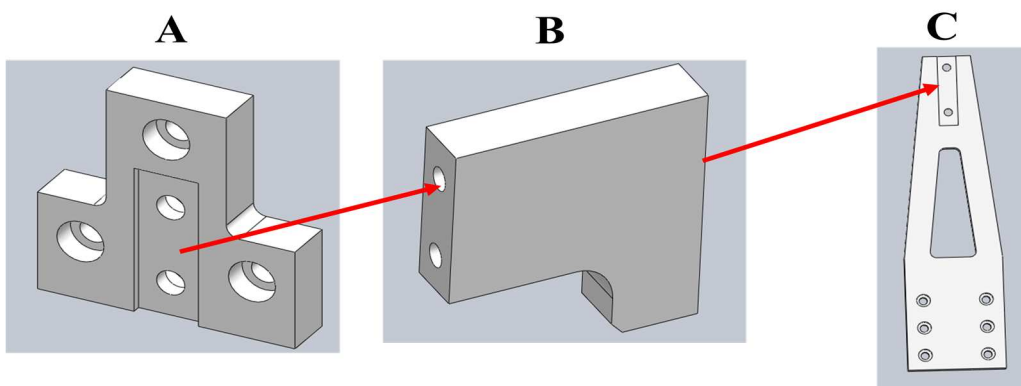


Figure D. 14 Cantilever Support for base plate

The base plate with all the optical and acoustic components is held vertically by a stiff cantilever beam support. There are three parts included in the design as shown in Figure D. 14. The overall dimension for A, B and C designs are 60 x 60 x 12 mm, 67 x 67 x 15 mm and 280 x 78 x 12 mm respectively.

Mount plate for multi element transducer in reflective mode detection

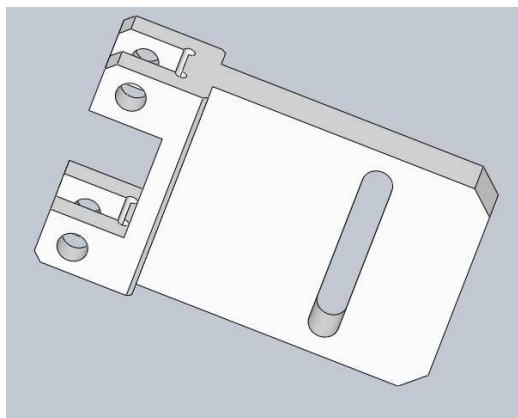


Figure D. 15 Mount plate for multi element transducer in reflective mode

The part shown in Figure D. 9 and Figure D. 15 is designed for setting the multi element transducer in the reflection mode detection. The mount design together with the transducer is then fixed to this mount plate that is finally mounted to the base plate. The overall dimension of the part is 85 x 22.10 x 50 mm.

Cuvette holder

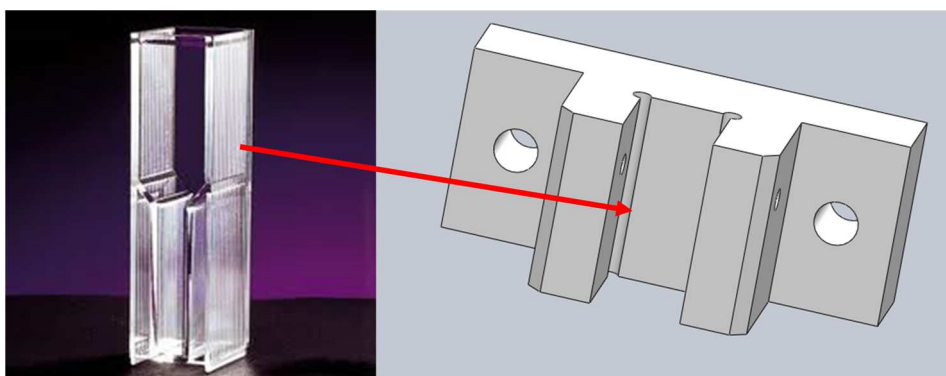


Figure D. 16 Cuvette holder

Figure D. 16 shows the cuvette and the designed holder for measuring the nanoparticles. This holder can be mounted to the base plate with variable heights according to the requirements. The overall dimension of this part is 60 x 30 x 25.40 mm.

Mount plate to the XYZ stage



Figure D. 17 Mount plate between the cantilever support and XYZ stage

A rectangular plate (Figure D. 17) of dimension 78 x 75 x 8 mm is designed to mount the cantilever support to the three axis moving stage.

APPENDIX E – Preparation of the Novel Nanohybrid

All starting materials were obtained from commercial suppliers and used as received. Electronic absorption spectra were recorded on a Shimadzu UV-3101 PC NIR scanning spectrophotometer. TEM images were captured by JEOL 2010 TEM at 200kV. SEM images were captured by Jeol-JSM-7600F. Raman spectra of the nanoparticles on cleaned silicon substrate were measured with a Raman microscope (LabRAM HR, Horiba Yvon). The excitation wavelength of the irradiating light was 633 nm (He-Ne Laser, Melles Griot) and signals were collected by using a $\times 100$ objective lens. FT-IR spectra were collected using Perkin Elmer FT-IR system (Spectrum GX).

Synthesis and characterization of AuNP, SiO₂@AuNP and GO-SiO₂@AuNP

For obtaining gold nanoparticles (AuNP) with uniform diameter (~20-25 nm) we followed the controlled nucleation procedure. In a typical experiment 1mL of HAuCl₄ (10 mM) was dissolved in 100 mL ultrapure water and refluxed for 5 minutes. To this vigorously stirring solution 0.6 mL of sodium citrate dehydrate (1% w/w) was added. The boiling solution turns purple indicating nucleation process. A gradual change of solution color to brilliant red indicates the formation Au nanoparticles. After 30min, the reaction was stopped and cooled to room temperature. Aliquots of the reaction mixture were centrifuged at 6000 rpm for 15 min and dispersed again in water to get the desired AuNP with ~20-25 nm which was characterized later using transmission electron microscopy (TEM). Figure E. 1 a shows the TEM image of as prepared AuNP's.

Freshly prepared AuNP's were then encapsulated with silica shell with a thickness of c. a. 44 nm using a modification process. 3 mL of as synthesized gold nanoparticle solution was concentrated by centrifuged at 6000 rpm for 15 min. The concentrated gold nanoparticle was dispersed in 0.5 mL ultrapure water followed by addition of 2.5 mL prepared isopropyl alcohol containing 5 μ L of 4-mercaptobenzoic acid (5 mM). This adding process was carried out under vigorously vortexing. After incubating for 30 min under room temperature without stirring, 1.2 μ L of triethyl orthosilicate (TEOS) and 90 μ L of ammonia solution were added for condensation. After 15 mins, 0.5 μ L APTES was added into the solution and then incubated over night at room temperature to ensure the complete encapsulation. Further purification was carried out before using SiO₂@AuNP for the next step. 1 mL of obtained solution was centrifuged at 6000 rpm for 15 min and dispersed again in 1 mL of ultrapure water. This process was repeated 3 times to separate the empty gold core silica spheres from SiO₂@AuNP. Figure E. 1 b and Figure E. 1 d shows the corresponding TEM and Field Emission Scanning Electron Microscopy (FE-SEM) images of SiO₂@AuNP.

GO was synthesized from natural graphite powder by modified Hummer's method which was then converted to GO-COOH based on the previous reported procedures²⁶. The readily prepared GO sheets can be dispersed well in aqueous solutions. GO sheets were then characterized using TEM and FT-IR spectroscopy [Figure E. 2 and Figure E. 3]. GO sheets were then centrifuged at 1400 rpm for 30 min and collected the supernatant solution. 0.5 mL of GO suspension in water was then added into the suspension of 0.5mL SiO₂@AuNP (—NH₂ modified, 0.1 mg/mL).

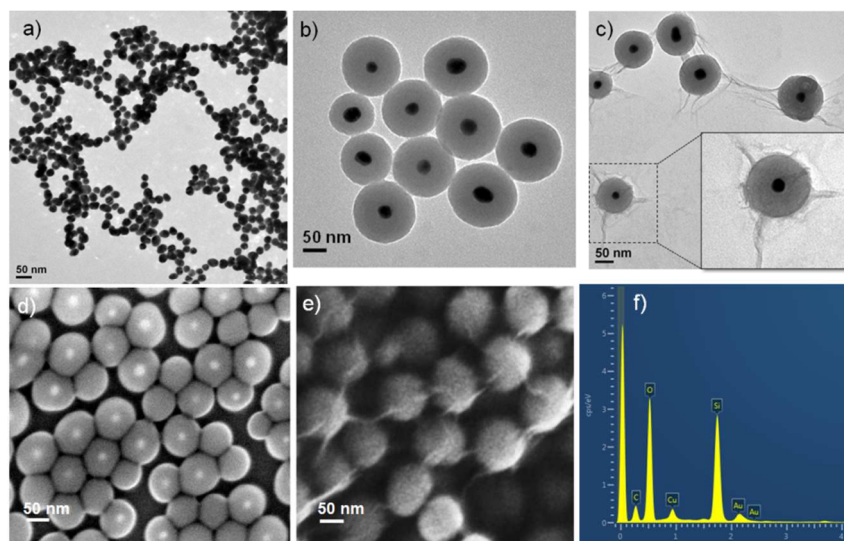


Figure E. 1 Transmission electron microscopy images (TEM) of as prepared (a) gold nanoparticles (AuNP), (b) SiO₂@AuNP and (c) GO-SiO₂@AuNP (Inset shows zoomed image of a single hybrid). d) FE-SEM image of SiO₂@AuNP and e) Scanning Transmission Electron Microscopy (STEM) image of GO-SiO₂@AuNP on TEM grid. f) Energy-dispersive X-ray spectroscopy (EDS) elemental mapping of GO-SiO₂@AuNP in Cu-TEM grid.

The reaction mixture was stirred at room temperature for 24 h to complete the electrostatic wrapping process to get GO-SiO₂@AuNP. After 24 h, GO-SiO₂@AuNP was collected by centrifugation at 6000 rpm and repeatedly washed with water to remove any suspended GO-sheets. The TEM image Figure E. 1 c shows freshly prepared GO-SiO₂@AuNP. Clear wrapping of ultrathin GO layer over SiO₂@AuNP is visible in the zoomed image (inset of Figure E. 1 c). We then carried out the Scanning Transmission Electron Microscopy (STEM) and Energy dispersive X-ray Spectroscopy (EDS) analysis of the final hybrid GO-SiO₂@AuNP on TEM Cu-grid. A uniform coating of ultrathin layer of GO covering SiO₂@AuNP is visible from STEM. Elemental and chemical characterization of the GO-SiO₂@AuNP was carried using EDS (Figure E. 1 f). EDS reveals strong signals corresponding to C, Au, Si and O present in the sample, which clearly indicates the composition of the formed plasmonic core-shell nano hybrids, GO-SiO₂@AuNP's.

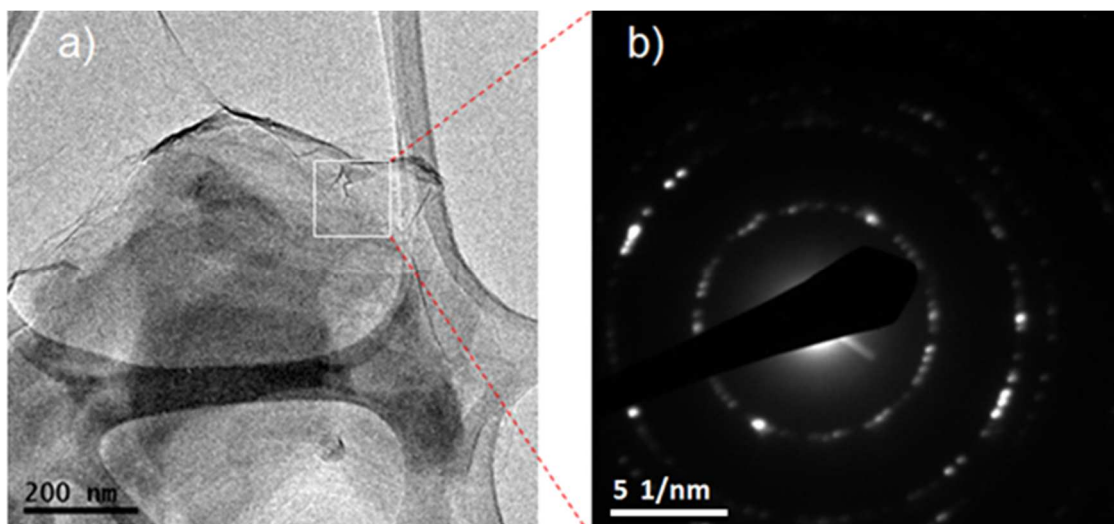


Figure E. 2 a) TEM image of multilayer GO sheets, and b) selected area electron diffraction pattern (SAED) of multilayer GO sheets.

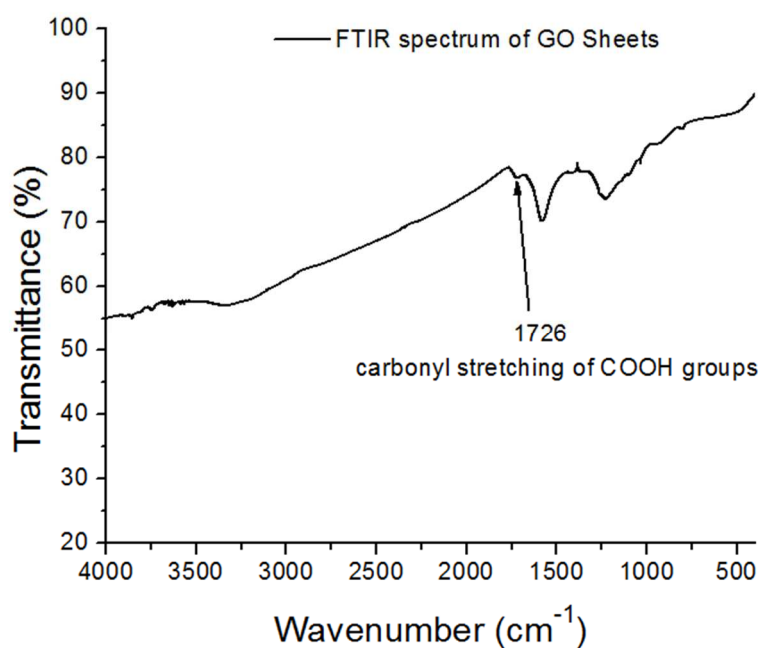


Figure E. 3 FT-IR spectrum of GO sheets.

Since Raman spectroscopy is particularly well suited to surface morphology characterization of carbon containing materials, to further confirm the surface modifications, we measured the Raman spectra of AuNP, SiO₂@AuNP and GO-SiO₂@AuNP (Figure E. 4) on plasma cleaned silicon wafers. It was observed that

the three spectrums have characteristic vibration bands of silicon at 520 and 933 cm^{-1} , which corresponds to silicon present in the substrate. Notably, for AuNP's in addition to the silicon peaks, a peak at 1580 cm^{-1} indicates the presence of ν (C—C) aromatic ring chain vibrations which corresponds to the stabilizer mercapto benzoic acids used during AuNP synthesis. Interestingly, the nano hybrid GO-SiO₂@AuNP clearly shows a combination of characteristic peaks from GO-sheets such as 'G' and 'D' band at 1593 cm^{-1} and 1332 cm^{-1} respectively. Thus the Raman spectral analysis provides doubtless evidence for the wrapping process of ultrathin GO layer on SiO₂@AuNP's.

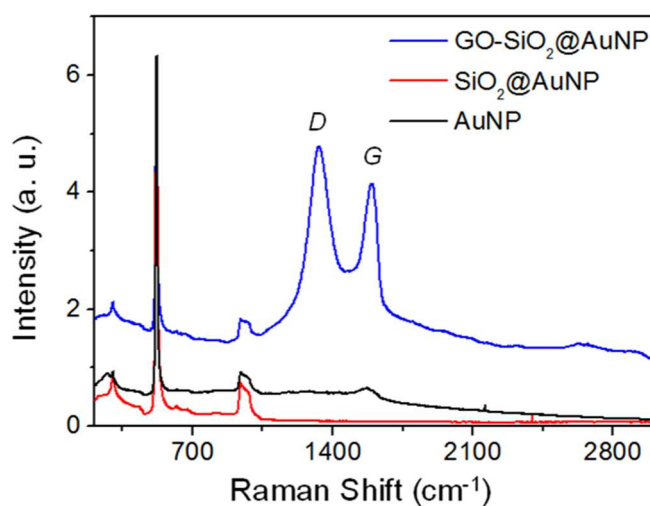


Figure E. 4 Raman spectra of AuNP, SiO₂@AuNP and GO-SiO₂@AuNP.

APPENDIX F – Low Frequency Photoacoustic Studies

Introduction

Based on the frequency of the generated photoacoustic wave, photoacoustic investigations can be broadly classified into two forms; 1) Low frequency photoacoustics and 2) High frequency photoacoustics. This section mainly deals with the low frequency photoacoustic investigations for conducting thermal diffusivity measurements.

The potential of using low frequency photoacoustics for determining the thermal properties of a sample would be further investigated as detailed in the following sections.

Significance of Thermal Diffusivity Measurement

Evaluation of heat-transfer mechanisms and physical properties of biological tissues occurring in tissues have attracted a great attention because of its importance to physical diagnostics and therapies etc. Determination of the thermal diffusivity of biological samples provides a direct method for measuring the energy absorbed by the sample (Sathiyamoorthy and Vijayan 2007) and holds significant role in studying the optical and thermal energy distribution in the tissue during various optical imaging and photothermal applications. The thermal diffusivity measurements are also essential in formulating the energy deposition dosage in biosamples during diagnostic investigations to avoid unwanted tissue burns and thermal coagulations. Thus the proposed methodology can be used to

derive various laser irradiation parameters such as incident fluence and exposure time for further photoacoustic and fluorescence imaging applications.

Various methods(Valvano, Cochran et al. 1985, Telenkov, Youn et al. 2001) have been reported to determine the thermal diffusivity of non-homogenous biological samples. However most of these techniques are destructive and requires careful sample preparation under suitable experimental conditions. Investigations performed on biological tissue often require employing safer techniques. In this context optical technique utilizing non-ionising radiation has been subjected to an appealing area of research.

Various photothermal and photoacoustic methods in multiple configurations have been employed in determining the thermal diffusivity of inhomogeneous biological samples(Qiu, Zhang et al. 2008). Photoacoustic study of the thermal properties of biological tissues using Polyvinylidene fluoride (PVDF) film transducer as detector was performed by Qui et al.(Qiu, Zhang et al. 2008). Photoacoustic piezoelectric (PAPE) technique utilizing PZT transducers has been also reported for determining thermal diffusivity of biological samples(Gao, Zhang et al. 2005). Thermal properties of biomaterials have been also measured using self-heated thermistors by Valvano et al(Valvano, Cochran et al. 1985). Balageas et al. used pulsed photothermal method in human skin for characterizing the thermal properties(Balageas, Krapez et al. 1986) and thermal diffusivity of human epidermis was measured using infrared radiation by Telenkov et al.(Telenkov, Youn et al. 2001).

Low frequency PA investigations can be performed under various configurations and open photoacoustic cell (OPC) configuration is one of the recently emerged photoacoustic detection schemes which can be effectively utilized in determining the thermal and optical properties of solid samples with a relatively simple and inexpensive experimental set-up. The merits of adopting OPC over other techniques include the non-requirement of any sample preparation and the potential capability of this technique to perform a variety of investigations with highly reflective samples as well as with powdered samples. OPC in transmission configuration proves to be an inexpensive and simpler method in performing PA investigations. No works have been reported so far in determining the thermal diffusivity of biological samples or tissue mimicking phantom samples using OPC configuration. Hence this work adopts OPC based photoacoustic investigations for thermal diffusivity measurements and the following section illustrates the fundamental theoretical concepts of this particular technique.

Theory

Thermal diffusivity α_a in general is the measure of heat diffusion and is expressed mathematically as,

$$\alpha_a = k / \rho C_p \quad \text{F-1}$$

Where k is the thermal conductivity, ρ is the density and C_p specific heat capacity of the sample. The OPC configuration in heat transmission configuration is depicted in Figure F. 1.

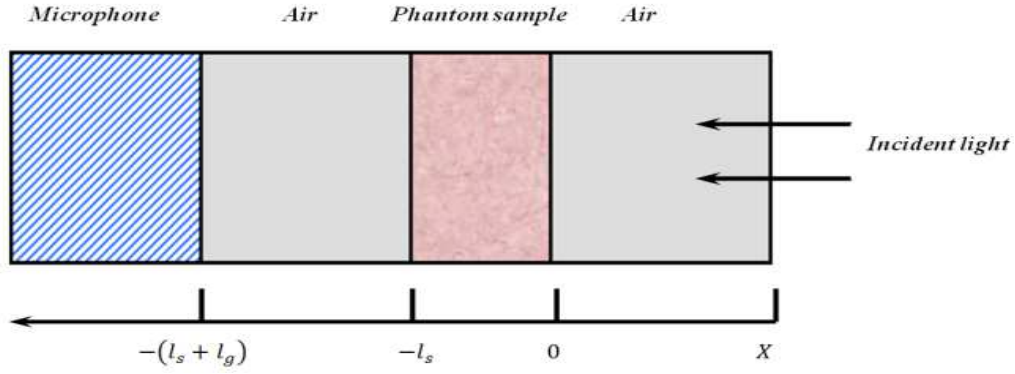


Figure F. 1 Schematic of OPC configuration in heat transmission mode

For the phantom sample in our study mounted over the OPC, the entire light incident on the sample surface is absorbed and periodically heated creating thermal waves at $X=0$, which further penetrates through the sample and propagates to the rear end. Thermal diffusion length μ can be obtained from the expression

$$\mu = \sqrt{2\alpha_a/\omega} \quad \text{F-2}$$

where α_a and ω denotes the thermal diffusivity and modulation frequency of the incident light. The periodic heating and generation of thermal waves at the air sample interface results in an acoustic piston effect in the air column between the microphone and the sample. The fluctuations in pressure lead to the generation of acoustic waves in the air chamber and can be captured using a microphone. Assuming a optically opaque sample and negligible heat flux into the air in contact with the irradiated surface of the sample, the pressure fluctuation inside the chamber is given by (Rosencwaig and Gersho 1976, George, Vallabhan et al. 2002)

$$Q = \frac{\gamma P_0 I_0 (\alpha_{as} \alpha_{ag})^{1/2}}{2\pi l_g T_0 k_s f \sinh(l_s \sigma_s)} e^{j(\omega t - \frac{\pi}{2})} \quad \text{F-3}$$

, where γ is the ratio of specific heat capacity of air, P_0 is the ambient pressure, T_0 is the ambient temperature, I_0 is the radiation intensity, f is the modulation frequency, α_{ai}, k_i, l_i are thermal diffusivity, thermal conductivity and length of the medium $i = g$ refers to gas and $i = s$ refers to solid sample. The complex

quantity $\sigma_i = (1 + j)a_{ai}$, where $a_i = \left(\frac{\pi f}{\alpha_a}\right)^{\frac{1}{2}}$ is the thermal diffusion coefficient of

the medium i . The expression in equation F.3 can be reduced considering whether the sample is thermally thick or thermally thin. A sample is considered to be thermally thick when heat is produced due to the absorption of light and if heat waves from the sample surface penetrates through the air column inside the photo acoustic cell. In thermally thin samples the heat waves are not transferred instead the pressure waves passes through the air column. For a thermally thin sample with the condition ($l_s a_{as} \ll 1$), equation F.3 can be deduced into

$$Q = \frac{\gamma P_0 I_0 (\alpha_g)^{\frac{1}{2}} \alpha_{ag}^{\frac{1}{2}} \alpha_{as} e^{j(\omega t - \frac{3\pi}{4})}}{(2\pi)^{\frac{3}{2}} T_0 l_g l_s k_s f^{\frac{3}{2}}} \quad \text{F-4}$$

Equation necessitate that the frequency varies $f^{-1.5}$ with the photo acoustic signal amplitude and the phase obtained from a thermally thin sample is not sensitive to the variation in modulation frequency. When the sample is thermally thick with the condition ($l_s a_{as} \gg 1$), then equation F.3 reduces to,

$$Q = \frac{\gamma P_0 I_0 (\alpha_{ag} \alpha_{as})^{\frac{1}{2}} \exp\left[-l_s \left(\frac{\pi f}{\alpha_{as}}\right)^{\frac{1}{2}}\right]}{\pi T_0 l_g k_s f} e^{j(\omega t - \frac{\pi}{2} - l_s a_s)} \quad \text{F-5}$$

From the above expression it is clear that the photo acoustic signal varies exponentially with the modulation frequency according to $[(\frac{1}{f}) \exp(-b\sqrt{f})]$,

where $b = l_s \left(\frac{\pi}{\alpha_{as}}\right)^{\frac{1}{2}}$ and the phase decreases linearly with $b\sqrt{f}$. Thus, thermal diffusivity α_{as} can be obtained either from the amplitude or phase data with respect to the modulation frequency for the optically opaque and thermally thick sample. From the amplitude data α_{as} obtained from fitting the coefficient b and with phase data, α_{as} can be obtained from the slope of phase plot as a function of \sqrt{f} .

Experimental Set-up

Experiments for determining the thermal diffusivity of the samples were carried out using Open Photoacoustic Cell (OPC) configuration. The experimental setup is depicted in Figure F. 2. The photoacoustic cell was fabricated with a solid aluminium cylinder of outer diameter 16 mm. Aluminium was chosen for fabricating the PA cell due to its large thermal mass. The PA cell had an acoustic chamber of 14 mm in diameter and thickness of 2 mm. The distance between the surface of PA chamber and the microphone was varied, by screw arrangement, to achieve resonance for maximum PA signal. The acoustic chamber was acoustically coupled to sample by a channel of length 5 mm and an opening of outer diameter 2.5 mm. The microphone (Brüel & Kjaer) with sensitivity of 51.3 mV/Pascal and dimension of diameter 13mm was used as the PA detector with a correction factor of -0.2 dB, cartridge capacitance of 19.9 pF with leakage resistance tested at 85% relative humidity. The microphone was inserted along the bore at the rear side of the PA chamber and was vacuum sealed using greased O ring to provide adequate insulation from external disturbances. The acoustic wave propagation from the

heated sample to the air chamber was achieved by placing the sample over the photoacoustic cell orifice which had an internal diameter of 2.5 mm.

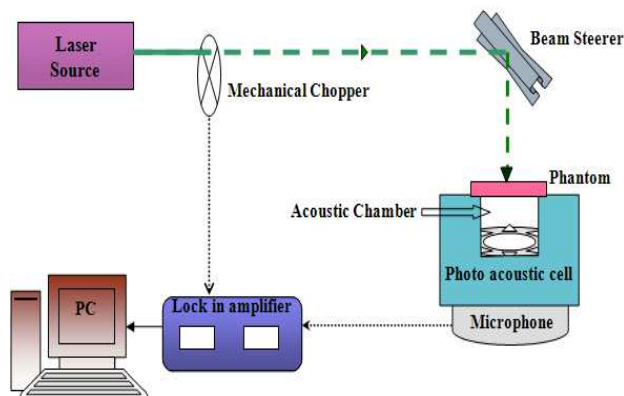


Figure F. 2 Schematic of OPC experimental setup

Continuous wave laser emission at 532 nm (SPR excitation wavelength of 50 nm gold nanosphere) at 5 mW power from a solid state laser (Suwtech LDC-1500) was used as the excitation source. Mechanical chopper (SciTech instruments 300CD) was used to modulate the pump laser beam at the desired frequency and the modulated laser beam of 1 mm diameter was made to fall over the sample surface that covered the opening of the acoustic chamber as shown in Figure F. 2.

The modulated energy deposition over the sample resulted in periodic heating of the sample which further resulted in the periodic heating of the air column inside the photoacoustic chamber. The periodic heating of the air column gave rise to pressure variations inside the chamber which was transformed itself as photoacoustic signals. The photoacoustic signal generated inside the photoacoustic cell was acquired by the microphone and the signal was fed into a dual phase lock-in amplifier (Stanford research systems SR830) via a pre-amplifier. The personal computer (PC) triggered the lock-in amplifier to drive the chopper at variable

frequencies and recorded the corresponding amplitude and phase of the resultant photoacoustic signal acquired by the lock-in amplifier. The amplitude and phase values of the photoacoustic signal were recorded as a function of the chopping frequency and the results are discussed in the ensuing section.

Thermal Diffusivity Measurement of Colon Phantom Tissue

Recently non biological researchers used the artificial phantoms as real tissue usage requires special clinical treatment, controlled environment and lab, to study the physical and chemical properties. The phantom used to study biological properties should exactly mimic the real tissue. The colon phantom procured from (Simulab Corp.) was used as the test sample in the present study. The phantom tissue was reported to exhibit similar optical and thermal properties as with the human colon tissue and has been employed in various studies (Sujatha, Murukeshan et al. 2003, Sujatha and Murukeshan 2004, Murukeshan and Sujatha 2005, Murukeshan and Sujatha 2007).

Figure F. 3 represents the image of the colon phantom tissue used for the present study. The thickness of the phantom was measured under a calibrated optical microscope (Figure F. 4) and found to be about 0.479 mm.



Figure F. 3 Image of colon phantom tissue



Figure F. 4 Microscopic image of Phantom

Figure F. 5 represents the optical absorbance spectrum of the phantom. The optical density (OD) of the phantom was then determined to be about 1.71.

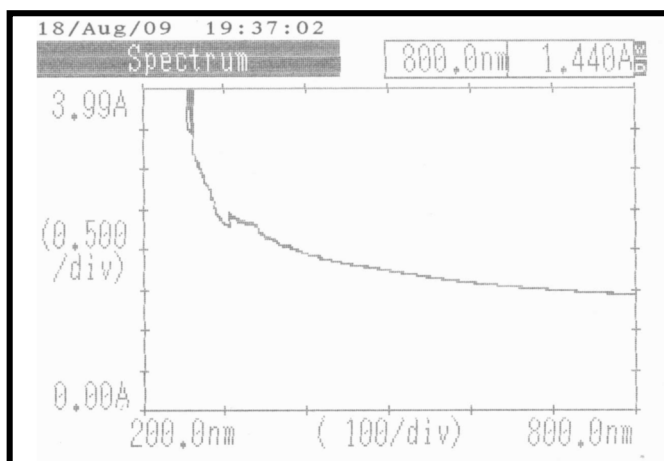


Figure F. 5 Optical absorbance spectrum of phantom

As the sample has low OD, it can be considered as thermally thick sample and is confirmed by phase dependence of PA signal on modulation frequencies. Figure F. 6 shows the phase dependence of the PA signal as a function of the square root of the chopping frequency.

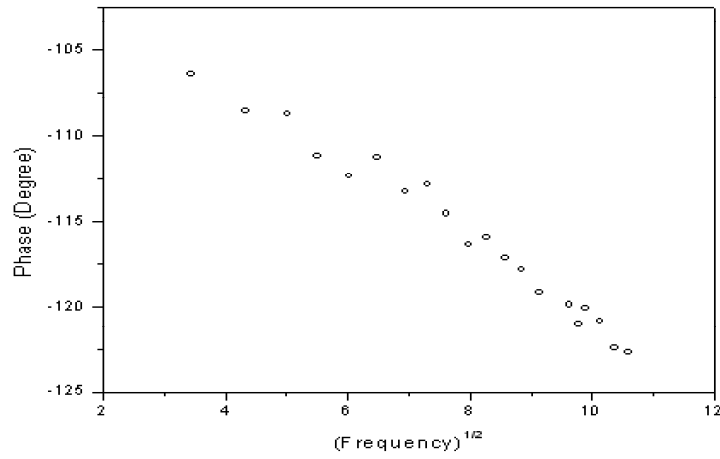


Figure F. 6 PA phase as function of the square root of frequency

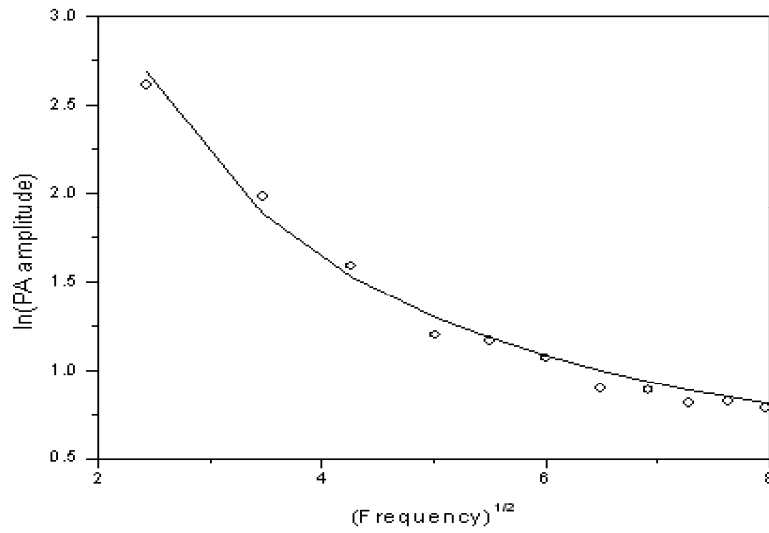


Figure F. 7 Logarithmic of PA amplitude as function of the square root of frequency

Figure F. 7 represents the logarithmic of PA amplitude as function of the square root of frequency. The thermal diffusivity values were then obtained from the theoretical fit of the experimental results with equation F.5 Circles represents the experimental data points and solid lines represent the theoretical fit.

The deviations of the plot from linear behaviour are due to the contribution of an additional phase by the thermoelastic bending of the thermally thick sample. The thermoelastic bending arose due to the temperature gradient developed along the thickness of the sample during laser excitation. From the theoretical fit, the thermal diffusivity was determined and found to be $5.65 \times 10^{-4} \text{ m}^2 \text{ s}^{-1}$. Based on the operational parameters, a larger value of thermal diffusivity contributed to a faster response as well as a slower rate to possible thermal damage. No physical damage of the material due to heating was observed.

Thermal Diffusivity Variations in Nanoparticle Administered Phantom Tissues

Optical imaging modalities supported by specific contrast enhancing nanoplateforms have gained much attention as a viable tool for various disease diagnostics and biological interventions. As discussed in section 2.7, plasmonic nanoparticles are one of the most favoured classes of contrast agents for various optical imaging studies. However, the presence of plasmonic nanoparticles alters the inherent physical and optical properties of the embedding tissue and introduces undesirable ambiguities into the efficacy of the particular modality. This is because the sensitivity, target specificity and efficiency of these techniques are highly dependent on the absorbed energy within the sample and therefore it is highly desirable to resolve the energy absorption inside the tissue. Hence, it is highly desirable to investigate the behaviour energy absorption in nanoparticle administered tissue. In this context, this work aims to study the thermal diffusivity variations in Poly Vinyl Alcohol (PVA) phantom tissue doped with gold nanospheres. The following sections detail the various aspects of thermal

diffusivity studies performed with bare PVA samples and PVA samples doped with gold nanoparticles.

Low frequency photoacoustic measurements with the OPC system were further performed. From the simulation results given in section 5.2.1.6 it was evident that gold nanospheres with an average diameter 40 nm - 50 nm exhibits good absorption and scattering properties and has a resonance peak around 532 nm which in turn matched with the laser wavelength used for the experiments. Therefore, gold nanospheres with an average diameter of 50 nm were synthesized and thermal diffusivity measurements were further performed in PVA phantom samples as detailed in the following section.

Synthesis of gold nanospheres

Gold nanospheres were synthesized by conventional technique which involved aqueous synthesis of gold particles by reducing $Au(III)Cl_3$ with trisodium citrate. Initially the citrate salt acted as a reducing agent to reduce the $Au(III)^{3+}$ ions to $Au(0)$ and later as a stabilizing agent by forming a layer of citrate ions over the gold nanoparticle surfaces. Citrate ion layer formed on the gold nanoparticles induces electrostatic repulsion between individual particles to keep them well dispersed in the medium. By this method, spherical nanoparticles with acceptable uniformity were obtained. The reduction process proceeded at a slow pace and took approximately 60 minutes for the complete reduction of $Au(III)^{3+}$, imparting a bright red color to the colloid (due to surface plasmon resonance) indicating the formation of Au particles.

The formation of gold nanoparticles confirmed by transmission electron microscopy (TEM) showed an average diameter of 50 nm and the obtained result is shown Figure F. 8. From the FDTD simulations presented in section 5.2.1.6, it was observed that the gold nanosphere with a diameter of 50 nm exhibits highest absorption at an excitation wavelength range of 530 nm – 536 nm and was experimentally confirmed with the absorption spectra of the nanoparticle solution given in Figure F. 9 b obtained from UV-Visible absorption spectroscopy.

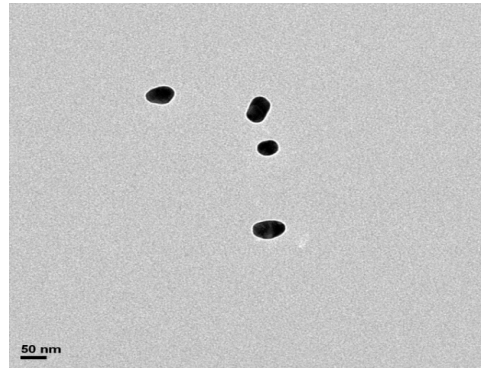


Figure F. 8 TEM image of Gold nanoparticle

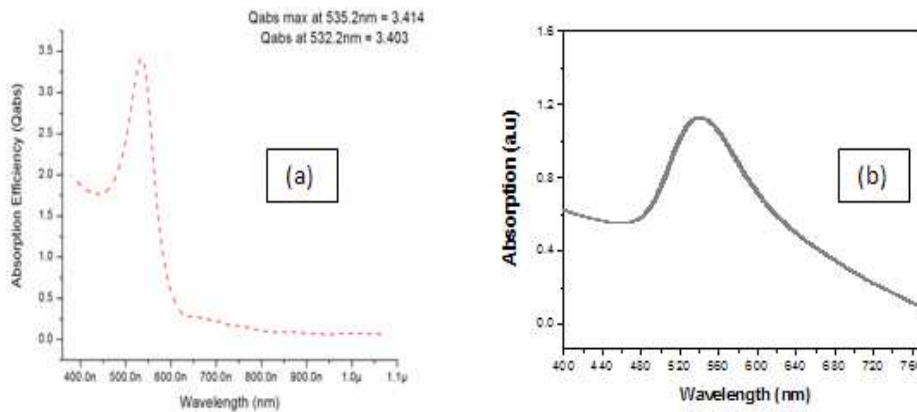


Figure F. 9 Absorption spectra of gold nanosphere. (a) Absorption efficiency (Qabs) obtained from FDTD simulation, (b) UV – Visible absorption spectrum of the nanoparticle solution

3.028g of PVA gel is then mixed with 1ml of gold nanoparticle solution to form the doped PVA samples with 3mm thickness and diameter of 15mm as given in Figure F. 10.

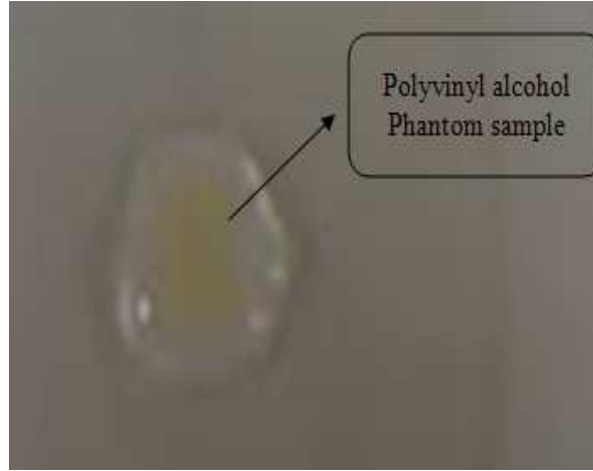


Figure F. 10 Doped PolyVinyl Alcohol sample

The optical absorption of gold nanoparticle showed that it has an absorption peak around 536 nm and has an optical density of about 0.16 at 536 nm. Thermal diffusivity experiments were repeated ten times for better SNR ratio and the average values were considered for further analysis. The mean amplitude of the PA signal was plotted against the square root of the frequency for bare PVA sample as well as PVA doped with gold nanospheres as shown in Figure F. 11 . The thermal diffusivity values were then obtained from the theoretical fit of the experimental results with equation F.5.

From the theoretical fit of the experimental results from the PA investigations, the thermal diffusivity of PVA and PVA mixed with gold nanoparticle were found to be $3.07 \times 10^{-4} m^2 s^{-1}$ and $1.22 \times 10^{-4} m^2 s^{-1}$ respectively. The gold incorporated PVA exhibited lower thermal

diffusivity as compared to raw PVA. Though the scattering property of metal nanoparticles significantly affects the total light entering the tissue, the doped sample exhibited approximately 1.85 times lower thermal diffusivity when compared to the raw PVA.

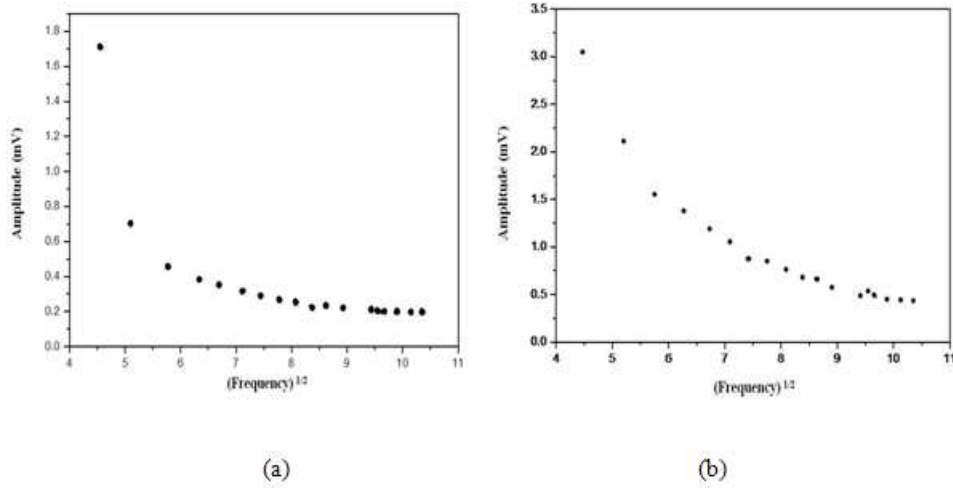


Figure F. 11 PA Amplitude as a function of square root of modulation frequency

a) Bare-PVA phantom b) Au-PVA phantom

It can be also observed that with the presence of gold nanoparticles, the PA signal amplitude is enhanced significantly compared to the PVA phantom sample making them potential photoacoustic signal amplifiers. Therefore the photoacoustic signal contrast of gold nanoparticles mixed with PVA sample is increased by approximately twice that of the PVA sample.

Conclusion

Low frequency photoacoustic investigations performed in OPC configuration demonstrated a non-destructive methodology for the measurement of thermal diffusivity of biological tissue. Thermal diffusivity studies were performed with

colon phantom tissue as well as nanoparticle administered phantom tissues. The reported investigation modality offered a highly accurate and relatively inexpensive measurement tool for determining the thermal diffusivity of various biosamples. FDTD simulations to determine the optical properties of spherical gold nanoparticles showed that larger nanoparticles exhibit dominant scattering efficiencies thus making it more favourable for scattering based imaging applications. Nevertheless, it should be noted that gold nanospheres exhibit lesser red shift and hence offers lesser tunability when compared to core/shell nanoparticles. The experimental results showed that the presence of plasmonic nanoparticles significantly altered the inherent physical and optical properties of the embedding tissue. Determination of these variations was significant as thermal diffusivity variations will introduce undesirable ambiguities into the efficacy of any particular optical imaging or therapeutic modality. A significant reduction in the thermal diffusivity of the PVA sample was observed when doped with gold nanospheres and therefore it is highly recommended to evaluate the thermal diffusivity of any doped sample prior to a diagnostic or therapeutic investigation. The investigations performed demonstrated the capability of plasmonic nanoparticles to act as photoacoustic signal amplifiers and show the proof of concept on the potential of this technique in performing molecular studies on the tissue when doped with bio-conjugated nanoparticles.

APPENDIX G – Methodology For Cancer Diagnostics Using The Proposed Multimodality Imaging System

The proposed diagnostic approach in this context was established from a ‘marker flow chart’ (Figure G. 1) derived from a thorough review and analysis on the various potential markers that can effectively identify the few among the six hallmarks of cancer.

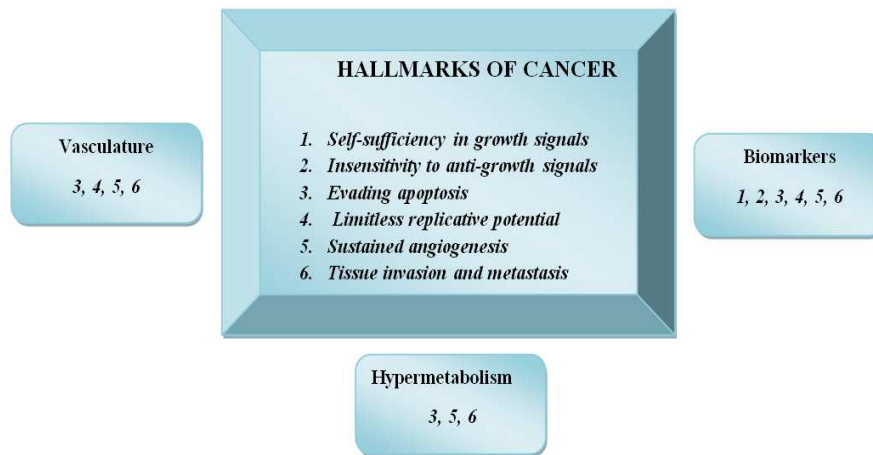


Figure G. 1 Marker flow chart

Figure G. 1 shows that the screening for each of the six hallmarks of cancer can be performed by identifying from the given targeted traits. The numbers in each of the targeted traits are directed at each of the specific hallmarks of cancer. The proposed approach should therefore target into the mapping the vasculature network, identification of the biomarkers as well as looking into various cell activities.

Of note, ultrasound imaging provides satisfactory images of growths from deeper layers of tissue and PA imaging has a unique capability in mapping the capillary network as blood is a very good absorber of light and provides very high intrinsic image contrast. The main contrast of interest is based on the optical

absorption in the photoacoustic excitation phase. Further, specific protein and gene expressions (biomarkers) pertaining to cancer can be targeted by applying particular molecular probes into the tissue. The molecular probes that are tagged into plasmonic nanoplateforms can be mapped with the aid of PAI from deeper layers and various fluorescent signatures from tissue surface can be obtained from the fluorescence data. The exogenous plasmonic nanoparticles and fluorophores when applied in real tissue samples would bind itself to the targeted proteins and genes to provide satisfactory photoacoustic and fluorescent signals that can be mapped into images as well quantitative data. In this context, the ‘marker flow chart’ given in Figure G. 1 can be extended by incorporating the targeted parameters, into a ‘Parameter flow chart’ given in Figure G. 2.

The parameter flow chart illustrated in Figure G. 2 shows that each of the targeted parameters (except hyper-metabolism) can be addressed by identifying two distinct tissue signatures. Vasculature imaging can be realized with the aid of two distinct imaging modalities, namely ultrasound imaging and photoacoustic imaging. Both these imaging modalities can provide high resolution images from thick layers of tissue. While ultrasound imaging produces images of growths and vasculature based on inherent acoustic inhomogeneities in tissue, photoacoustic imaging builds on optical absorption contrast in tissue.

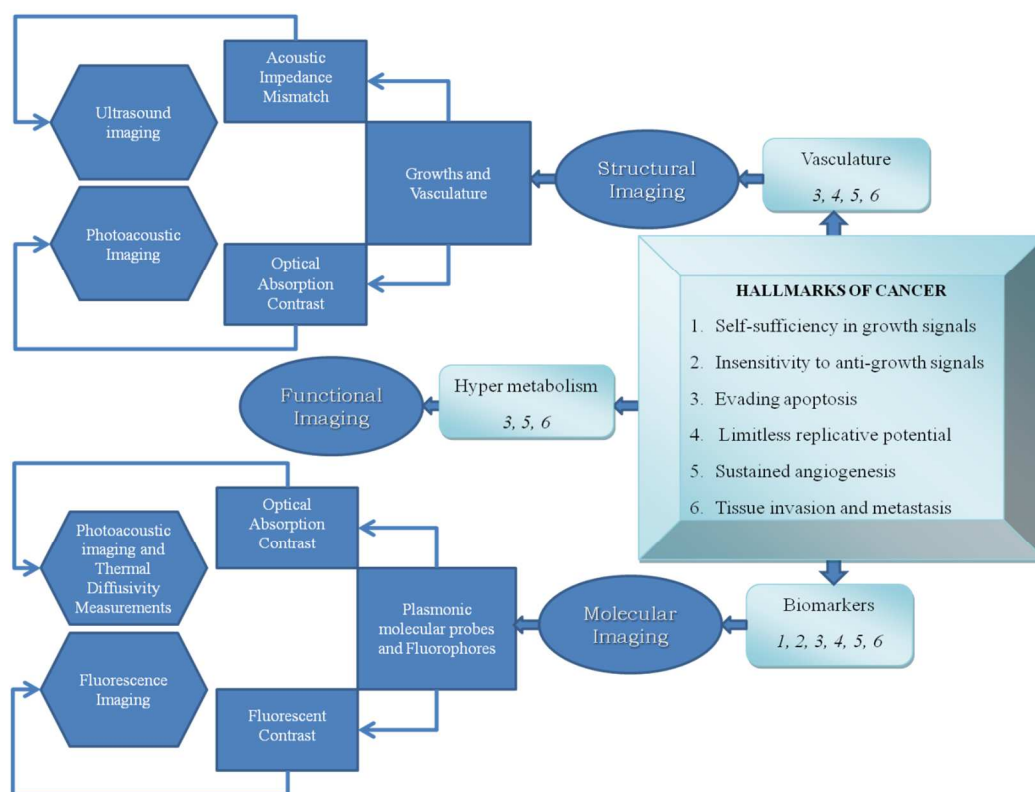


Figure G. 2 Parameter flow chart

Molecular investigations can be realized with both photoacoustic and fluorescence techniques. Photoacoustic and fluorescent molecular probes can be employed with the aid of several kinds of bio-conjugated plasmonic nanomaterials as well as exogenous and indigenous fluorophores. Photoacoustic techniques also have the potential to perform thermal diffusivity and imaging studies with nanoparticle administered tissues. Both these work areas have high prospects in extracting useful information (both quantitative as well as images) based on optical signatures from deep layers of tissue. Fluorescent imaging can be explored towards performing high resolution imaging of the surface layers of tissue which can reveal molecular hallmarks of cancer with single cell resolution. Thus, by leveraging on the acoustic and optical properties of tissue and exogenous molecular probes, the

novel multi-modal imaging scheme proposed in this research is expected to open several avenues for early disease diagnostics such as in cancer.

PUBLICATIONS

Journal Publications

1. **James Joseph**, Krishnan Sathiyamoorthy, T. Visalatchi, V. M. Murukeshan and Lye Sun Woh, ‘Laser-induced photoacoustic spectroscopy investigation of colon phantom tissue’, *Applied Physics A: Materials Science & Processing*, Volume 101, Number 3, 567-571 (2010).
2. **James Joseph**, V. M. Murukeshan, and Lye Sun Woh, ‘Effect of Composition, Dimension and Shape on the Optical Properties of Gold Nanoparticles-A Theoretical Analysis’ *Advanced Science Engineering and Medicine*. 3, 188-196 (2011).
3. **James Joseph**, K Sathiyamoorthy, V. M. Murukeshan, and Lye Sun Woh, ‘Thermal Diffusivity Variations in Nanoparticle Administered Phantom Tissues –A Photoacoustic Investigation’, *European Physical Journal-Applied Physics*, 59, 30501(2012).
4. **James Joseph**, V. M. Murukeshan, and Lye Sun Woh, ‘Integrated photoacoustic, ultrasound and fluorescence imaging for tissue diagnostics’, (Under Review in *Physics in Medicine and Biology*).
5. **James Joseph**, V. M. Murukeshan, and Lye Sun Woh, ‘Integrated laser photoacoustic, ultrasound and fluorescence imaging (PAUSFI) for diagnostic bio-imaging applications’, (Under Review in *Laser physics Letters*).
6. **James Joseph**, V. M. Murukeshan, and Lye Sun Woh, ‘Enhanced Photoacoustic Signal Generation Using Fluorophore-Metal Nanoparticle Platforms in an Integrated Photoacoustic - Fluorescence System’, (Under Review in *Light: Science and Applications*).

7. Sivaramapanicker Sreejith, **James Joseph**, Kim Truc Nguyen, Vadakke Matham Murukeshan, Lye Sun Woh and Yanli Zhao, 'Photoacoustic Signal Enhancement in Graphene Oxide Wrapped Core-Shell Nanohybrids for Multimodal Imaging in Visible Region', (Equal Contribution - Submitted to Nature Asia Materials).

Conference Publications

1. **James Joseph**, Algie Toh, V.M Murukeshan, Lye Sun Woh and Wei Jun, 'Photoacoustic Investigations into the Thermal diffusivity Variations in Optical Phantoms', International Conference on Biomedical Systems, Signals and Images, November 28 – December 1, Chennai, India.
2. **James Joseph**, Murukeshan V.M, Lye Sun Woh, 'Calculation of optical properties of nanoparticles for biomedical applications'. SPIE International Conference on Applications of Optics and Photonics, May 3 to 7, 2011, Braga, Portugal, (*Oral Presentation*).
3. **James Joseph**, Krishnan Sathiyamoorthy, V.M Murukeshan, Lye Sun Woh, 'Photoacoustic investigations of the thermal diffusivity of polyvinyl alcohol (PVA) samples doped with gold nanoparticles for biomedical diagnostics', International Conference on Cellular & Molecular Bioengineering (ICCMB2), 2 – 4 August 2010, Singapore, (*Oral Presentation*).
4. **James Joseph**, Krishnan Sathiyamoorthy, T. Visalatchi, V. M. Murukeshan and Lye Sun Woh, 'Laser-induced photoacoustic spectroscopy investigation of colon phantom tissue', 10th annual Conference on Laser Ablation (COLA), 22-27 November 2009, Singapore, (*Oral Presentation*).

REFERENCES

Adams, M. J. and G. F. Kirkbright (1977). "Analytical optoacoustic spectrometry Part III. The optoacoustic effect and thermal diffusivity." The Analyst **102**(1213): 281-292.

Agarwal, A., et al. (2007). "Targeted gold nanorod contrast agent for prostate cancer detection by photoacoustic imaging." Journal of Applied Physics **102**(6).

Ale, A., et al. (2012). "FMT-XCT: In vivo animal studies with hybrid fluorescence molecular tomography-X-ray computed tomography." Nature Methods **9**(6): 615-620.

Alivisatos, A. P. (1996). "Semiconductor clusters, nanocrystals, and quantum dots." Science **271**(5251): 933-937.

Alric, C., et al. (2008). "Gadolinium Chelate Coated Gold Nanoparticles As Contrast Agents for Both X-ray Computed Tomography and Magnetic Resonance Imaging." Journal of the American Chemical Society **130**(18): 5908-5915.

Arridge, S. R. (1999). "Optical tomography in medical imaging." Inverse Problems **15**(2): R41-R49.

Ayers, F., et al. (2008). "Fabrication and characterization of silicone-based tissue phantoms with tunable optical properties in visible and near infrared domain." SPIE Vol. 6870.

Balageas, D. L., et al. (1986). "Pulsed photothermal modeling of layered materials." Journal of Applied Physics **59**(2): 348-357.

Barone, P. W., et al. (2005). "In vivo fluorescence detection of glucose using a single-walled carbon nanotube optical sensor: Design, fluorophore properties, advantages, and disadvantages." Analytical Chemistry **77**(23): 7556-7562.

Barrow, S. J., et al. (2012). "The surface plasmon modes of self-assembled gold nanocrystals." Nature Communications **3**: 1275.

Bays, R., et al. (1997). "Three-dimensional optical phantom and its application in photodynamic therapy." Lasers in Surgery and Medicine **21**(3): 227-234.

Beckmann, N., et al. (2001). "From anatomy to the target: Contributions of magnetic resonance imaging to preclinical pharmaceutical research." Anatomical Record **265**(2): 85-100.

Bednov, A. A., et al. (2003). Glucose monitoring in whole blood by measuring laser-induced acoustic profiles [4960-04], International Society for Optical Engineering; 1999.

Bell, A. G. (1880). "On the production and reproduction of sound by light." American Journal of Science **20**: 305-324.

Beyer, T., et al. (2000). "A combined PET/CT scanner for clinical oncology." Journal of Nuclear Medicine **41**(8): 1369-1379.

Bioud, F.-Z. and Y. Bérubé-Lauzière (2008). "Fabrication and characterization of optical phantoms." Proc. SPIE 7099, 709906.

Bolin, F. and L. Preuss (1989). "Refractive index of some mammalian tissues using a fiber optic cladding method." Applied Optics: 28:2297-2303.

Brown, J. A. and G. R. Lockwood (2005). "A digital beamformer for high-frequency annular arrays." IEEE Transactions on Ultrasonics, Ferroelectrics, and Frequency Control **52**(8): 1262-1269.

Burgholzer, P., et al. (2007). "Temporal back-projection algorithms for photoacoustic tomography with integrating line detectors." Inverse Problems **23**(6): S65-S80.

Burgholzer, P., et al. (2005). "Thermoacoustic tomography with integrating area and line detectors." IEEE Transactions on Ultrasonics, Ferroelectrics, and Frequency Control **52**(9): 1577-1583.

Burgholzer, P., et al. (2007). "Exact and approximative imaging methods for photoacoustic tomography using an arbitrary detection surface." Physical Review E - Statistical, Nonlinear, and Soft Matter Physics **75**(4).

Campion, A., et al. (1980). "Electronic energy transfer to metal surfaces: A test of classical image dipole theory at short distances." Chem. Phys. Lett. **73**(3): 447-450.

- Catana, C., et al. (2006). "Simultaneous acquisition of multislice PET and MR images: Initial results with a MR-compatible PET scanner." Journal of Nuclear Medicine **47**(12): 1968-1976.
- Chan, W. C. W. and S. Nie (1998). "Quantum dot bioconjugates for ultrasensitive nonisotopic detection." Science **281**(5385): 2016-2018.
- Chance, R. R., et al. (1978). "Molecular fluorescence and energy transfer near interfaces." Adv. Chem. Phys. **37**: 1-65.
- Chardon, D. and S. J. Huard (1982). "Thermal diffusivity of optical fibers measured by photoacoustics." Applied Physics Letters **41**: 341.
- Charron, M., et al. (2000). "Image analysis in patients with cancer studied with a combined PET and CT scanner." Clinical Nuclear Medicine **25**(11): 905-910.
- Chen, H. and G. Diebold (1995). "Chemical generation of acoustic waves: A giant photoacoustic effect." Science **270**(5238): 963-966.
- Cherry, S. R. (2006). "Multimodality in vivo imaging systems: Twice the power or double the trouble?" Annual Review of Biomedical Engineering **8**: 35-62.
- Cherry, S. R. (2009). "Multimodality Imaging: Beyond PET/CT and SPECT/CT." Seminars in Nuclear Medicine **39**(5): 348-353.
- Cherry, S. R., et al. (2008). "The integration of positron emission tomography with magnetic resonance imaging." Proceedings of the IEEE **96**(3): 416-438.
- Choukeife, J. and J. P. L'Huillier (1999). "Measurements of Scattering Effects Within Tissue-like Media at Two Wavelengths of 632.8nm and 680nm." Lasers in medical Science, **14**: 286-296.
- Christensen, D. A. (1988). Ultrasonic bioinstrumentation. Newyork, Wiley.
- Chu, Y., et al. (2008). "Experimental observation of narrow surface plasmon resonances in gold nanoparticle arrays." Applied Physics Letters **93**(18): 181108-181108-181103.

Committee, A. S. (1984). Standard Specification of Echoscope Sensitivity and Noise Level Including Recommended Practice for Such Measurements, AIUM Publications.

Da Silva, A. J., et al. (2001). "Absolute quantification of regional myocardial uptake of ^{99m}Tc -sestamibi with SPECT: Experimental validation in a porcine model." Journal of Nuclear Medicine **42**(5): 772-779.

Dulkeith, E., et al. (2005). "Gold nanoparticles quench fluorescence by phase induced radiative rate suppression." Nano Letters **5**(4): 585-589.

Dykman, L. A. and V. A. Bogatyrev (2007). "Gold nanoparticles: Preparation, functionalisation and applications in biochemistry and immunochemistry." Russian Chemical Reviews **76**(2): 181-194.

Elghanian, R., et al. (1997). "Selective colorimetric detection of polynucleotides based on the distance-dependent optical properties of gold nanoparticles." Science **277**(5329): 1078-1081.

Fahrig, R., et al. (2008). "Design, performance, and applications of a hybrid X-Ray/MR system for interventional guidance." Proceedings of the IEEE **96**(3): 468-480.

Firbank, M. and D. T. Delpy (1993). "A design for a stable and reproducible phantom for use in near infra-red imaging and spectroscopy." Physics in Medicine and Biology **38**(6): 847-853.

Firbank, M., et al. (1995). "An improved design for a stable and reproducible phantom material for use in near-infrared spectroscopy and imaging." Physics in Medicine and Biology **40**(5).

Flusberg, B. A., et al. (2005). "In vivo brain imaging using a portable 3.9 gram two-photon fluorescence microendoscope." Optics Letters **30**(17): 2272-2274.

Futamata, M., et al. (2003). "Local electric field and scattering cross section of Ag nanoparticles under surface plasmon resonance by finite difference time domain method." The Journal of Physical Chemistry B **107**(31): 7607-7617.

Gans, R. (1915). "Form of ultramicroscopic particles of silver." Annals of Physics **47**: 270-284.

- Gao, C. M., et al. (2005). "Thermal diffusivity of porcine tissues characterized by photoacoustic piezoelectric technique." Journal De Physique. IV : JP **125**: 777-779.
- Gao, X., et al. (2002). "Quantum-dot nanocrystals for ultrasensitive biological labeling and multicolor optical encoding." Journal of Biomedical Optics **7**(4): 532-537.
- George, N. A., et al. (2002). "Photoacoustic studies on n-type InP." Optical Engineering **41**(1): 251-254.
- Gibson, A. P., et al. (2005). "Recent advances in diffuse optical imaging." Physics in Medicine and Biology **50**(4): R1-R43.
- Han, G., et al. (2007). "Functionalized gold nanoparticles for drug delivery." Nanomedicine **2**(1): 113-123.
- Hanahan D, W. R. (2000). "The Hallmarks of Cancer " Cell **100**: 57-70.
- Hasegawa, B. H., et al. (2002). "Dual-modality imaging of function and physiology." Academic Radiology **9**(11): 1305-1321.
- Hayakawa, T., et al. (1999). "Field enhancement effect of small Ag particles on the fluorescence from Eu³⁺-doped SiO₂ glass." Applied Physics Letters **74**(11): 1513-1515.
- Health, H. (2012). "Guide to Diagnostic Tests." Retrieved 16 July 2012.
- Hedrick, W. R., et al. (2005). Ultrasound Physics And Instrumentation. Maryland Heights, Mosby.
- Heller, D. A., et al. (2005). "Single-walled carbon nanotube spectroscopy in live cells: Towards long-term labels and optical sensors." Advanced Materials **17**(23): 2793-2799.
- Heller, D. A., et al. (2006). "Optical detection of DNA conformational polymorphism on single-walled carbon nanotubes." Science **311**(5760): 508-511.
- Hidović-Rowe, D. and E. Claridge (2005). "Modelling and validation of spectral reflectance for the colon." Physics in Medicine and Biology **50**(6): 1071-1093.

- Hill, D. L. G., et al. (2001). "Medical image registration." Physics in Medicine and Biology **46**(3): R1-R45.
- Hofmann, M., et al. (2008). "MRI-based attenuation correction for PET/MRI: A novel approach combining pattern recognition and atlas registration." Journal of Nuclear Medicine **49**(11): 1875-1883.
- Huang, X., et al. (2009). "Gold Nanorods: From Synthesis and Properties to Biological and Biomedical Applications." Advanced Materials **21**(48): 4880-4910.
- Huang Z, Z. W., Xie S, Chen R (2004). "Laser induced autofluorescence microscopy of normal and tumor human colonic tissue." International Journal of Oncology **24**: 59-63.
- Iwata, K., et al. (2002). "Development of combined CT-SPECT system for small animal imaging with A-SPECT." Radiology **225**(SUPPL. S): 409.
- Jaeger, M., et al. (2007). "Fourier reconstruction in optoacoustic imaging using truncated regularized inverse k-space interpolation." Inverse Problems **23**(6): S51-S63.
- Jain, P. K. and M. A. El-Sayed (2007). "Universal scaling of plasmon coupling in metal nanostructures: Extension from particle pairs to nanoshells." Nano Letters **7**(9): 2854-2858.
- Jain, P. K., et al. (2006). "Calculated absorption and scattering properties of gold nanoparticles of different size, shape, and composition: Applications in biological imaging and biomedicine." Journal of Physical Chemistry B **110**(14): 7238-7248.
- Jain, R. K., et al. (2002). "Dissecting tumour pathophysiology using intravital microscopy." Nature Reviews Cancer **2**(4): 266-276.
- James Joseph, K. S., T. Visalatchi, V. M. Murukeshan and Lye Sun Woh (2010). "Laser-induced photoacoustic spectroscopy investigation of colon phantom tissue." Applied Physics A: Materials Science & Processing **101**(3).
- James Joseph, K. S., V. M. Murukeshan, and Lye Sun Woh (2012). "Thermal Diffusivity Variations in Nanoparticle Administered Phantom Tissues –A Photoacoustic Investigation." European Physical Journal- Applied Physics **59**.

- James Joseph, V. M. M., Lye Sun Woh (2011). "Effect of Composition, Dimension and Shape on the Optical Properties of Gold Nanoparticles - A Theoretical Analysis" Advanced Science, Engineering and Medicine **3**(3): 176-182.
- Jin, Y., et al. (2010). "Multifunctional nanoparticles as coupled contrast agents." Nature Communications **1**: 41.
- Johnson, P. B. and R. W. Christy (1972). "Optical constants of the noble metals." Physical Review B **6**(12): 4370-4379.
- Judenhofer, M. S., et al. (2008). "Simultaneous PET-MRI: A new approach for functional and morphological imaging." Nature Medicine **14**(4): 459-465.
- Jung, I., et al. (2008). "Characterization of Thermally Reduced Graphene Oxide by Imaging Ellipsometry." The Journal of Physical Chemistry C **112**(23): 8499-8506.
- Jung, J. C., et al. (2004). "In vivo mammalian brain imaging using one- and two-photon fluorescence microendoscopy." Journal of Neurophysiology **92**(5): 3121-3133.
- Kalki, K., et al. (1997). "Myocardial perfusion imaging with a combined X-ray CT and SPECT system." Journal of Nuclear Medicine **38**(10): 1535-1540.
- Kam, N. W. S., et al. (2005). "Carbon nanotubes as multifunctional biological transporters and near-infrared agents for selective cancer cell destruction." Proceedings of the National Academy of Sciences of the United States of America **102**(33): 11600-11605.
- Kiesslich, R., et al. (2004). "Confocal laser endoscopy for diagnosing intraepithelial neoplasias and colorectal cancer in vivo." Gastroenterology **127**(3): 706-713.
- Kim, C., et al. (2010). "Deeply penetrating in vivo photoacoustic imaging using a clinical ultrasound array system." Biomedical Optics Express **1**(1): 278-284.
- Kim, C., et al. (2008). "Optical Phantoms for ultrasound modulated optical tomography." SPIE Vol. 6870 68700M-1.
- Kim, D., et al. (2007). "Antibiofouling Polymer-Coated Gold Nanoparticles as a Contrast Agent for in Vivo X-ray Computed Tomography Imaging." Journal of the American Chemical Society **129**(24): 7661-7665.

- Kramer, A., et al. (2002). "Optical near-field enhancement at a metal tip probed by a single fluorophore." Applied Physics Letters **80**(9): 1652-1654.
- Krenn, J. R., et al. (1999). "Direct observation of localized surface plasmon coupling." Physical Review B - Condensed Matter and Materials Physics **60**(7): 5029-5033.
- Kreuzer, L. B. (1971). "Ultralow gas concentration infrared absorption spectroscopy" Journal of Applied Physics **42**: 2934-2943
- Kruger, R. A., et al. (1999). "Thermoacoustic computed tomography-technical considerations." Medical Physics **26**(9): 1832-1837.
- Ku, G. and L. V. Wang (2005). "Deeply penetrating photoacoustic tomography in biological tissues enhanced with an optical contrast agent." Optics Letters **30**(5): 507-509.
- Kunyansky, L. A. (2007). "A series solution and a fast algorithm for the inversion of the spherical mean Radon transform." Inverse Problems **23**(6): S11-S20.
- Lakowicz, J. R. (2001). "Radiative decay engineering: Biophysical and biomedical applications." Analytical Biochemistry **298**(1): 1-24.
- Lee, K. S. and M. A. El-Sayed (2005). "Dependence of the enhanced optical scattering efficiency relative to that of absorption for gold metal nanorods on aspect ratio, size, end-cap shape, and medium refractive index." Journal of Physical Chemistry B **109**(43): 20331-20338.
- Levene, M. J., et al. (2004). "In Vivo Multiphoton Microscopy of Deep Brain Tissue." Journal of Neurophysiology **91**(4): 1908-1912.
- Li, C. and L. V. Wang (2009). "Photoacoustic tomography and sensing in biomedicine." Physics in Medicine and Biology **54**(19): R59-R97.
- Li, C., et al. (2011). "Simultaneous PET and multispectral 3-dimensional fluorescence optical tomography imaging system." Journal of Nuclear Medicine **52**(8): 1268-1275.

Li, X. and D. C. Liu (2009). Dynamic persistence of ultrasound images after local tissue motion tracking. 3rd International Conference on Bioinformatics and Biomedical Engineering, iCBBE 2009 Beijing.

Lihong V. Wang, H.-I. W. (2007). Biomedical Optics: Principles and Imaging, Wiley-Interscience.

Lim, M. Y., et al. (2009). "Photoacoustic measurement of thermal diffusivity of polypyrrole conducting polymer composite films." American Journal of Applied Sciences **6**(2): 313-316.

Link, S. and M. A. El-Sayed (2000). "Shape and size dependence of radiative, non-radiative and photothermal properties of gold nanocrystals." International Reviews in Physical Chemistry **19**(3): 409-453.

Link, S. and M. A. El-Sayed (2005). "Erratum: Simulation of the optical absorption spectra of gold nanorods as a function of their aspect ratio and the effect of the medium dielectric constant (Journal of Physical Chemistry B (1999) 103B)." Journal of Physical Chemistry B **109**(20): 10531-10532.

Link, S., et al. (1999). "Simulation of the optical absorption spectra of gold nanorods as a function of their aspect ratio and the effect of the medium dielectric constant." Journal of Physical Chemistry B **103**(16): 3073-3077.

Liu, M., et al. (2007). "Optical properties of rodlike and bipyramidal gold nanoparticles from three-dimensional computations." Physical Review B **76**(23): 235428.

Liu, X., et al. (2008). "A one-step homogeneous immunoassay for cancer biomarker detection using gold nanoparticle probes coupled with dynamic light scattering." Journal of the American Chemical Society **130**(9): 2780-2782.

Liu, Z., et al. (2007). "In vivo biodistribution and highly efficient tumour targeting of carbon nanotubes in mice." Nature Nanotechnology **2**(1): 47-52.

Loo, C., et al. (2004). "Nanoshell-Enabled Photonics-Based Imaging and Therapy of Cancer." Technology in Cancer Research and Treatment **3**(1): 33-40.

Loo, C., et al. (2005). "Immunotargeted nanoshells for integrated cancer imaging and therapy." Nano Letters **5**(4): 709-711.

- Lualdi, M., et al. (2001). "A phantom with tissue-like optical properties in the visible and near infrared for use in photomedicine." Lasers in Surgery and Medicine: 28:237-243.
- Lucas, A. J., et al. (2006). "Development of a combined microPET®-MR system." Technology in Cancer Research and Treatment 5(4): 337-341.
- Luo, P. G. and F. J. Stutzenberger (2008). "Nanotechnology in the Detection and Control of Microorganisms." Advances in Applied Microbiology 63: 145-181.
- Lyon, J. L., et al. (2004). "Synthesis of Fe oxide Core/Au shell nanoparticles by iterative hydroxylamine seeding." Nano Letters 4(4): 719-723.
- Malko, J. A., et al. (1986). "SPECT liver imaging using an iterative attenuation correction algorithm and an external flood source." Journal of nuclear medicine : official publication, Society of Nuclear Medicine 27(5): 701-705.
- Mallidi, S., et al. (2011). "Photoacoustic imaging in cancer detection, diagnosis, and treatment guidance." Trends in biotechnology 29(5): 213-221.
- Manohar, S., et al. (2007). "Initial results of in vivo non-invasive cancer imaging in the human breast using near-infrared photoacoustics." Optics Express 15(19): 12277-12285.
- Marchesini, R., et al. (1994). "Ex vivo optical properties of human colon tissue." Lasers in Surgery and Medicine 15(4): 351-357.
- Maslov, K., et al. (2008). "Optical-resolution photoacoustic microscopy for in vivo imaging of single capillaries." Optics Letters 33(9): 929-931.
- Michels, R., et al. (2008). "Optical properties of fat emulsions." Optics Express 16(8).
- Mie, G. (1908). "Beiträge zur optik trüber medien, speziell kolloidaler metallösungen." Annals of Physics 25: 377-445.
- Mincu, N., et al. (2008). "Diffuse optical tomography and spectroscopy performance assessment: phantoms and methodology." SPIE Vol. 6870 68700O-1.

- Modgil, D., et al. (2009). "Image reconstruction in photoacoustic tomography with variable speed of sound using a higher-order geometrical acoustics approximation." Progress in Biomedical Optics and Imaging - Proceedings of SPIE **7177**.
- Moffitt, T., et al. (2006). "Preparation and characterization of polyurethane optical phantoms." Journal of Biomedical Optics, **11**, 041103.
- Moghim, S. M. and T. Kissel (2006). "Particulate nanomedicines." Advanced Drug Delivery Reviews **58**(14): 1451-1455.
- Mohr, M., et al. (2001). "Analysis of type 2 immunity in vivo with a bicistronic IL-4 reporter." Immunity **15**(2): 303-311.
- Moriggi, L. c., et al. (2009). "Gold Nanoparticles Functionalized with Gadolinium Chelates as High-Relaxivity MRI Contrast Agents." Journal of the American Chemical Society **131**(31): 10828-10829.
- Murugesan, V. M. and N. Sujatha (2007). "All fiber based multispeckle modality endoscopic system for imaging medical cavities." Review of Scientific Instruments **78**(5).
- Murugesan, V. M. and N. U. Sujatha (2005). "Integrated simultaneous dual-modality imaging endospeckle fluoroscope system for early colon cancer diagnosis." Optical Engineering **44**(11).
- Nehme, S. A., et al. (2004). "Four-dimensional (4D) PET/CT imaging of the thorax." Medical Physics **31**(12): 3179-3186.
- Ng, T. S. C., et al. (2012). "Quantitative, simultaneous PET/MRI for intratumoral imaging with an MRI-compatible PET scanner." Journal of Nuclear Medicine **53**(7): 1102-1109.
- Novotny, L. (1996). "Single molecule fluorescence in inhomogeneous environments." Applied Physics Letters **69**(25): 3806-3808.
- Ntzachristos, V. (2006). "Fluorescence molecular imaging." Annual Review of Biomedical Engineering **8**: 1-33.
- Ntzachristos, V., et al. (2005). "Looking and listening to light: The evolution of whole-body photonic imaging." Nature Biotechnology **23**(3): 313-320.

- Ntziachristos, V., et al. (2004). "Visualization of antitumor treatment by means of fluorescence molecular tomography with an annexin V-Cy5.5 conjugate." Proceedings of the National Academy of Sciences of the United States of America **101**(33): 12294-12299.
- Ntziachristos, V., et al. (2000). "Concurrent MRI and diffuse optical tomography of breast after indocyanine green enhancement." Proceedings of the National Academy of Sciences of the United States of America **97**(6): 2767-2772.
- Ntziachristos, V., et al. (2002). "MRI-guided diffuse optical spectroscopy of malignant and benign breast lesions." Neoplasia **4**(4): 347-354.
- Oldenburg, S. J., et al. (1998). "Nanoengineering of optical resonances." Chemical Physics Letters **288**(2-4): 243-247.
- Oldenburg, S. J., et al. (1999). "Light scattering from dipole and quadrupole nanoshell antennas." Applied Physics Letters **75**(8): 1063-1065.
- Oraevsky, A. A., et al. (1997). "Measurement of tissue optical properties by time-resolved detection of laser-induced transient stress." Applied Optics **36**(1): 402-415.
- Ota, T., et al. (2005). "In situ fluorescence imaging of organs through compact scanning head for confocal laser microscopy." Journal of Biomedical Optics **10**(2): 024010.
- Palik, E. D. (1985). Handbook of Optical Constants of Solids. Orlando, Academic Press.
- Paltauf, G., et al. (2007). "Photoacoustic tomography using a Mach-Zehnder interferometer as an acoustic line detector." Applied Optics **46**(16): 3352-3358.
- Panyala, N. R., et al. (2009). "Gold and nano-gold in medicine: Overview, toxicology and perspectives." Journal of Applied Biomedicine **7**(2): 75-91.
- Patel, C. K. N. and A. C. Tam (1979). "Optical absorption coefficients of water[4]." Nature **280**(5720): 302-304.
- Patel, C. K. N. and A. C. Tam (1981). "Pulsed optoacoustic spectroscopy of condensed matter." Reviews of Modern Physics **53**(3): 517-550.

- Patterson, M. S. and B. W. Pogue (2006). "Review of tissue simulating phantoms for optical spectroscopy, imaging and dosimetry." Journal of Biomedical Optics 11 (4), 041102: 9-10.
- Phelps, M. E. (2000). "Positron emission tomography provides molecular imaging of biological processes." Proceedings of the National Academy of Sciences of the United States of America 97(16): 9226-9233.
- Popovtzer, R., et al. (2008). "Targeted Gold Nanoparticles Enable Molecular CT Imaging of Cancer." Nano Letters 8(12): 4593-4596.
- Prescott, S. W. and P. Mulvaney (2006). "Gold nanorod extinction spectra." Journal of Applied Physics 99(12).
- Prout, D. L., et al. (2004). "Detector concept for OPET - A combined PET and optical imaging system." IEEE Transactions on Nuclear Science 51(3 II): 752-756.
- Qiu, P. F., et al. (2008). "Photoacoustic study of thermal properties of biological tissues detected by PVDF film transducer." European Physical Journal: Special Topics 153(1): 487-490.
- Rao, B., et al. (2011). "Real-time four-dimensional optical-resolution photoacoustic microscopy with Au nanoparticle-assisted subdiffraction-limit resolution." Optics Letters 36(7): 1137-1139.
- Razansky, D., et al. (2011). "Volumetric real-time multispectral optoacoustic tomography of biomarkers." Nature Protocols 6(8): 1121-1129.
- Razansky, D., et al. (2009). "Multispectral opto-acoustic tomography of deep-seated fluorescent proteins in vivo." Nature Photonics 3(7): 412-417.
- Rosencwaig, A. (1973). "Photoacoustic spectroscopy of biological materials." Science 181(4100): 657-658.
- Rosencwaig, A. (1980). Photoacoustics and Photoacoustic Spectroscopy.
- Rosencwaig, A. and A. Gersho (1976). "Theory of the photoacoustic effect with solids." Journal of Applied Physics 47(1): 64-69.

- Rudin, M., et al. (1999). "In vivo magnetic resonance methods in pharmaceutical research: Current status and perspectives." NMR in Biomedicine **12**(2): 69-97.
- Sathiyamoorthy, K. and C. Vijayan (2007). "Photoacoustic investigations on self-organization effects in metalloporphyrins on glass substrates." Materials Letters **61**(19-20): 4156-4159.
- Sathiyamoorthy, K., et al. (2007). "Simple technique for obtaining photoacoustic spectra corrected for the spectral variation of the source in single scan." Review of Scientific Instruments **78**(4).
- Schlemmer, H. P. W., et al. (2008). "Simultaneous MR/PET imaging of the human brain: Feasibility study." Radiology **248**(3): 1028-1035.
- Schultz, S., et al. (2000). "Single-target molecule detection with nonbleaching multicolor optical immunolabels." Proceedings of the National Academy of Sciences of the United States of America **97**(3): 996-1001.
- Selvan, S. T., et al. (1999). "Remarkable influence of silver islands on the enhancement of fluorescence from Eu³⁺ ion-doped silica gels." Journal of Physical Chemistry B **103**(34): 7064-7067.
- Shekhar, R., et al. (2005). "Automated 3-dimensional elastic registration of whole-body PET and CT from separate or combined scanners." Journal of Nuclear Medicine **46**(9): 1488-1496.
- Shim, S. Y., et al. (2008). "Ultrasensitive optical biodiagnostic methods using metallic nanoparticles." Nanomedicine **3**(2): 215-232.
- Shimizu, K. T., et al. (2002). "Surface-enhanced emission from single semiconductor nanocrystals." Physical Review Letters **89**(11): 117401/117401-117401/117404.
- Sigrist, M. W., et al. (2000). Sensitive and selective monitoring of trace gases by laser photoacoustic spectroscopy.
- Slomka, P. J., et al. (2001). "Evaluation of voxel-based registration of 3-D power Doppler ultrasound and 3-D magnetic resonance angiographic images of carotid arteries." Ultrasound in Medicine and Biology **27**(7): 945-955.

Sokolov, K., et al. (1998). "Enhancement of Molecular Fluorescence near the Surface of Colloidal Metal Films." Analytical Chemistry **70**(18): 3898-3905.

Solomon, M., et al. (2011). "Optical imaging in cancer research: Basic principles, tumor detection, and therapeutic monitoring." Medical Principles and Practice **20**(5): 397-415.

Sönnichsen, C., et al. (2005). "A molecular ruler based on plasmon coupling of single gold and silver nanoparticles." Nature Biotechnology **23**(6): 741-745.

Srinivasan, R., et al. (2002). "Optical Tissue-Equivalent phantoms for Medical Imaging." **15 (2), pp 42-47**.

Stewart, M. E., et al. (2008). "Nanostructured plasmonic sensors." Chemical Reviews **108**(2): 494-521.

Studholme, C., et al. (2000). "Accurate alignment of functional EPI data to anatomical MRI using a physics-based distortion model." IEEE Transactions on Medical Imaging **19**(11): 1115-1127.

Sujatha, N., et al. (2003). "An all fiber optic system modeling for the gastrointestinal endoscopy: Design concepts and fluorescent analysis." Optics Communications **219**(1-6): 71-79.

Sujatha, N. U. and V. M. Murukeshan (2004). "Nondestructive inspection of tissue/tissue like phantom curved surfaces using digital speckle shearography." Optical Engineering **43**(12): 3055-3060.

Sukowski, U., et al. (1996). "Preparation of solid phantoms with defined scattering and absorption properties for optical tomography." Physics in Medicine and Biology, **41**: 1823-1844.

Swindle, L. D., et al. (2003). "View of Normal Human Skin In Vivo as Observed Using Fluorescent Fiber-Optic Confocal Microscopic Imaging." Journal of Investigative Dermatology **121**(4): 706-712.

Szabó, T. L. (2004). Diagnostic Ultrasound Imaging: Inside Out: Inside Out, Academic Press.

Tahir, K. and C. Dainty (2005). "Experimental measurements of light scattering from samples with specified optical properties." Journal of Optics A: Pure and Applied Optics **7**: 207-214.

Tam, A. C. and C. K. N. Patel (1979). "OPTICAL ABSORPTIONS OF LIGHT AND HEAVY WATER BY LASER OPTOACOUSTIC SPECTROSCOPY." Applied Optics **18**(19): 3348-3358.

Tanev, S., et al. (2006). "Light scattering effects of gold nanoparticles in cells: FDTD modeling." Laser Physics Letters **3**(12): 594-598.

Tang, H. R., et al. (1997). "Use of X-ray CT-defined regions of interest for the determination of SPECT recovery coefficients." IEEE Transactions on Nuclear Science **44**(4 PART 1): 1594-1599.

Telenkov, S. A. and A. Mandelis (2006). "Fourier-domain biophotoacoustic subsurface depth selective amplitude and phase imaging of turbid phantoms and biological tissue." Journal of Biomedical Optics **11**(4).

Telenkov, S. A., et al. (2001). "Non-contact measurement of thermal diffusivity in tissue." Physics in Medicine and Biology **46**(2): 551-558.

Thomasson, D. M., et al. (2004). "A primer on molecular biology for imagers: VIII. Equipment for imaging molecular processes." Academic Radiology **11**(10): 1159-1170.

Townsend, D. W., et al. (2003). "PET/CT scanners: A hardware approach to image fusion." Seminars in Nuclear Medicine **33**(3): 193-204.

Townsend, D. W. and S. R. Cherry (2001). "Combining anatomy and function: The path to true image fusion." European Radiology **11**(10): 1968-1974.

Trabesinger, W., et al. (2002). "Single-molecule near-field optical energy transfer microscopy." Applied Physics Letters **81**(11): 2118-2120.

Tuchin, V. V. (2007). Tissue Optics: Light Scattering Methods and Instruments for Medical Diagnosis, SPIE Press.

Tuchin, V. V. (2007). "Tissue optics: Light scattering methods and instruments for medical diagnosis ed 2." Bellingham SPIE Publications.

- Tung, C. H. (2004). "Fluorescent peptide probes for in vivo diagnostic imaging." Biopolymers - Peptide Science Section **76**(5): 391-403.
- Ungureanu, C., et al. (2009). "Discrete dipole approximation simulations of gold nanorod optical properties: Choice of input parameters and comparison with experiment." Journal of Applied Physics **105**(10).
- Valvano, J. W., et al. (1985). "Thermal conductivity and diffusivity of biomaterials measured with self-heated thermistors." International Journal of Thermophysics **6**(3): 301-311.
- Viator, J. A. and S. A. Prahl (1999). "Photoacoustic imaging of gelatin phantoms using matched field processing." PROC SPIE, 3601: 276-283.
- Wagner, R. (1839). Erläuterungstafeln Zur Physiologie und Entwicklungsgeschichte.
- Wang, L. V. (2008). "Prospects of photoacoustic tomography." Medical Physics **35**(12): 5758-5767.
- Wang, L. V. (2008). "Tutorial on photoacoustic microscopy and computed tomography." IEEE Journal on Selected Topics in Quantum Electronics **14**(1): 171-179.
- Wang, L. V. and S. Hu (2012). "Photoacoustic tomography: In vivo imaging from organelles to organs." Science **335**(6075): 1458-1462.
- Wang, L. V. and H. Wu (2007). Biomedical Optics: Principles and Imaging, Wiley.
- Wang, L. V., et al. (1999). "Microwave-induced acoustic imaging of biological tissues." Review of Scientific Instruments **70**(9): 3744-3748.
- Wang, Y. H., et al. (2012). "Photoacoustic/ultrasound dual-modality contrast agent and its application to thermotherapy." Journal of Biomedical Optics **17**(4): 045001.
- Weisenberger, A. G., et al. (2003). "SPECT-CT system for small animal imaging." IEEE Transactions on Nuclear Science **50** I(1): 74-79.

Weissleder, R. (2002). "Scaling down imaging: Molecular mapping of cancer in mice." Nature Reviews Cancer **2**(1): 11-18.

Weissleder, R. and V. Ntziachristos (2003). "Shedding light onto live molecular targets." Nature Medicine **9**(1): 123-128.

Weissleder, R. and M. J. Pittet (2008). "Imaging in the era of molecular oncology." Nature **452**(7187): 580-589.

Weissleder, R., et al. (1999). "In vivo imaging of tumors with protease-activated near-infrared fluorescent probes." Nature Biotechnology **17**(4): 375-378.

Wells, P. N. T. (1977). "Ultrasonics in medicine and biology." Physics in Medicine and Biology **22**(4): 629-669.

Wells, P. N. T. (2006). "Ultrasound imaging." Physics in Medicine and Biology **51**(13): R83-R98.

Wells, P. N. T. (2006). "Ultrasound imaging." Physics in Medicine and Biology **51**(13): R83.

Wilson, K., et al. (2012). "Biomedical photoacoustics beyond thermal expansion using triggered nanodroplet vaporization for contrast-enhanced imaging." Nature Communications **3**.

Xu, M. and L. V. Wang (2006). "Photoacoustic imaging in biomedicine." Review of Scientific Instruments **77**(4).

Yguerabide, J. and E. E. Yguerabide (2001). "Resonance light scattering particles as ultrasensitive labels for detection of analytes in a wide range of applications." Journal of cellular biochemistry. Supplement **Suppl 37**: 71-81.

Zell, K., et al. (2007). "Acoustical Properties of selected phantom materials for optoacoustics." Physics in Medicine and Biology **52**: N475-N484.

Zhang, H. F., et al. (2006). "Functional photoacoustic microscopy for high-resolution and noninvasive in vivo imaging." Nature Biotechnology **24**(7): 848-851.

Zucker, R. (2006). Evaluation of Confocal Microscopy System Performance. Cell Imaging Techniques. D. Taatjes and B. Mossman, Humana Press. **319**: 77-135.